HIGH QUALITY SILICON PHOTONIC DEVICES BASED ON HETEROGENEOUS INTEGRATION METHOD

A Dissertation
SUBMITTED TO THE FACULTY OF
UNIVERSITY OF MINNESOTA
BY

Yu Chen

IN PARTIAL FULFILLMENT OF THE REQUIREMENTS
FOR THE DEGREE OF
DOCTOR OF PHILOSOPHY

Mo Li

August 2014

ACKNOWLEDGEMENT

First and foremost, I would like to thank my advisor, Prof. Mo Li, for all his support and guidance throughout all my Ph.D. years. I joined the group as his very first generation of graduate students, without too much knowledge background in silicon photonics, I started very slowly at the beginning. However, Prof. Mo Li is extremely patient and gives me unconditional trust, I learnt so much not only from building the lab and discussing research issues with him, but also solely from his prudent and uncompromised attitude towards scientific research, which has encouraged me and lightened the path along my Ph.D. years. On the other hand, he is extremely helpful and supportive beyond the academia, he truly cares the group members like friends. His insight, creativity and passions towards both research and life will always be the most invaluable thing I learnt from him through all these years and I feel extremely lucky to be able to be his students.

In addition to my advisor, I want to thank many other extraordinary professors that I have met at University of Minnesota. Especially, Prof. Heiko O Jacobs, within whose group I have stayed for half a year. It is him who makes me become interested in the field of heterogeneous integration method and bring such idea into the field of silicon photonics. Moreover, I would like to thank Prof. Steven J Koester for his guidance in my semiconductor studies and Prof. Joey Talghader for his guidance in my microsystem and optoelectronics studies.

With great honor, I have been able to collaborate with other extraordinary researchers from other institutions during my Ph.D. study, and I would like to thank Prof.

Juejun Hu and his graduate student Hongtao Lin for their help and support during our collaboration towards the development of heterogeneously integrated mid-infrared silicon photonic devices. Also, I would like to thank Prof. Axel Scherer and his graduate student William Fegadolli from Caltech for their great contributions towards the development of nanobeam cavity based gas phase chemical sensor.

Within our group, I have received innumerous help from all of my group members in both aspects of research and life. I would like to thank Huan Li, Semere Tadesse, Nathan Youngblood, Li He and Che Chen for their support and meaningful suggestions while I stumbled during my research.

At last I would like to thank my parents and my beloved Diane, thanks for all your love and care for all these years, with which I can always find courage and passion at even the darkest moment of my life. You are always the most invaluable and irreplaceable people in my life, I feel, deep in my heart, lucky to have all of you in my life and this thesis is dedicated to all three of you.

ABSTRACT

Having been widely utilized as the foundation material for CMOS industry, with high refractive index and large spectrum transparency window, silicon has also long been considered as a perfect platform for photonics applications. Optical structures such as microcavities, photonic crystals, interferometers and etc. have already been demonstrated as on-chip silicon photonic devices. Such platforms have already been utilized in different applications such as high speed optical signal processing, optomechanical system demonstration, optical nonlinearity research and etc. Moreover, since the optical property of integrated silicon photonic devices are highly susceptible to the change of the refractive index of the surrounding medium, ultrasensitive optical sensor has also been demonstrated in various fields such as chemical and biological sensing, fiber strain analysis, EM (electromagnetic) field sensing, mechanical motion sensing and etc. However, silicon dioxide, as the material for the buried layer of silicon on insulator (SOI) substrate, which is the most widely adopted silicon photonic device platform, has limited both the optical and mechanical potential for silicon based optical sensor since it possesses a very narrow transparency window and is highly rigid. Within the past decades, flexible electronics based on inorganic material has been successfully demonstrated by using stamp-assisted heterogeneous integration method, which could also be applied to the field of silicon photonics. This thesis has been focusing on utilizing various heterogeneous fabrication methods such as integrating high quality silicon photonic devices onto materials other than silicon dioxide, or applying polymer based materials on top of SOI substrate in order to demonstrate devices with novel applications

which are inaccessible with traditional silicon photonic devices. Firstly, a highly sensitive strain sensor is demonstrated by transferring silicon ring resonator and Mach-Zehnder Interferometer (MZI) onto stretchable PDMS substrate. Secondly, fully integrated silicon photonic circuit with grating couplers and ring resonators has been successfully transferred onto thin and flexible plastic substrate. Thirdly, by using a photoresist-pedestal assisted transfer method, a microcavity-enhanced mid-infrared optical chemical sensor is successfully demonstrated by using a silicon-on-calcium difluoride platform. Lastly, by applying a thin layer of polymer on one-dimensional photonic crystal cavity, an ultrasensitive infrared optical chemical sensor is realized.

Table of Contents

LIST OF TABLES

LIST OF FIGURES

CHAPTER 1: INTRODUCTION

1.1 Inorganic Flexible Electronic and Optical Devices

With the fast development of non-traditional micro fabrication techniques, more and more traditional planar and rigid electronics have been demonstrated in an alternative form – flexible electronics [1]. Compared with their rigid counterparts, electronic devices in flexible form could bring dramatic advantages in various applications such as wearable devices, artificial human tissue, implantable medical devices, and portable electronics. Various flexible electronic devices based on organic material and SAM (self assembled monolayer) has already been demonstrated such as flexible OLED (Organic Light Emitting Diode) [2]–[4], TFT (Thin Film Transistor) [5], [6], FET (Field Effect Transistor) [7], [8], solar cell [9]–[11], and etc. Although these small molecules and organic materials are generally considered naturally suitable and fully compatible with flexible electronics applications, the performance of the electronic devices based on such platforms can still not compete with the ones fabricated with pristine inorganic materials since the undeniable weakness exists in the electrical properties of organic materials such as low carrier mobility, poor reliability, low on/off ratio, high energy consumption and etc. These considerations have led to the interest of developing flexible electronics based on inorganic materials such as monocrystalline silicon, III-V group semiconductors, and etc., in which, only the substrates or the passive elements are organic [12]–[18].

However, inorganic materials have some compatibility issues with the integration process with flexible organic substrate such as: bulky and rigid design, high temperature processing and poor bendability. In order to solve these issues, several strategies have

been developed:

(1) Decrease the dimension of the inorganic material down to micro- and nanometer scale before integrating them with organic substrates. The bendability of the inorganic material will be inversely proportional to its thickness and width. This principle has already been demonstrated in 2D silicon nanoribbons and 1D silicon nanowires on plastic substrates [19], [20];

(2) Separate the processing of inorganic material and organic material in order to avoid the deformation and destruction of organic substrate under high temperature. To achieve this goal, a stamp assisted transfer method has been utilized to transfer processed inorganic electronic devices onto arbitrary receiving substrates [21]–[23]. By using this versatile method and with proper pattern design, various inorganic electronic devices have been demonstrated on plastic substrates such as: CMOS circuit [24], LED arrays [25], photodetector [26], temperature sensor [27], [28] and etc. as shown in Fig. 1.1.

(3) By using low temperature deposition technique, amorphous inorganic material could be directly deposited onto flexible plastic substrate. Such heterogeneous platform could be utilized for different applications such as TFT [29] and etc. The advantage of such technique is the capability of manufacturing large area flexible electronics. However, the performance of such amorphous semiconductor based flexible electronics is compromised due to the limitation of the materials themselves.

By comparing these three routes of realizing flexible inorganic electronics, the

transfer printing method is the only way to attain both the high flexibility of the substrate

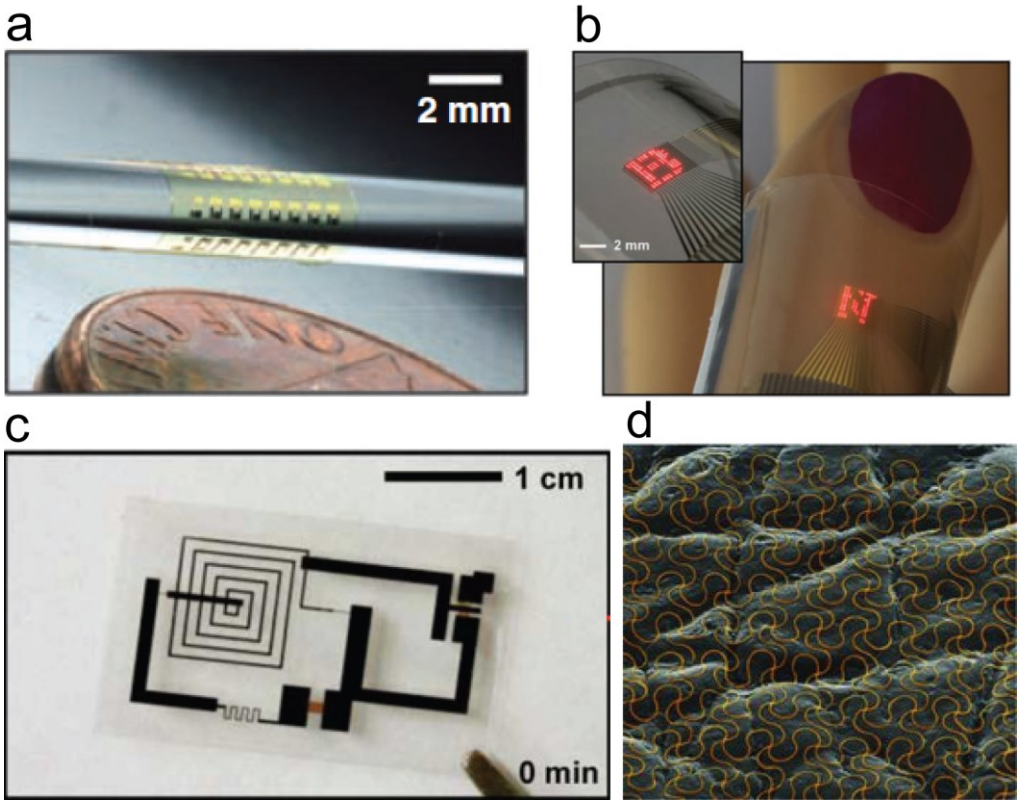

Figure 1.1 *Various inorganic electronic devices on flexible substrate which include: (a) CMOS circuits [24], (b) LED arrays [25], (c) transient form electronics [26] and (d) temperature sensors [27].*

and the high performance of the inorganic devices. Since silicon photonics is based on the very same platform, such method could also be applied to heterogeneously integrate fully functional monocrystalline silicon based photonic devices onto flexible organic substrates, which could find important applications in neuroscience research, implantable biomedical devices, mid-infrared silicon photonics and etc.

In my doctoral research, the primary goal is to realize the heterogeneous integration of high quality silicon photonic devices with other materials by either using the stamp-

assisted transfer technique or other methods. Firstly, comprehensive experiments and theoretical analysis of a high quality silicon photonic strain sensor on PDMS substrate is demonstrated with a modified transfer printing technique. Secondly, with further improvement of such fabrication method, fully integrated silicon and silicon nitride photonic circuit which include ring resonators and grating couplers are successfully transferred onto thin plastic substrate with uncompromised performance. Thirdly, with a photoresist-pedestal assisted stamp printing method, large area silicon nanomembrane with fully functional mid infrared silicon photonic devices are able to be transferred onto a calcium difluoride substrate, which, for the first time, achieve cavity-enhanced mid-infrared spectroscopic sensing at 5.4μm wavelength. Lastly, instead of transferring silicon on top of organic material, by functionalizing the nanobeam photonic crystal cavity with a layer of fluoroalcohol polysiloxanes polymer on top, an ultrasensitive chemical gas sensor with an innovative threshold mode is realized.

1.2 Strategies for Efficient Stamp-Assisted Printing

Transfer printing technique possesses the potential of realizing large-area heterogeneous integration of micro-/nanoscale devices with a wide variety of selections of materials onto exact location of the receiving substrate, which is unachievable by utilizing traditional microelectronic fabrication techniques. The recent rapid development in this field has expanded the capability of such transfer printing technique, in terms of both the collection of materials for transferring and types of devices can be realized. At the very heart of this technique, is the utilization of a transfer tool (which is a polymer

stamp in most cases) to print “inks”, which are defined as the materials that have been transferred. As demonstrated in literature, the collection of “inks” could vary from as complex as large area inorganic material based nanomembrane with fully integrated system on top [24], [30], [31], LEDs [25], neural probes [32] to as simple as nanowire [33] , single layer of graphene [34], self-assembled monolayers (SAMs) [35] and etc.

In most embodiment of transfer printing, an elastomeric stamp is brought into conformal contact with the “inks” which are supposed to have weak adhesion force to the host substrate by various means. With conformal contact of stamp with the devices, the Van der Waals force [36] at the stamp/device interface will surpass the adhesion force between the device/host wafer interface, which will serve as the basis for picking up devices from the original host wafer. Effective transfer printing, relies, fundamentally, on the control of Van der Waal interaction and the fracture mechanics at the critical interfaces between ink/stamp, ink/host wafer and ink/receive wafer. Ideally, the only permanent bonding interface should be the one between ink and receive wafer, all others should possess reversibility and preferably, should be switchable between a passive mode (difficult to be separated) and an active mode (easy to be separated). In order to achieve efficient and controllable transfer process, different strategies are developed such as:

(1) Engineer the ink/host wafer interface in order to largely decrease the adhesion force between the ink and the host wafer. The widely adopted method include partially remove the buffer layer of the host wafer by using wet etch [37], [38] and dry etch [39].

(2) Chemically treat both the surfaces of the soft, elastomeric stamp and the ink to increase the adhesion force between the ink and stamp.

(3) Use the rate-dependent method [21], [36], [40]–[42] to control the competing fracture mode in the ink/stamp/wafer system.

The first and the second method mainly depend on the physical and chemical properties of the materials, however, the third method could dynamically control the transfer process. With the very same material platform, with different transfer rate, the role of host wafer and receiver wafer is switchable. The velocity of separation of the stamp from a surface influences the adhesion force at the interface, which has been extensively studied by using various type of elastomeric stamps such as Poly Dimethylsiloxane (PDMS) [43]–[50], the most common, commercially available elastomer used as a stamp material. This process can be modeled as the initiation and propagation of interfacial fracture mode [51], [52]. Interfacial fracture at any of these interfaces is a manifestation of the critical value of energy release rate G defined as:

$$G = \frac{F}{w} \tag{1.1}$$

where F is the force applied to the stamp in the normal direction and w is the stamp width (the length of the side perpendicular to the peeling direction). G is a measure of interfacial adhesion strength between two surfaces. Separation at either the stamp/ink or ink/host wafer interface corresponds to a critical value of energy release rates, which is $G_c^{stamp/ink}$ or $G_c^{host/ink}$, respectively. In general, the criteria for deciding retrieval or printing of the ink is provided by the comparison of these two values [36]:

$$G_c^{stamp/ink} < G_c^{host/ink} \text{ (printing)} \tag{1.2a}$$

$$G_c^{stamp/ink} > G_c^{host/ink} \text{ (picking up)} \tag{1.2b}$$

The viscoelasticity of the stamp results in a velocity dependence of $G_c^{stamp/ink}$. Therefore, we can rewrite it as $G_c^{stamp/ink}(v)$. A general relationship between G and v has been predicted by Gent and others [53]–[56], as:

$$G_c^{stamp/ink}(v) = G_0[1 + (\frac{v}{v_0})^n] \tag{1.3}$$

where G_0 is the energy release rate at the static state, v_0 is a reference value calculated from experimental result, and n is the scaling parameter [64]. From Equation 1.3, the critical separation velocity could be expressed as:

$$v_c = v_0[\frac{G_c^{stamp/ink} - G_0(v)}{G_0}]^{\frac{1}{n}} \tag{1.4}$$

from which, we can tell that the critical energy release rate is positively proportional to the critical transfer velocity. Therefore, under the circumstance of retrieving inks, the stamp needs to be removed from the host wafer with a fast velocity in order to generate a higher $G_c^{stamp/ink}(v)$. In contrary, a slow velocity is a mandatory condition when executing the printing process. According to the literature, the ink retrieval and printing can occur efficiently at velocity on the order of 10 cm/s and a few mm/s, respectively[57].

1.3 PDMS Stamp Fabrication and Treatment

PDMS, as mentioned previously, is the most widely used stamp material in the literatures. There are several most significant advantages of PDMS as the stamp material:

(1) PDMS could be molded into any shape with micrometer precision, thus its surface could be easily designed to optimize the transfer process of devices with various geometries.

(2) The hardness of commercialized PDMS stamp could be easily controlled during its fabrication procedure by using different mixture ratio of the two reagents provided by the manufacturer, which has direct relationship with the value of surface energy release rate.

(3) Ultraviolet Ozone (UVO) or oxygen plasma could be utilized to hydroxylate the surface of PDMS stamp (to generate –SiOH group), which could increase the adhesion force at the ink/stamp interface. If the ink is comprised of silicon dioxide, silicon nitride, silicon, PDMS, polystyrene, or polyethylene, such UVO treatment could result in a covalent Si-O-Si bonding across the whole interface.

(4) PDMS is highly flexible and stretchable, which could enable innovative applications for inorganic flexible devices such as biomimetic structure [58], [59] and foldable devices [60], [61].

Generally speaking, both the physical and chemical properties of PDMS stamp could be changed by using various methods. In order to define the surface geometry of the PDMS stamp, a replica molding process (which is also called soft lithography process) is widely used. This process, at very beginning, was utilized in the fabrication of

microfluidics devices [62]–[67]. The fabrication process flow is shown in Fig. 1.2, which starts with standard cleaning process of silicon wafer. SU8 photoresist is then spun on top of the cleaned silicon wafer and patterned with photolithography technique. Afterwards, an anti-adhesion layer composed with fluoroalkyl trichlorosilane is deposited onto the surface of the SU8 structure and that of the exposed silicon wafer within a vacuumed desiccator. As the next step, the degassed PDMS gel with specific mixture ratio is poured onto the SU8 mold. With either a heated curing process or a room-temperature curing process, the PDMS will form a fully cross-linked structure and could be peeled off from the SU8 based mold easily with the application of the anti-adhesion layer. The geometry of the PDMS stamp surface will be an inverse replica of the patterned SU8 structures with micrometer scale precision. Since SU8 photoresist possesses the capability to generate structures with extremely high aspect ratio (more than 200) [68], the geometries for which the PDMS could be molded into could vary from simple square stamp, microfluidic channel to nanorod-mimic structure. With such large collection of available shapes, the functionality and versatility of PDMS based stamp has been largely expanded. With appropriate design, PDMS stamp could realize highly selective transfer printing with extremely high precision [22], [23], [25], [38], [69], [70]. Besides, 3 dimensional heterogeneous integration, which is believed as a route to further extend Moore's Law by utilizing both the combination of different powerful materials that could not be integrated with traditional microelectronic fabrication method and the 3D space

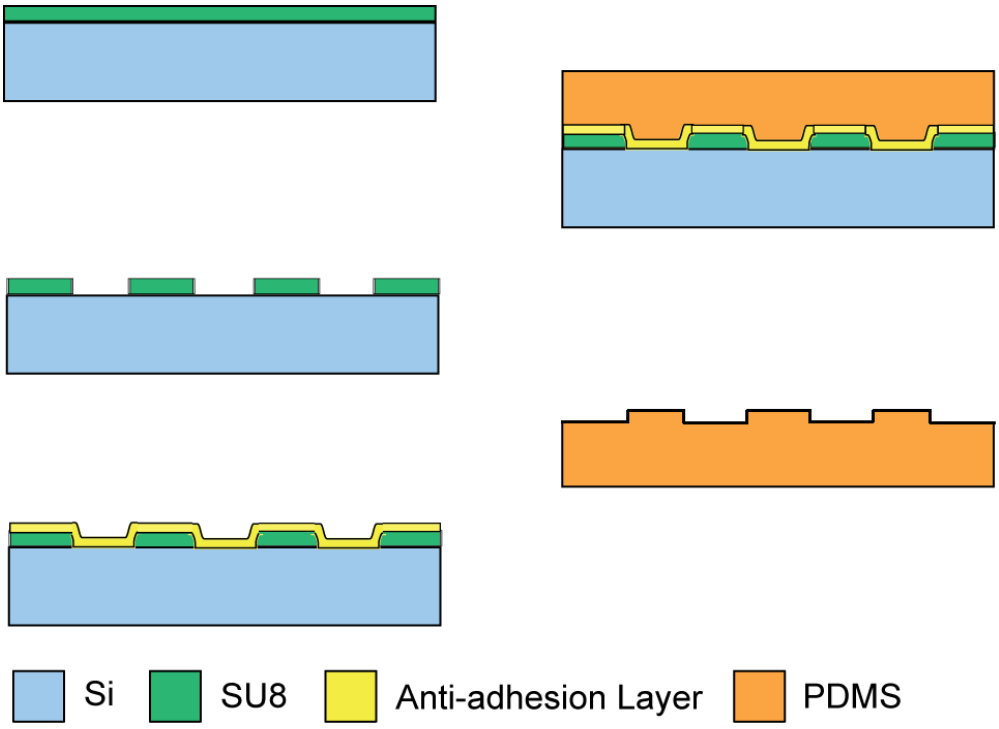

Figure 1. 2 *Fabrication process flow for the PDMS stamp with specific geometry*

layout technique, would also be enabled by using the PDMS stamp assisted pickup-and-place transfer method.

In consideration of all the advantages that have been described above, we choose PDMS as the stamp material for all the transfer work in this thesis.

1.4 Overview of the Thesis

In chapter 2, at first, the coupled mode theory is introduced and strictly followed as one of the primary design principles. Then, we generally introduce the physics fundamentals of silicon photonic devices that have been utilized in this thesis which include ring resonator, Mach-Zehnder interferometer, nanobeam photonic crystal cavity

and grating coupler. Besides, their physical and electromagnetic concepts and modeling methods are discussed. The propagation loss caused by the instability brought by fabrication process and material dispersion is also briefly discussed.

In chapter 3, we present fully integrated flexible silicon based ring resonator and Mach-Zehnder interferometer on PDMS substrate by using stamp-transfer method. At first, the fabrication method is described in detail. Then an interesting phenomenon is investigated, which is that with uniaxial strain applied to the PDMS stamp, the optical performance of the silicon photonic devices on top will change accordingly. Full theoretical analysis is also provided to explain such optical performance change. Excellent agreement is shown between the experimental results and quantitative analysis results.

In chapter 4, by using a modified photoresist pedestal assisted stamp-transfer method, fully functional photonic circuit based on both silicon and silicon nitride, which includes ring resonator and grating couplers, has been demonstrated on thin, flexible polyethylene terephthalate (PET) substrate with extremely high yield. The optical performance before and after the transfer process is compared, which proves the transfer process will render devices with uncompromised optical quality.

In chapter 5, by using similar but not identical fabrication method as mentioned in chapter 4, a large silicon based nanomembrane with integrated mid-infrared silicon photonic devices is heterogeneously integrated onto a calcium difluoride substrate. By using the very platform, a cavity-enhanced mid-infrared optical sensor with the capability of executing spectroscopic sensing is demonstrated. Several different chemicals are

utilized as the analyte in the sensing experiment and the FTIR measurement result agrees quite well with the on-chip spectroscopic sensing result. Such platform has also been demonstrated to be able to detect both the change of dielectric constant and that of absorption coefficient of the analyte.

In chapter 6, a silicon nanobeam photonic crystal cavity was chemically functionalized by applying a layer of fluroalcohol polysiloxane polymer on top. Such platform is then utilized as an optical chemical sensor with the capability to detect gas-phase methyl salicylate (MeS) analyte with an ultralow limit of detection (LOD) as 2 parts per billion (ppb). Moreover, the nonlinear effect of the optical resonance which is called thermo-optical bistability is investigated within this platform. A novel dosage threshold sensor is realized by harnessing such nonlinear characteristic of the nanobeam photonic crystal cavity with relatively large input optical power.

In chapter 7, all the work mentioned in this Ph.D. thesis is concluded. Many possible future applications which could be realized by using such heterogeneous integration method are also introduced.

CHAPTER 2: PHYSICS AND MODELING OF FUNDAMENTAL SILICON PHOTONIC DEVICES

2.1 Silicon Waveguide Design

The very fundamental photonic structure which is responsible for the delivery of light on-chip is the waveguide. Most of silicon photonic devices are based on SOI substrate, which possesses a high refractive index contrast between the top silicon layer and the buried oxide layer. Thus, with appropriate design, light with specific wavelength could propagate within the waveguide structures patterned on the top silicon layer of the SOI substrate with a small propagation loss.

There are two basic geometries of on-chip waveguide which are ridge and rib waveguide, as shown in Fig. 2.1a and Fig. 2.1b respectively. The most important parameters during the design of silicon waveguide will be the etch depth (which is the rib height) and the waveguide width, which, combine together, will decide the eigenmode of propagating light inside the waveguide at a specific wavelength. In other words, these two parameters will decide the effective mode index of the waveguide, which could be further utilized to derive the eigenmode solution of specific waveguide geometry. Unlike silica waveguide which could be easily designed to be single mode, SOI waveguide with dimensions larger than several hundreds of nanometers in cross section will potentially support multiple modes. Such multimode waveguide is usually undesirable in silicon photonic circuit since most photonic components are designed to be operated under single mode condition. By utilizing Maxwell equations with effective index method [71], the single mode conditions at a specific wavelength with given silicon thickness could be

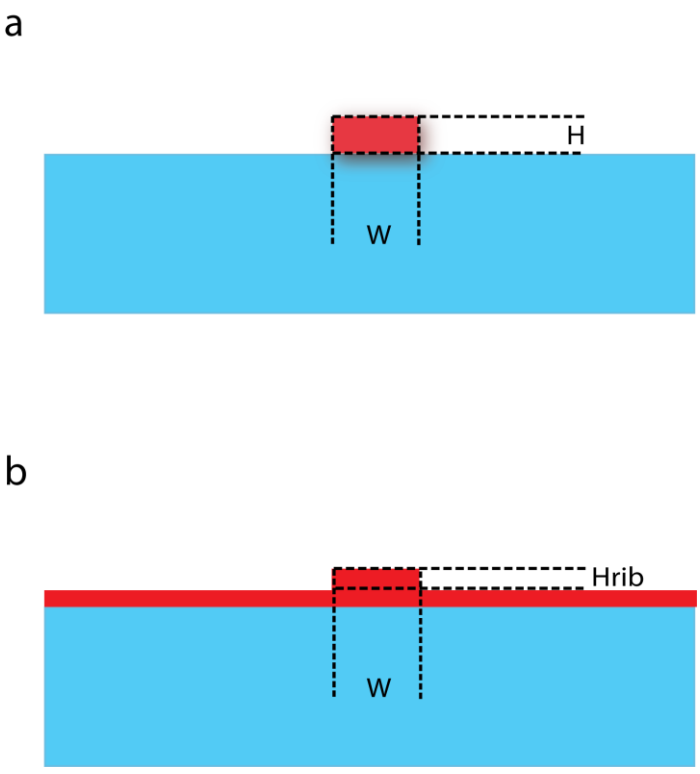

Figure 2.1 *Schematics of (a) ridge waveguide and (b) rib waveguide*

calculated. Also, design guidelines for various types of silicon waveguide are reported in many literatures as well, such as:

(1) As reported by Soref et al [72], for large rib waveguide with multimicron cross-section dimension, which could serve perfectly for the purpose of coupling light to and from optical fiber with low loss. The single mode condition (SMC) for such type of waveguide could be described as:

$$\frac{W}{H} \le 0.3 + \frac{r}{\sqrt{1-r^2}}, (0.5 \le r \le 1.0) \qquad (2.1)$$

W and H are the width and overall rib height of the waveguide, respectively, r is the ratio between the slab height and the overall rib height. The application of such SMC has

several prerequisites which include: r is larger than 0.5 and the waveguide dimension is assumed to be larger than the scale of the operating wavelength. The analysis is based on the assumption that the higher order mode will be coupled to the outer slab region during the propagation and only the fundamental mode will be confined in the rib region.

(2) As reported by Chan et al [73], for relatively smaller rib waveguide with cross-section dimensions around 1 micron, the SMC will change accordingly which could be described as:

$$\frac{W}{H} \le 0.05 + \frac{(0.94 + 0.25H)r}{\sqrt{1-r^2}} \quad for(0 \le r \le 0.5) and (1.0\mu m \le H \le 1.5\mu m) \tag{2.2}$$

and

$$D_{\min} = 0.06 * 10^{-6} + 0.556H \tag{2.3}$$

while Equation 2.2 provides the guidance of the geometrical limitation to maintain single-mode for deep-etched or even fully etched rib waveguide, Equation 2.3 defines the minimum etch depth requirement for obtaining polarization independence of the waveguide.

(3) To be even more specific, as reported by Lim et al [74], at 1550nm wavelength, the SMC for submicron silicon waveguides could be described as:

$$0.2\mu m + 162e^{(-H/0.03)} \le W \le 0.3\mu m + 5.9e^{(-H/0.08)} \tag{2.4}$$

H and W are the height and width of the waveguide in unit of μm, this SMC is suitable for waveguide with submicron dimension working at the wavelength of 1550nm. For 220nm thick silicon waveguide, the width of the single mode waveguide could lie within the range between 306nm to 677nm.

With these design guidance, SMC could always be met in different situations. Even if the geometrical requirements of the waveguide are out of the range discussed here, Maxwell equations and effective index method could still be utilized to give general guidance during the design process of any type of single mode waveguide.

2.2 Silicon Ring Resonator

2.2.1 Fundamentals of Optical Microresonator

Optical microresonators have demonstrated great promises as basic building blocks in various applications in photonics. They can be implemented for diverse applications such as lasers [75]–[77], optical sensor [78], [79], amplifier [80], [81], optical add/drop filter [82], [83], optical switch [84], logic gates [85] and etc. The fundamental function and feature of an optical microresonator is the spatial and temporal localization of optical (electromagnetic) energy at multiple particular wavelengths within a limited length scale and for a much longer time compared to the photon life time outside the resonator structure. In Fig. 2.2, several different types of resonators are shown [82] as a demonstration.

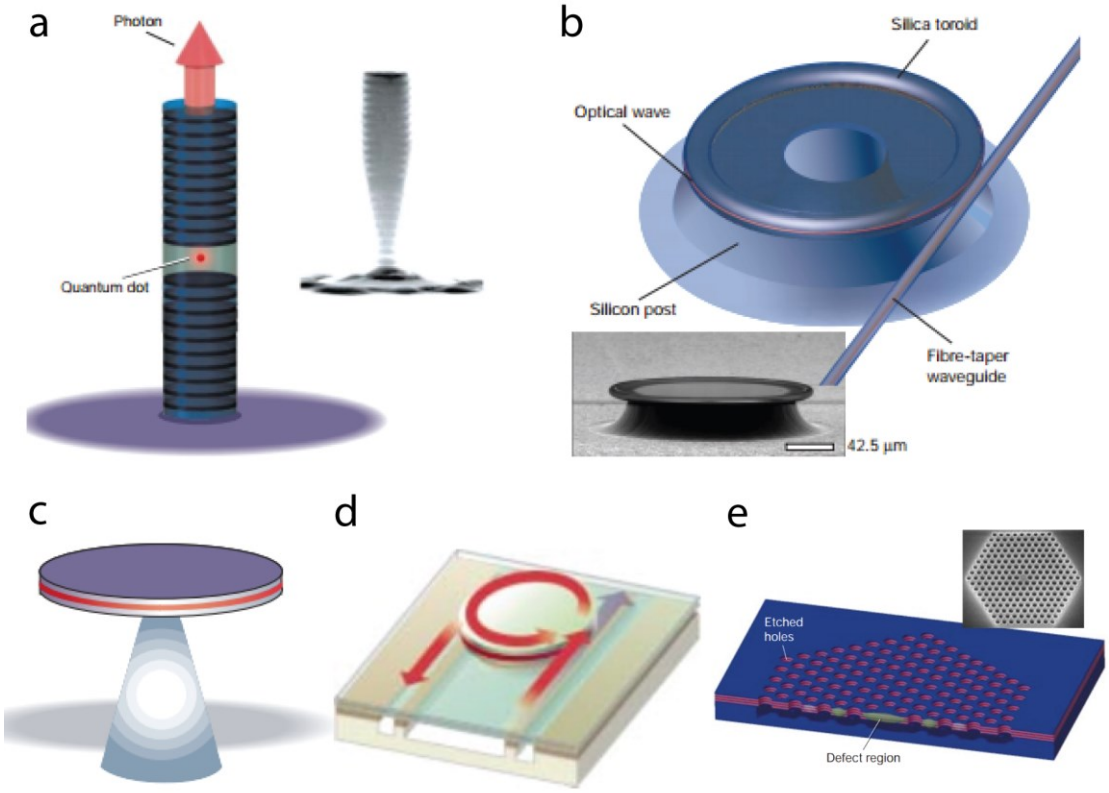

Figure 2.2 *Various types of optical microcavity [82] such as: (a) micropillar cavity, (b) microtoroid cavity, (c), (d) microdisk cavity, (e) 2D photonic crystal cavity.*

Maxwell's curl equations in the frequency domain for a linear dielectric and nonmagnetic material are expressed as:

$$\begin{aligned} \nabla \times E &= -i\omega\mu_0 H, \\ \nabla \times H &= i\omega\varepsilon_0 n^2 E, \end{aligned} \tag{2.5}$$

Where μ_0 and ε_0 are the permeability and permittivity of the vacuum, respectively, and n is the refractive index, which includes an imaginary part indicating the loss of the media. Through Equations (2.5), the Helmholtz equation in terms of E or H could be expressed as:

$$\nabla \times [\frac{1}{p^2} \nabla \times F] = (\frac{\omega}{c})^2 \frac{n^2}{p^2} F, \begin{cases} F = H, p = n \\ or \\ F = E, p = 1 \end{cases} \tag{2.6}$$

where *c*, represents the speed of light in vacuum. By solving Equation (2.6) for a given resonator structure, both the resonance frequency and the mode profile in terms of electromagnetic field distribution can be obtained.

The temporal localization capability of energy in an optical microresonator is quantified by a figure of merit called quality factor (*Q)* which is defined as:

$$Q = \frac{2\pi f_0 \varepsilon}{P}, P = -\frac{d\varepsilon}{dt} \tag{2.7}$$

where f_0 is the optical resonance frequency, ε is the stored energy in the cavity, and *P* is the power dissipated. The larger the *Q* is, the longer the photon life time will be inside the microresonator structure.

The spatial localization capability of energy in an optical microresonator is quantified by another figure of merit called mode volume (V_m), which is defined as:

$$V_m = \frac{\frac{1}{2}\int \varepsilon_0 n^2(r) \left|E(r)\right|^2 dr^3}{\frac{1}{2}\varepsilon_0 \left|nE\right|^2_{peak}} \tag{2.8}$$

It can be seen, from Equation (2.8), that a smaller mode volume V_m results in a larger peak value of electric field *E* when the total resonator energy is fixed. In addition, we can also tell that the larger *n* is, the smaller the mode volume could be achieved, which means higher refractive index contrast between the resonator and its surrounding material is desired when compact cavity designed is required.

2.2.2 Optical Ring Resonator

Ring resonator is such a type of device exhibiting periodic cavity resonances when light traversing the ring acquires a phase shift corresponding to an integer multiple of 2π radians. A regular waveguide coupled ring resonator could be mathematically formulated from two components: a coupling region and a feedback path as depicted in Fig. 2.3a.

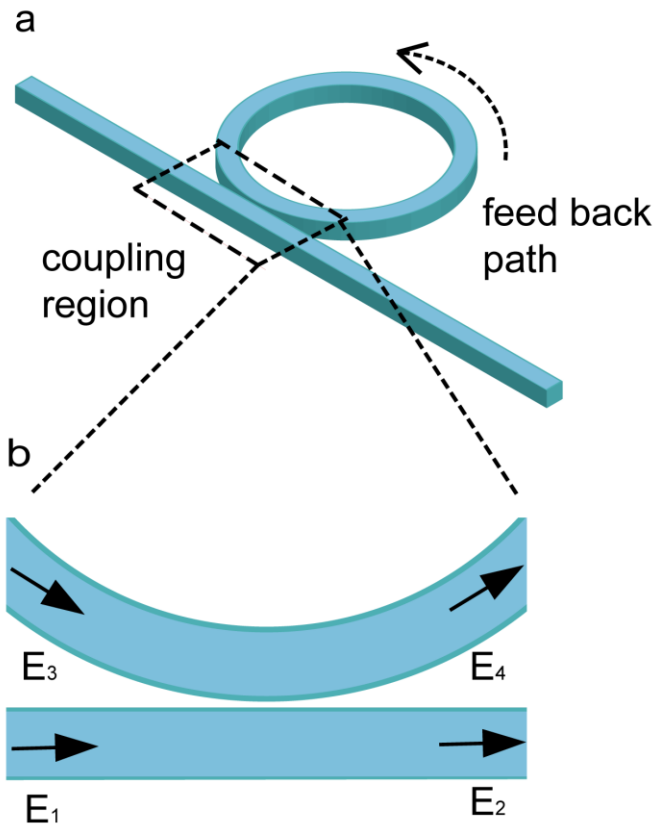

Figure 2.3 *(a) Schematic of a regular ring resonator. (b) The enlarged view of the coupling region of the all-pass ring resonator.*

Such waveguide coupled ring resonator could be simplified as a four port device as illustrated in Fig. 2.3b. The electric field from the incident waveguide and the

roundtrip ring resonator is defined as E_1 and E_3, and the transmitted electric field out from the output waveguide and the ring resonator is defined as E_2 and E_4. In the spectral domain, the fields exiting the coupling region are related to the input fields following the relationship defined via the unitary matrix below:

$$\begin{pmatrix} E_4(\omega) \\ E_2(\omega) \end{pmatrix} = \begin{pmatrix} r & it \\ it & r \end{pmatrix} \begin{pmatrix} E_3(\omega) \\ E_1(\omega) \end{pmatrix}, \tag{2.9}$$

where r and t represent the self- and cross-coupling coefficients, which, presumably, are independent of frequency and satisfy the lossless relation which is $r^2 + t^2 = 1$. The field input from input port 3, which is E_3, could be expressed as:

$$E_3 = e^{-\frac{\alpha_r}{2} 2\pi R} e^{ik2\pi R} E_4 = a e^{i\phi} E_4, \tag{2.10}$$

where α_r represents the ring attenuation coefficient, a represents the single-pass amplitude transmission and φ represents the single-pass phase shift. Because the resonance condition is always met with adding or subtracting an integer number m of 2π radians from the single-pass phase shift, the single-pass phase shift for the resonance is defined such that its value is zero. From Equation (2.9) and (2.10), we obtain:

$$\frac{E_2}{E_1} = \frac{-a + re^{-i\varphi}}{-ar + e^{-i\varphi}}, \tag{2.11}$$

Therefore, the power transmission passing the resonator through the coupling region is:

$$T = \left| \frac{E_2}{E_1} \right|^2 = \frac{a^2 + r^2 - 2at\cos\varphi}{1 + a^2 r^2 - 2ar\cos\varphi}, \tag{2.12}$$

As mentioned in previous text, when the cavity is on resonance, the phase change per round trip is zero, or, in other words, an integer number of 2π. Therefore, from Equation (2.12), we can have the power transmission on resonance T_o, which is:

$$T_o = \left| \frac{a - r}{1 - ar} \right|^2 , \tag{2.13}$$

From Equation (2.13), some important information could be obtained while the cavity is on resonance. Zero transmission could be achieved when $r=a$, which, referred to as critical coupling, is due to complete destructive interference in the output waveguide port 2 between the transmitted field from port 1 and the field coupled from the ring resonator port 3. However, in real situation, due to the fabrication imperfection, the zero transmission is extremely difficult to be achieved. Nevertheless, the extinction ratio of the resonance could be more than 60dB when critical coupling condition is met. Non-zero transmission could be obtained while the critical coupling condition is not met. When $r < a$ and $r > a$, resonator works in the under-coupled and over-coupled regimes, respectively.

The quality factor of ring resonator is always defined as the ratio between the resonance frequency and the full width at half maximum (FWHM) of the corresponding resonance, which could be express as: $Q = \omega / \Delta\omega$. Combined with Equation (2.12), the quality factor could be rewritten as:

$$Q = \frac{2\pi^2 n_{eff} R}{\lambda} \frac{\sqrt{ar}}{1 - ar} \tag{2.14}$$

where R is the radius of the resonator, n_{eff} is the effective refractive index, and λ is the resonance wavelength.

Since *t*, which is the coupling coefficient, is more interesting to most people than the transmission coefficient r, all the Equations from (2.11) to (2.14) could be rewritten by utilizing the relationship between *r* and *t*, namely $r^2 + t^2 = 1$. For example, Equation (2.13) could be rewritten as:

$$T_o = \left(\frac{1 - a^2 - t^2}{1 - a^2 + t^2} \right)^2, \tag{2.15}$$

Since *a* represents the total gain coefficient per round trip of the cavity, $\sqrt{1-a^2}$ could represent the loss coefficient per round trip of the cavity. Therefore, at critical coupling, $\sqrt{1-a^2} = t$, which means the power coupled into the cavity through the waveguide is all dissipated after the light has travelled a round trip through the ring resonator.

In reality, internal attenuation mechanisms are always present which could be caused by material dispersion or fabrication imperfection and thus render limitations as to when a ring resonator could closely approximate a real all-pass filter. Therefore, the width of the resonance also broadens, lowering the quality factor of the resonator. That's why microresonators with extremely high quality factors always possess ultra-smooth sidewalls since the diffraction loss could be minimized from such structures.

The separation of successive resonances is termed as the free spectral range (FSR). At resonance, $\omega t_R = m2\pi$, where t_R is the time for photon to travel round-trip along the resonator and m is an integer. And FSR could be expressed as:

$$FSR = \frac{\lambda_0^2}{Ln_g} \tag{2.16}$$

As we can see, the FSR will change accordingly to different resonance wavelength.

Inside traveling wave resonator such as ring resonator, at resonance, the electromagnetic waves interfere with each other constructively. As a result, a field enhancement will occur in such type of resonator structure. Since the photons will finally escape from the cavity (which corresponds to the finite photon life, or in other words, the finite quality factor of the cavity), the total number of roundtrips is finite and approximately equals to $2\tau_P / T_{roundtrip}$, where τ_P denotes the photon lifetime inside the cavity and $T_{roundtrip}$ represents the time it takes the photon to travel roundtrip. Therefore we can define the intensity buildup factor as:

$$\mathrm{B} = \left|\frac{E_3}{E_1}\right|^2 = \frac{(1-r^2)a^2}{1-2ra\cos\varphi + r^2a^2} = \frac{2\tau_P}{T_{roundtrip}} \tag{2.17}$$

In order to characterize the sharp peak resonance caused by the intensity buildup, a parameter called finesse is introduced which could be expressed as:

$$Finesse = \frac{2\pi}{2\arccos(\frac{2r}{1+r^2})} \tag{2.18}$$

the physical meaning of which is defined as the FSR divided by the FWHM of a resonance.

$$\mathrm{B} = \left|\frac{E_3}{E_1}\right|^2 = \frac{(1-r^2)a^2}{1-2ra\cos\varphi + r^2a^2} = \frac{2\tau_P}{T_{roundtrip}} = \frac{2}{\pi}\frac{FSR}{FWHM_{resonance}} = \frac{2}{\pi}Finesse \tag{2.19}$$

2.2.3 Ring Resonator Based Add-Drop Filter

The optical ring resonator could mimic the performance of Fabry-Perot cavity by simply adding a second side-coupled waveguide to it as shown in Fig. 2.4. Since this type

of configuration behaves as a narrow-band wavelength filter that can add or drop a frequency band from an incoming optical signal, it is usually defined as an add-drop filter.

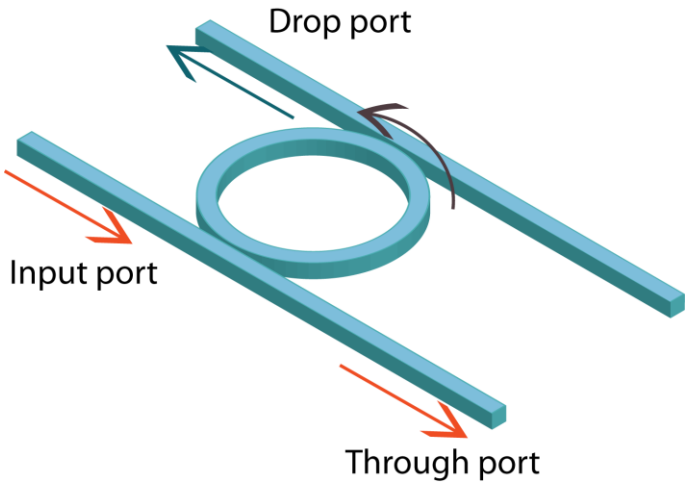

Figure 2.4 *Schematic of a ring resonator based add-drop filter*

Similar to ring resonator, such add-drop filter could be easily defined as a four-port device. The four ports are input, throughput, drop and add port, the electric field of each port is defined as E_1, E_2, E_3 and E_4, respectively. The electric field intensity coming from the throughput port in ratio to the input port could be expressed as:

$$T_1 = \frac{I_2}{I_1} = \frac{r_2^2 a^2 - 2r_1 r_2 a\cos\varphi + r_1^2}{1 - 2r_1 r_2 a\cos\varphi + (r_1 r_2 a)^2}\ , \tag{2.20}$$

Where r_1 and r_2 represent the transmission coefficients of the two coupling regions, respectively, if these two waveguides are identical with the same coupling gap, then $r_1 = r_2$, if $a = 1$ and Equation (2.20) could be simplified as:

$$T_1 = \frac{I_2}{I_1} = \frac{\frac{4r^2}{(1-r^2)^2}\sin^2(\frac{\varphi}{2})}{1 + \frac{4r^2}{(1-r^2)^2}\sin^2(\frac{\varphi}{2})}\ , \tag{2.21}$$

The field intensity of extracted band at the drop port in ratio to the field intensity of the input port could be expressed as:

$$T_3 = \frac{I_3}{I_1} = \frac{(1-r_1^2)(1-r_2^2)a}{1-2r_1r_2a\cos\varphi+(r_1r_2a)^2} \xrightarrow[a=1,r_1=r_2=r]{} \frac{1}{1+\frac{4r^2}{(1-r^2)^2}\sin^2(\frac{\varphi}{2})} \quad , \qquad (2.22)$$

For an add-drop filter, it is always desirable to operate at critical coupling regime for both of the two coupling regions. Here the sum of all losses incurred in the filter system should include the waveguide loss from the drop port.

2.3 Silicon Mach-Zehnder Interferometer

Another type of commonly used interferometer is the Mach-Zehnder interferometer which has long been utilized as a tool to measure the phase difference between two collimated beams separated by a beam splitter. The basic setup of a conventional Mach-Zehnder interferometer is shown in Fig. 2.5, which is

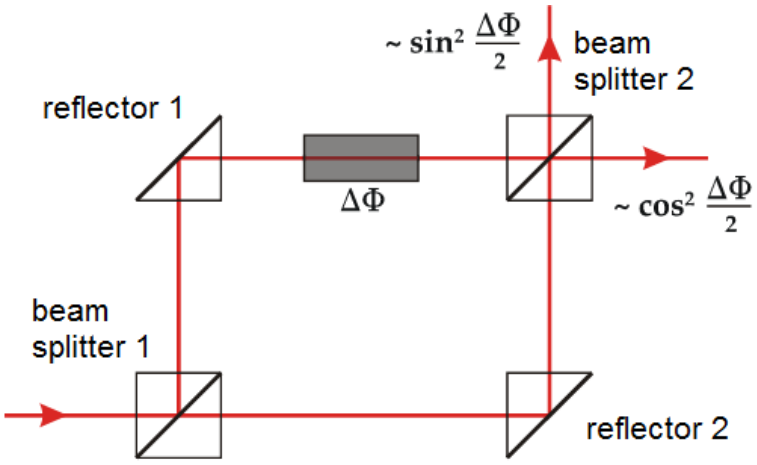

Figure 2.5 *Schematic of a basic Mach-Zehnder interferometer*

composed of two beam splitters and two beam reflectors. Mach-Zehnder interferometers are central to many optical circuits and have been utilized in a variety of silicon photonic devices such as photodetector [86], phase modulator [87]–[89], chemical sensor [90]–[92], optical switches [93], [94] and filters [95], [96].

A most basic Mach-Zehnder interferometer based on SOI platform could be simply composed by two Y junctions and two arms as shown in Fig. 2.6. Assuming the

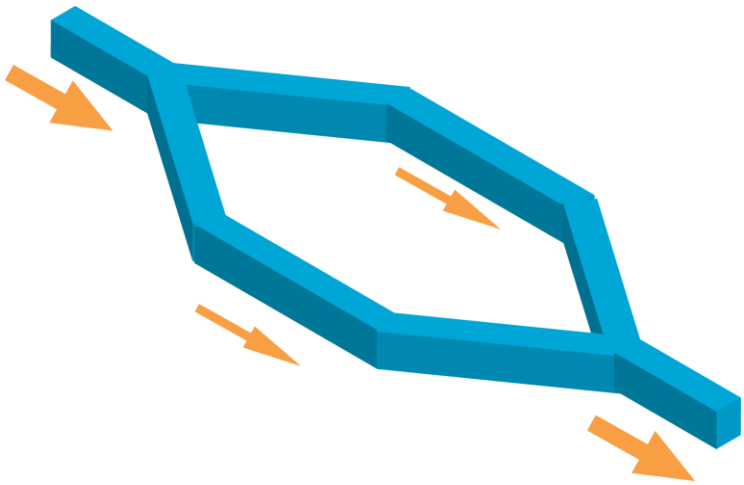

Figure 2.6 *Schematic of an on-chip Mach-Zehnder interferometer*

waveguide splitter (Y-junction) at the input of the interferometer divides the wave perfect evenly, then the intensities in the upper arm and the lower arm of the interferometer will be exactly the same, which could be represented as:

$$E_U = E_I \sin(\omega t - \beta_U z) \tag{2.23a}$$

$$E_L = E_I \sin(\omega t - \beta_L z) \tag{2.23b}$$

When the first Y-junction divides the input field, the E_U and E_L will have the same amplitude and in phase. However, due to the different propagation constant or the different optical path length, when the two fields recombine at the second Y-junction,

they may no longer be in phase. The intensity at the output waveguide could be described as:

$$S_T = S_0 \left\{ E_0^2 [1 + \cos(\beta_L L_L - \beta_U L_U) \right\} \tag{2.24}$$

Equation (2.24) is the transfer function of the interferometer. The transfer function will have maxima when the phase difference equals a multiple of 2π radians. Similarly, the transfer function will have minima when the phase difference equals an odd multiple of π radians. The term $\beta_L L_L - \beta_U L_U$ represents the phase difference between the waves after propagating through the two arms of the Mach-Zehnder interferometer. Clearly, in order to tune the phase difference, we can either change the propagation constant or the optical path lengths of the two arms. On conventional SOI platform, there are several methods to realize such tuning purpose:

(1) By designing the two arms with specific different optical path lengths, in order to obtain desired phase difference at the output port [97], [98].

(2) By depositing certain type of material on top of one arm of the interferometer, in order to bring the difference of propagation constant between the two arms of the Mach-Zehnder interferometer [99], [100].

(3) By integrating micro heater to one of the two arms, in order to change the propagation constant of one arm by utilizing the thermo-optic effect of the silicon material [101], [102].

(4) By integrating a silicon based optical phase modulator (other than micro heater) to one or both arms of the Mach-Zehnder interferometer [103], [104].

Therefore, for most of SOI platform based Mach-Zehnder interferometer, the output could be manipulated between maxima and minima by changing the propagation constant difference of the two arms.

2.4 Silicon Nanobeam Photonic Crystal

Photonic crystal, by mimicking the lattice structure in solid crystal structure with periodic optical structure, could affect the behavior of photons. Similar to existence of electric potential bandgap in some crystalline semiconductors, optical bandgap also exists in the photonic crystal structure which prohibits photons with certain wavelength to propagate as an eigenmode. By utilizing such photonic bandgap, light could be manipulated by varying the design of the photonic crystal. Depending on the geometry, photonic crystals can be categorized into three different types as one dimensional, two dimensional or three dimensional photonic crystal as shown in Fig. 2.7.

The fundamental physics of photonic crystal is based on diffraction, therefore the periodicity of the photonic crystal structure is on the same order of half wavelength of the light. Thus, an appropriate design of nanobeam photonic crystal for the telecomm wavelength at 1550nm needs a periodicity on the order of hundreds of nanometers, which is fully within the capability of modern nanofabrication technology.

Since photonic crystal structure possesses the capability of manipulating photons, cavity structure could be easily integrated into such system by breaking the periodicity of the geometry. Photonic crystal cavities [105], [106] have demonstrated advantages over other cavity geometries due to their extra-large quality factor to mode volume ratio which

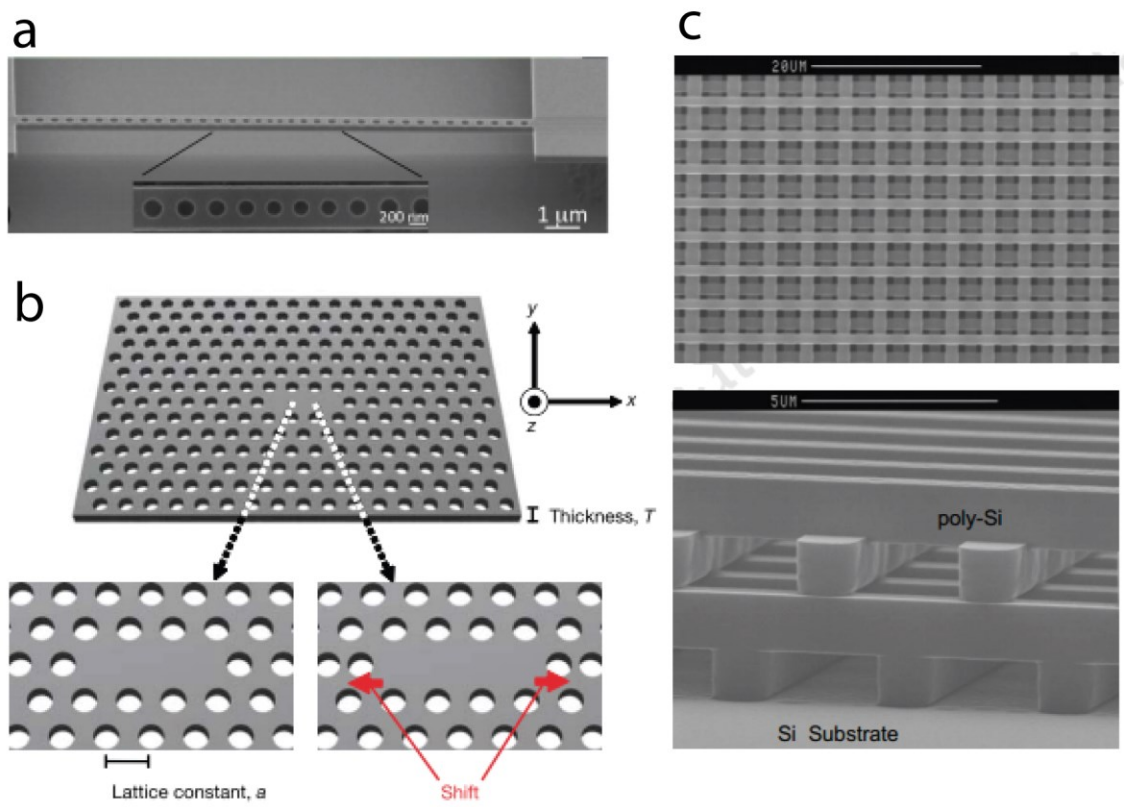

Figure 2.7 *Various types of photonic crystals reported in literatures, which include (a) one dimensional nanobeam photonic crystal cavity* [198]*, (b) two dimensional photonic crystal slab cavity* [105]*, (c) three dimensional photonic crystal* [199].

will lead to an extra-large Purcell factor [105], [107]–[112]. However, although the small mode volume could be easily realized in the photonic crystal cavity system, high quality factor is highly challenging to be achieved, which, is attributed to the time consuming physical structure optimization process and the uncontrollable uncertainties coming from the fabrication process.

Nanobeam photonic crystal cavities as shown in Fig. 2.7a have recently been extensively investigated rather than the two dimensional slab-based photonic crystal cavities. Being capable of attaining high quality factor on par with those achieved in

other 2D photonic crystal cavities, nanobeam photonic crystal cavities could be fabricated with a much smaller footprint which provides an even smaller mode volume and the capability for large area integration.

Most of the nanobeam photonic crystal cavities are composed of a cavity structure which supports propagating mode of specific wavelength that sandwiched between two Bragg mirror sections. Light could be confined by the two Bragg reflectors in the cavity. Therefore, by increasing the number of the Bragg mirror pairs, the optical energy that leaks out the cavity section could be accordingly decreased. And with minimized light coupled into the radiation mode, the quality factor of the cavity could be maximized. The radiated power could be expressed as:

$$P_{radiation} \propto \int_{<lightcone} dk(|FT(H_z)|^2 + |FT(E_z)|^2 \tag{2.25}$$

where *FT* means the spatial Fourier transform and z denotes the direction perpendicular to the surface of the nanobeam photonic crystal cavity [113], [114]. For generality considerations, the optimization process will be based on the existence of a single TE mode inside the cavity, which has H_z as the major field component. At first, the evanescent field inside the Bragg mirror could be expressed as:

$$H_{z,Bragg}(x) = \sin(\beta_{Bragg} x)\exp(-\gamma x) \tag{2.26}$$

where β_{Bragg} denotes the propagation constant of the Bragg mirror with the value of π / a, and γ is the attenuation coefficient. The magnetic field in the cavity region could be expressed as:

$$H_{z,cavity}(x) = \sin(\beta_{Wg} x) \tag{2.27}$$

Therefore, since only the spatial harmonics inside the light cone will contribute to the radiation energy, localizing the spatial Fourier component far away from the light cone could substantially minimize the radiation energy. Also, by setting $\beta_{Wg} = \beta_{Bragg}$ will reduce the scattering loss caused by the phase mismatch between the Bragg mirror section and the cavity section. According to literatures [115], following three deterministic design rules, ultra-high quality factor could be achieved in 1D photonic crystal cavity, which are:

(1) Spatial frequencies within the light cone could be minimized if the attenuation of field inside the Bragg mirror region follows a Gaussian envelope shape, which could be easily realized by making the Bragg mirror attenuation coefficient γ to be a linear increasing function of the light propagation direction within the mirror, such as: $\gamma = \sigma x$.

(2) The quality factor of 1D photonic crystal cavity will reach maximum when point-shift cavity (L0 cavity) structure is adopted.

(3) A constant length of each Bragg mirror section is required, even with a modulated Bragg mirror.

Following these three rules, the optimal field distribution could be expressed as:

$$H_z(x) = \sin(\frac{\pi}{a}x)\exp(-\sigma x^2) \tag{2.28}$$

where a denotes the period of the Bragg mirror and σ represents the variance of the Gaussian distribution function.

2.5 Grating Coupler on SOI Platform

2.5.1 Grating Coupler Overview

Due to the large refractive index contrast between the top silicon layer and the buried oxide layer in the conventional SOI platform, propagation mode of light is well confined within the appropriately designed photonic structure in the surface silicon layer. At telecommunication wavelength of 1550nm, the dimension of single mode waveguide is on the order of hundreds of nanometers, which enables the on-chip large-area integration of silicon photonic devices. However, such small cross-section also brings a huge mode mismatch between the commonly used single-mode fiber and the silicon waveguide, which may bring large insertion loss.

Invented in the 1970's as a way of coupling free space highly coherent light with specific wavelength into glass film, the grating coupler has been widely utilized in a variety of photonic platform. Since the beginning of 21st century, it has also been integrated onto the SOI platform [116], [117]. For silicon photonics, there are two major methods to couple laser light into the waveguide, which are butt-coupling method and grating coupler coupling method. Comparing to butt-coupling method, although grating coupler is a relatively narrow-band device, its compact design, high coupling efficiency and the capability to emit light perpendicularly to the surface has made it attractive for different applications of silicon photonic circuits such as demonstration of optical force [97], [118], sensing analyte with silicon photonic sensor [119], emitting circularly polarized light [120] and etc.

The grating coupler is essentially a Bragg grating designed to diffract light from a free space light source into a dielectric substrate or vice versa. The most general implementation of grating coupler in silicon photonic system is shown in Fig. 2.8a, in which the light delivered to the grating coupler is through a single mode fiber, and the same type of fiber is also utilized to collect light coupled out from the grating coupler.

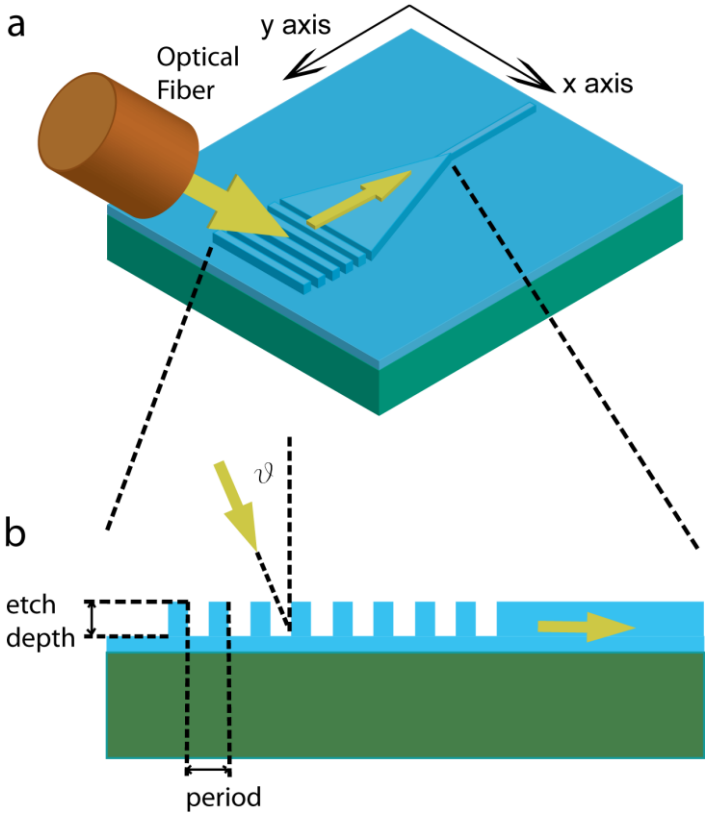

Figure 2.8 *(a) 3D illustration of the general implementation of on-chip silicon based grating coupler. (b) 2D illustration of shallow etched grating coupler structure.*

Fig. 2.8b shows the 2D schematic of a grating coupler with shallow-etched geometry on SOI platform. Several important parameters for a standard grating coupler are:

(1) Coupling efficiency (Insertion loss): the ratio between the power coupled into the grating coupler and the power delivered to the surface of grating coupler, which is always expressed in the unit of dB as $10*log_{10}$.

(2) Directionality: the *k*-vector direction of the optical mode emitted from the grating coupler, this is always decided by the effective refractive index and period of the grating coupler.

(3) Back reflection to the waveguide: due to the refractive index change between the silicon waveguide and the grating structures, part of the optical power will be reflected back to the waveguide structure. There are various method to minimize the reflected power such as utilizing the apodized grating geometries.

2.5.2 Coupling Theory

Based on the Bragg's Law of diffraction, the Bragg condition of the grating coupler could be written as:

$$k_{eff} = k_{top-clad} \cdot \sin(\theta) + 2\pi \frac{m}{\Lambda} \tag{2.29}$$

where k_{eff} is the *k*-vector of the optical field inside the grating coupler, $k_{top-clad}$ is the k-vector of the optical field emitted from or delivered to the grating coupler, m is an integer number and Λ is the period of the grating structure. Since $k = \frac{2\pi n}{\lambda}$, Equation (2.29) could be rewritten as:

$$n_{eff} = n_{top-clad} \cdot \sin(\theta) + m \frac{\lambda}{\Lambda} \tag{2.30}$$

where n_{eff} and $n_{top-clad}$ denotes the effective refractive index of the grating coupler and the top cladding, respectively. Higher order optical modes could be emitted from the grating coupler if both m and Λ are increased. However, under such circumstance, the optical power will be split into several different modes, which may not be desirable depending on the application of the grating coupler. It should also be noted that the Bragg condition of grating coupler is only precise for infinite gratings, i.e, two-dimensional grating with infinite number of grating. As reported in literature [121], in a finite grating, there is not a discrete k-vector for diffraction to happen with a preset grating period, but a range of k-vectors around the one decided by the Bragg condition.

2.5.3 Focused Grating Coupler

In order to minimize the footprint of the device and the mode mismatch between the single mode waveguide and the grating coupler, by using a tapered triangular structure, focused grating couplers have also been developed, which use the same grating structures as straight couplers but with curved gratings. When the curvature of the grating is properly chosen, the light could efficiently travels from the curved gratings to a single mode waveguide in a very short distance [122]. The geometry of the focused grating could be designed by using the equation:

$$q\lambda_c\alpha = yn_{top-clad}\sin(\theta) + n_{eff}\sqrt{x^2 + y^2} \tag{2.31}$$

where q is a negative integer corresponding to each grating, λ_c is the wavelength of incoming light in vacuum, α is a correction factor to match the grating spacing at x=0 with results of a corresponding straight grating coupler, x and y are two coordinate axis

defined in Fig. 2.8a, the origin of which both locate at the focal spot of the curvature (where the waveguide begins).

With coupling efficiency on par with conventional straight grating coupler, the curved grating structure could bring a much compact footprint of the device, which will benefit the large area integration of grating couplers on-chip.

CHAPTER 3: FLEXIBLE SILICON PHOTONIC STRAIN SENSOR

3.1 Flexible Silicon Photonics Overview

The transfer-and-bond method has been successfully implemented to fabricate flexible microelectronics and improved further with innovative mechanical designs to achieve stretchable and even foldable devices as mentioned in the first chapter, which enabled many unprecedented applications, most notably, in bio-inspired and implantable biomedical devices. The new hybrid form of flexible microelectronics combines the high performance of crystalline inorganic materials and the mechanical flexibility of organic ones. Sophisticated analog and digital CMOS circuits can be transferred from silicon wafer substrates to a variety of polymeric films and retain their electrical performance and functionality in the flexible form and under mechanical deformation. Beyond silicon microelectronics, the hybrid approach of flexible devices has been successfully applied to a wide range of micro-devices in diverse materials, including microwave electronics [123], [124], carbon electronics [125]–[127], optoelectronics [128], [129], and very recently plasmonics [130], [131] and meta-materials [60].

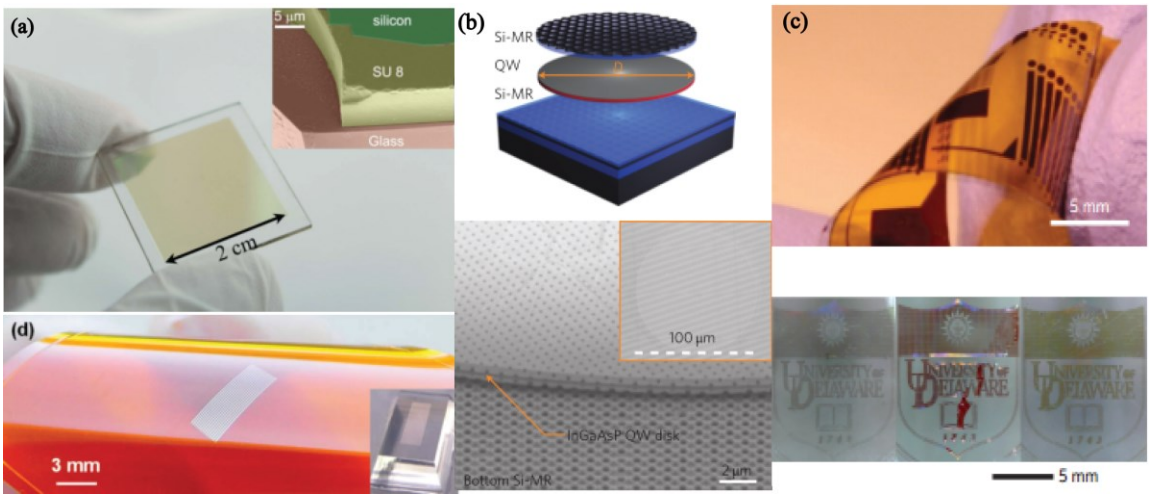

Figure 3.1 *Various heterogeneously integrated photonic devices reported in literatures. (a) Silicon nanomembrane on top of glass substrate* [137]*; (b) Quantum well laser sandwiched between two silicon nanomembrane based reflector* [134]*; (c) Chalcogenide glass based flexible photonic devices on plastic substrate; (d) Flexible silicon photonic waveguide transferred onto plastic substrate* [133].

Silicon photonics will enjoy the success of flexible electronics if they can also be transformed into a flexible form as shown in Fig. 3.1. Currently, there are mainly three types of fabrication methods which could bring flexible form of silicon photonic devices, namely:

(1) By using stamp-assisted transfer-and-bond method to integrate monocrystalline based silicon photonic devices on top of elastomeric or regular plastic substrate. With this technique, a variety of silicon photonic devices have already been demonstrated on top of flexible plastic substrates such as : waveguide [132], photonic crystals waveguide (PCW), multimode interference (MMI) devices [133] and on-chip laser [134].

(2) By using low-temperature physical vapor deposition (PVD) or chemical vapor deposition (CVD) technique, amorphous silicon or dichalcogenide glass could be directly deposited onto plastic substrate and then be patterned into photonic devices. With such technique, various fully integrated flexible photonic structures have also been demonstrated such as ring resonator [135] and multi-layer photonic devices [136]

(3) By utilizing a bond-and-etch method, large area silicon membrane could be transferred onto rigid substrate. The details of the method are: First a regular SOI wafer is glued to a glass substrate by using an adhesive layer such as SU8, then a back-side dry etch process is executed to fully remove the bottom bulk silicon. After the buried oxide layer is removed by wet etch process, the top silicon layer will be left flat and steady on the receiving substrate. Various silicon photonic devices on transparent glass substrate have been demonstrated with this technique, such as grating coupler, waveguide and MMI [137].

The transfer-and-bond approach is particularly appealing to silicon photonics because crystalline silicon, comparing to amorphous silicon and glass material, has superior optical properties which include a high refractive index and low optical loss. There are several additional considerations that make the prospect of flexible integrated photonics uniquely promising. First, the path of light can be bent when it is guided in optical fibers or waveguides. Although glass fibers typically can only be bent to a radius of 1 cm before incurring significant loss, thanks to silicon's high refractive index (n=3.5), silicon waveguides can make a turn with a radius as small as a few microns without significant loss. Second, unlike electronic devices, optical devices can be coupled with

each other without being in physical contact — light can propagate through transparent material to couple multiple layers of optical devices. This attribute of contact-free connection could enable three-dimensional integration of photonic systems. Third, there are abundant compliant and patternable plastic materials with low refractive index and low optical absorption that are suitable for optical applications, including elastomer such as polydimethylsiloxane **(**PDMS), polyester such as PET (polyethylene terephthalate) and PEN (polyethylene naphthalate), and transparent epoxies such as SU8. Finally, the concern of silicon devices' mechanical fragility and structural stability can be addressed by the same design strategies developed for flexible electronics.

In this chapter, we demonstrate a flexible form of silicon photonics using the transfer-and-bond fabrication method. Photonic circuits including interferometers and resonators have been successfully transferred onto flexible plastic substrates with preserved functionalities and performance. By mechanically deforming the flexible substrates, the optical characteristics of the devices can be tuned reversibly over a large range. The demonstration of flexile silicon-on-plastic (SOP) photonics could open the door to a plethora of applications including biomechanical sensing and bio-photonic probing.

3.2 Fabrication Method

Comparing to the fabrication process of traditional silicon or III-V material based flexible electronic devices, there are more stringent requirements for the realization of flexible silicon photonics devices since not only the photonic structure always possesses

an extremely high length to width ratio, the performance of most silicon photonic devices are highly susceptible to their relative positions. Therefore, a reliable and highly stable transfer process is needed.

As mentioned in the first chapter, the transfer-and-bond process highly relies on the competition of surface adhesion force between the ink/stamp interface and the host/ink interface. Therefore, the basic strategy to realize such reliable transfer process for silicon photonic devices is to maximumly increase the contrast between the Van-der-Waal forces at these two interfaces.

The fabrication process flow is shown in Fig. 3.2 below:

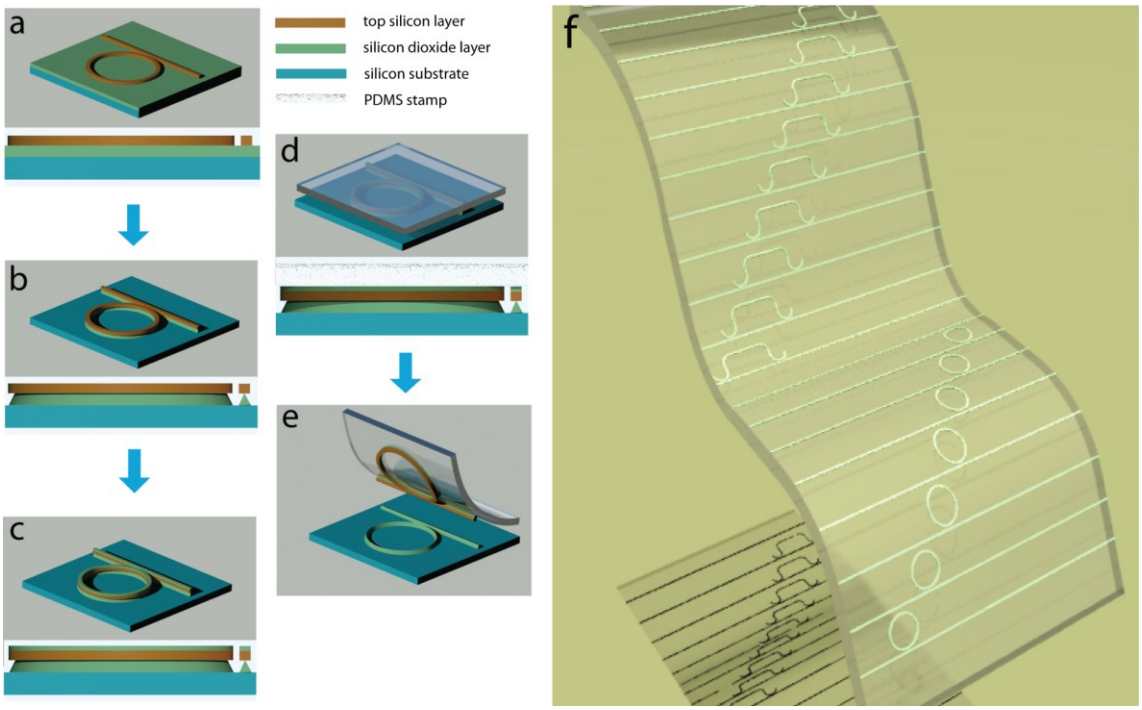

Figure 3.2 *The fabrication process flow for the flexible silicon photonic devices on PDMS substrate: (a) Patterning the silicon photonic devices on SOI substrate by using Ebeam lithography and dry etch; (b) Extremely undercut the buried oxide layer underneath the top*

photonic structure by using wet etch; (c) Increase the surface adhesion force between the silicon/PDMS interface by using surface treatment technique; (d), (e): Transfer the silicon photonic devices onto flexible PDMS substrate; (f) 3D illustration of final devices.

At first, a standard wafer cleaning process is executed with acetone, IPA, methanol and DI water, in sequence. Afterwards, the customized SOI wafer (Soitec Inc.) with 220nm silicon layer and 3um oxide layer is baked at 180 degree Celsius for 4 minutes, followed by spinning 100nm HSQ Ebeam resist (XR-1541) on top. By utilizing Ebeam lithography (Vistec EBPG5000+), different types of devices are patterned onto the wafer. The dimension of the waveguide is 500nm wide, 220nm tall and with various lengths up to 5mm. The smallest feature is the coupling gap which is about 100nm wide. With a dosage of 1500μC/cm^2 and development in CD-26 developer for 4 to 6 minutes, all the photonic structures (including the coupling gap) are resolved perfectly.

Deep trench etcher (SLR-770) with CF_4 and SF_6 based recipe is used to transfer these Ebeam lithography defined patterns into the top silicon layer of the SOI wafer. Then, in order to largely reduce the surface adhesion force between the host/ink interface, the oxide layer underneath the photonic structures is undercut by using 10:1 buffered oxide etch (BOE). In order to maintain a constant and relatively slow etch speed, the BOE solution was kept at 0 degree Celsius during the whole undercut process. After such critical wet etch process, all the silicon photonic structures are merely supported by the remaining oxide as shown in Fig. 3.3. To further increase the Van der Waal force contrast between the silicon/oxide interface and silicon/stamp interface, a thin layer of silicon dioxide around 20nm is deposited on top of the undercut devices by using plasma enhanced chemical vapor deposition (PECVD, Plasmatherm 340) at high temperature.

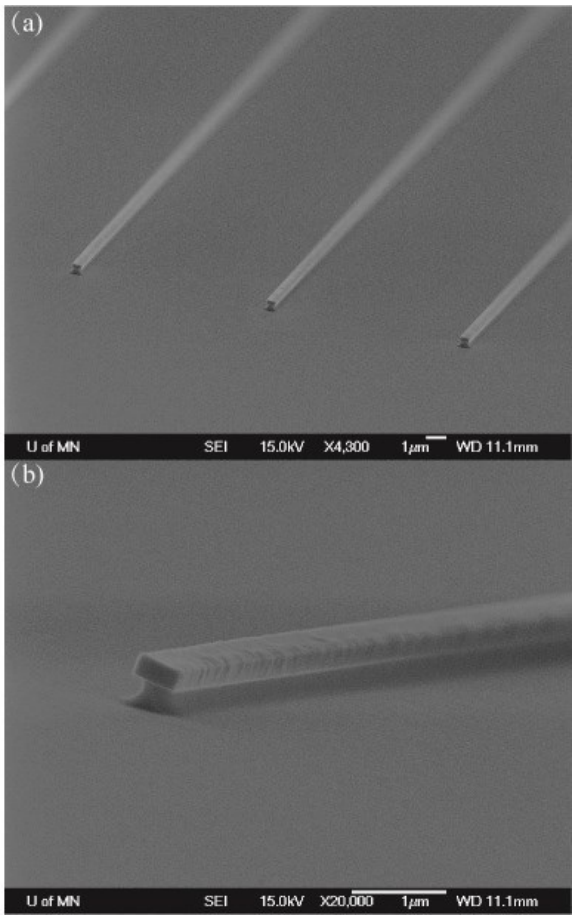

Figure 3.3 *SEM images of the silicon waveguide structure after critical wet etch process. (a) angled view of an array of silicon waveguides after critical wet etch process; (b) enlarged view of a single silicon waveguide after critical wet etch process.*

The PDMS stamp is made from the Sylgard 184 (Dow Corning, Inc.) mixture with 10 to 1 ratio and cured at 90 degree Celsius for 1 hour. Prior to the surface treatment, the PDMS stamp is thoroughly cleaned by isopropyl alcohol (IPA) and then dried. UV-induced ozone (Jelight UVO-Cleaner) is utilized to treat both the PECVD grown oxide surface and the PDMS stamp surface for 2 minutes. Besides the surface treatment, the peeling direction highly affects the yield of the transfer process, which is shown in Fig.

3.4. When the peeling direction is perpendicular to the longitudinal direction of the waveguide, most of the waveguide can be successfully transferred onto the elastomeric substrate without wrinkles and break as shown in Fig. 3.4a, c. However, if the peeling direction is parallel to the longitudinal direction of the waveguide, wavy structure will show up on almost all the waveguide structures as shown in Fig. 3.4b and Fig. 3.4d. If the peeling direction is angled with the photonic structure between 0 degree and 90 degree, the transfer yield will highly rely on the aspect ratio and geometry of the pattern.

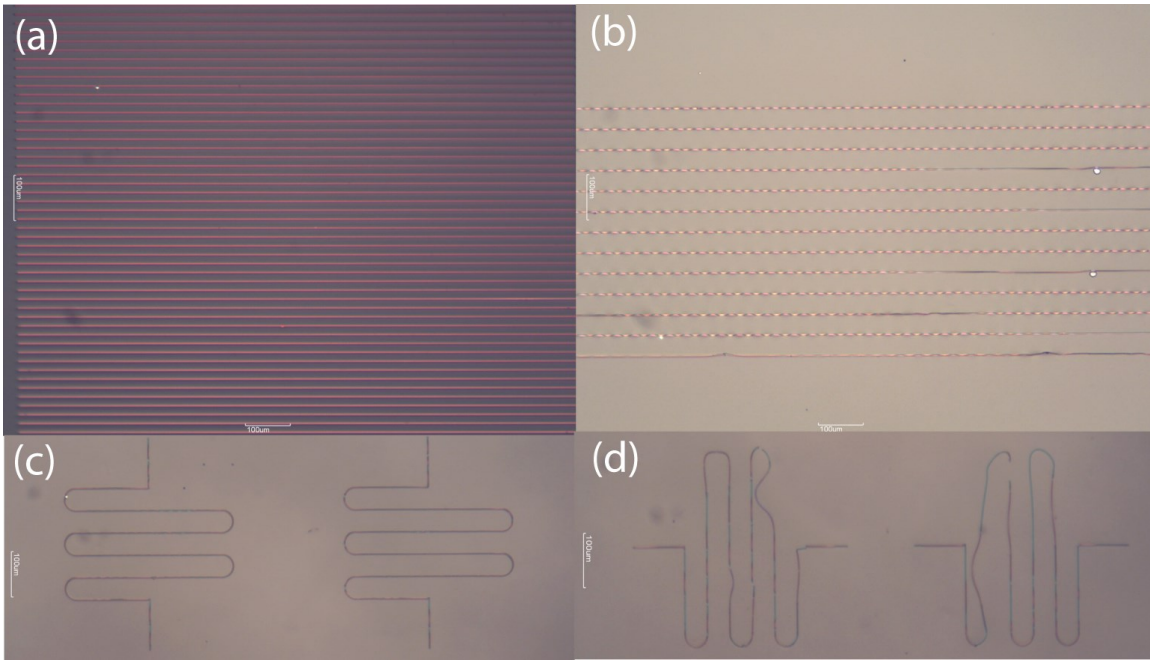

Figure 3.4 *The transferred silicon photonic waveguide with different peeling directions: (a) silicon waveguide array on PDMS with peeling direction perpendicular to the waveguide longitudinal direction; (b) silicon waveguide array on PDMS with peeling direction parallel to the waveguide longitudinal direction; (c) meander shape silicon waveguide on PDMS with peeling direction perpendicular to the longer meander shape; (d) meander shape silicon waveguide on PDMS with peeling direction parallel to the longer meander shape.*

By finely designing the photonic structure and controlling the peeling direction, a large array of silicon waveguides could be transferred onto PDMS substrate with extremely high yield as shown in Fig. 3.5.

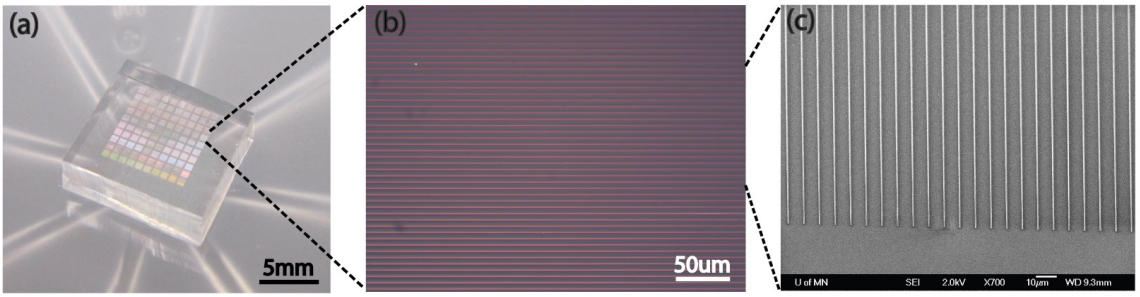

Figure 3.5 *A dense array of silicon waveguides transferred onto PDMS substrate. (a) 10 by 10 array of silicon waveguides with different density on PDMS substrate; (b) optical microscope image of a single array of silicon waveguide on PDMS substrate; (c) SEM image of (b).*

Then, by using a modified probe station, the surface treated PDMS stamp and the oxide coated silicon photonic devices will be brought into contact with each other with precise alignment to make sure both ends of each silicon waveguide will be right at the edge of the PDMS stamp as shown in Fig. 3.6, which is the prerequisite to realize the following butt coupling measurement. Since most of the waveguide we transferred is around 1cm long and the diameter of the optical fiber we use is 250μm, a 9.95mm x 9.95mm x 200μm rectangular cuboid is designed to extrude outside the surface of the PDMS stamp as shown in Fig.3.6, which could help us to well align the optical fiber and the transferred waveguide.

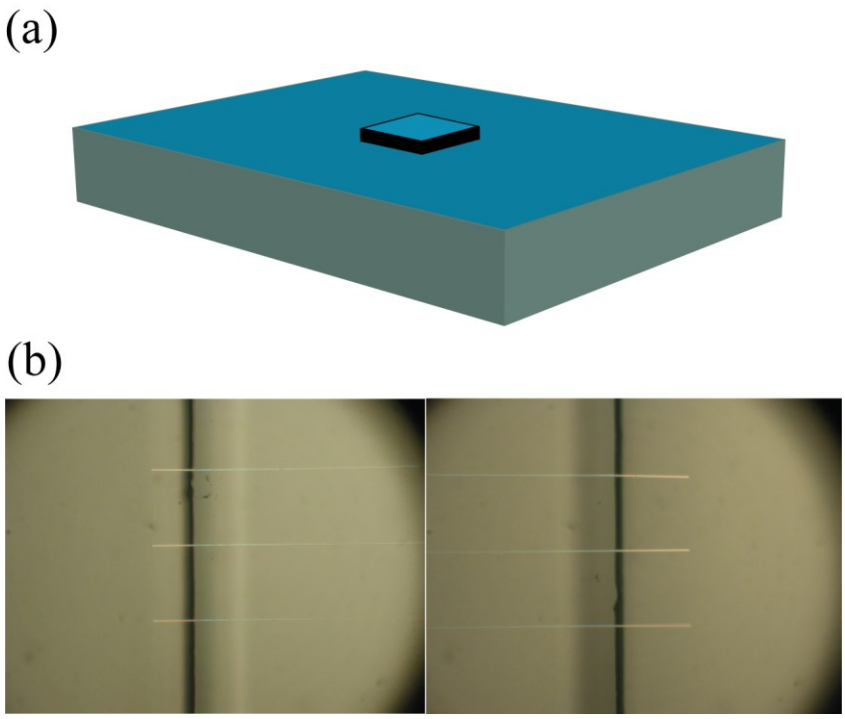

Figure 3.6 *(a) PDMS stamp geometry; (b) the ends of silicon waveguides transferred on PDMS stamp*

After precise alignment has been achieved, certain amount of uniform pressure is applied on top of the PDMS stamp. After the conformal contact is reached between the PDMS and silicon, the PDMS stamp will be peeled off from the SOI substrate. In this way, the whole silicon photonic layer is lifted off from the substrate and transferred to the flexible PDMS film. Because no adhesive material is used in the procedure, contamination to the photonic devices and consequent adverse effects on their optical performance is minimal. The strong bonding force between silicon and PDMS surfaces, however, can ensure high-yield transfer with low occurrence of dislocations and deformations. Various silicon photonic devices including ring resonator, Mach-Zehnder

interferometers (MZI) and micro-ring add-drop filters (ADF) have been successfully transferred onto PDMS substrate as shown in Fig. 3.7. The devices consist of single-mode silicon waveguides (width, 500 nm; thickness, 220 nm) with a total length as long as 1 centimeter — an aspect ratio of 2×10^4. As shown in the images, deformations and dislocations are hardly noticeable in the transferred devices. Most notably, high magnification images in Fig.3.7c, d reveal that the coupling gaps between the waveguides as small as 100 nm wide are precisely preserved in the fabrication process.

During the fabrication process, there are several important parameters that need to be well controlled in order to achieve highly reliable transfer of silicon photonic structures with extremely high aspect ratio, which are:

(1) The temperature of Hydro Fluoride (HF) acid needs to be precisely controlled since the etch rate of oxide will increase exponentially with the rising temperature of the solution. To achieve the critical wet etch point, the etch rate needs to be well controlled with the precision on the order of nanometer scale. To further guarantee the realization of critical wet etch, several calibration bars whose widths are slightly smaller than the photonic structure have been utilized during the fabrication process, the implementation of which could be used as a real-time monitor for the wet etch process. Since the wet etch process is not thoroughly uniform across the whole chip, the wet etch calibration bars need to be patterned uniformly across the substrate

(2) The thickness of the oxide deposited on top of the undercut silicon waveguide needs to be well controlled since a thick PECVD oxide layer may wrap around the whole photonic device and make the adhesion force at the ink/host interface too large. On the

other hand, an extremely thin PECVD oxide layer may lead to poor uniformity of such "adhesion" layer which could render a poor adhesion force at the ink/stamp interface.

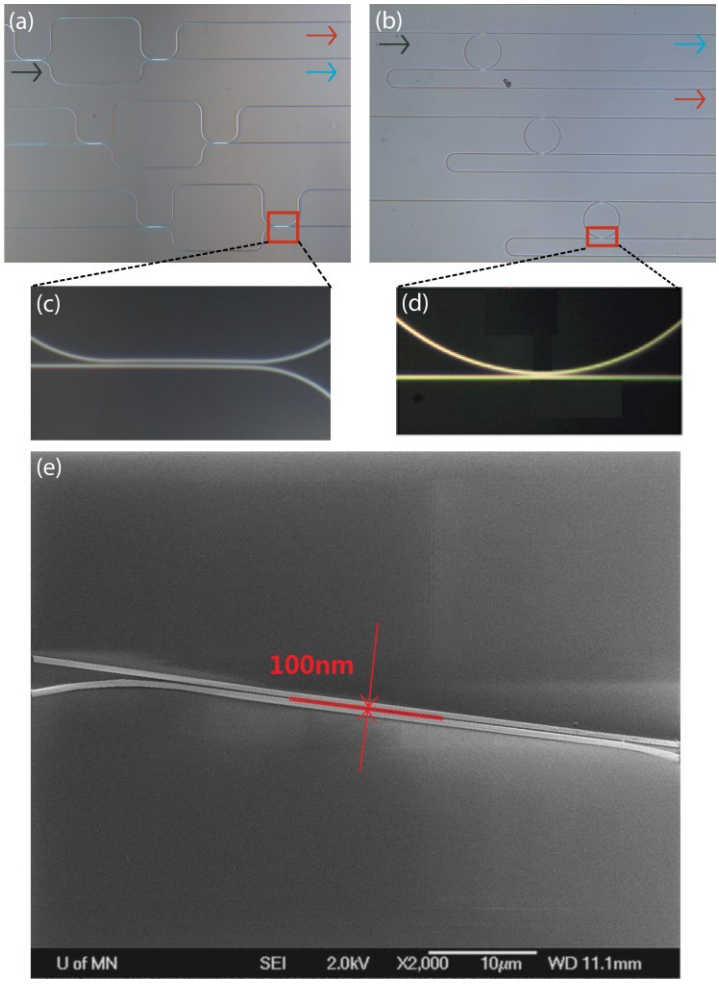

Figure 3.7 *Optical and SEM images of transferred silicon photonic devices on PDMS substrate: (a) Optical microscope images of Mach-Zehnder interferometers (MZI) (b) and micro-ring add-drop filters (ADF) after being transferred onto PDMS substrate. The enlarged view of the coupling gap of these two structures is shown in (c) and (d), respectively. (e) The SEM image (lower panels) shows that the coupling gaps of 100 nm between the waveguides are precisely preserved during the transfer process.*

3.3 Characterization of silicon photonic devices on PDMS

To characterize the optical performance of the transferred photonic devices, fiber butt-coupling method was used to couple light from a tunable laser source into the devices and to deliver optical output signals to a photo detector. The measurement stage setup is shown in Fig. 3.8 below. The laser was provided by the Agilent 8163B control panel with 81940A laser source module. Two telecomm tapered fiber with 125μm diameter, 2.5μm spot size and 14μm working distance were used for butt coupling as the transmitting and receiving end. The output signal from the photo detector is sent to an automatic data acquisition (DAQ) system for visualization and further analysis purposes.

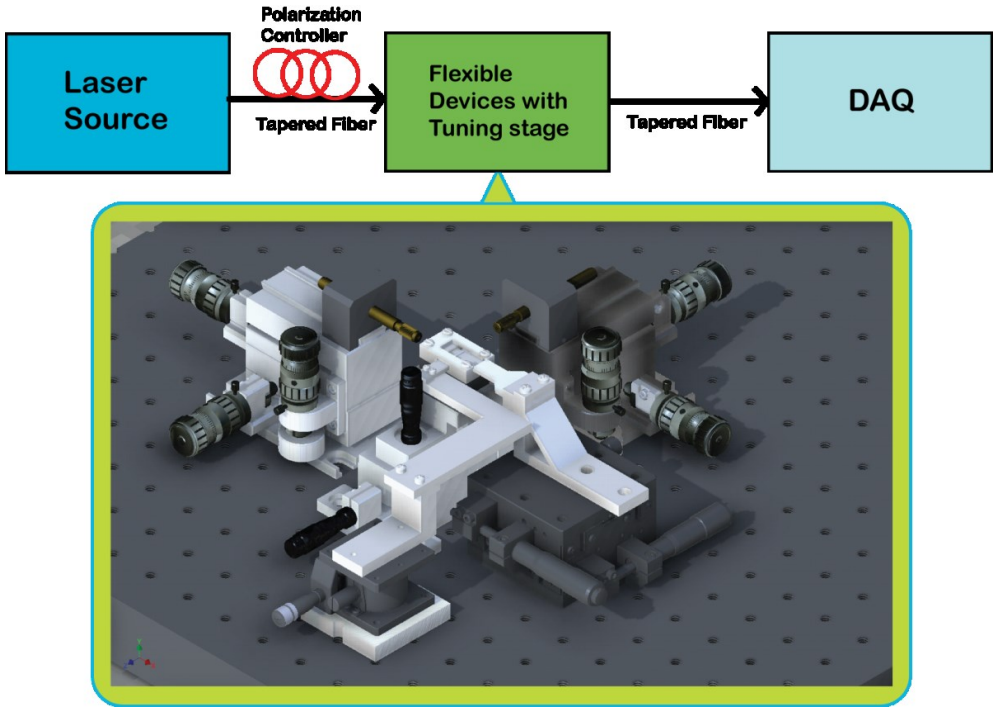

Figure 3.8 *Schematics for the measurement set up and the picture for the opto-mechanical stage designed for realizing the butt coupling scheme.*

Fig. 3.9 shows the typical transmission spectra of transferred MZI and micro-ring ADF devices. A directional coupler structure is utilized in the MZI structure, and the optical power output from each port after the directional coupler should be around 50%. The spectra measured at the two output ports of the MZI device are completely complementary to each other with a high extinction ratio, which proves that the directional coupler exactly split the optical power by half and the transfer process does not change the performance of the directional coupler. Similarly, the output spectra at the "through" port and the "drop" port of the micro-ring filter are also complementary. Those indicate that the optical coupling between the waveguides on the PDMS substrate remains efficient with a very low loss, in agreement with the observed uniform coupling gap. Fig. 3.9c shows the broadband transmission spectrum of a critically coupled ring resonator, showing a group of resonances with the highest extinction ratio of 25 dB. From the measured quality factors Q of the ring resonators, the propagation loss in the transferred waveguide can be determined. Fig. 3.9d shows an under-coupled resonance at 1593.55 nm with a waveguide loaded Q of 9.3×10^4. It corresponds to an intrinsic Q of 1.5×10^5 and a propagation loss of 3.8 dB/cm. This value of propagation loss is comparable to that of the original silicon waveguides on a SOI substrate, which typically is in the range of 3-4 dB/cm if no special fabrication optimization is used. It is unlikely that optical absorption in the PDMS substrate causes an increase of loss because of its transparence in the near-infrared spectral range [138]. We attribute any excessive loss to oxide residue and other contaminations on the waveguide surface, which can be etched away or reduced with improved transfer process. The above results demonstrate that the

transfer method developed here preserves the optical performance and functionalities of the silicon photonic devices on the new plastic substrate.

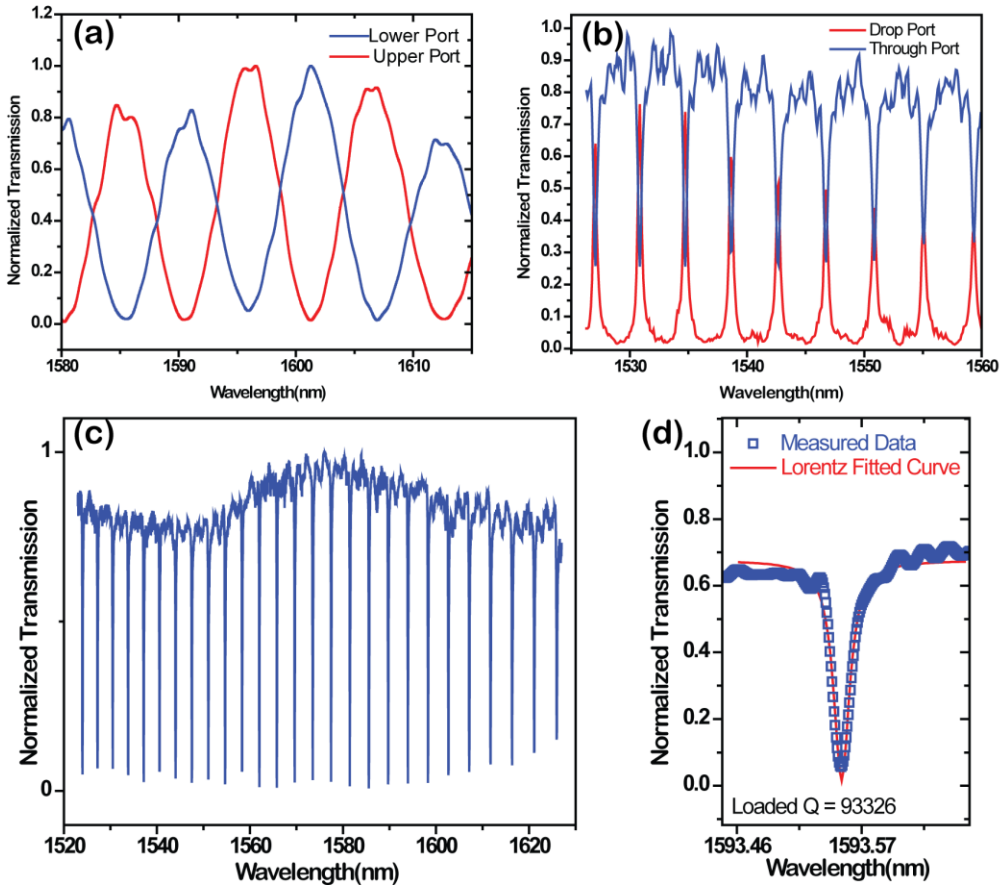

Figure 3.9 *Preserved optical functionalities of silicon photonic circuits on PDMS substrate. (a), The transmission spectra of the MZI circuit measured at its two output ports, showing high extinction ratio and complementary interference fringes. (b), Transmission spectra of the micro-ring ADF measured at the "through" and the "drop" ports, also showing complementary resonance peaks. (c), Broadband transmission spectrum of a ring resonator critically coupled to a waveguide on PDMS substrate, showing a high extinction ratio up to 25 dB. (d), Measured high-Q resonance (blue symbols) and Lorentzian fitting (red line) of a transferred ring resonator*

with loaded quality factor of 9.3×10^4 and intrinsic quality factor of 1.8×10^5. The corresponding value of waveguide propagation loss is 3.8 dB/cm.

3.4 Application of Strain Sensing and Theoretical Analysis

3.4.1 Tunability of Flexible Silicon Photonic Devices

Tunable photonic devices are highly desirable for applications in optical network systems that can be frequently reconfigured. Conventional tuning or modulation methods either use the electro-optical effects in non-silicon materials such as lithium niobate ($LiNbO_3$) [139], [140], which is difficult to integrate with silicon devices, or rely on thermo-optical effect by electrically heating the devices [141], [142]. The heating method, although integratable, needs to continuously consume electrical power to maintain the tuning. Because the optical characteristics of the flexible devices apparently will change when the substrate is deformed, their functionalities can be precisely tuned by applying a controlled force, using a piezoelectric actuator for instance. Below the yield limit of the substrate material which is significantly higher for plastic materials (~50% for PDMS) than for crystalline materials (less than 1% for crystalline silicon), the device structure will respond elastically to the applied force, and reversible and reliable tuning can be achieved over a remarkably large range.

To demonstrate the tunability, the flexible photonic devices were mounted on a precision mechanical stage modified from the measurement stage as shown in Fig. 3.8 that can apply uniaxial compressive strain on the devices. The tuning range was counted by the micrometer whose smallest scale is 10μm, which is also the smallest tuning step

we executed. The alignment of the tapered fiber with the end of silicon waveguide was realized by a long working distance microscope and an attached colored CCD camera. The Fig. 3.10 shows the results of tuning a Mach-Zehnder interferometer device when a compressive force is applied in the direction normal to the horizontal waveguides in the interferometer arms or the waveguide side coupled to the ring resonator (Fig. 3.10a). As shown in Fig. 3.10b, when the substrate is compressed in steps to a distance of 300μm, which corresponds to 3% strain, the output interference fringes of the MZI shift continuously toward shorter wavelength by 12 nm, more than one free-spectral range (FSR=10 nm). When the compression is gradually released, the fringes recover to the initial positions precisely. However, the effect of mechanical tuning on the micro-ring resonators is quite different from that of Mach-Zehnder interferometers. As shown in Fig. 3.10c, when the sample is compressed with up to 9% strain (which corresponds to 900μm distance), the resonance peaks only shift slightly by ~0.25 nm toward shorter wavelengths, about one sixteenth of the free spectral range (4 nm) of the micro-rings. In contrast, as displayed in Fig. 3.10d, both the extinction ratio and the Q factor of the ring change rapidly with applied strain. When the sample is compressed by 4%, the extinction ratio first increases from 3 dB to a maximal value of 22 dB, indicating the resonator reaches the critical coupling condition. At the same time, the loaded Q factor increases from 5×10^3 to 1.5×10^4, suggesting that the intrinsic Q factor of this micro-ring device is $\sim3.0\times10^4$. Further compression reduces the extinction ratio until the resonances disappear while the Q factor continues to rise to 2.5×10^4, approaching the intrinsic value. The change of both extinction ratio and quality factor of the ring resonator shows that the

device is shifting from the over-coupled regime into under-coupled regime during the compression process.

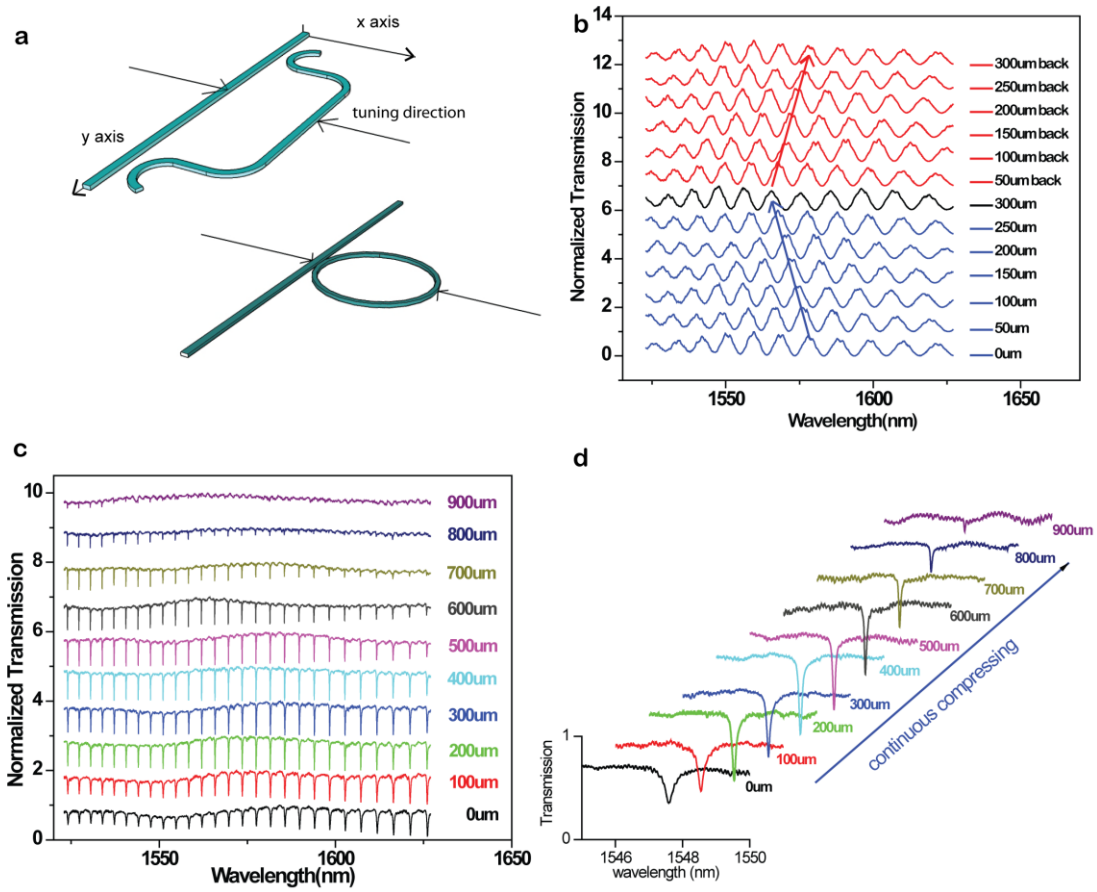

Figure 3.10 *Mechanical tuning of a Mach-Zehnder interferometer and a ring resonator on an elastic substrate. (a), Schematics showing how the uniaxial strain is applied to the MZI and ring resonator. (b), Under increasing compression, the interference fringes in the output of MZI continuously shift toward shorter wavelength. When the compression is relaxed, the fringes recover to their initial spectral positions. (c), Under increasing compression, the wavelengths of the resonances only shift slightly whereas the resonance extinction ratios and quality factors changes dramatically. (d), The change of a single optical resonance under increasing compression up to 9% strain in total.*

The extremely high susceptibility of the flexible silicon photonic devices' performance to the PDMS surface deformation has determined our tuning method, which is compressing but not stretching. Since the PDMS surface will always have certain amount of deformation once clamped, it is difficult to remain a steady start point for the measurement during the stretching process. However, such issues do not exist during the compression tuning process since no mechanical force needs to be exerted onto the PDMS stamp at the very beginning. In the stretching experiment, larger tuning range means larger friction force between the clamp and the PDMS, which will accordingly change the performance of the flexible devices with unwanted surface deformation. Thus, in order to maintain the systematic continuity of the measurement data set, the tuning range could only reach up to 200μm during the stretching process. The stretching data of the ring resonators had exhibited the same shift trend as that of the compressing data, which is shown in Fig. 3.11 below, the reason for such shift here is simply because the coupling gap between silicon waveguide and ring resonator has been enlarged during the stretching process.

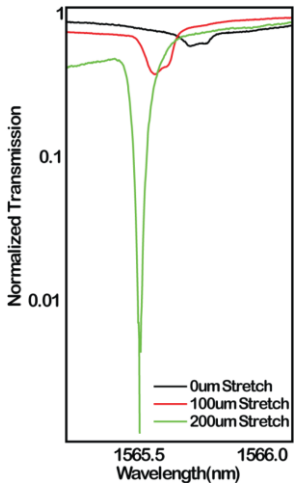

Figure 3.11 *Stretching data from 0um to 200μm for ring resonators at 1565.5nm resonance*

3.4.2 Theoretical Analysis for Tuning Process of MZI

The shift of transmission fringes of MZI during the tuning process is induced by both photo-elastic effect [143] of silicon material and the geometrical change induced by the strain inside of silicon.

For the MZI structure

$$\Delta\varphi = \frac{2\pi n_{eff}}{\lambda} L \tag{3.1}$$

where $\Delta\varphi$ denotes the phase difference between the two arms of the MZI. In our design, the path length difference $L \approx 200\mu m$, with a linear compressing tuning, the transmission spectrum of MZI will be linearly blue-shifted accordingly. At 1550nm the phase difference will decrease by 2 π by compressing the PDMS up to 200μm.

The phase difference decrease could be attributed to the decrease of both n_{eff} and L, which could be expressed as:

$$\Delta(n_{eff}L) = \Delta L n_{eff} + L\Delta n_{eff} \tag{3.2}$$

ΔL will only be caused by the deformation of silicon, and Δn_{eff} will be induced by both the photoelastic effect of silicon and that of PDMS.

Since the phase difference will only be related to the part of the upper arm along the tuning direction as shown in Fig. 3.12a, we will mainly focus on this region. Its dimension is about 220nm thick, 500nm wide and $40*(\pi-1)\mu m$ long. The dimensions of our PDMS substrate are about 3mm thick, 1cm wide and 1.5cm long. As shown in Fig. 3.12b below:

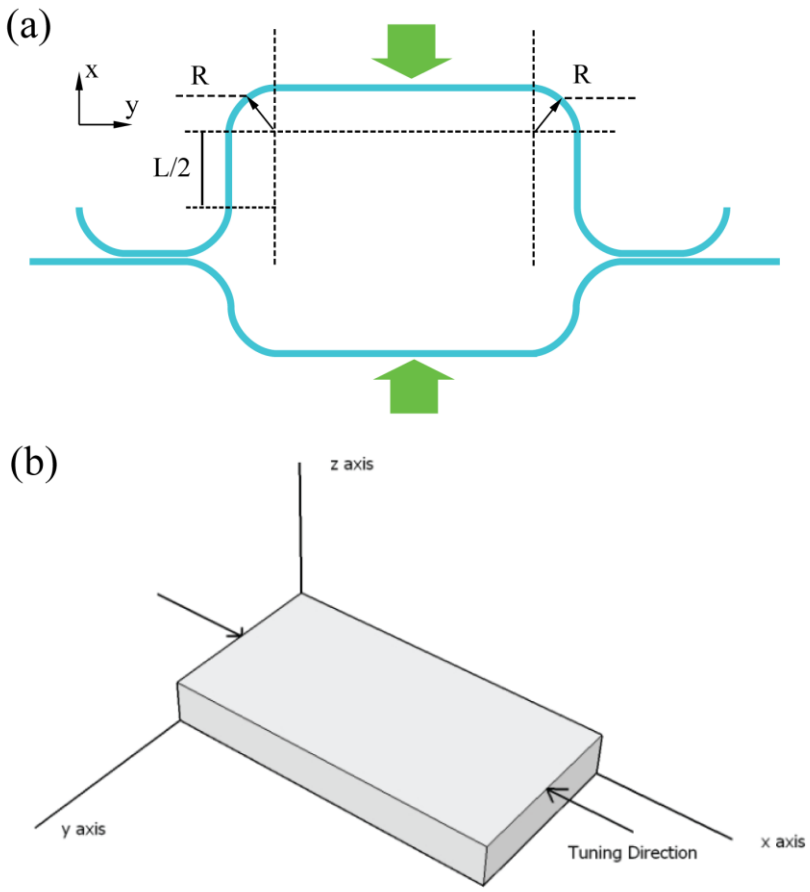

Figure 3.12 *(a) Geometry of Mach-Zehnder interferometer device used in the experiment under uniaxial compression. (b) Geometry of the PDMS stamp used in the experiment under uniaxial compression.*

(a) Photoelastic effect in silicon

In consideration of photoelastic effect of silicon and PDMS, we need to know several important parameters for both of these two materials, such as Elastic Modulus *E* and Poisson Ratio υ, as shown in Table 3.1 below:

	Elastic Modulus *E* (Pa)	Poisson Ratio υ
PDMS Mechanical Properties	2×10^6	0.48
Silicon Mechanical Properties	170×10^9	0.22

Table 3.1 *Mechanical Properties of PDMS and silicon*

Subject to a compressive membrane force, the rigid silicon nanostrip or nanoribbon on top of a compliant substrate like PDMS will spontaneously generate ordered sinusoidal buckling patterns as shown in Fig. 3.13 [144]–[147]. When the compressive membrane force induces a strain inside the PDMS substrate which surpass the critical strain ε_c, a sinusoidal wave shape buckling pattern will be generated in the layer of silicon structures with an amplitude A, and a period λ. The equations for the sinusoidal wave shape and the critical strain ε_c are listed below**:**

$$w = A\sin(\frac{2\pi}{\lambda}x) \tag{3.3}$$

$$A = h\sqrt{-\frac{\varepsilon_a}{\varepsilon_c}-1} \tag{3.4}$$

$$\lambda = 2\pi h(\frac{\overline{E_f}}{3\overline{E_s}})^{\frac{1}{3}}\frac{(1+\varepsilon_a)}{(1+\varepsilon_a+\xi)^{\frac{1}{3}}} \tag{3.5}$$

$$\varepsilon_c = \frac{1}{4}(\frac{3\overline{E_s}}{\overline{E_f}})^{\frac{2}{3}} \tag{3.6}$$

Where $\overline{E_s} = \frac{E_s}{1-\upsilon_s^2}$ and $\overline{E_f} = \frac{E_f}{1-\upsilon_f^2}$, which are the plain-strain modulus for the substrate and the film, respectively. ε_a is the applied strain and $\xi = -5\varepsilon_a / 32$. For PDMS substrate and silicon structures on top, by utilizing the Young's modulus and Poisson ratio provided above in Table. 3.1, the critical strain could be calculated as $\varepsilon_c \approx 0.03\%$. In our tuning stage, the smallest controllable tuning distance is 10μm, and the corresponding strain is $10\mu m / 1cm = 0.1\%$, which means the buckling pattern had always existed since the very beginning of the tuning process.

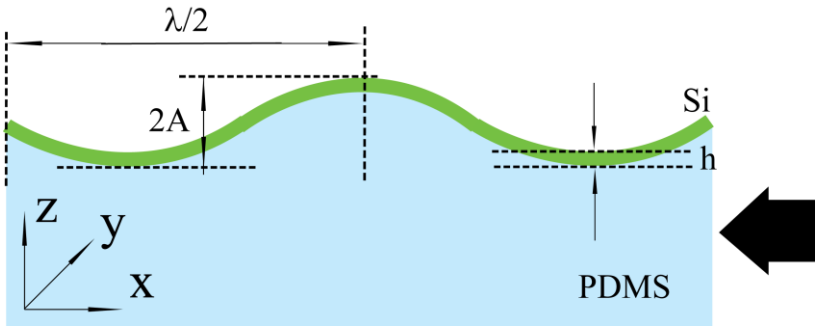

Figure 3.13 *Periodically buckled rigid film on a compliant substrate when a compressive strain is applied.*

The strain inside the silicon waveguide buckled with the sinusoidal wave shape is mainly attributed to three different components: the initial strains, the gradients of the in-plane displacements, and the rotation caused by the deflection. Thus, the strain could be expressed as**:**

$$\varepsilon_{xx} = \varepsilon_{xx}^0 + \frac{\partial u}{\partial x} + \frac{1}{2}(\frac{\partial w}{\partial x})^2, \tag{3.7}$$

in which, u is the in plane displacement, and w is the out of plane displacement as shown in Fig. 3.14:

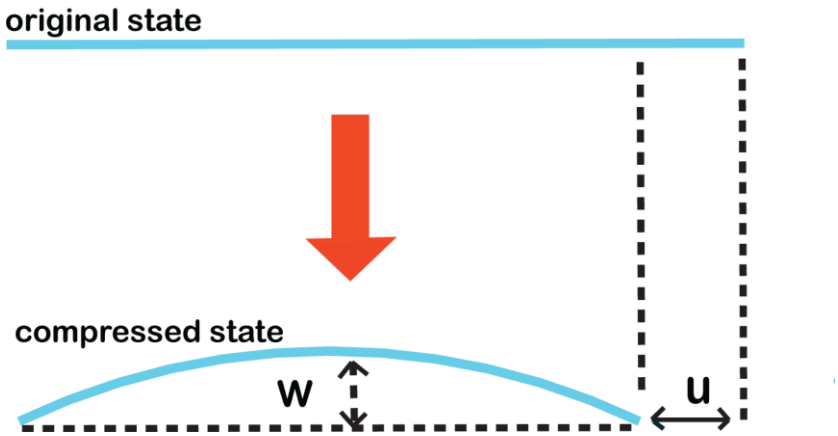

Figure 3.14 *Displacement of buckled silicon waveguide*

According to Hooke's law, the membrane force in the x direction and the membrane strain satisfy the expression:

$$N_{xx} = h\frac{E}{1-\upsilon^2}[(1-\upsilon)\varepsilon_{xx} + \upsilon\varepsilon_{zz}] \tag{3.8}$$

The buckled film remains bonded to the compliant substrate. On the film/substrate interface, we could consider the shear stress is zero [148], then the membrane force N_{xx} needs to be uniform in the waveguide:

$$\frac{\partial N_{xx}}{\partial x} = 0 \tag{3.9}$$

Combining Equations (3.3), (3.7), (3.8) and (3.9)， we can calculate the in-plane displacement as well as the x direction strain, which are:

$$u = \frac{A^2\pi}{4\lambda}\sin(\frac{4\pi x}{\lambda}) \tag{3.10}$$

$$\varepsilon_{xx} = \varepsilon_{xx}^{0} + \frac{\pi^2 A^2}{\lambda^2} \tag{3.11}$$

By using Equations (3.4), (3.5) and (3.11), we can derive the relationship between the x-direction strain inside the silicon waveguide ε_{xx} and the applied strain ε_a:

$$\varepsilon_{xx} = \frac{1}{4} \frac{(-\frac{\varepsilon_a}{\varepsilon_c} - 1)(1 + \frac{27}{32}\varepsilon_a)^{2/3}}{(\frac{\overline{E_f}}{3\overline{E_s}})^{\frac{2}{3}}(1+\varepsilon_a)^2} \tag{3.12}$$

Consider $\varepsilon_c = 0.0003$, $(\frac{\overline{E_f}}{3\overline{E_s}})^{\frac{2}{3}} = 806.75$, and the initial strain $\varepsilon_{xx}^{0} = 0$.

The strain tensor in this buckled silicon waveguide could be described as:

$$\varepsilon = \begin{pmatrix} \varepsilon_{xx} \\ \varepsilon_{yy} \\ \varepsilon_{zz} \\ \varepsilon_{yz} \\ \varepsilon_{zx} \\ \varepsilon_{xy} \end{pmatrix} = \begin{pmatrix} \varepsilon_{xx} \\ -\upsilon\varepsilon_{xx} \\ -\upsilon\varepsilon_{xx} \\ 0 \\ \varepsilon_{zx} \\ 0 \end{pmatrix} \tag{3.13}$$

The photoelastic effect is caused by the change of the optical indicatrix [149] as:

$$\Delta(\frac{1}{n^2})_i = \sum_{j=1}^{6} \rho_{i,j}\varepsilon_j \tag{3.14}$$

since our waveguide only support TE_{11} mode, therefore, the only refractive index we care about is the one along y-direction. Silicon has a cubic crystal structure, so its elasto-optic coefficient matrix could be written like:

$$\rho_{i,j} = \begin{pmatrix} \rho_{11} & \rho_{12} & \rho_{12} & 0 & 0 & 0 \\ \rho_{12} & \rho_{11} & \rho_{12} & 0 & 0 & 0 \\ \rho_{12} & \rho_{12} & \rho_{11} & 0 & 0 & 0 \\ 0 & 0 & 0 & \rho_{44} & 0 & 0 \\ 0 & 0 & 0 & 0 & \rho_{44} & 0 \\ 0 & 0 & 0 & 0 & 0 & \rho_{44} \end{pmatrix} \tag{3.15}$$

By utilizing equations (3.13), (3.14) and (3.15), we can have the equation below:

$$\Delta(\frac{1}{n^2})_y = \rho_{12}\varepsilon_{xx} - (\rho_{11} + \rho_{12})\upsilon\varepsilon_{xx} \tag{3.16}$$

$$\Delta n_y = \frac{n^3}{2}(-\rho_{12}\varepsilon_{xx} + (\rho_{11} + \rho_{12})\upsilon\varepsilon_{xx}) \tag{3.17}$$

$n = 3.42$, $\rho_{11} = -0.101$, $\rho_{12} = 0.0094$ [150]. Subsequently, by using equations (3.12) and (3.17), we can have the relationship between Δn_y and ε_a:

$$\Delta n_y = \frac{n^3}{2}[(\upsilon - 1)\rho_{12} + \upsilon\rho_{11}]\frac{1}{4}\frac{(-\frac{\varepsilon_a}{\varepsilon_c} - 1)(1 + \frac{27}{32}\varepsilon_a)^{2/3}}{(\frac{\overline{E_f}}{3\overline{E_s}})^{\frac{2}{3}}(1 + \varepsilon_a)^2} \tag{3.18}$$

The plot of the relationship between $-\Delta n_y$ of silicon and ε_a is shown in Fig. 3.15, by using,

$n = 3.42$, $\rho_{11} = -0.101$, $\rho_{12} = 0.0094$, $\varepsilon_c = 0.0003$, $(\frac{\overline{E_f}}{3\overline{E_s}})^{\frac{2}{3}} = 806.75$,

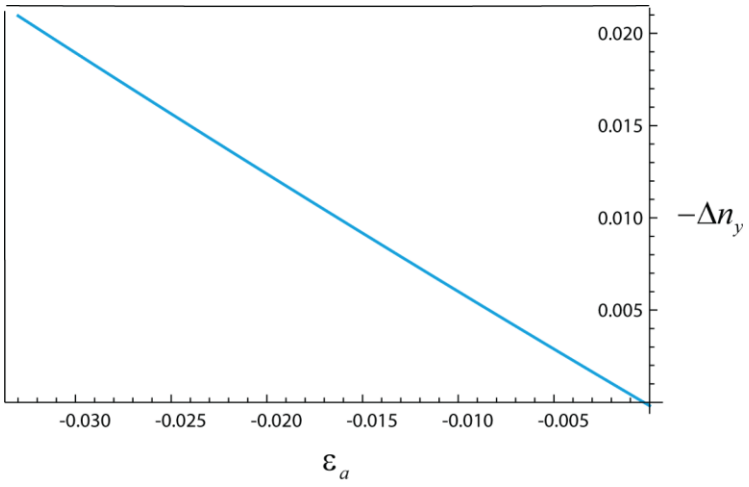

Figure 3.15 *Derived relationship between* $-\Delta n_y$ *of silicon and* ε_a

Also, by utilizing equations (3.12), (3.13), (3.14) and (3.15), we can have the equation for Δn_x :

$$\Delta n_x = \frac{n^3}{2}[2\upsilon\rho_{12} - \rho_{11}]\frac{1}{4}\frac{(-\frac{\varepsilon_a}{\varepsilon_c} - 1)(1 + \frac{27}{32}\varepsilon_a)^{2/3}}{(\frac{\overline{E_f}}{3\overline{E_s}})^{\frac{2}{3}}(1+\varepsilon_a)^2} \tag{3.19}$$

The path length difference ΔL of the two MZI arms is shown in Fig. 3.12a, the power transmission of the MZI can be written as:

$$\begin{aligned} T(\varepsilon_a) &= \frac{1}{2}\left[1 + \cos(\Delta\phi)\right] \\ &= \frac{1}{2} + \frac{1}{2}\cos\left\{\frac{2\pi\,\Delta L}{\lambda}\left[n_{\text{eff}} + \Delta n_{\text{eff}}^{\text{y}}(\varepsilon_a)\right]\right\} \end{aligned} \tag{3.20}$$

and the wavelength of the fringe peak of order N is:

$$\lambda_N = \frac{1}{N}(n_{\text{eff}} + \Delta n_{\text{eff}}^{\text{y}}) \cdot \Delta L \tag{3.21}$$

(b) Photoelastic effect in PDMS

PDMS is also a type of photoelastic material with weak intrinsic birefringence. Within 40% strain [151], the PDMS could be considered as a linear isotropic material which will deform linearly with a constant elastic modulus. our PDMS stamp's dimension is 10mm×10mm×3mm, and the tuning range is smaller than 500μm, so our strain is $500\mu m/1cm = 5\% << 40\%$.

Without applied pressure, PDMS exhibits an isotropic optical indicatrix. However, with applied force, due to its photoelastic characteristic, the refractive index change along the pressure direction will be different to that normal to the pressure direction.

The applied pressure is along -x direction. The strain is a 3-component vector since the shear strain is negligible, which is:

$$\varepsilon = \begin{bmatrix} \varepsilon_{xx} \\ \varepsilon_{yy} \\ \varepsilon_{zz} \end{bmatrix} = \begin{bmatrix} \varepsilon_a \\ -\upsilon\varepsilon_a \\ -\upsilon\varepsilon_a \end{bmatrix} \tag{3.22}$$

The elasto-optic coefficient matrix for isotropic PDMS without shear strain could be expressed as:

$$\rho_{i,j} = \begin{bmatrix} \rho_{11} & \rho_{12} & \rho_{12} \\ \rho_{12} & \rho_{11} & \rho_{12} \\ \rho_{12} & \rho_{12} & \rho_{11} \end{bmatrix} \tag{3.23}$$

So, by using equation (3.6), (3.11) and (3.12), we can calculate the increase of the refractive index along y direction for PDMS is:

$$\Delta n_y = -\frac{n^3}{2}[\rho_{12}\varepsilon_a - (\rho_{11} + \rho_{12})\upsilon\varepsilon_a] \tag{3.24}$$

By using the elasto-optic constant expression [152], equation (3.24) could also be expressed as:

$$\Delta n_y = C_1 P_y + C_2 (P_x + P_z) \tag{3.25}$$

and $P_x = -\varepsilon_a E$, $P_y = P_z = 0$, $C_1 - C_2 = 1.8e-10 Pa^{-1} = 180 Br$ [153], $1 Br = 1e-12 Pa^{-1}$.

We can presume $C_1 = 90 Br$ and $C_2 = -90 Br$, then we can have the relationship between Δn_y and ε_a:

$$\Delta n_y = C_2 P_x = -C_2 E \varepsilon_a \tag{3.26}$$

The plot of the relationship between $-\Delta n_y$ of PDMS and ε_a is shown in Fig. 3.16:

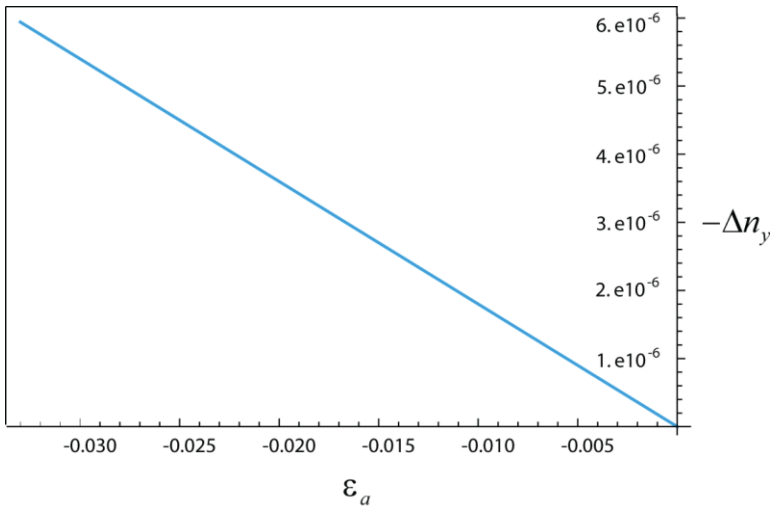

Figure 3.16 *Derived relationship between* $-\Delta n_y$ *of PDMS and* ε_a

(c) Silicon waveguide deformation

Since we presume the silicon waveguide will only bend rather than be compressed since it is much more rigid than PDMS, therefore, the path length difference between two arms will maintain the same. In other words, we presume the path length difference

between the two arms of the MZI will not change during the whole tuning process since the strain induced inside of silicon is relatively small which will not be sufficient enough to induce path length change.

(d) Fitting experimental data with theoretical model

By combining the analysis result from sections (a) to (c), we will be able to write the relationship between the applied strain ε_a and the change of n_{eff} of the fundamental TE mode of the waveguide along the direction of strain as:

$$\Delta n_{\text{eff}} = \eta \cdot n^3 \left[-\rho_{12} + (\rho_{11} + \rho_{12})\upsilon \right] \varepsilon_{\text{a}} / 2$$

Where η=1.15 is the proportional coefficient that relates the change of the waveguide mode index and the change of the material refractive index and is determined by theoretical calculation with all the values provided by references. We also know from Eq. (3.20) that the transmission of the MZI at a specific wavelength will change sinusoidally in relation to the applied strain. The results calculated from the theoretical model of the optical transmission spectrum shift of MZI during the tuning process are shown in Fig. 3.17, which shows good agreement with the experimental results with small discrepancy. Such discrepancy can be attributed to the imprecision of the tuning setup used in the experiment.

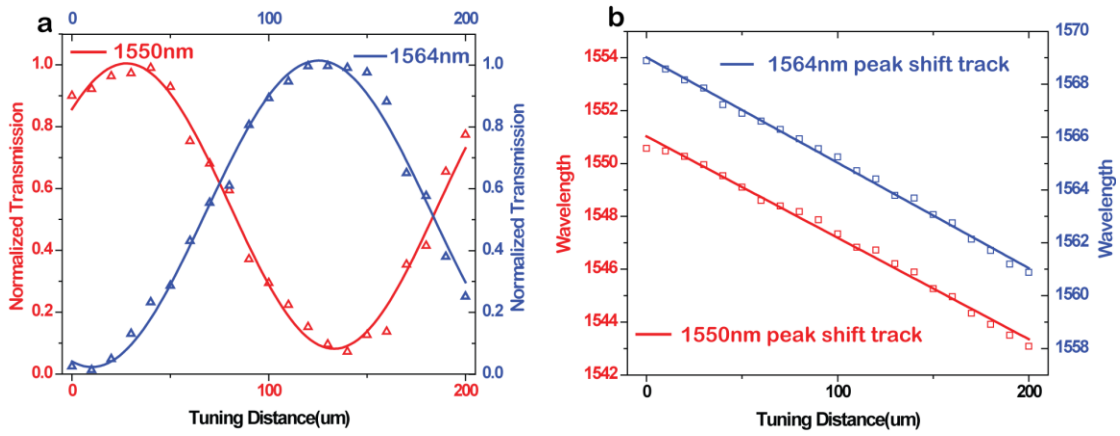

Figure 3.17 *(a) At given wavelengths (1550nm, blue; 1564nm, red), the measured transmission (symbols) varies sinusoidally with the increasing compressive strain, in excellent agreement with the results of the theoretical model (lines). (b), The peak wavelengths (symbols) of the interference fringes shift linearly with the increasing compressive strain toward shorter wavelengths as expected from the theory (lines).*

(e) Energy Consumption for such tuning

For tuning PDMS up to 200μm, we can calculate the energy consumption during this process. Assume the work we do is W, the cross section area of PDMS is A, the force we apply is F, the PDMS stamp length is L_p, then length change is ΔL ,then:

$$E = \frac{P}{\varepsilon} = \frac{F/A}{\Delta L / L_p} \tag{3.27}$$

$$W = F\Delta L = \frac{E\Delta L A}{L_p}\Delta L \tag{3.28}$$

During our tuning process, we consider PDMS as a linear, isotropic material,

therefore, its Young's Modulus will maintain unchanged. By using equation (3.16), we can have:

$$W = \int_0^{200um} \frac{E\Delta LA}{L_p}\Delta L d\Delta L = \frac{EA}{3L_p}(\Delta L)^3 \,|_0^{200um} \approx 2e-9J \tag{3.29}$$

This energy consumption is positively proportional to the cross-section area of PDMS as well as to the distance we tuned. In this experiment, we shift the transmission fringe by 8.6nm and the cross section area of our PDMS stamp is 3mm×1cm, however, if we can shrink the PDMS's thickness down to 100μm and width down to 500μm, meanwhile, we only shift a ring resonator's transmission fringe by one FWHM. Assuming its quality factor is 100,000, then the energy consumption for switching this device on and off once will be $6*10^{-14}J$.

3.4.3 Theoretical Analysis for Tuning Process of Ring Resonator

For ring resonators, we presume that the whole ring will also buckle like the MZI structure. However, there will be no y direction displacement or deflection, which means the x direction strain is still uniform along the waveguide that could be derived from equation (3.12):

$$\varepsilon_{xx} = \frac{1}{4}\frac{(-\frac{\varepsilon_a}{\varepsilon_c}-1)(1+\frac{27}{32}\varepsilon_a)^{2/3}}{(\frac{\overline{E_f}}{3\overline{E_s}})^{\frac{2}{3}}(1+\varepsilon_a)^2} \tag{3.12}$$

The ring's diagram is shown below in Fig. 3.18:

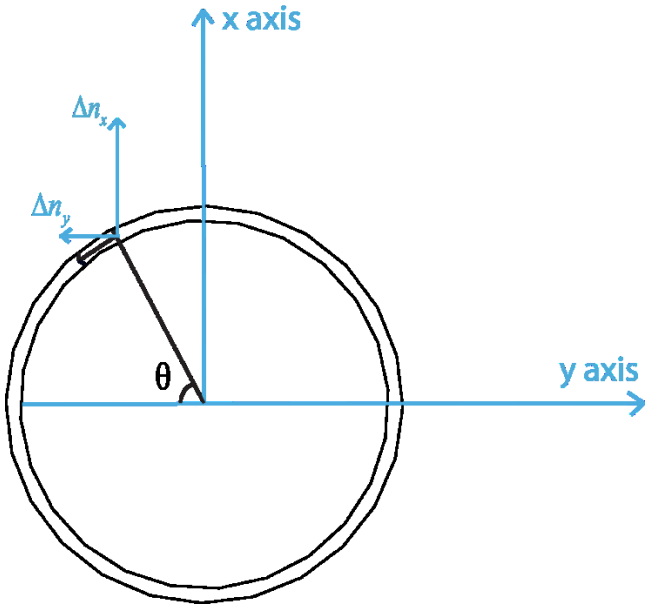

Figure 3.18 *Diagram of the ring resonator under uniaxial strain*

As we can see that both the Δn_x and Δn_y will affect the E field of the light propagating along the ring. For a small portion of the ring with an angle θ as shown in Fig. 3.18, the change of the refractive index is:

$$\Delta n = \Delta n_x \sin\theta + \Delta n_y \cos\theta \tag{3.30}$$

Therefore, to calculate the refractive index change along the peripheral path of the ring resonator, we could have:

$$\Delta n_T = 4\int_0^{\frac{\pi}{2}} (\Delta n_x \sin\theta + \Delta n_y \cos\theta) d\theta = 4(\Delta n_x + \Delta n_y) \tag{3.31}$$

We can rewrite the expression of $\Delta n_x, \Delta n_y$ as $\Delta n_y = Af(\varepsilon_a), \Delta n_x = Bf(\varepsilon_a)$, by utilizing Eq. (3.18) and (3.19), we can derive that:

$$\frac{A}{B} = \frac{(\upsilon - 1)\rho_{12} + \upsilon\rho_{11}}{2\upsilon\rho_{12} - \rho_{11}} \approx -0.281 \tag{3.32}$$

Therefore, if the ring is actually buckled up, the roundtrip refractive index change will not be zero, but rather to be:

$$\Delta n_T = 4(\Delta n_x + \Delta n_y) = 2.876\Delta n_x \tag{3.32}$$

The reason why the resonance did not shift during the uniaxial tuning is that the closed loop shape of the ring resonator performs as a shield which prevents the formation of surface wrinkles of the PDMS substrate [154], [155], which means the PDMS inside and underneath the ring resonator is not buckled. However, compressing the substrate will cause both the buckling of the waveguide and consequently the lateral and vertical offset between the waveguide and the ring resonator. This increase in the coupling gap reduces the coupling coefficient κ and causes the waveguide-ring system to be tuned gradually from the initial over-coupled condition to critically-coupled and further to under-coupled conditions. Analysis using standard theory of optical resonators (lines in Fig. 3.19a and b) indicates that the effective coupling gap is tuned from the initial value of 80 nm to about 112 nm to reach critical coupling when 3.7% compressive strain is applied.

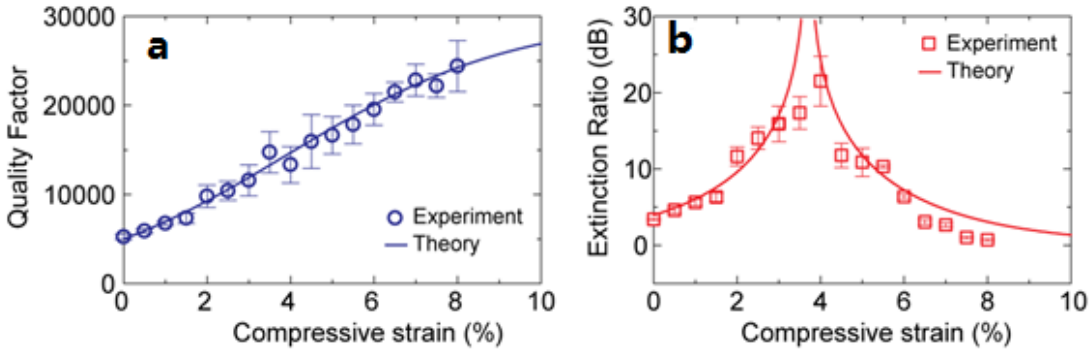

Figure 3.19 *Quality factor (c) and extinction ratio (d) versus the applied compressive strain. The quality factor increases five folds over a range of 8% strain. The extinction ratio can obtain a maximal value of 22 dB when the critical coupling condition is reached at a strain level of*

3.7%. The results agree with a theoretical model (lines) assuming the coupling gap increases linearly with the applied compressive strain.

At small mechanical deformation range, we can presume the coupling gap changes linearly with the applied strain, and the theoretical result predicted with such presumption agrees quite well with the experimental result as shown in Fig. 3.19a and b.

3.4.4 Repeatability Test of the Tuning Process

To test the repeatability and reversibility of mechanical tuning of the flexible devices, we have repeated the tuning process for more than fifty cycles of compressing and releasing. Fig. 3.20 shows the results from a Mach-Zehnder interferometer (a) and a micro-ring resonator (b). For the MZI device, the output interference fringes shift when the sample is compressed. Fig. 3.20a~d show the transmission measured at 1570 nm and spectral shift of the fringes of a MZI device when the sample is repeatedly compressed and released in steps of 50 μm for ten times. After each cycle, the transmission recovers to within 1.8% (standard deviation, the same below) of the original value and the fringe peak wavelengths return to the original value within 0.4% of the free-spectral range (FSR). In the intermediate tuning step, the variations of transmission and fringe peak wavelengths are within 9.6% and 1.1% FSR, respectively. This large variation of measured transmission is due to the misalignment between the input/output tapered fibers and the sample when it is deformed. This issue of misalignment can be alleviated if the fibers are permanently attached to the sample, using optical epoxy for example.

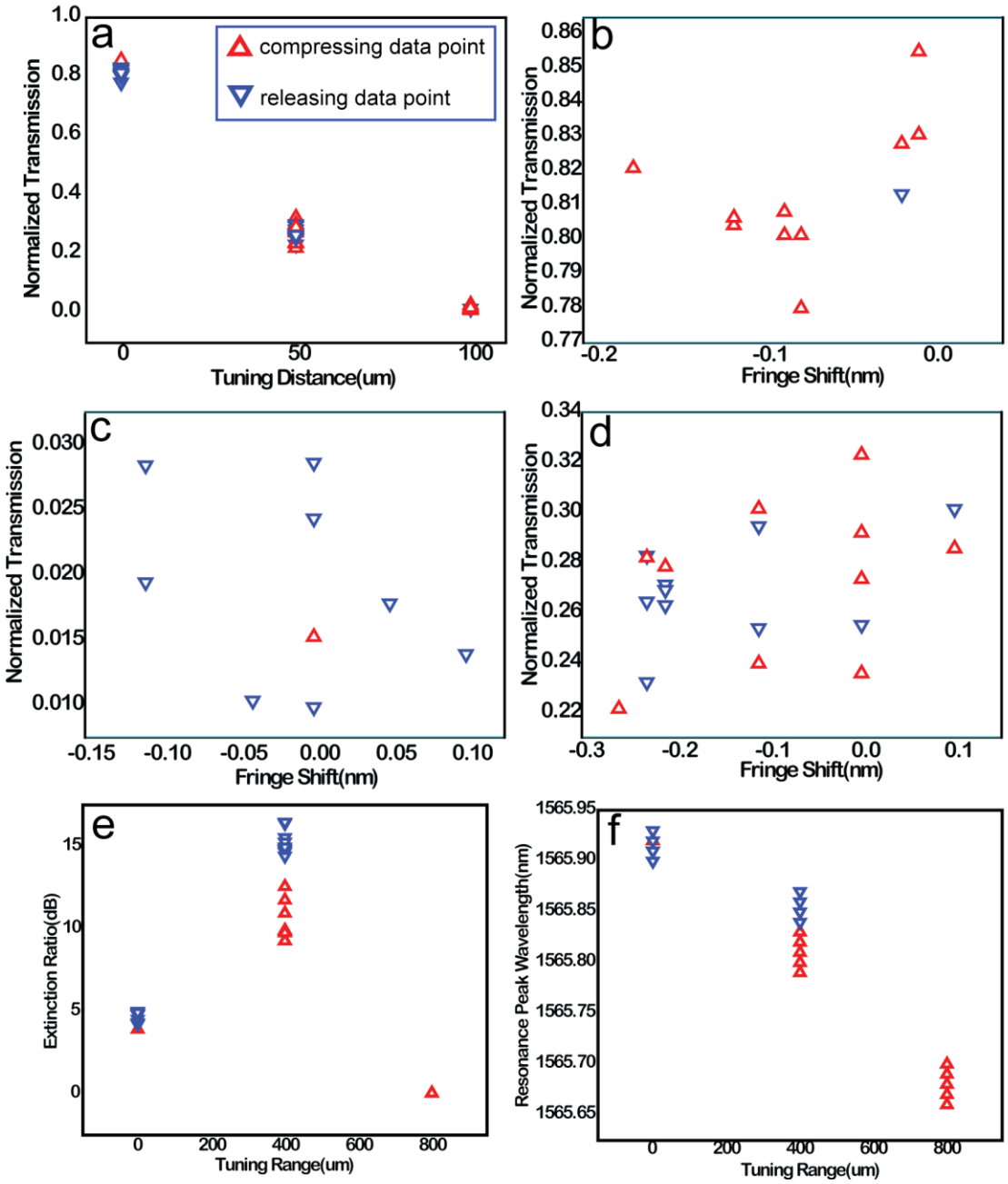

Figure 3.20 *Repeatability test result of tuning process of MZI structure and ring resonator structure. (a) Transmission change of MZI at 1570nm during the tuning process at original position,, 50μm tuning position and 100μm tuning position, red rectangle and blue rectangle represent the data read through the compressing and releasing processes, respectively; (b) MZI*

transmission fringe shift measured at (b)100μm tuning position, (c)50μm tuning position and (d)original position from 10 repetitive tuning experiments; (e) Extinction ratio change and (f) resonance frequency shift of the ring resonator at 3 different tuning distances during several repetitive tuning experiments.

For the micro-ring resonator, mechanically tuning changes its extinction ratio and quality factor dramatically but only slightly affects the resonance wavelengths. Fig. 3.20b shows the result of repeatability test in which the extinction ratio and the shift of resonance wavelengths are measured in repeated tuning cycles of compression and releasing in steps of 400 μm. Like the MZI, after every cycle, the device's optical properties recover to the original value within 5% for extinction ratio and 0.2% of FSR for resonance wavelengths, indicating excellent reversibility of the device. However, in the intermediate steps of tuning, large variations of ER and resonance wavelengths were observed along with a hysteretic effect between compressing and releasing. It suggests that the friction between the sample and the mechanical stage is high and the manual control of the stage displacement is imprecise. These can be solved by using an integrated actuator for mechanical tuning or a more properly designed mechanical system to avoid the friction induced hysteresis. Nevertheless, the demonstrations above show that the flexible photonic devices have very good repeatability and reversibility properties. They thus are promising to be applied in reconfigurable and adaptive optical systems.

3.5 Conclusion

In this chapter, by utilizing bond-and-transfer method, various flexible silicon photonic devices have been successfully demonstrated on top of PDMS substrates, with preserved optical functionalities, mechanical resilience and tunability. This is a significant first step toward a fully integrated flexible photonic system. The devices on PDMS substrate can be subsequently transferred onto a variety of plastic materials. By advancing the method demonstrated here and those developed in flexible electronics research and solving the challenge of precise alignment, it will be possible to assemble multiple layers of flexible silicon photonic devices with active optical devices made of non-silicon material (such as germanium and III-V semiconductors) in three dimensions. However, the critical wet etch method has a stringent requirement for the geometry of the photonic devices which means the structures with non-uniform geometry such as grating couplers, tapered waveguides and etc. could not be heterogeneously integrated by using such method.

CHAPTER 4: FULLY INTEGRATED FLEXIBLE PHOTONIC CIRCUIT BASED ON SILICON AND SILICON NITRIDE

4.1 Modified Transfer Method

In order to extend the versatility and functionality of flexible silicon photonic devices, the geometry limitation imposed by the critical wet etch process needs to be overcome. Although low temperature deposition method could be utilized to solve such issues, the performance of the photonic devices will be compromised since the optical quality of amorphous silicon is not comparable with that of the monocrystalline silicon. To keep the high quality of pristine silicon, we try to develop alternative transfer method to extend the capability of the stamp-assisted fabrication method. Also, the butt-coupling method we utilized in the work described in Chapter 3 is not ideal for integrated devices, in consideration of the integration density of the future devices. Therefore, we started to try various methods to transfer the ring resonators with integrated grating couplers onto PDMS and flexible plastic substrates.

4.1.1 SU8 Assisted Transfer Method

The uniform width of all the geometries is the fundamental requirement of the original transfer method, since the level of undercut has to maintain uniform all around the SOI substrate. However, with the introduction of grating couplers, the geometry uniformity has been broken and another method was needed for maintaining everything in position before the transfer process. One way to realize such purpose is to fix all the geometries with certain protection layer during the wet etch process, and we decide to use

SU8 epoxy since it is both physically and chemically stable. The fabrication flow chart is shown below in Figure. 4.1

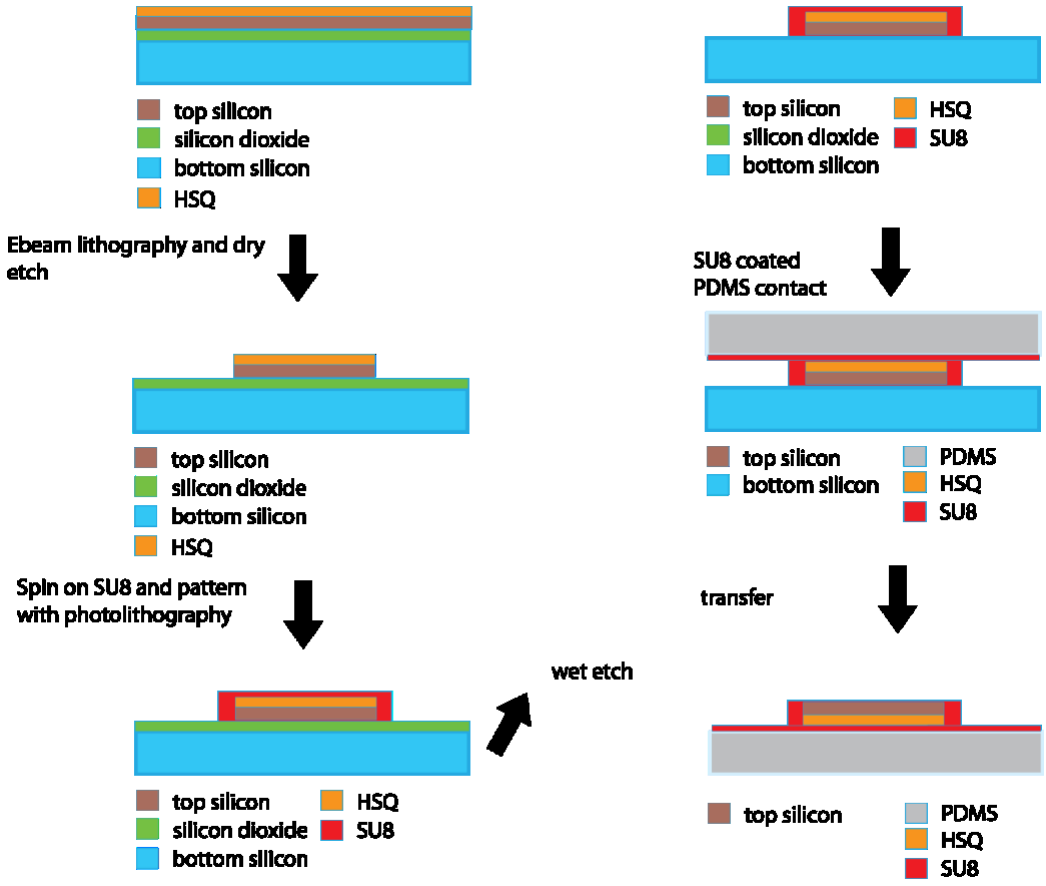

Figure 4.1 *Fabrication flow chart of SU8 assisted transfer method*

The results of the devices after wet etch and transfer by using this method are shown in Fig. 4.2(a) and (b), respectively. As we can see, there are two main drawbacks of this method:

(1) Even by using SU8 protection layer, the devices will shift around during the wet etch process, which may bring potential damage to the delicate integrated silicon photonic devices.

(2) By using this method, the transfer yield will be low, which is resulted from the poor uniformity of the SU8 layer spun on top of the PDMS stamp. Such poor uniformity will make the conformal contact between the SU8 and silicon layer hard to be achieved.

Moreover, after transferring the devices from SOI wafer to PDMS substrate, it is almost impossible to transfer them back onto other plastic substrate due to the strong adhesion force between the SU8 and silicon. Therefore, this method is not really suitable for transferring integrated silicon photonic devices onto plastic substrate.

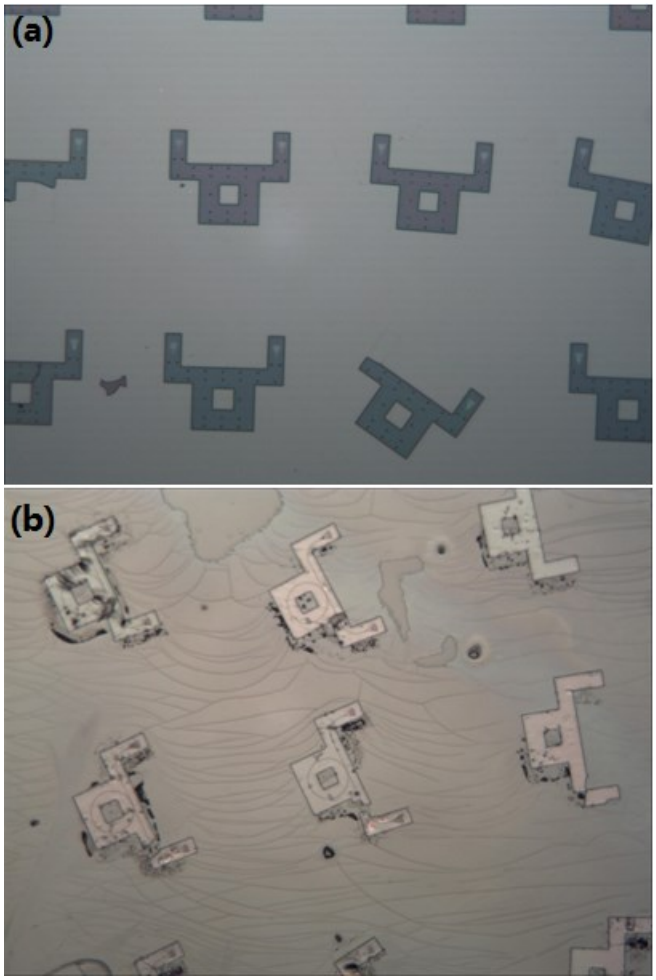

Figure 4.2 *(a) SU8 covered ring resonators with grating couplers after wet etch. (b) Transferred devices with their SU8 cover onto the SU8 coated PDMS substrate.*

4.1.2 Rib Waveguide Based Transfer Method

Instead of using traditional strip waveguide, the usage of rib waveguide structure could provide unique advantages in such transfer method. The slab structure could perform as a natural supporting layer for the integrated silicon photonic devices, and with appropriately designed rib/slab ratio, the propagation loss and bending loss of the rib waveguide should be comparable to that of traditional strip waveguides.

We have tried several methods to realize an efficient and simple transfer of silicon photonic devices based on shallow etched structures, which will be described below:

(a) Anchor assisted rib waveguide transfer method

The first method we adopt is to utilize some photoresist based anchors to stabilize the shallow etched photonic structures during the wet etch process. The detailed fabrication process is described below (This is for SOI wafer with 400nm silicon and 200nm buried oxide) and shown in Fig. 4.3:

(1) Thoroughly clean the SOI sample with acetone, IPA and DI water, then blow dry
(2) Bake the sample at 180 degree Celsius for 5 minutes
(3) Spin ZEP on top of the sample with 3000rpm for 1min and then bake at 180 degree Celsius for another 2 minutes
(4) Use ebeam lithography to pattern the photonic structure
(5) Develop in ZED-N50 developer for 2mins and then in IPA for 30 seconds
(6) Use RIE to etch the top silicon layer for 300nm
(7) Strip ZEP by using NMP for 15 minutes, then use Piranha solution to clean the residue for 5 minutes

(8) Dehydrate the sample at 115 degree Celsius for 2 minutes

(9) Spin on S1805 at 3000rpm for 30 seconds

(10) Bake the sample at 115 degree Celsius for 1 minute

(11) Pattern the carrier slab shape by using photolithography

(12) Soft bake at 115 degree Celsius for 1 minute

(13) Develop in MF-319 for 30 seconds, rinse with DI water then blow dry

(14) Use RIE etcher to etch through both the top silicon and buried oxide layer

(15) Strip S1805 by using 1165 for 5 minutes and then use Piranha(H_2SO_4:H_2O_2=1:1) solution to remove the photoresist residue for 2 minutes

(16) Dehydrate at 115 degree Celsius for 2minutes

(17) Use HMDS to treat the surface of sample for 3 minutes

(18) Spin on S1805 at 3000rpm for 30 seconds

(19) Bake at 115 degree Celsius for 1 minute

(20) Pattern the anchor structure by using photolithography

(21) Soft bake at 115 degree Celsius for 1minute

(22) Develop in MF-319 for 30 seconds, rinse with DI water then blow dry

(23) Wet etch with HF(49%) solution for 30 minutes

(24) Rinse with DI water, then blow dry

(25) Dry etch with Oxygen plasma for 10 minutes

(26) Treat the surface of PDMS and that of SOI sample with UV Ozone for 2 minutes and 1 minute, respectively.

(27) Contact PDMS with SOI sample and then peel with fast speed

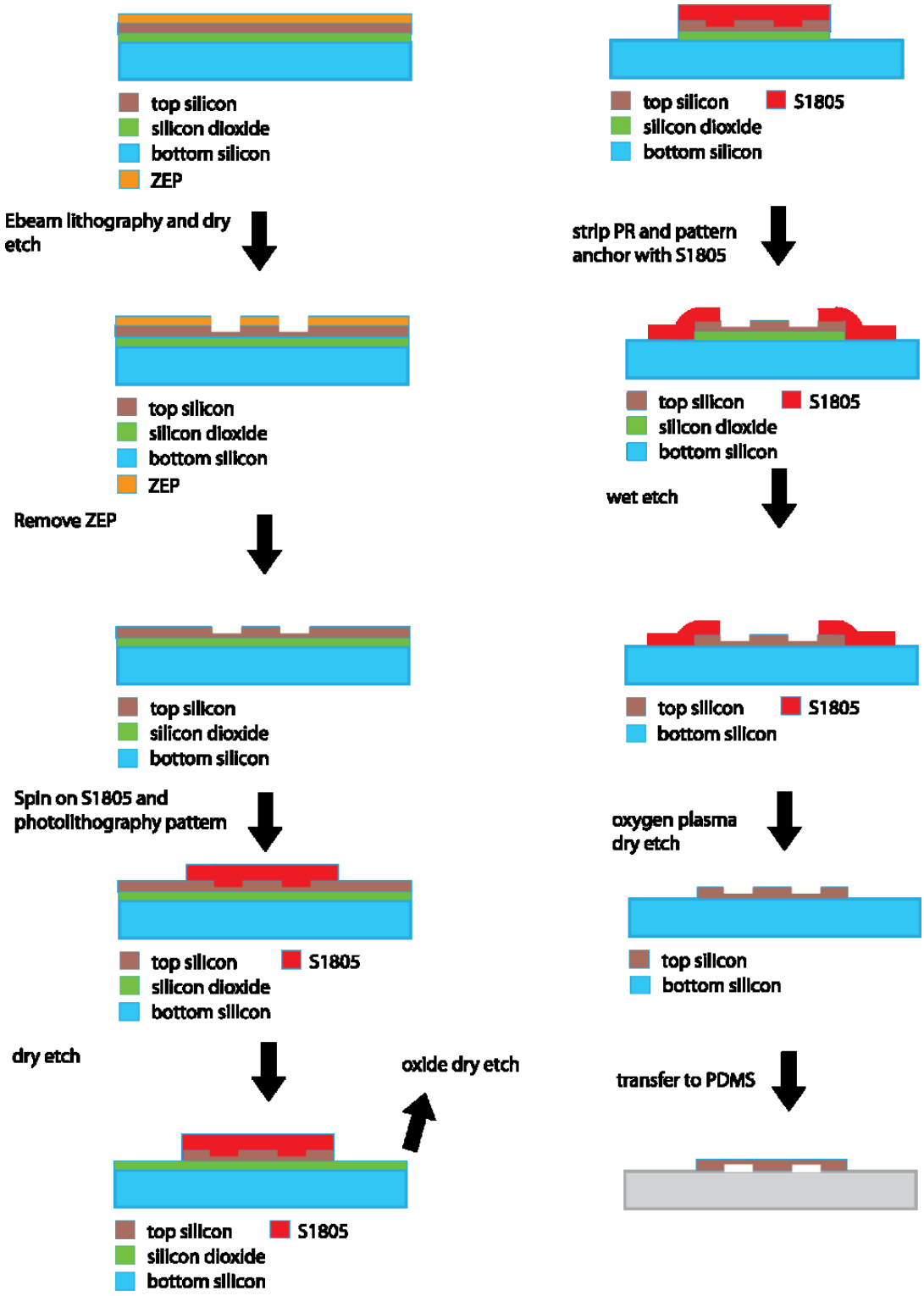

Figure 4.3 *Process flow for transferring rib waveguide*

The transfer results by using this method is shown in Fig.4.4 below:

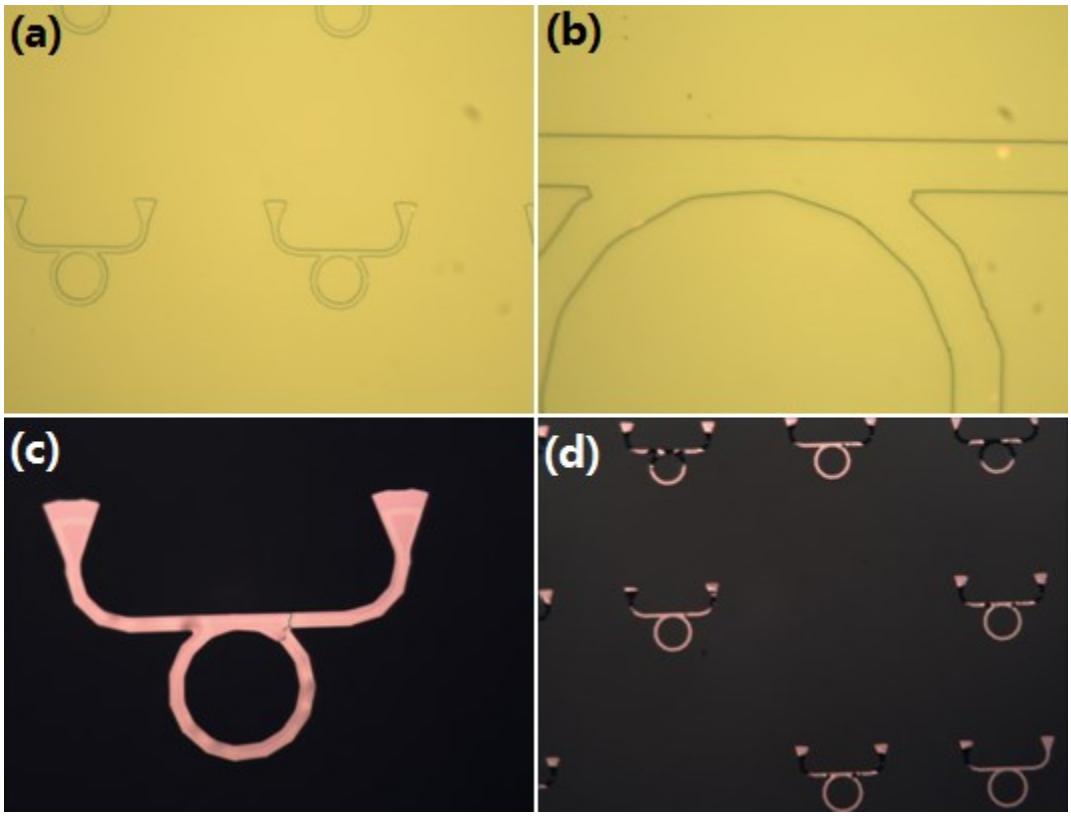

Figure 4.4 *(a) silicon photonic devices sitting on top of bottom silicon layer after wet etch and photoresist anchor stripping. (b) details of (a). (c) transferred devices onto PDMS. (d) arrays of transferred devices onto PDMS*

As we can tell from the figures above, although the transfer result is much better than the SU8 assisted transfer method, there are still several issues of such method:

(1) After wet etch, water or other liquids may be trapped between top silicon layer and bottom silicon layer, like the bright spot shown in Fig. 4.4(b), which will largely reduce the transfer yield since they may dramatically increase the surface adhesion force between top silicon layer and bottom silicon layer.

(2) The fabrication method is really complicated

(3) Silicon to silicon conformal contact is difficult to be realized in solution based wet etch method, which may lead to a lower final transfer yield

Therefore, the transfer yield shown in Fig. 4.4(d) is not high enough, and devices are buckled up mainly due to the trapped liquid underneath the top silicon layer as well as to the unoptimized geometry of the devices.

(b) Photoresist pedestal with anchor assisted transfer method

Since the trapped liquid is the main barrier for high transfer yield, we could utilize photoresist pedestal to support the top silicon layer in order to avoid any trapped liquid, the process flow is shown in Fig. 4.5 and the detailed process flow is listed below (This is for SOI wafer with 400nm silicon and 200nm buried oxide):

(1) Thoroughly clean the SOI sample with acetone, IPA and DI water

(2) Bake at 180 degree Celsius for 5 minutes

(3) Spin ZEP with 3000rpm for 1minute

(4) Use ebeam lithography to pattern the photonic structure

(5) Develop in ZED-N50 for 2minutes and then IPA for 30 seconds

(6) Use RIE to etch the silicon layer for 300nm

(7) Strip ZEP by using NMP for 15 minutes, then use Piranha for 5 minutes

(8) Dehydrate at 115 degree Celsius for 2 minutes

(9) Spin on S1805 at 3000rpm for 30 seconds

(10) Bake at 115 degree Celsius for 1 minute

(11) Pattern the carrier slab shape by using photolithography

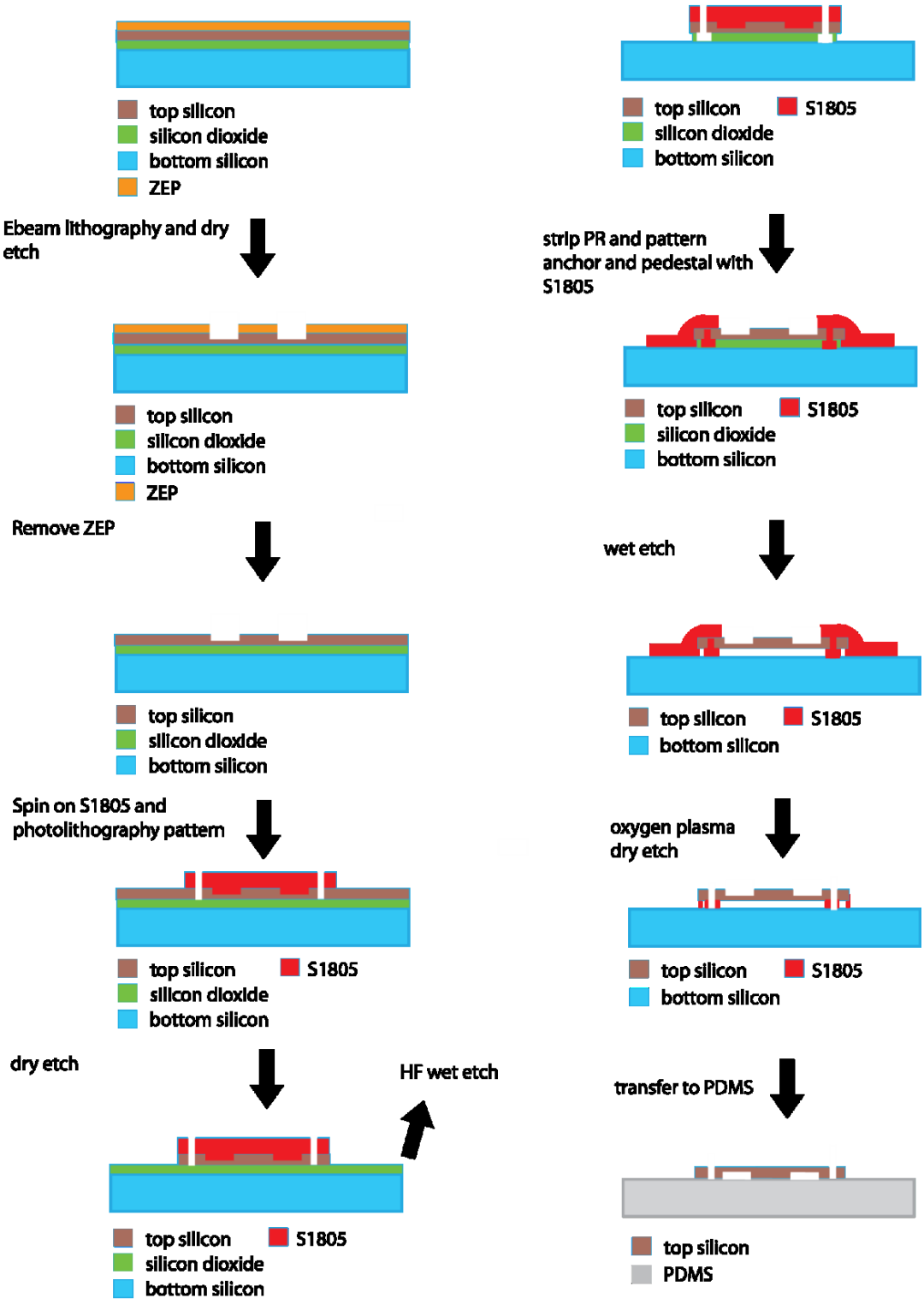

Figure 4.5 *Process flow of photoresist pedestal with anchor assisted transfer method*

(12) Soft bake at 115 degree Celsius for 1 minute

(13) Develop in MF-319 for 30 seconds, rinse with DI water then blow dry

(14) Use deeptrench etcher to thoroughly etch through the top silicon layer

(15) Strip S1805 by using 1165 for 5 minutes and then Piranha for 2 minutes

(16) Immerse in HF(49%) solution for 90 seconds

(17) Dehydrate at 115 degree Celsius for 2 minutes

(18) Spin on S1805 at 3000rpm for 30 seconds

(19) Bake at 115 degree Celsius for 1 minute

(20) Pattern the anchor structure by using photolithography

(21) Soft bake at 115 degree Celsius for 1minute

(22) Develop in MF-319 for 30 seconds, rinse with DI water then blow dry

(23) Wet etch with HF(49%) solution for 30 minutes

(24) Rinse with DI water, then blow dry

(25) Dry etch with Oxygen plasma for 10 minutes

(26) Treat the surface of PDMS and that of SOI sample with UV Ozone for 5 seconds and 1 minute, respectively.

(27) Contact PDMS with SOI sample until conformal contact is reached and then peel the PDMS stamp with fast speed

There are several important parameters that need to be well controlled during this photoresist pedestal assisted transfer method, which are:

(1) The first wet etch time which is described as 90 seconds here needs to be tuned accordingly when different pattern design is used. It should be long enough for the HF

acid to etch through the buried oxide layer. However, on the other hand, it could not be too long which may cause the collapse of the top silicon layer.

(2) After spinning the photoresist on top of the SOI wafer in step (17), a low vacuum needs to be applied to the device for a short period of time which may help the photoresist to fill into the cavity formed underneath the top silicon layer.

The transfer result by using such method is shown in Fig. 4.6 below:

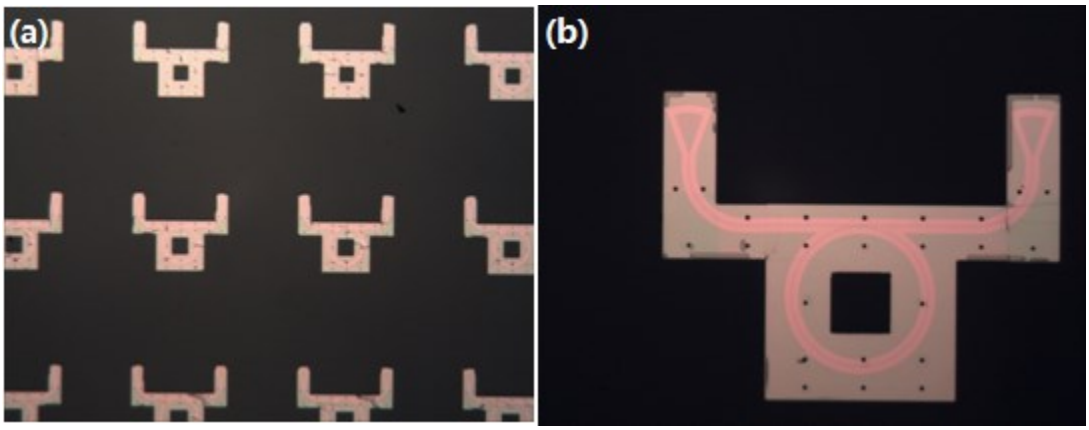

Figure 4.6 *(a) transferred array of integrated silicon photonic devices with their grating couplers on PDMS substrate. (b) Single integrated silicon photonic device with its grating couplers on PDMS substrate.*

Compare the transfer results shown in Fig. 4.6 and Fig. 4.4, the transfer yield is much higher (close to 100%) when photoresist pedestal assisted transfer method is used. The only issue existed now is that there are still some minor cracks among the 90 degree sharp turns of the transferred devices, whose formation may be attributed to two reasons:

(1) The design of the supporting slab geometry is not optimized, the 90 degree sharp turn should be avoided.

(2) Due to the existence of the frames of photolithography mask, the conformal contact may not be reached between the PDMS and the silicon devices, which is shown in Fig. 4.7 below:

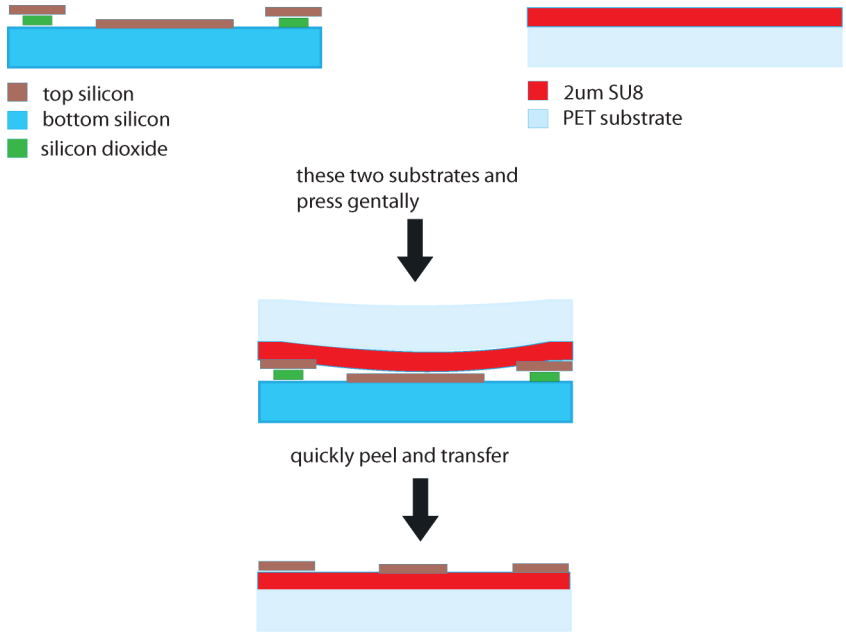

Figure 4.7 *Frames prevent the reaching of conformal contact between PDMS and silicon photonic devices*

Besides, even without the anchor structure, only the photoresist pedestal will be strong enough to maintain everything in their original position after the wet etch step. Therefore, a simplified photoresist pedestal assisted method has been developed.

(c) Simplified photoresist pedestal assisted transfer method

Since anchor structures are no longer needed in the photoresist pedestal assisted transfer method, the transfer method could be further simplified with modified mask

design. The process flow of the simplified process flow is shown in Fig. 4.8 below. The detailed process flow for such simplified fabrication process is listed below as well (This is for SOI wafer with 400nm silicon and 200nm buried oxide):

(1) Thoroughly clean the SOI sample with acetone, IPA and DI water, then blow dry

(2) Bake at 180 degree Celsius for 5 minutes

(3) Spin ZEP with 3000rpm for 1 minute

(4) Ebeam lithography pattern define the photonic structure

(5) Develop in ZED-N50 for 2 minutes and then IPA for 30 seconds

(6) Use deeptrench etcher to etch top silicon layer for 300nm

(7) Strip ZEP by using NMP for 15 minutes, then use Piranha solution for 5 minutes

(8) Dehydrate the sample at 115 degree Celsius for 2 minutes

(9) Spin on S1805 at 3000rpm for 30 seconds

(10) Bake at 115 degree Celsius for 1 minute

(11) Pattern the carrier slab shape by using photolithography

(12) Soft bake at 115 degree Celsius for 1 minute

(13) Develop in MF-319 for 30 seconds, rinse with DI water then blow dry

(14) Fully etch through the top silicon layer by using deeptrench etcher again

(15) Strip S1805 by using 1165 for 5 minutes and then treat with Piranha for 5 minutes

(16) Immerse in HF(49%) solution for 90 seconds

(17) Dehydrate at 115 degree Celsius for 2minutes

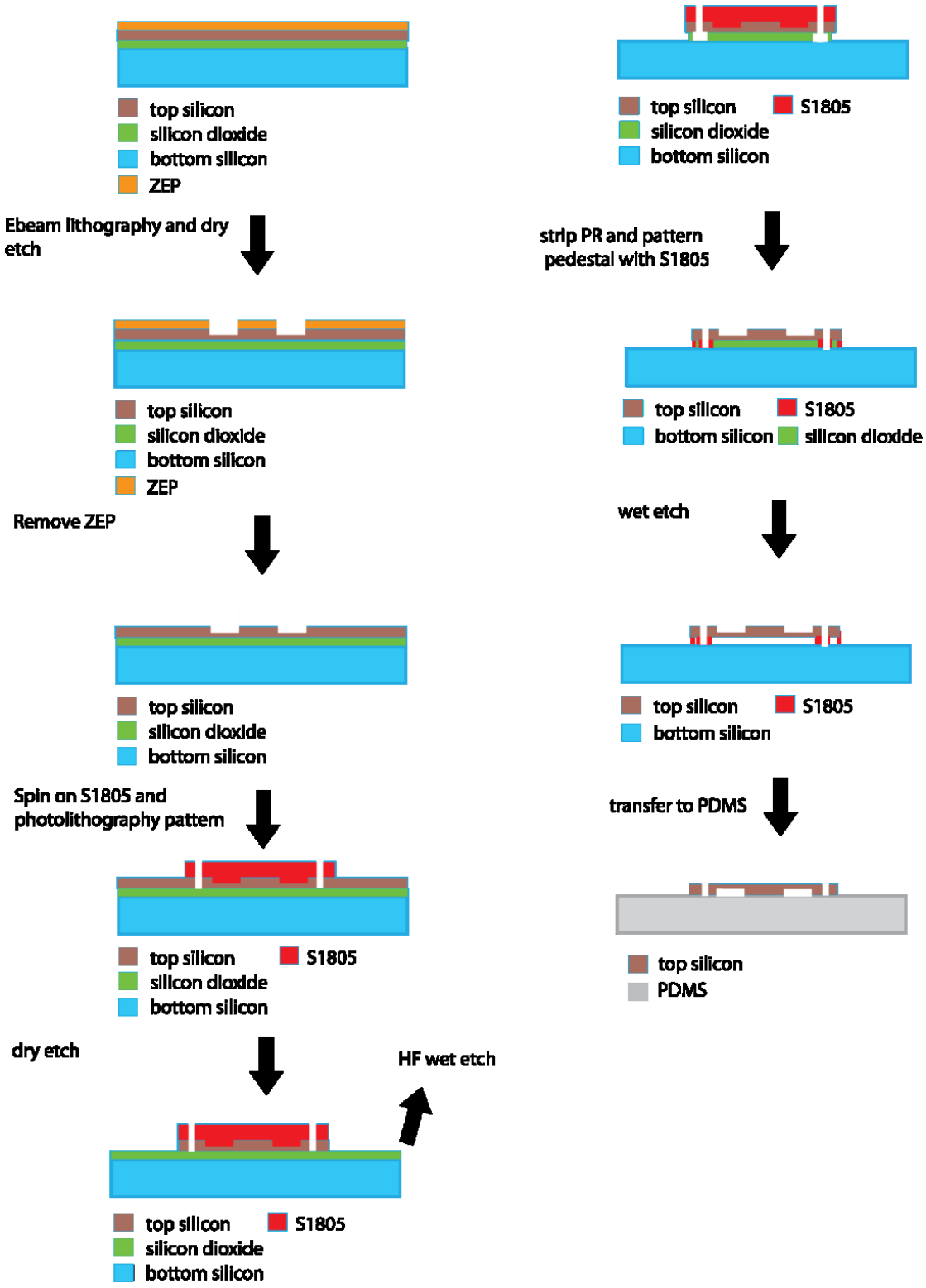

Figure 4.8 *Fabrication flow of simplified photoresist pedestal assisted transfer method*

(18) Spin on S1805 at 3000rpm for 30 seconds

(19) Bake at 115 degree Celsius for 1 minute

(20) Flood exposure by using photolithography

(21) Soft bake at 115 degree Celsius for 1minute

(22) Develop in MF-319 for 40 seconds, rinse with DI water then blow dry

(23) Wet etch with HF(49%) solution for 1 hour

(24) Rinse with DI water, then blow dry

(25) Keep in atmosphere for 10 minutes or in desiccators for 2 minutes

(26) Treat the surface of PDMS with UV Ozone for 5 seconds, treat the surface of SOI sample with UV Ozone for 1 minute

(27) Contact PDMS with SOI sample until conformal contact is reached and then peel the PDMS stamp with fast speed

By using this simplified transfer method, the transfer yield could be as high as 100%. Averagely speaking, the transfer yield is about 98%, which is also much higher than the other transfer methods. The only two steps that will affect the transfer yield is step (24) and step (26). The purpose of step (24) is to make sure all the water left between the two silicon layers could be utterly dried. The usage of hot plate should be avoided in step (24), in case the adhesion force between the photoresist pedestal and the silicon layers would increase.

The transfer results are shown in Fig. 4.9 below, as we can see from which, the transfer yield by using this method is the best among all the experimental results. Moreover, the transferred devices are fully intact and free of wrinkles and cracks, which

means, if these devices could be transferred back to another substrate, in principle, their optical performance could remain unchanged. Therefore, we need to have a perfect 2nd transfer step in order to have fully integrated silicon photonic circuits on flexible substrates.

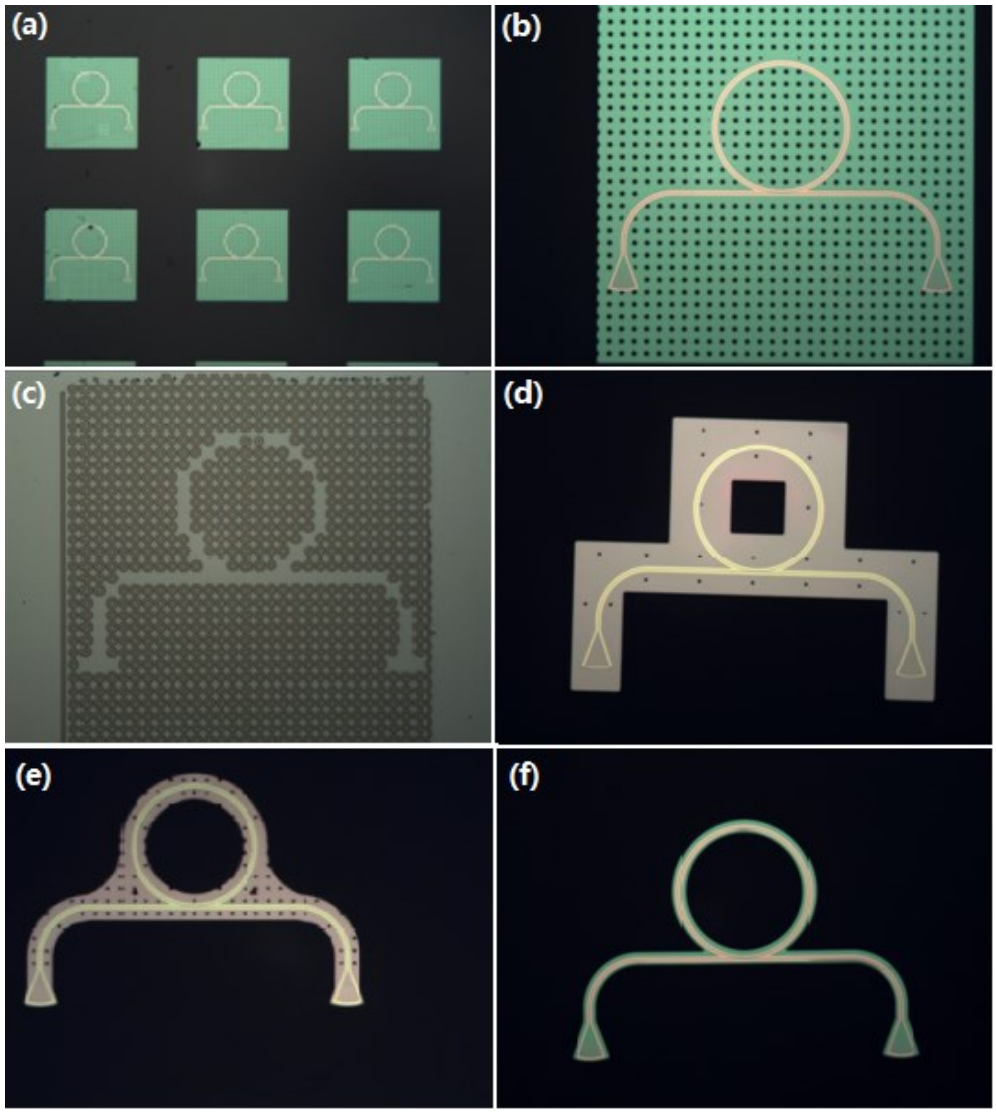

Figure 4.9 *(a) Transferred devices on square shape membrane on PDMS. (b)A single transferred device. (c) Photoresist pedestal left on original SOI substrate. (d),(e),(f) Transferred device with different membrane geometry.*

4.1.3 SU8 Assisted 2nd Transfer Process

To transfer the device from PDMS back onto other plastic substrates, for example, polyethylene terephthalate (PET) substrate, the prerequisite is that the adhesion force between the reception layer and silicon is larger than that between PDMS and silicon. In our case, the adhesion force between the silicon and S1805 pedestal is super weak since the surface of PDMS has only been treated with UV Ozone for 5 seconds, and there is no deposited silicon dioxide on top of the silicon photonic devices. Such weak Van der Waal force makes it possible to transfer the integrated silicon photonic devices from PDMS stamp onto the SU8 reception layer since the adhesion force between semi-cured SU8 and silicon is much larger than that between the silicon and PDMS. The process flow is shown in Fig. 4.10:

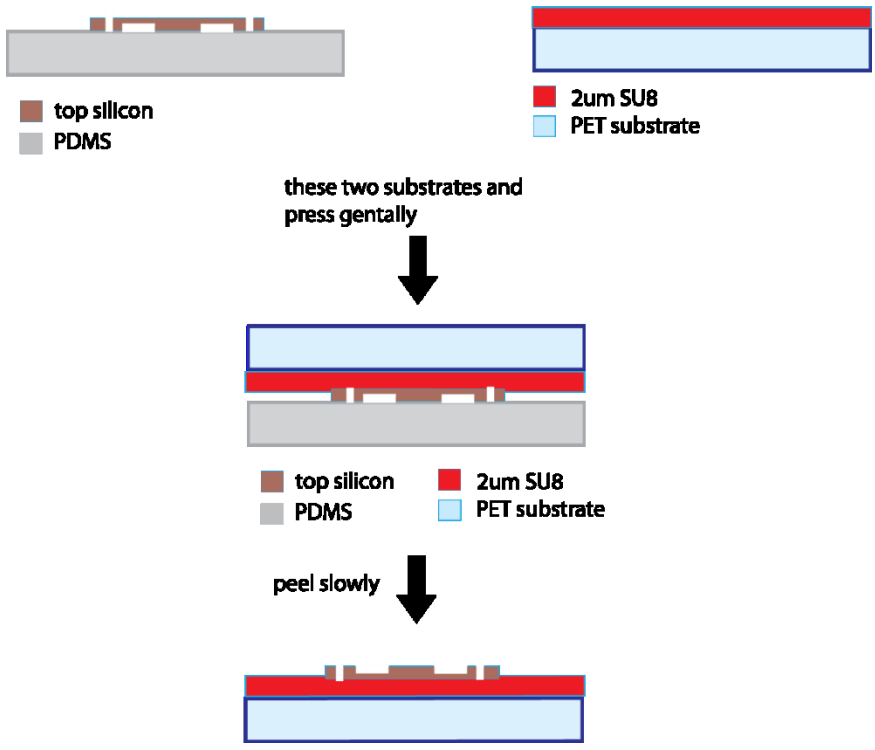

Figure 4.10 *SU8 assisted 2nd transfer process flow.*

The detailed process flow is listed below:

(1) Use acetone, IPA, DI water to thoroughly clean the PET substrate, then blow dry

(2) Use Oxygen plasma to treat the surface of PET substrate for 90 seconds

(3) Spin 2 micron thick SU8 onto PET substrate.

(4) Pre cure the SU8 on 60 degree Celsius hot plate for 1 minute.

(5) Clean the surface of PDMS stamp with the silicon photonic devices with IPA and then blow dry (The PDMS stamp should be put in ambient environment for more than 24 hours after the 1st transfer step).

(6) Contact the PDMS stamp with the PET substrate with certain pressure and keep them onto 85 degree Celsius hot plate for 1 minute

(7) Slowly peel the PDMS stamp off from the PET substrate.

The transfer result after such 2nd transfer process is shown in Fig.4.11.

After the transfer process, bake the PET with silicon photonic devices on 115 degree Celsius hot plate for 5 minutes, then flood exposure the SU8 from backside of the PET for 10 seconds, followed with another 5 minutes bake at 115 degree Celsius. After such process, the SU8 will be fully cured and the sample is ready to be rinsed with acetone and IPA. Otherwise, the SU8 will be destroyed if been exposed to organic solvent such as acetone and etc. However, the final curing process will reflow the SU8 photoresist, which may lead to the position shift of the silicon photonic devices on top.

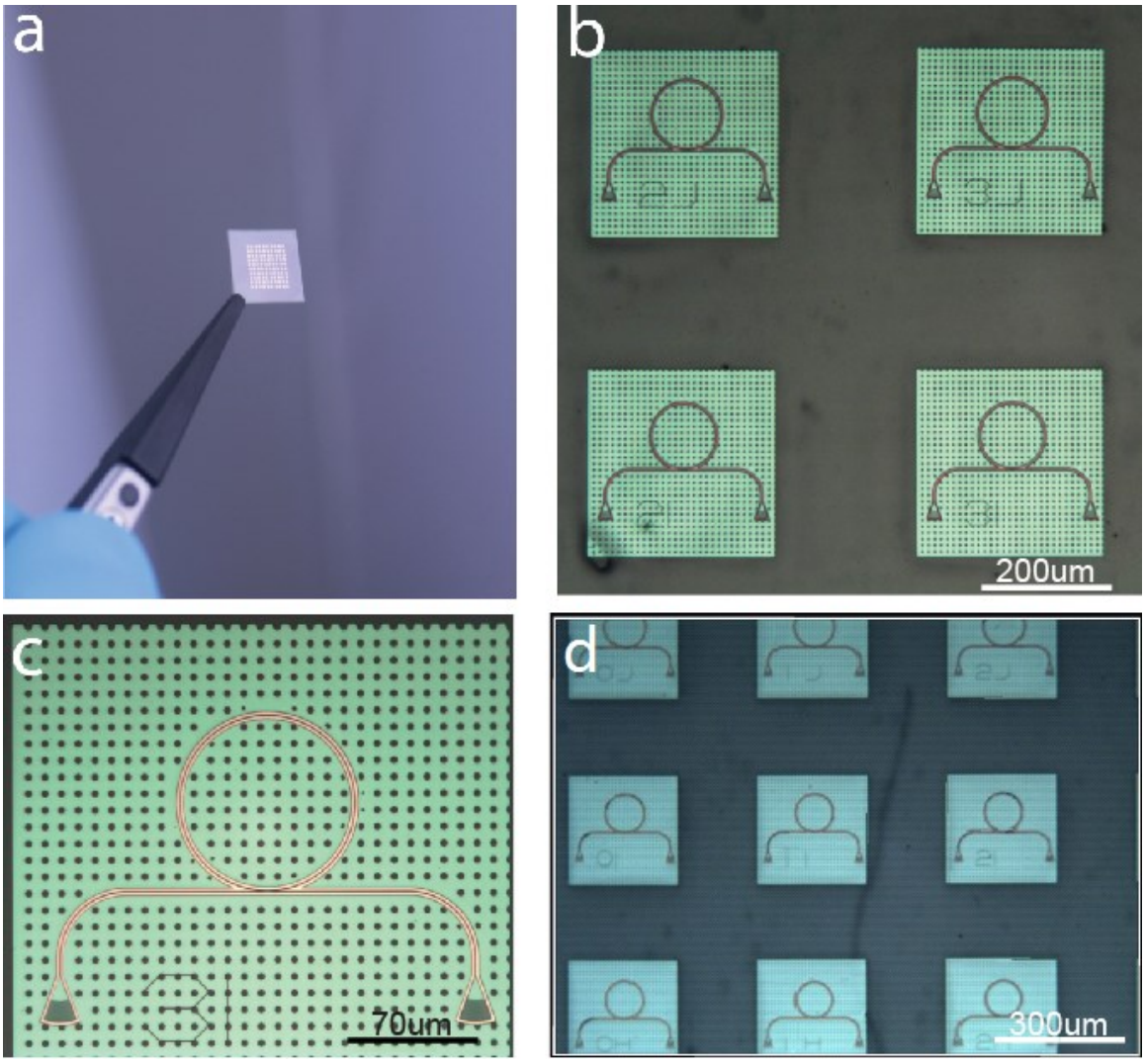

Figure 4.11 *(a) Optical image of an array of transferred silicon nanomembranes on a flexible PET substrate. (b)-(d) Optical microscope image of silicon nanomembrane on the PET substrate with various magnification.*

4.1.4 Transfer method for silicon nitride based photonic devices

For telecomm wavelength, silicon is the best candidate for large area integration of on-chip photonic devices since it possesses high refractive index and extremely low

propagation loss. However, silicon is highly absorptive if the working wavelength is shorter than 1100nm. Therefore, if we want to design some photonic devices which are compatible with visible wavelength, new material needs to be used instead of silicon. Silicon nitride, one of the most widely used thin film materials in microelectronics industry, is highly transparent down to 460nm~500nm (depending on the stoichiometry of the material). For most biomedical device applications, flexible photonic devices working at visible wavelength is highly desired. Therefore, we have also developed the transfer method for silicon nitride based photonic devices. With our current measurement setup, the silicon nitride photonic devices working at telecomm wavelength are transferred onto flexible substrate as a preliminary demonstration.

During the transfer process, the only difference between silicon nitride material and silicon material is their wet etch selectivity with silicon dioxide in HF acid solution. The etch selectivity between silicon nitride and silicon dioxide by HF acid highly depends on the ion groups contained inside the HF acid solution and the temperature of the acid [156]. In 0 degree Celsius 49% concentrated HF acid, the wet etch selectivity between silicon nitride and silicon oxide is less than 1:200, the specific etch rate of silicon nitride highly depends on the stoichiometry of the material itself as well. However, even with an extremely slow etch rate, the silicon nitride material will still be slowly consumed by HF acid, which means they will be gradually lifted off from the photoresist pedestals as mentioned in section 4.1.2. Therefore, some anchor structures are needed around the membrane structure in order to stabilize the devices during the long wet etch process. Another route has been originally proposed, which is to use silicon as the

sacrificial layer and use xenon difluoride as the etchant. Fig. 4.12 shows the partially undercut silicon nitride membrane on silicon sacrificial layer by using xenon difluoride etchant. However, we find out the xenon difluoride will still attack silicon nitride, and the by-product SiF_4 will remain on the bottom of the silicon substrate which will result the contamination of the PDMS substrate. On the other hand, the heat generated during the long dry etch process will also make the membrane start to buckle, which could also be seen in Fig. 4.12.

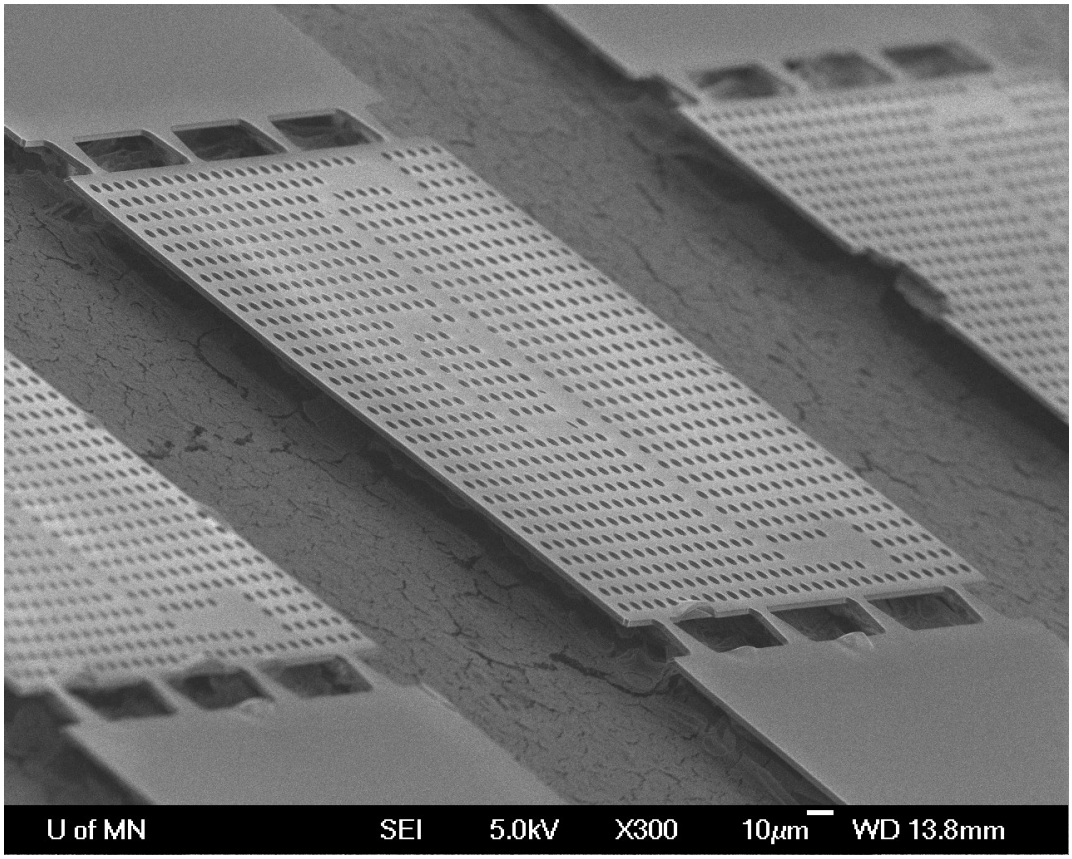

Figure 4.12 *SEM image of the silicon nitride membrane on silicon with photoresist on top after certain time of xenon difluoride dry etch.*

Therefore, we still choose to utilize the HF acid wet etch process with high concentration of HF and low temperature (0 degree Celsius). After such process, the result proves that the silicon nitride has only been consumed around 20nm, and the final transferred devices on flexible PET substrate are shown in Fig. 4.13:

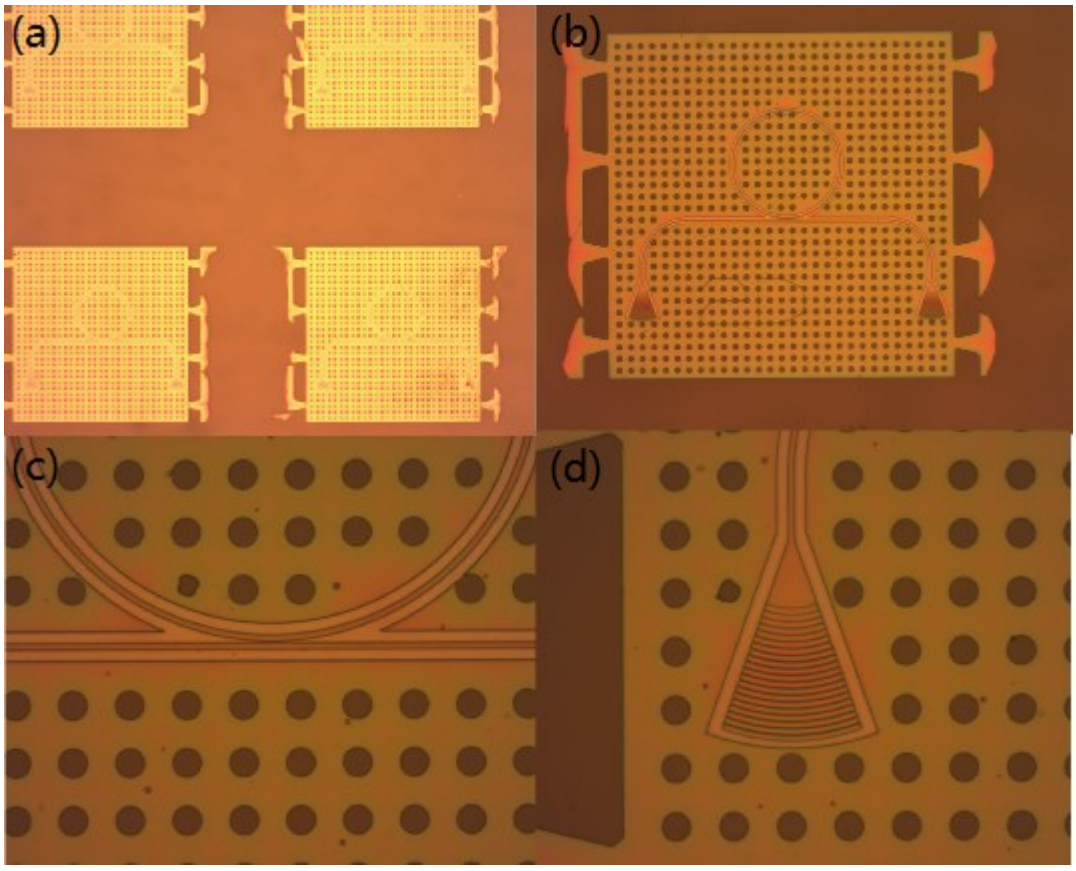

Figure 4.13 *Transferred silicon nitride devices on flexible PET substrate. (a) Transferred silicon nitride nanomembrane without photonic structures on PET substrate. (b) A single silicon nitride photonic device on PET substrate. (c) The coupling gap and (d) grating coupler of the silicon nitride based photonic device on PET substrate.*

As we can see from Fig. 4.13 that, even be etched by HF acid for about 20nm, the silicon nitride based photonic devices are still intact and free of cracks even after been

transferred onto plastic substrate. Thus, in principle, their optical performance should be measurable, although certain transmission spectrum shift is expected.

4.2 Characterization of Flexible Photonic Devices

4.2.1 Characterization of Flexible Silicon Photonic Devices

Since the grating coupler can be transferred onto the flexible substrate, a regular measurement setup as we use for the characterization of traditional rigid silicon photonic devices can be utilized here to measure the optical performance of these flexible silicon photonic devices. A simple diagram of the measurement stage is shown in Fig. 4.14:

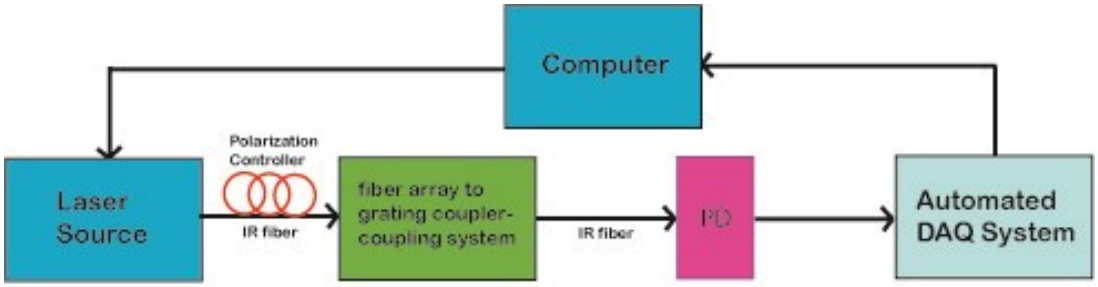

Figure 4.14 *Measurement setup for flexible silicon photonic devices on PET substrate*

At first, the grating couplers with different periods connected by a waveguide (but no side coupled ring resonator) are characterized, whose transmission spectrums are shown in Fig. 4.15s. The coupling efficiency for each grating coupler is about 15% which is comparable with their counterparts fabricated on original SOI wafer. Also, with increased period, obviously we can see that the general transmission fringe gradually shifts to the longer wavelength. However, since the regular grating structure is applied to

these transferred devices, strong Fabry-Perot noise could be observed on almost all of the transmission spectrum of the transferred flexible silicon photonic devices.

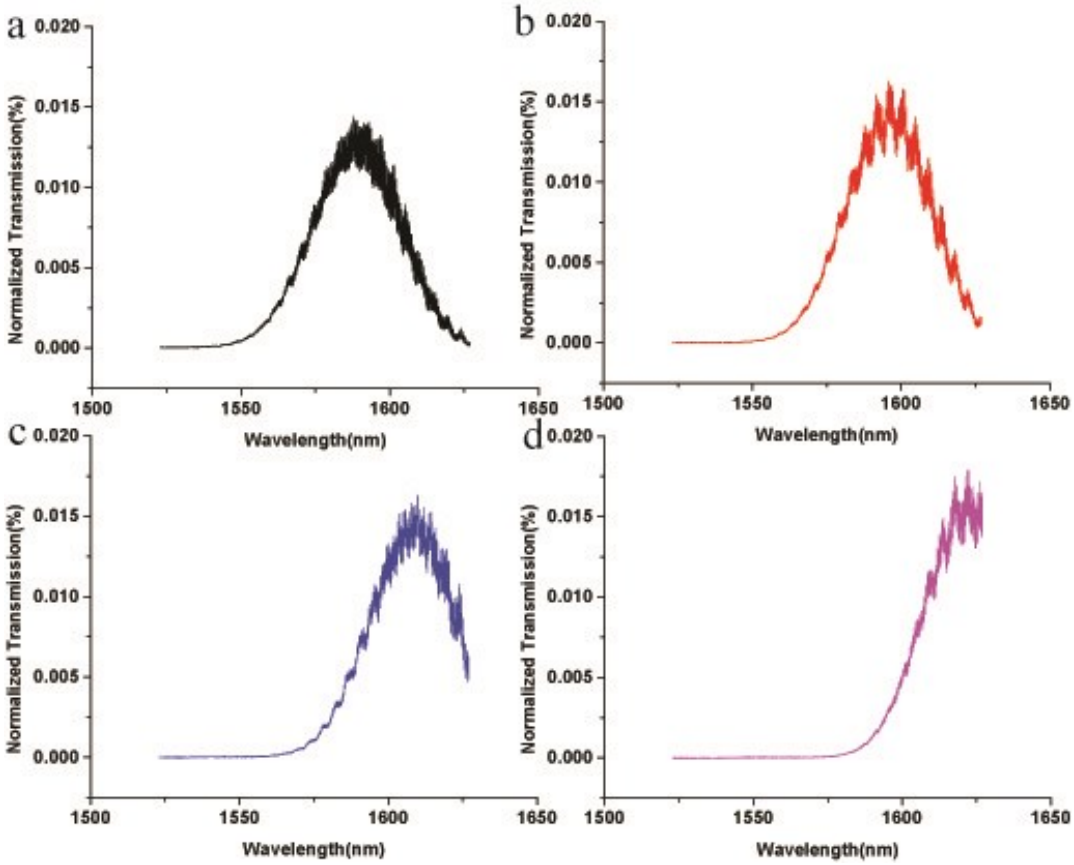

Figure 4.15 *Transmission spectrum of flexible silicon waveguide connected with two grating couplers with different period such as (a) 602nm, (b) 607nm, (b) 612nm, and (d) 617nm.*

Then, the waveguide side-coupled ring resonators with regular grating couplers are also measured, whose transmission spectrums are shown in Fig. 4.16s. As we can see, when the coupling gap is between 200nm to 240nm, the extinction ratio of the resonances will reach its maximum value, which means the devices are working around the critical

coupling regime. In Fig. 4.16 (d), the average value of quality factor of these resonances is about 30000. We can calculate the intrinsic quality factor is close to 80000, and the FSR is about 1.95nm, therefore, the propagation loss of the transferred device is about 7.8dB/cm. This value could be further improved by modified fabrication process which includes: cold ZEP development, chlorine based low RF power dry etch, and further clean of the transferred devices.

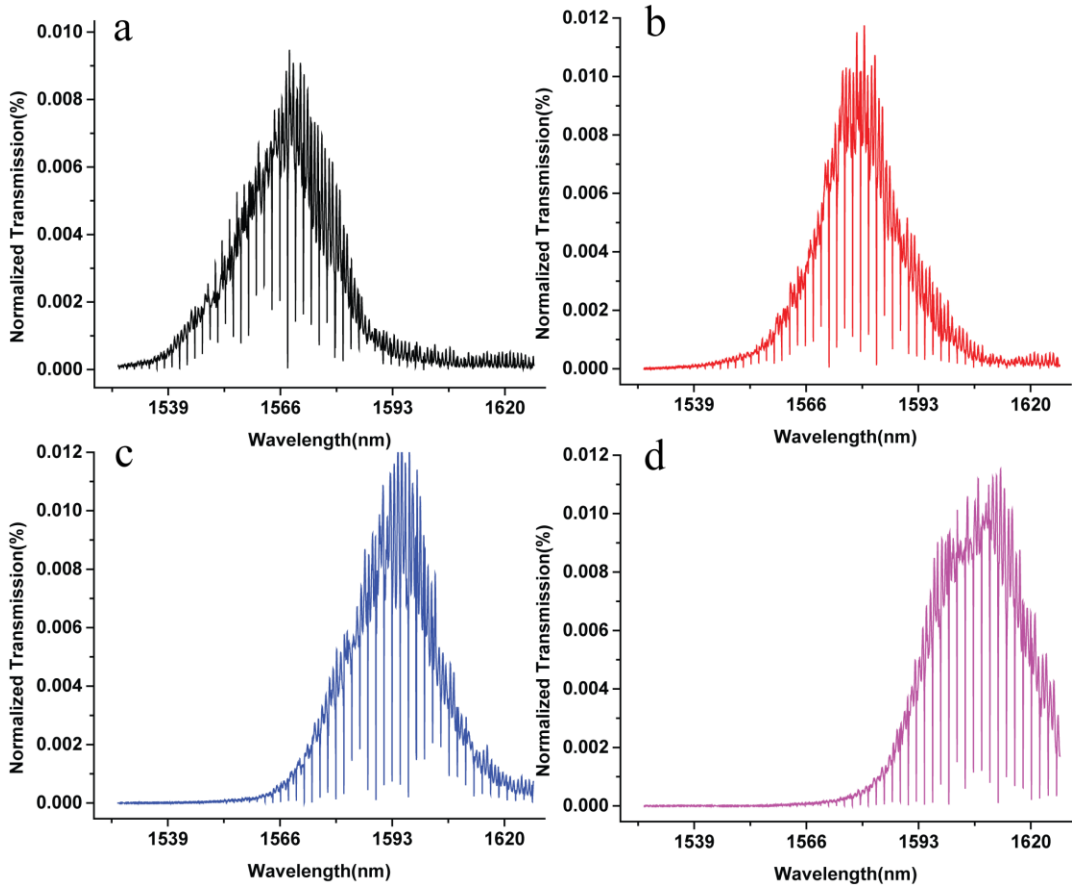

Figure 4.16 *Transmission spectrum of transferred silicon ring resonators with different coupling gap and regular grating couplers such as: (a) coupling gap = 180nm, grating period = 592nm; (b) coupling gap = 190nm, grating period= 597nm; (c) coupling gap = 200nm, grating period = 602nm; (d) coupling gap = 210nm, grating period = 612nm.*

Afterwards, by using cold ZEP development method and with apodized grating coupler structure, silicon ring resonator with higher optical performance have been transferred onto flexible PET substrates , whose optical performance are shown in Fig. 4.17:

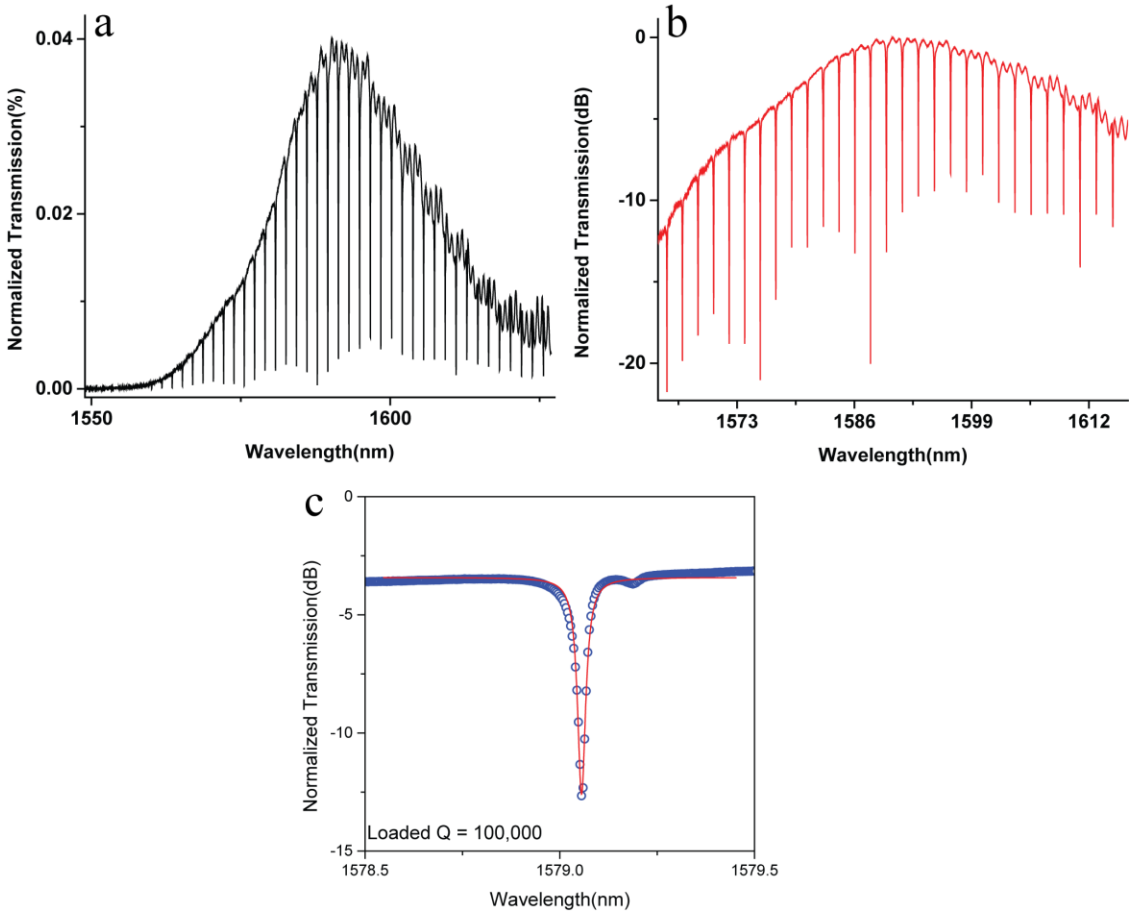

Figure 4.17 *Transmission spectrum of silicon ring resonator on flexible PET substrate by using cold development with apodized grating couplers (a) Transmission spectrum in linear scale. (b) Transmission spectrum in l g scale. (c) Single resonance of the transferred ring resonator.*

As we can see from the measurement results shown in Fig. 4.17, both the measured quality factor (Q) of the ring resonator and the propagation loss of the transferred waveguide can be benchmarked. The highest extinction ratio of the resonance shown in Fig. 4.17b is about 20dB, which proves that the ring resonator works around the critical coupling regime as designed. Fig. 4.17c shows a critical-coupled resonance at 1579.12 nm with a waveguide loaded Q of 4.9×10^4. It corresponds to an intrinsic Q of 1.0×10^5 and a propagation loss of 6 dB/cm. This value of propagation loss is slight higher than that of silicon waveguides on the original SOI substrate which is typically in the range of 3 to 4 dB/cm without applying surface smoothing processes. The extra loss should be attributed to both the utilization of a rib waveguide structure and the absorption caused by the SU8 receiving layer.

4.2.2 Characterization of Flexible Silicon Nitride Photonic Devices

By using the same measurement setup, the optical performance of silicon nitride devices prior to and after the transfer process are both measured. The reason for the optical performance measurement comparison is that we try to analyze the effect brought by the HF process as mentioned above.

The transmission spectrum of transferred silicon nitride micro-ring resonator is shown in Fig. 4.18a and b. The highest extinction ratio of the resonances is about 20dB. The loaded quality factor on original wafer is 5.0×10^4, which, after the transfer process, decreased to around 4.0×10^4. A slight blue shift of the transmission spectrum after the transfer process could also be observed as shown in Fig. 4.18c. From the loaded quality factor, the propagation loss of silicon nitride photonic rib waveguide on original substrate and flexible PET substrate was determined to be

6.5dB/cm and 8dB/cm, respectively. The increased propagation loss and the spectral shift of the resonance can be attributed to, respectively, the extra absorption caused by the SU8 receiving layer and the etching of the silicon nitride layer during the HF etching process. Since the fabrication processes prior to the transfer for both the silicon and silicon nitride based devices are far from being optimized, their optical performance is anticipated to be improved in the future.

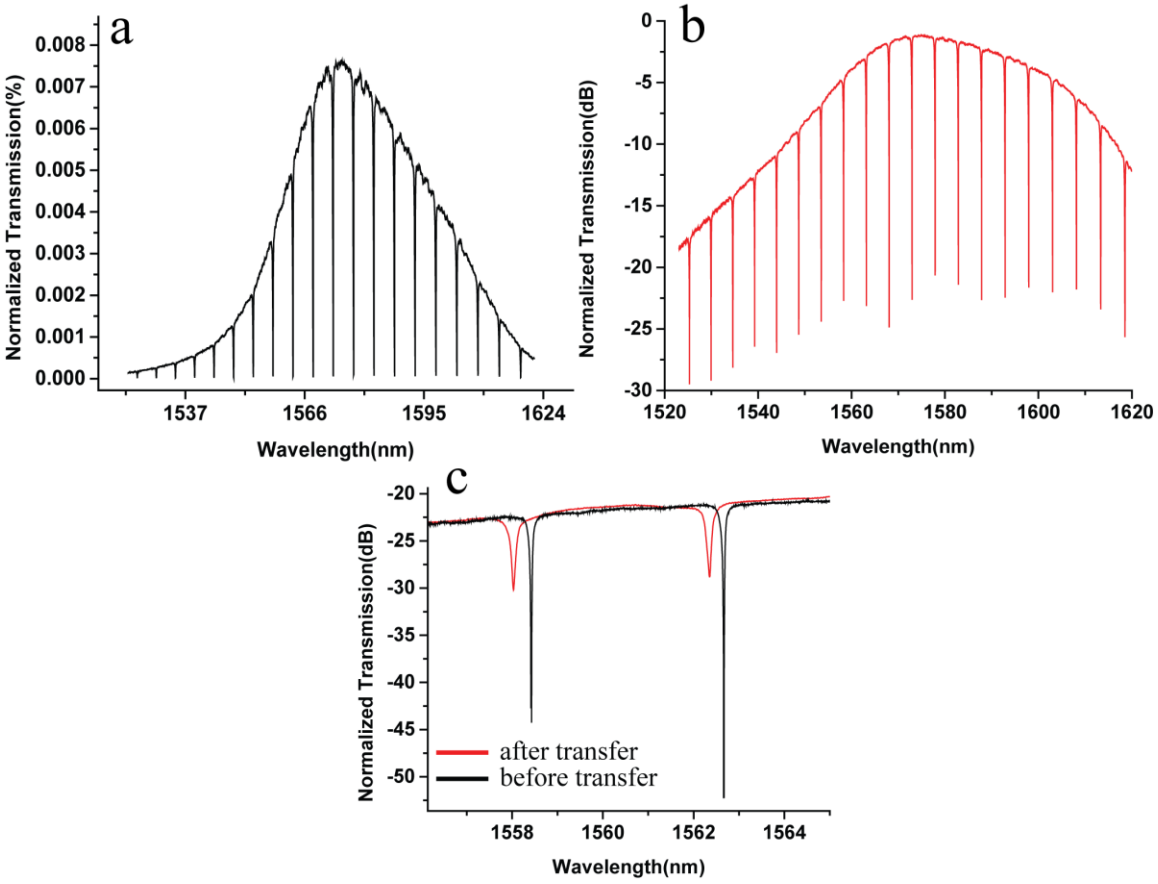

Figure 4.18 *Transmission spectrum of transferred silicon nitride ring resonator on flexible PET substrate in (a) linear scale and (b) log scale. (c) Comparison of optical resonance before and after the transfer process.*

4.3 Conclusion

In this chapter, we have first demonstrated several different transfer methods which all possess the capability to break the geometrical limitation imposed by the transfer method described in Chapter 3. Afterwards, by using the photoresist pedestal assisted transfer method, extremely high transfer yield has been realized. Furthermore, with the very same method, fully integrated silicon photonic circuit which includes grating couplers, waveguide and ring resonator has been successfully transferred onto flexible PET substrate, whose optical performance has been then characterized. The measurement results are comparable with those of the devices directly fabricated onto SOI platform, which proves that the transfer process will not degrade the optical properties of the devices. The generally same but not identical transfer method has later been applied to the fabrication process of silicon nitride based flexible photonic circuit which includes similar components as those of flexible silicon photonic circuit. Due to the fact that silicon nitride will be slowly etched by HF acid during the releasing process, the optical performance of silicon nitride based flexible photonic devices will deviate a bit from their original values after the transfer. More specifically, the extinction ratio and quality factor of the originally critically coupled ring resonator will both decrease after transferred onto plastic substrate due to the increase of the coupling gap.

The best intrinsic quality factor, extinction ratio and propagation loss values for transferred silicon ring resonator device are 1.0×10^5, 25dB and 6dB/cm, respectively. For silicon nitride based device, these values are 8×10^4, 20dB and 8dB/cm. As mentioned in the last section, the fabrication process for the photonic devices is far from optimized. By

using extra steps, we believe these values could be further improved. Also, there are several options for solving the wet etch issue of the silicon nitride material such as: (1) Intentionally design thicker and wider photonic structure which takes the material consumption into account. (2) By applying a protection layer on top of silicon nitride before the wet etch process. Such protection layer should have a good adhesion force to silicon nitride and be also immune to HF acid etch, such as different type of metal material. Such protection layer should be removable after the wet etch process.

These flexible photonic devices could find important applications in a variety of fields such as in-vivo biomedical research, curved sensor array, 3-dimensional integration of photonic devices and chip-to-chip optical connection.

CHAPTER 5: HETEROGENEOUSLY INTEGRATED MID-INFRARED SILICON PHOTONIC DEVICE

5.1 Introduction

Not only being the foundation material for microelectronic industry, with high refractive index and wide transparency window up to 8μm as shown in Fig. 5.1[157], silicon has long been utilized to perform as the material for mid-infrared application such as lens and mirrors. The traditional silicon-on-insulator (SOI) platform provides a very high index contrast between silicon (n = 3.48) and its cladding, silicon dioxide (n = 1.45), enabling low-loss, ultrahigh density integration of silicon photonics in the near-infrared

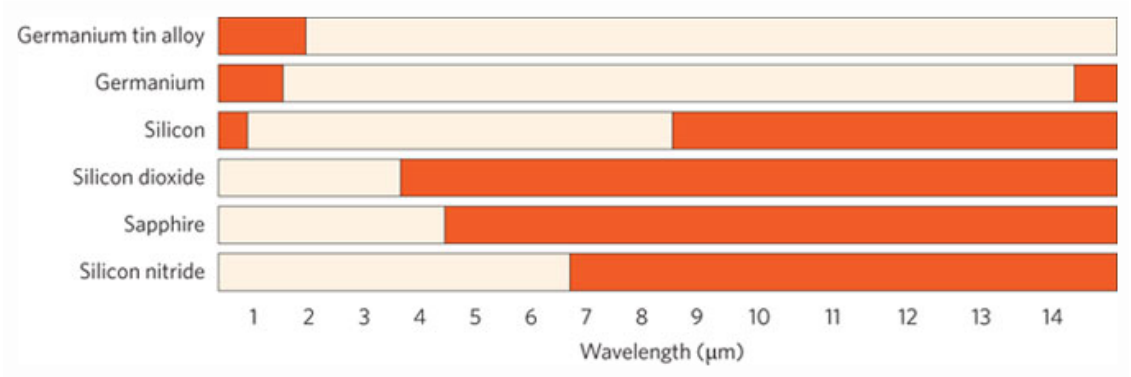

Figure 5.1 *The transparent window(white area) for various materials*.[157]

(near-IR) telecommunication band. However, the use of silicon oxide as the cladding also imposes a limitation on the spectral range that silicon photonics can operate within since the oxide will become highly absorptive when the wavelength is longer than 3.4μm. Although silicon is transparent in the ~1−8 μm wavelength range [158], [159], silicon

dioxide starts to absorb light strongly above ~4 μm. Thus, a very wide wavelength range from ~4 to 8 μm where remarkable performance can be obtained with silicon becomes inaccessible to the SOI platform. Due to such limitation of tradition SOI platform, numerous efforts have been made to investigate the alternative substrate or method for on-chip mid-infrared photonic devices based on group IV materials. Generally speaking, there are three different platform (or method) :

(1) By using germanium-on-silicon platform to fabricate mid-infrared devices [160]. Since germanium is transparent up to 14μm and possesses a higher refractive index (*n=4.1*) than silicon (*n=3.4*), mid-infrared photonic structures could be realized on such platform. However, since the index contrast between germanium and silicon is much lower than that between silicon and oxide, the dimension of the devices will increase proportionally.

(2) By using silicon-on-sapphire platform to fabricate mid-infrared devices [161]–[163]. Silicon-on-sapphire substrate could be fabricated by using similar technique as that for the fabrication of SOI substrate. Since sapphire is transparent up to 4.3μm and possesses a much smaller refractive index (*n=1.7*) , the silicon-on-sapphire substrate could be utilized to fabricate compact integrated mid-infrared devices. However, such platform will still not be able to utilize a large portion of the wavelength between 4.3μm up to 8μm, which is transparent to silicon.

(3) By using alternative methods to maximally explore the potential of SOI platform in the application of mid-infrared devices. These methods include: (a) Use optimum

design of photonic structure to decrease the optical energy coupled into the oxide layer [164]; (b) Partially remove the buried oxide layer to create suspended silicon photonic structure on original SOI platform [165], [166]. However, such method, like the critical wet etch process mentioned in Chapter 3, will impede some limitations to the geometrical design of the photonic devices.

In addition, since amorphous silicon dioxide has no electro-optical effects and only exhibits very weak nonlinearity, the oxide layer in SOI merely acts as an inert cladding material providing no other functionalities much needed for integrated photonic systems, such as on-chip light modulation and nonlinear optical signal processing. If integrated silicon photonic devices can be built on materials that are transparent over a wider band, have strong electro-optical and nonlinear optical effects, or possess optical gain, the potential of silicon photonics with advanced active photonic functionalities, in addition to their established role as a passive optical platform, can be fully leveraged in future large scale integrated photonic systems. However, to date, direct growth or bonding of crystalline silicon on materials other than silicon dioxide remains to be difficult, unreliable or too expensive for large scale integrated device [167]–[169].

By using the transfer-and-bond technique as developed and demonstrated in Chapter 3 and Chapter 4, in principle, we can fully utilize the transparent window of silicon material in the mid-infrared wavelength range by transferring the silicon photonic devices onto another mid-infrared compatible material. In this chapter, we describe a method to unleash silicon's tremendous potential for integrated photonics by transferring fully integrated silicon photonic circuit from the traditional SOI platform to a new

substrate-Calcium Difluoride (CaF_2). Notably this method does not involve the use of adhesives that may compromise the pristine optical properties of silicon, especially in the infrared, and induce process complexity and unreliability. The new method is capable of integrating silicon photonic devices with virtually any technically important substrate materials including sapphire, silicon carbide, diamond, graphene, chalcogenide glasses, and III-V compound semiconductors, just to name a few. As a result, heterogeneously integrated silicon-on-anything photonics can be achieved to potentially realize unprecedented optoelectronic functionalities. As a proof of concept, in this work we demonstrate silicon photonic devices integrated on calcium fluoride (CaF_2) substrates to enable low loss operation in the mid-infrared (mid-IR) band and apply this novel platform to demonstrate, for the first time, on-chip cavity-enhanced mid-IR spectroscopic analysis of organic chemicals.

5.2 Design of the Mid-Infrared Silicon Photonic Device

5.2.1 Mid-Infrared Waveguide Design

The wavelength we propose to use is between 5.3μm to 5.5μm, therefore, we will redesign all the photonic structure which include the waveguide and the ring resonator. Also, since the coupling coefficient and bending loss will change accordingly, we also have to redesign the coupling gap for the ring resonators with different radius.

For a single mode waveguide, to efficiently guide the light with 5.3μm ~5.5μm wavelength, the width of the waveguide needs to be 1.8μm and the appropriate rib height

is 500nm with a slab height of 100nm. The fundamental mode profile of such geometry for 5.4μm wavelength is shown in Fig. 5.2 below:

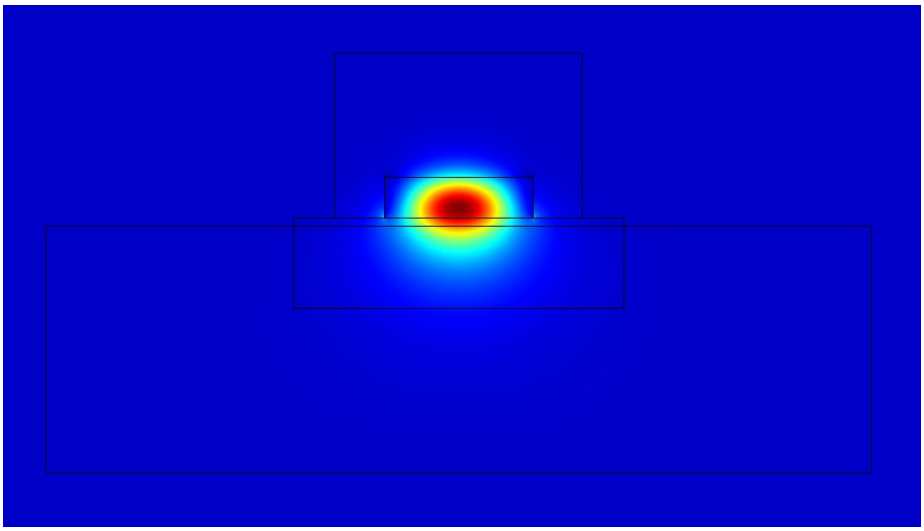

Figure 5.2 *Fundamental mode profile of single mode rib waveguide for 5.4μm wavelength.*

5.2.2 Mid-Infrared Ring Resonator Design

The width of the ring resonator could be simply defined as 1.8μm as well, however, the coupling gap needs to be predicted theoretically.

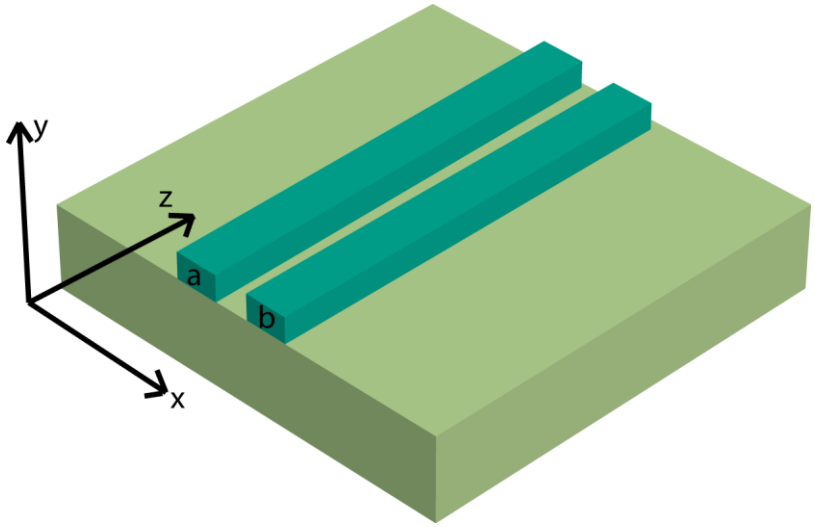

Figure 5.3 *Schematics of coupled waveguides*

From the basic coupled mode theory of two coupled waveguides as shown in Fig. 5.3, The field in each waveguide could be described by the Equations (5.1)

$$\begin{aligned} E_a &= a_0(x,y)e^{i\beta z}e^{i\omega t} \\ E_b &= b_0(x,y)e^{i\beta z}e^{i\omega t} \end{aligned} : \tag{5.1}$$

The coupling between these two fields could be simply described as:

$$\begin{aligned} da_0 / dz &= \kappa b_0 \\ db_0 / dz &= -\kappa a_0 \end{aligned} \tag{5.2}$$

Then, the relationship between these two field's amplitude could be written as:

$$\frac{d^2a(z)}{dz^2} - \frac{1}{\kappa}\frac{d\kappa}{dz}\frac{da(z)}{dz} + \kappa^2 a(z) = 0 \tag{5.3}$$

Since both the ring resonator and waveguide will only support single mode, therefore, according to coupling mode theory [170], the coupling coefficient κ could be expressed as:

$$\kappa = \frac{\beta_{co} + \beta_{contra}}{2} \tag{5.4}$$

Where β_{co} and β_{contra} denotes the propagation constant of the co-directional coupling situation and the contra-directional coupling situation of two parallel single mode waveguide, respectively. Therefore, by gradually changing the coupling gap size between two waveguides with specified waveguide cross-section in the FEM or FDTD simulation tool, the relationship between κ and the coupling gap could be plotted with finite number of data points. Then, the data points will be fitted with Equation (5.5),

$$\kappa = ae^{(bg(z))} + ce^{(dg(z))} \tag{5.5}$$

which is the relationship between coupling coefficient κ and $g(z)$, the value of a~d could be derived with the fitting result as shown in Fig. 5.4.

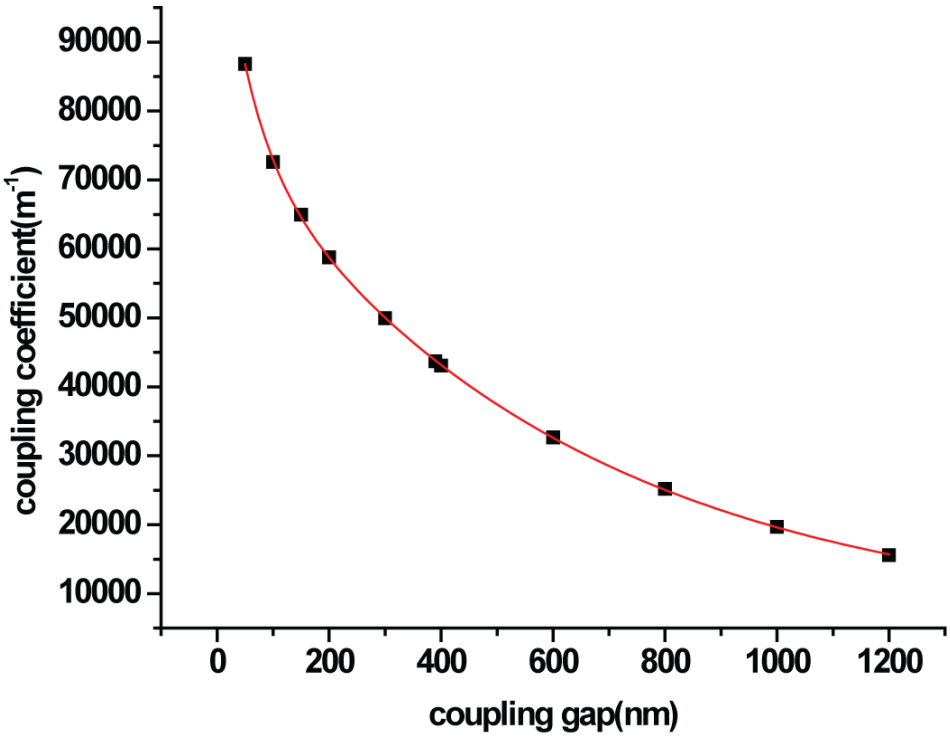

Figure 5.4 *Coupling coefficient κ calculated from simulation result with different coupling gap value (dot) and the fitted result with Eq(5.5) (line).*

Since the coupling distance between the curved ring resonator and the straight waveguide is continuously changing, we consider the distance between the ring resonator and the side coupled waveguide is a function of z, which could be written as:

$$g(z) = g_{\min} + R - \sqrt{R^2 - z^2} \tag{5.6}$$

The coupling schematic for a ring resonator and a straight waveguide is shown in Fig. 5.5. The effective coupling regime is divided into multiple infinite small parts as shown in orange color. Each infinite small area could be considered as two parallel waveguides with a certain coupling gap g(z), and we only consider the coupling

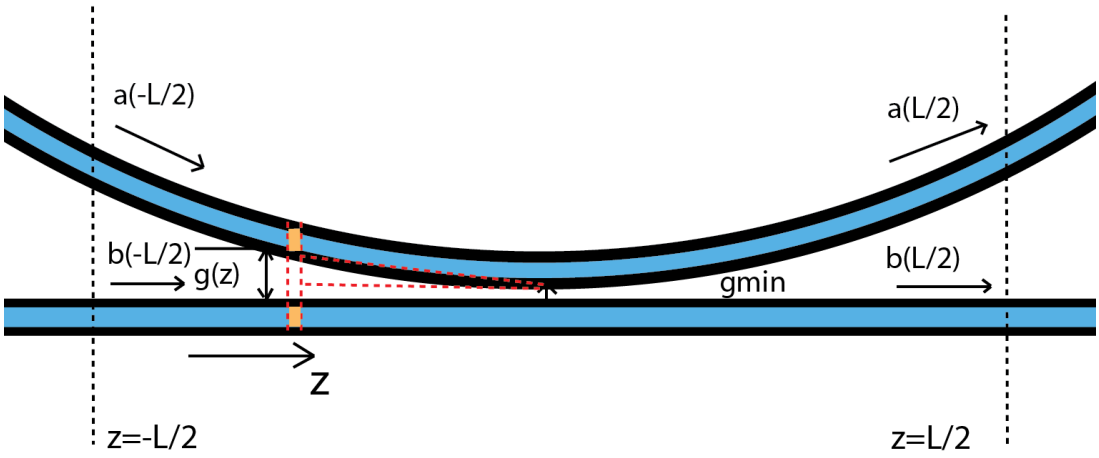

Figure 5.5 *Schematic of the coupling section of a waveguide side-coupled ring resonator.*

regime where z is ranging from *–L/2* to *L/2*. *L* is called the effective coupling length, which could be decided by numerical calculation. Therefore, by combing equation (5.3), (5.5),and the coupling schematic in Fig. 5.5, a set of second order derivative equations could be derived at the critical coupling condition as:

$$\begin{gathered}\frac{d^2a(z)}{dz^2}-\frac{1}{\kappa}\frac{d\kappa}{dz}\frac{da(z)}{dz}+\kappa^2 a(z)=0\\ \kappa=a\exp(bg(z))+c\exp(dg(z))\\ g(z)=g_{\min}+R-\sqrt{R^2-z^2}\\ \left.\frac{da(z)}{d(z)}\right|_{\frac{-L}{2}}=\kappa b(z)\Big|_{\frac{-L}{2}}\\ a(z)\Big|_{\frac{-L}{2}}=a(z)\Big|_{\frac{L}{2}}\times\exp(-\frac{\alpha_{ring}}{2}2\pi R)\\ b(z)\Big|_{\frac{L}{2}}=0\end{gathered} \tag{5.7}$$

According to the numerical calculation, the value of *L* could be set as 20μm when the radius of ring resonator is 60μm. When solve the equation set (5.7) from z=-10μm to z=10μm, the energy exchange between the ring resonator and the straight waveguide

could be fully covered and the solved coupling gap g_{min} when the critical coupling happens is 300nm. If the radius of the ring resonator changes, then the value of g_{min} will change accordingly. Also, due to the standard deviation brought by the fabrication process, during the pattern design process, we manually bring a 20 percent standard deviation to the value of the coupling gap.

5.3 Fabrication Method

5.3.1 Ebeam then Transfer Method

The first fabrication method we utilized for the realization of silicon photonic device on CaF_2 substrate is identical to that for the realization of silicon photonic devices on flexible PET substrate as mentioned in Chapter 4. However, there are several differences during the transfer process of mid-infrared silicon photonic devices which are:

(1) Due to the limitation of mid-infrared device measurement setup, we can only use butt-coupling method to characterize the transferred device. In order to fully avoid receiving the stray light from the input fiber, a more than 5mm lateral offset distance is needed between the input waveguide and the output waveguide, which is shown in Fig. 5.6. Thus, the size of the silicon nanomembrane needs to be minimally 8mm by 5mm, which is much larger than that of the flexible telecomm silicon photonic devices (300μm by 300μm).

(2) The adhesion layer we utilize in the fabrication process in Chapter 4, which is SU8, is absorptive at the wavelength of 5μm

(3) Due to utilization of butt-coupling method, both ends of silicon waveguide needs to sit right at the edge of the CaF_2 substrate.

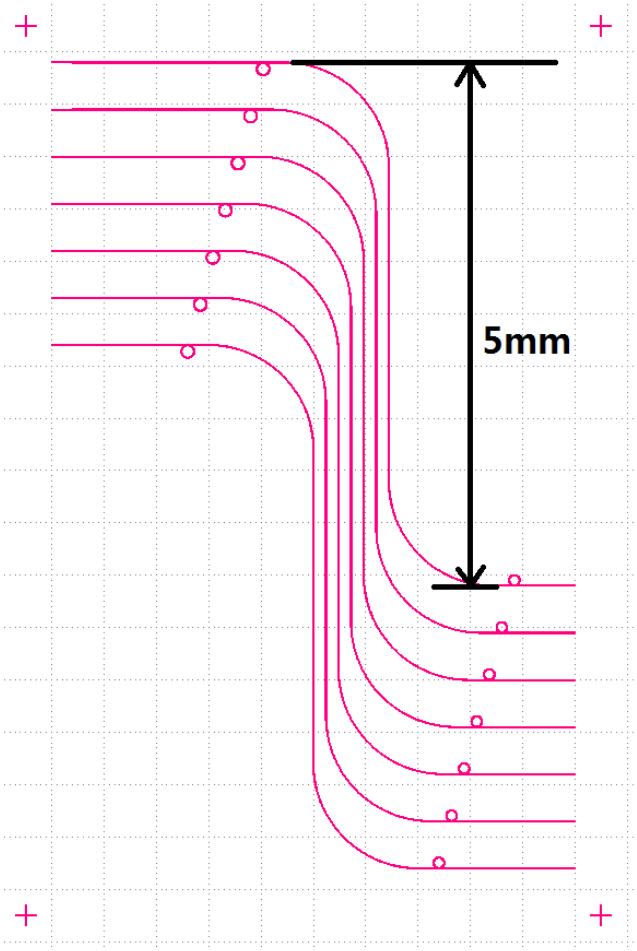

Figure 5.6 *Layout of mid-infrared silicon photonic devices.*

These three differences, to some degree, will make the original fabrication method, as described in Chapter 4, incapable of realizing the transfer of mid-infrared silicon photonic devices onto CaF_2 substrate. Therefore, we have made several changes to the original transfer method as described in Fig. 4.8 and Fig. 4.9. The changes are listed below:

(1) Due to the large area of the silicon nanomembrane, any small disturbance during the transfer process may induce the formation of wrinkles. Besides, the shallow etched photonic structure has further decrease the mechanical sustainability of the membrane. Therefore, we take extra care when bring the PDMS stamp and the SOI wafer into contact. Afterwards, the PDMS stamp is slowly delaminated from the SOI wafer instead of swiftly. The reason for such change is to maximally decrease the disturbance caused by the delamination process.

(2) Since PDMS shows swelling characteristic when is immersed into certain type of solvents [171] such as acetone and IPA. The PDMS stamp will be rinsed with acetone and IPA for certain time after the silicon nanomembrane has been transferred on top of it. The swelling effect of PDMS stamp will lead to the stretch of top silicon layer, which, to some degree, will flatten the silicon membrane if any wrinkle is generated during the transfer process.

(3) Since the adhesion layer SU8 is no longer usable in this process, a direct 2nd transfer step is needed. Therefore, instead of using a PDMS stamp made from a mixture ratio of 10 to 1, new PDMS stamps are used whose mixture ratio is 5 to 1. The reason for decreasing the mixture ratio is to optimize the surface adhesion force. During this specific application, we need

$$\begin{aligned} G_c^{silicon/PDMS} &> G_c^{photoresist/silicon} \\ G_c^{CaF2/silicon} &> G_c^{silicon/PDMS} \end{aligned} \tag{5.8}$$

With a mixture ratio 5 to 1, the surface adhesion force between silicon and PDMS stamp is still larger than that between silicon and photoresist pedestal, but smaller than the Van

der Waal force between silicon and CaF_2 interface. Furthermore, before executing the final transfer step, both the silicon nanomembrane (on PDMS stamp) and the CaF_2 will be thoroughly cleaned to make sure conformal contact could be reached between the silicon nanomembrane and the CaF_2 substrate. Finally, a slow peeling speed in the order of 1mm/sec is needed for the final transfer process.

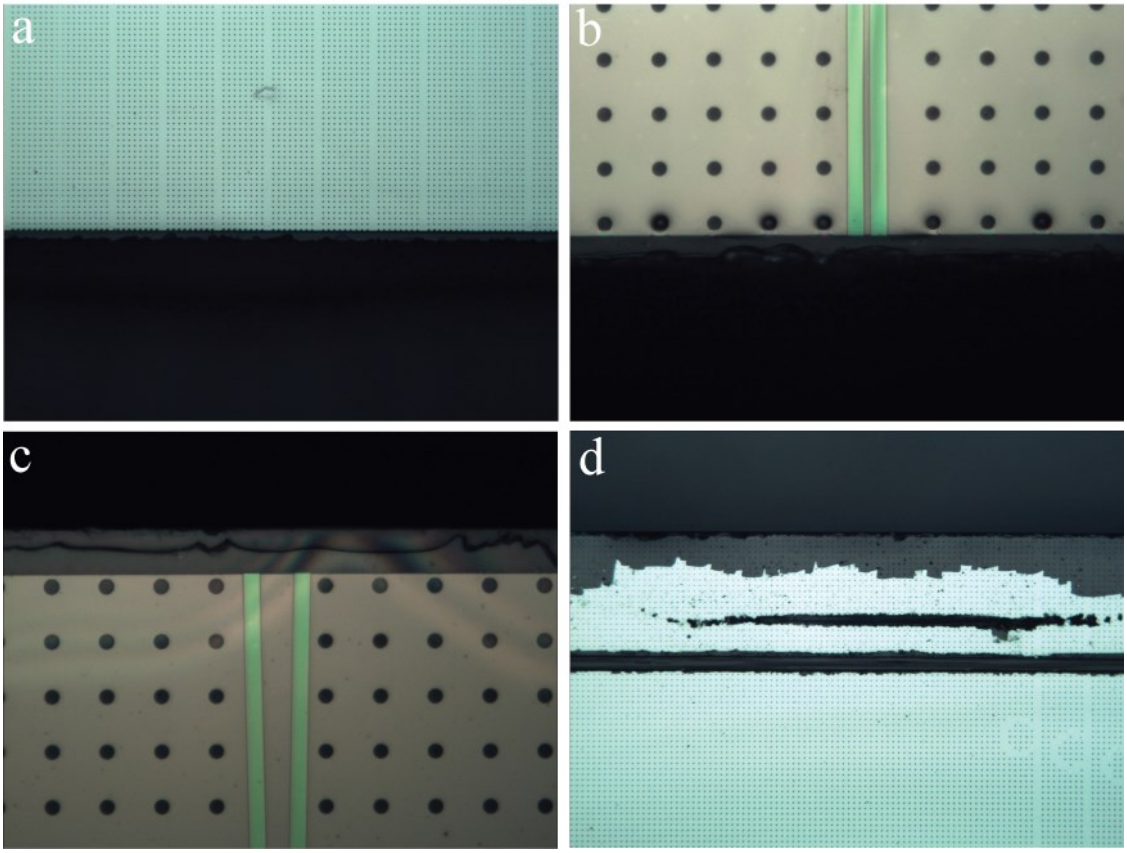

Figure 5.7 *Optical microscope images of the edge of silicon nanomembrane on top of diced CaF_2. (a) Silicon nanomemebrane without photonic devices on top of diced CaF_2 wafer. (b) Output port of the mid-infrared device. (c)Input port of the mid-infrared device. (d) silicon nanomembrane on CaF_2 destroyed during the dicing process*

(4) In order to realize the butt-coupling measurement, the CaF_2 wafer is diced right along the side of the silicon nanomembrane, the result of which could be seen in Fig. 5.7. Due to the stringent requirement of the butt-coupling method, the distance between the end of input waveguide and the edge of CaF_2 may not exceed 10μm. For regular SOI devices, the waveguide could be directly diced through and then the facets of which could be further polished. However, such method could not be applied in our situation since the silicon nanomembrane will be destroyed by the vibration of the dicing blade as shown in Fig. 5.7d.

With all these changes, the detailed fabrication process flow for the mid-infrared devices is listed below and shown in Fig. 5.8 (This is for SOI wafer with 600nm silicon and 2000nm buried oxide)

(1) Thoroughly clean the SOI sample with acetone, IPA and DI water, then blow dry
(2) Bake at 180 degree Celsius for 5 minutes
(3) Spin ZEP with 5000rpm for 1minute
(4) Use ebeam lithography to pattern the photonic structure with 280μc/cm^2 dosage
(5) Develop in ZED-N50 for 2 minutes and then rinse with IPA for 30 seconds
(6) Use deeptrench etcher to etch the top silicon layer for 500nm
(7) Strip ZEP by using NMP for 15 minutes, then use Piranha to treat the sample for 5 minutes
(8) Dehydrate at 115 degree Celsius for 2 minutes
(9) Spin on S1805 at 3000rpm for 30 seconds
(10) Bake at 115 degree Celsius for 1 minute

(11) Pattern the carrier slab shape by using photolithography

(12) Soft bake at 115 degree Celsius for 1 minute

(13) Develop in MF-319 for 30 seconds, rinse with DI water then blow dry

(14) Strip S1805 by using 1165 for 5 minutes and then treat with Piranha for 5 minutes

(15) Immerse in HF(49%) solution for 90 to 100 seconds

(16) Dehydrate at 115 degree Celsius for 2minutes

(17) Cover the sample with S1805, then put it into low vacuum (2 Torr) for 5 seconds

(18) Put the sample on spinner at 3000rpm speed for 30 seconds

(19) Bake at 115 degree Celsius for 1 minute

(20) Flood exposure by using photolithography for 2.5 seconds

(21) Soft bake at 115 degree Celsius for 1minute

(22) Develop in MF-319 for 1 minutes, rinse with DI water then blow dry

(23) Wet etch with HF(49%) solution for 1 hour

(24) Rinse with DI water, then blow dry

(25) Keep in atmosphere for 10 minutes or in desiccators for 2 minutes

(26) Use thoroughly cleaned PDMS stamp (with 5 to 1 mixture) to pick up the silicon nanomembrane with photonic structures on top.

(27) Thoroughly clean the PDMS stamp with silicon membrane and CaF_2 substrate with acetone, IPA and DI water (which may also help to remove the existing wrinkles on the membrane)

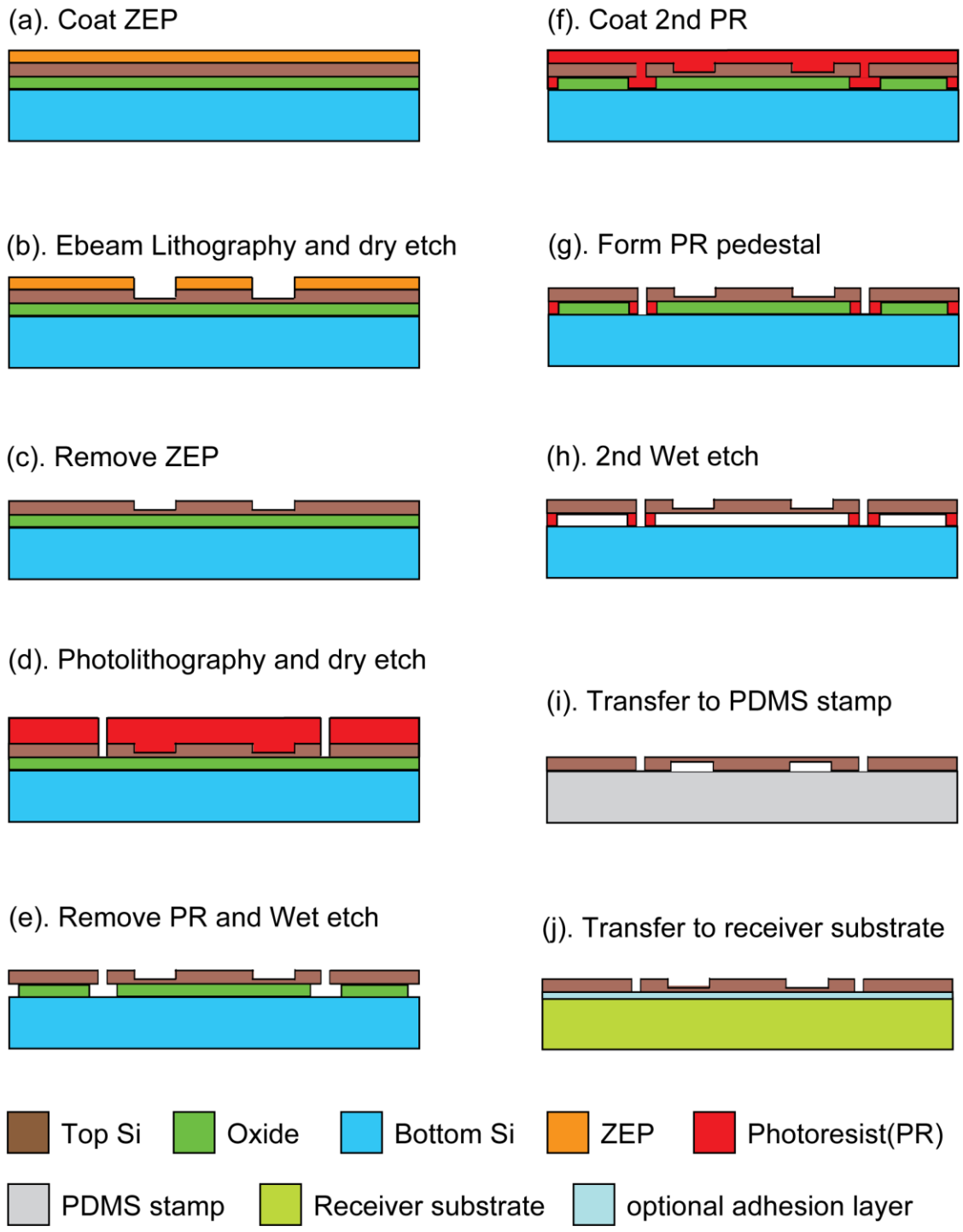

Figure 5.8 *Process flow for the heterogeneous integration of mid-infrared silicon photonic devices on CaF_2 substrate by using the Ebeam then transfer method.*

(28) Firmly compress the PDMS stamp on CaF_2 substrate to ensure the reach of conformal contact. Then slowly peel off the PDMS stamp.

(29) Dice the CaF_2 substrate right along the edge of the silicon nanomembrane by using dicing saw.

However, the final transfer yield of such method is not ideal, which could be seen from Fig. 5.9. The main reason for the low yield is that the shallow etched silicon membrane is highly vulnerable since the thickness of slab is only 100nm. Any vibration or mechanical disturbance caused during the transfer or dice process may have a chance to destroy the silicon nanomembrane. Although the utilization of extremely shallow etched photonic structure may solve such issue. Still, new issues may emerge such as low optical performance and large device footprint when the rib height is too small. Therefore, we have developed an alternative fabrication method for such mid-infrared device which possesses a much higher and stable yield.

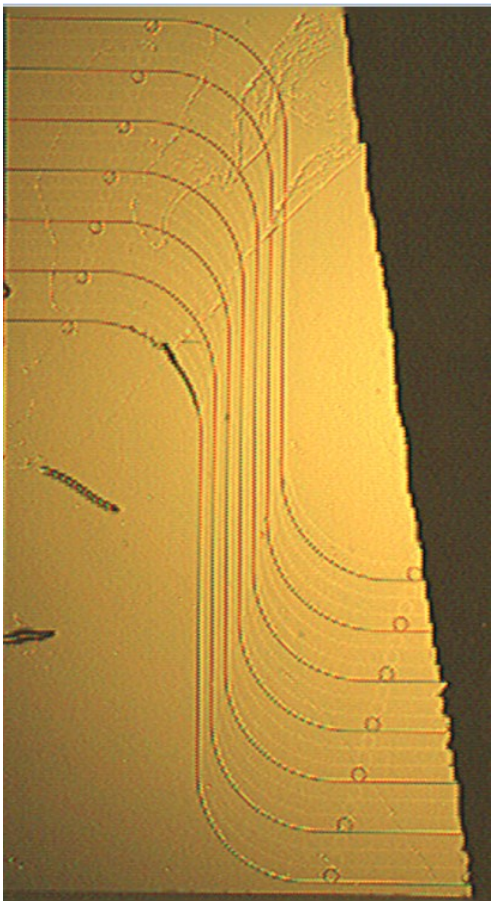

Figure 5.9 *Optical microscope image of the mid-infrared silicon photonic devices on top of diced CaF_2 substrate fabricated by using Ebeam-then-tranfer method.*

5.3.2 Transfer then Ebeam Method

Since the main reason for the low transfer yield is the fragile nature of the patterned silicon photonic devices, then we will consider to separate the Ebeam process from the transfer process. More specifically, we will directly transfer the whole silicon membrane to the CaF2 substrate first and then pattern the photonic devices with Ebeam lithography. The fabrication process flow for this method is depicted below in Fig. 5.10.

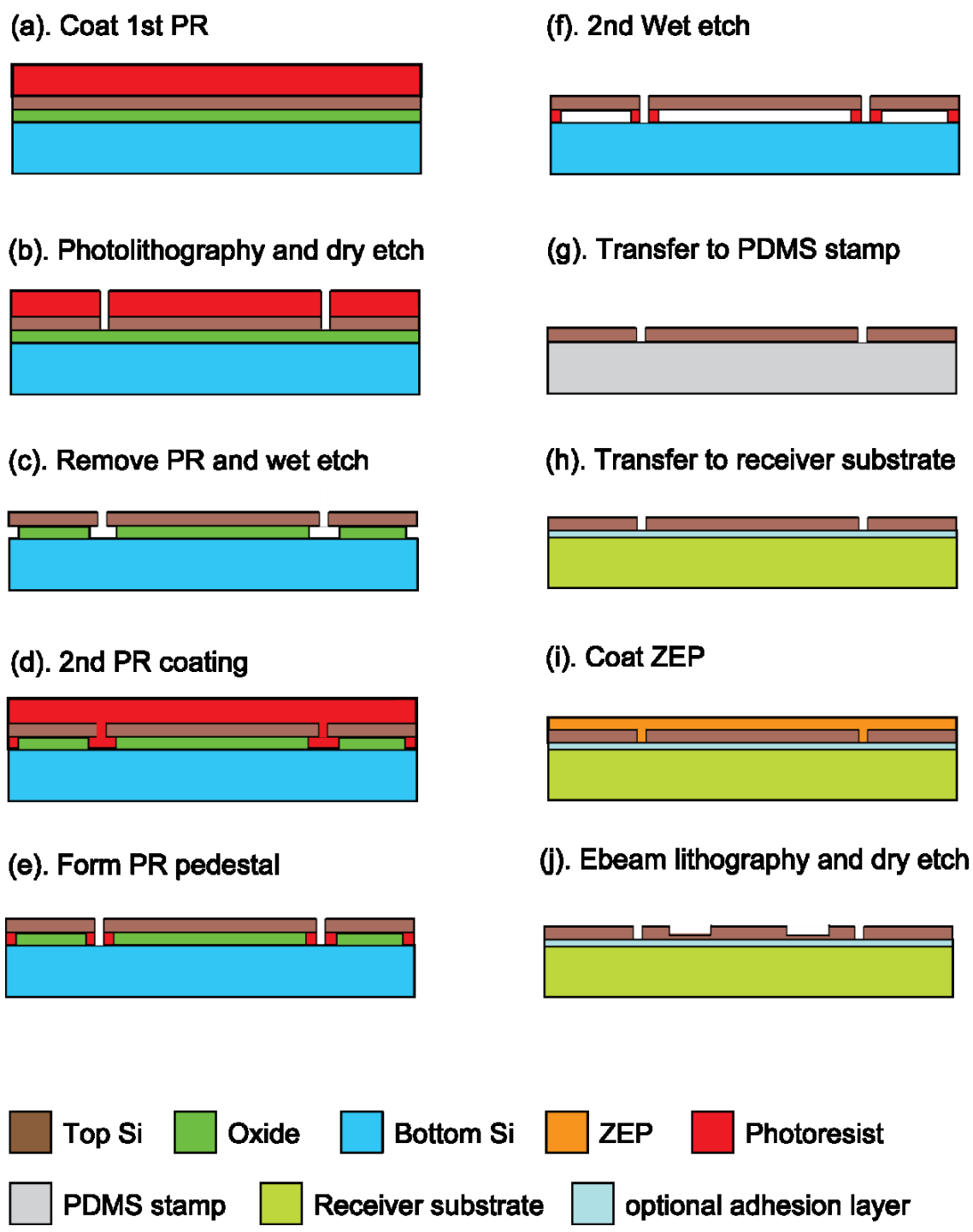

Figure 5.10 *Process flow for the heterogeneous integration of mid-infrared silicon photonic devices on CaF_2 substrate by using transfer then Ebeam method.*

The basic idea of this new fabrication method is to pattern the silicon photonic devices after the silicon nanomembrane (SiNM) has already been transferred onto the CaF_2 substrate since the yield of transferring silicon membrane without shallow etched photonic structure is much higher. However, there are several issues need to be resolved for this new fabrication method.

(a) How to uniformly spin ZEP on top of SiNM transferred onto CaF_2 substrate

(b) How to execute Ebeam lithography patterning on an insulating substrate (CaF_2)

The adhesion force between ZEP and SiNM is good enough, however, in order to get uniform coverage of ZEP all around the transferred membrane, we need to increase the adhesion force between ZEP and CaF_2 substrate. Basically, ZEP is hydrophobic and CaF_2 is hydrophilic, therefore, before spinning the ZEP, we could treat the surface of CaF_2 with oxygen plasma which may temporarily change the surface of CaF_2 to hydrophobic by generating some dangling –O group on the top surface of CaF_2 substrate.

However, to realize Ebeam lithography patterning on top of an insulating substrate is much more complicated. The issue mainly rises from the surface charge induced by the insulating nature of the substrate. Therefore, we could utilize several different methods to bypass this issue, such as:

(a) Spin-on some AquaSave which is a type of water soluble conductive polymer on top of the ZEP to dissipate the surface charge

(b) Evaporate some gold film on top of the ZEP to dissipate the surface charge

(c) Evaporate some gold film on top of the Espacer/ZEP double layer to dissipate the surface charge.

All these three methods have been tested, the detailed fabrication process flow are listed below (This is for SOI wafer with 600nm silicon and 2000nm buried oxide):

(1) Thoroughly clean the SOI sample with acetone, IPA and DI water, then blow dry

(2) Bake at 115 degree Celsius for 2 minutes to dehydrate

(3) Spin S1805 at 3000rpm for 30 seconds

(4) Bake at 115 degree Celsius for 1minute

(5) Pattern the silicon membrane shape by using photolithography

(6) Soft bake at 115 degree Celsius for 1 minute

(7) Develop in MF-319 for 30 seconds, rinse with DI water then blow dry

(8) Use deeptrench etcher to etch through the top silicon layer

(9) Immerse the sample into Piranha for 5 minutes to remove the surface photoresist

(10) Immerse in HF(49%) solution for 90 to 100 seconds

(11) Cover the sample with S1805, then put it into low vacuum until the pressure drops down to 2Torr.

(12) Take the sample out from the low vacuum and spin at 3000rpm for 30 seconds

(13) Bake the sample at 115 degree Celsius for 1 minute

(14) Flood exposure using photolithography for 2.5 seconds

(15) Develop in MF-319 for 30 seconds, rinse with DI water and then blow dry

(16) Immerse in HF(49%) solution for another 1 hour

(17) Rinse the sample with DI water, then blow dry

(18) Keep in atmosphere for 10 minutes or in desiccators for 2 minutes

(19) Use 5:1 ratio mixed PDMS stamp (newly fabricated in two weeks and can't be

exposed to high humidity environment for more than 1 hour)

(20) Contact PDMS with SOI sample and then peel with relatively fast speed (10cm/sec)

(21) Rinse the SiNM on PDMS with acetone and IPA in order to remove the left photoresist pedestal

(22) Rinse the CaF2 substrate with acetone, IPA and DI water and then blow dry

(23) Contact PDMS stamp with the CaF2 substrate with moderate pressure and then peel off the PDMS stamp with slow speed (< 1mm/s)

(24) Rinse the SiNM on CaF2 substrate with acetone and IPA carefully and then blow dry

(25) Bake on 180 degree Celsius hotplate for 5 minutes

(26) Take the CaF2 substrate with SiNM with tweezers and cool it with nitrogen gun for 30 seconds before landing it onto any other room temperature platform to avoid the heat shock which may destroy the substrate

(27) Treat the surface of the CaF2 with SiNM on top with oxygen plasma (100 sccm oxygen flow, RF power = 100W) for 60 seconds

(28) Spin ZEP on top of the sample with 3000rpm for 1min

(29) Bake on 180 degree Celsius hotplate for 2 minutes

(30) Take the CaF2 substrate with SiNM with tweezers and cool it with nitrogen gun for 30 seconds.

(31) (a) Spin on AquaSave solution on top of ZEP with 3000rpm for 1min and then bake at 100 degree Celsius for 2 min

(b) Use ebeam evaporator to deposit 15nm gold on top of the ZEP

(c) Spin on Espacer (a type of solution based dielectric polymer) on top of ZEP with 3000rpm for 1 minute, then use ebeam evaporator to deposit 15nm gold on top of the Espacer

(32) Mount the sample onto the piece-part holder of Ebeam lithography machine and tape the surface of the CaF2 substrate with the holder by using any conductive tape in order to create a path to dissipate the surface charge.

(33) Use Ebeam lithography to pattern the ZEP

(34) (a) Use water to rinse off the AquaSave

(b) Use GE6 to remove evaporated gold

(c) Use water to rinse off the Espacer and lift off the evaporated gold film

(35) Develop ZEP in ZED-N50 for 45 seconds and then rinse with IPA for 15 seconds

(36) Rinse with DI water and then blow dry

(37) Use deeptrench etcher to etch the sample for 90 seconds (500nm rib), or 82 seconds (400nm rib) by using single bosch process.

(38) Dice the device right along the edge of the SiNM by using the dicing saw.

Then, the results from all these three methods could be compared:

(a) The developed photonic pattern from the 1st method by using AquaSave is shown in Fig.5.11, from which we can see that both mainfield stitch error and subfield stitch error exist when only use AuqaSave as the conductive layer.

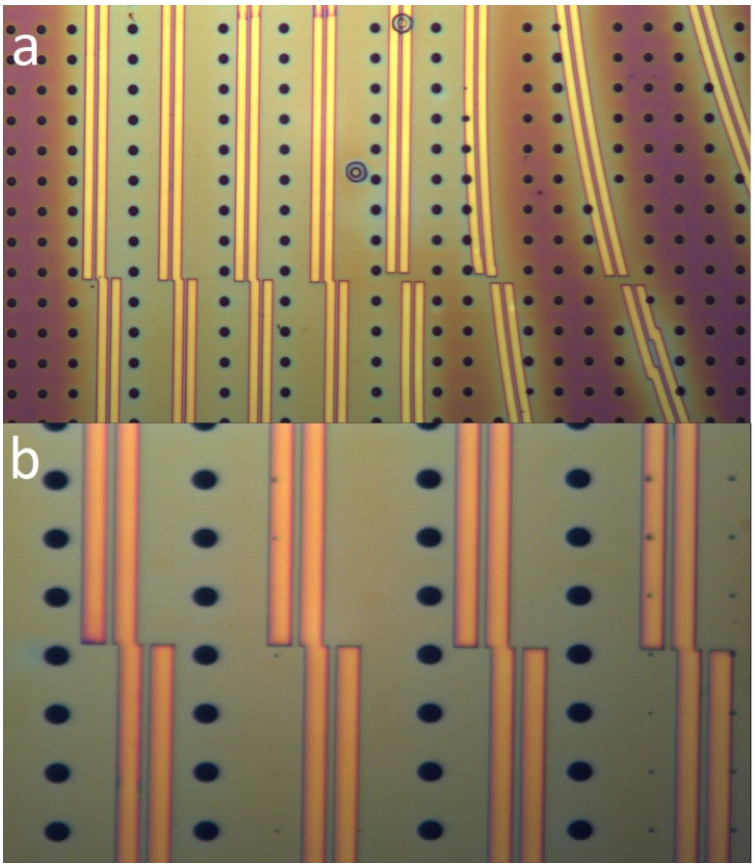

Figure 5.11 *Photonic structure pattern defined by using ZEP on top of SiNM/CaF_2 substrate by using AquaSave as charge dissipation layer*

(b) Then, the developed ZEP pattern from the 2nd method by using 15nm thick ebeam evaporator deposited gold film as the conductive layer is shown in Fig. 5.12. As we can see that the mainfield stitch error still exist when replace AquaSave with 15nm thick gold film, however, its magnitude has been largely decreased and the subfield stitch error could not be observed anymore. Although the utilization of gold film has, to some degree, diminish the pattern distortion, there is another emerging issue when use gold etchant GE6 to remove the deposited gold film. After removal of the gold film, the surface of ZEP became really rough, which

means ZEP has also been slowly etched by the gold etchant. Such extra roughness of the ebeam resist brought by the gold etchant will dramatically degrade the optical performance of the resulted photonic structures. Therefore, we have to use some protection layer, more specifically, the Espacer to protect the ebeam resist during the gold removal process. Moreover, since Espacer is a type of water soluble dielectric polymer, it could perform as a lift off layer. Thus, we do not even need to use GE6 to strip the gold layer. Simply by using DI water, the deposited gold will be lifted off with the Espacer layer.

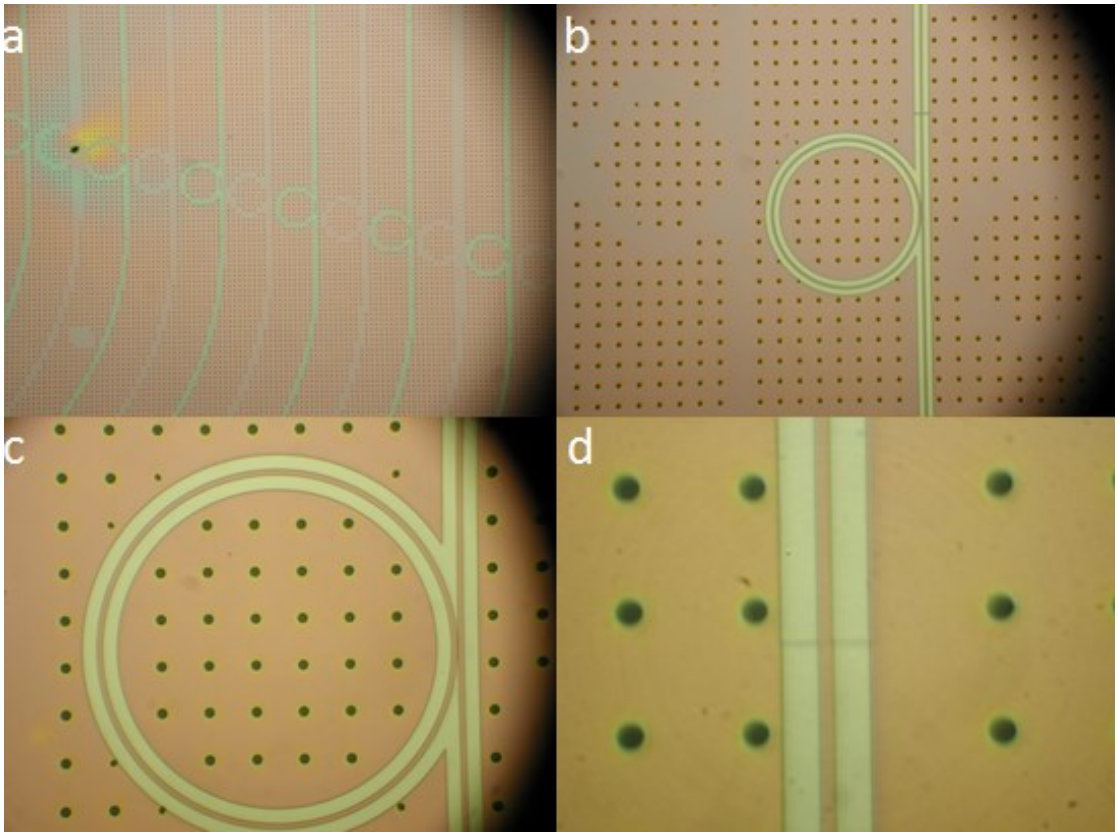

Figure 5.12 *Photonic structure pattern defined by using ZEP on top of SiNM/CaF_2 substrate by using 15nm gold film as charge dissipation layer.*

(c) The developed ZEP pattern by using Espacer along with the 15nm gold film as the charge dissipation layer is shown below in Fig. 5.13:

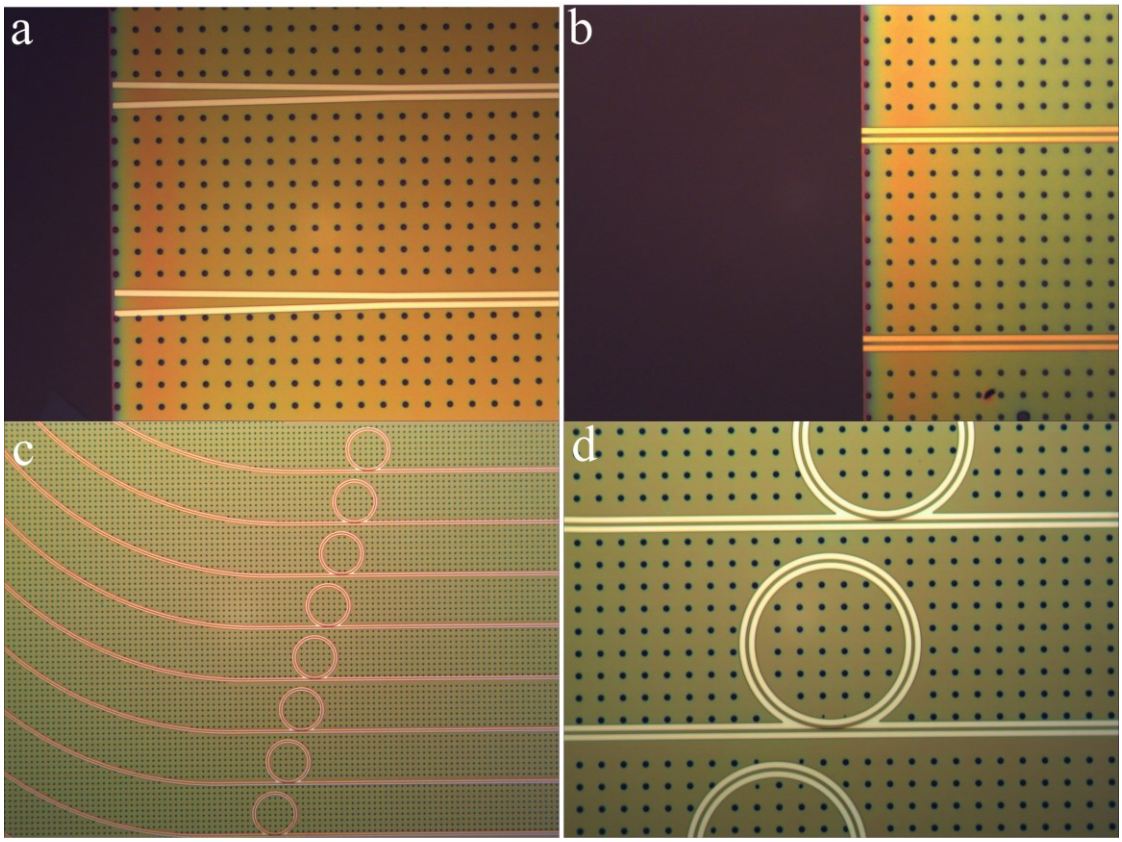

Figure 5.13*Photonic structure pattern defined by using ZEP on top of SiNM/CaF_2 substrate by using 15nm gold film and Espacer as charge dissipation layer. (a)The input port of the device; (b)The output port of the device; (c)Ring resonator arrays; (d)Enlarged view of (c).*

As we can see from the results of the 3rd method, mainfield stitch error or subfield stitch issue could not be observed anymore, meanwhile, due to the protection of Espacer, the ZEP film will remain intact and sharp. Both the input port and output port of the mid-infrared silicon photonic devices are well aligned with the edge of the SiNM, which proves the alignment precision brought by the ebeam lithography. Besides, since the

device is immersed into DI water for 1 minute right after the ebeam lithography process, all gold with the Espacer will be stripped. As shown in Fig. 5.13, no gold remnant could be observed on top of the device after the DI water rinse and development process. Another advantage brought by such transfer then ebeam method is that the etch depth could now be set arbitrarily, which means not only that shallow etch could be easily realized, the fully etched photonic structure on top of CaF_2 substrate is also becoming

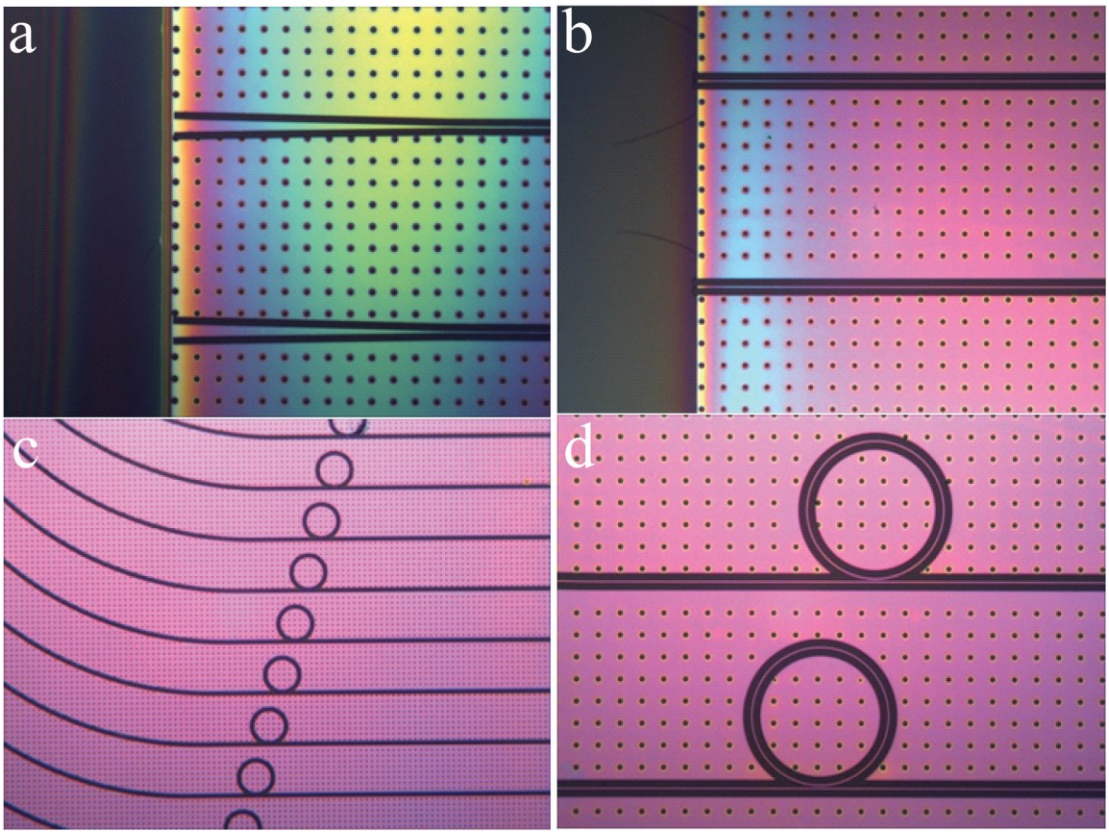

Figure 5.14 *Fully etched photonic structure pattern defined by using ZEP on top of SiNM/CaF_2 substrate by using 15nm gold film and Espacer as charge dissipation layer. (a)The input port of the device; (b)The output port of the device; (c)Ring resonator arrays; (d)Enlarged view of (c).*

possible. Since ridge photonic structure should possess a better mode confinement factor and lower propagation loss, which may lead to a higher quality factor of the ring resonator, we also fabricate some fully etched mid-infrared silicon photonic devices on CaF_2 substrate as shown in Fig. 5.14. In order to tell the sidewall roughness of the silicon photonic structure on top of the CaF_2 substrate, SEM images are also taken for both the rib structure devices and ridge structure devices as shown in Fig. 5.15s and Fig. 5.16s, respectively. The rib structure of the photonic devices could be clearly seen in Fig. 5.15s, the sidewall of the waveguide is relatively smooth after the dry etch process. Besides, the conformal contact between the SiNM and the CaF_2 substrate could be also observed from both Fig. 5.15a and Fig. 5.16a, which further proves the reliability of the direct transfer process. The distance between the edge of the diced CaF_2 substrate and the edge of the silicon waveguide, as shown in Fig. 5.15a and Fig. 5.16s is smaller than 10μm, which exhibits the precision of the dicing process. With such well diced edges, the optical performance of these devices should be able to be measured by utilizing the fiber to waveguide butt-coupling method.

To tell the difference between these two fabrication methods more intuitively. Step by step 3D illustrations are provided for both methods as shown in Fig. 5.17.

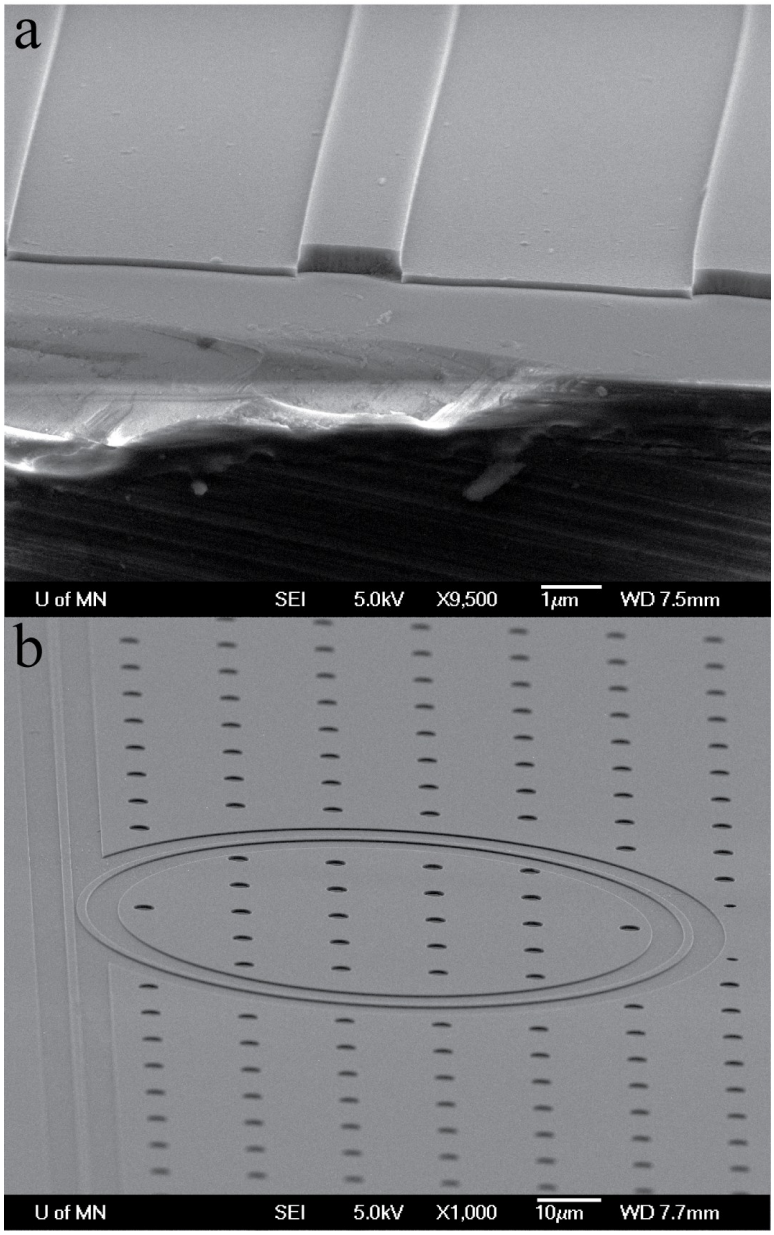

Figure 5.15 *SEM images of rib structure based silicon photonic devices on CaF_2 substrate. (a) SEM image of the rib waveguide output. (b)SEM image of the rib structure based silicon ring resonator.*

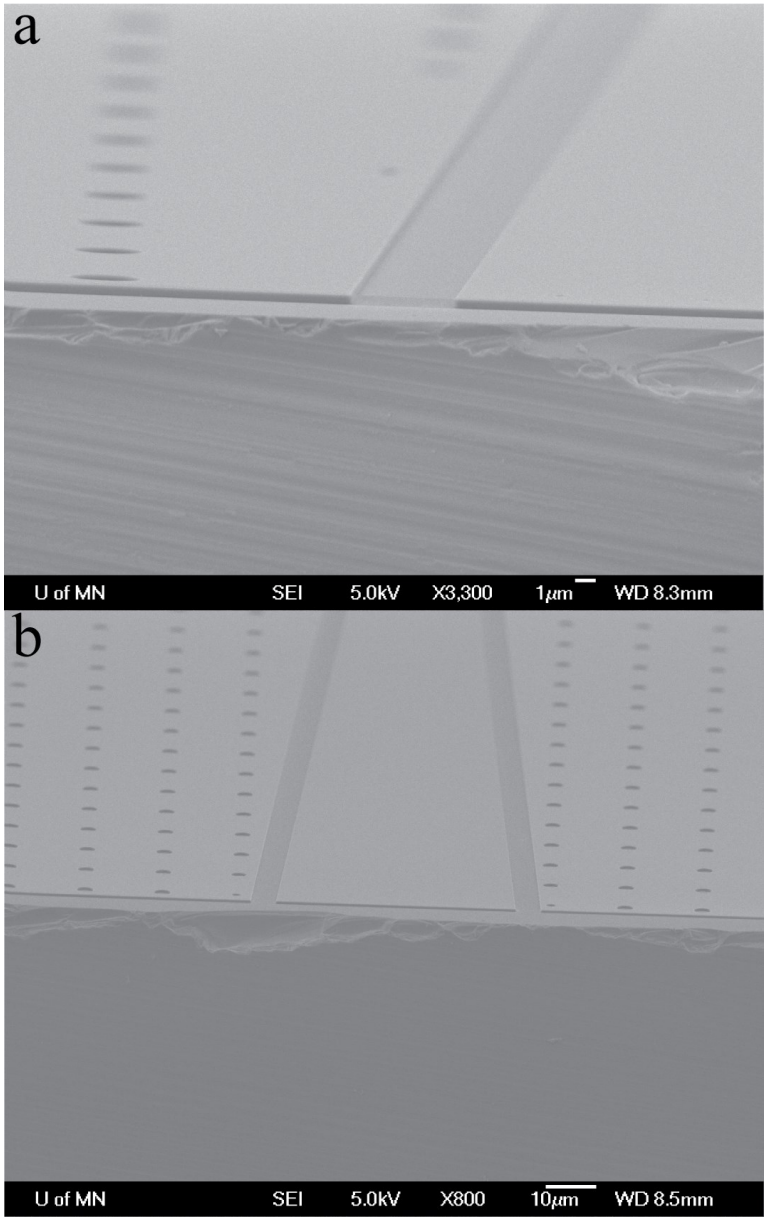

Figure 5.16 *SEM images of strip structure based silicon photonic devices on CaF_2 substrate. (a) side view SEM image of the strip waveguide input. (b)top view SEM image of the strip waveguide input.*

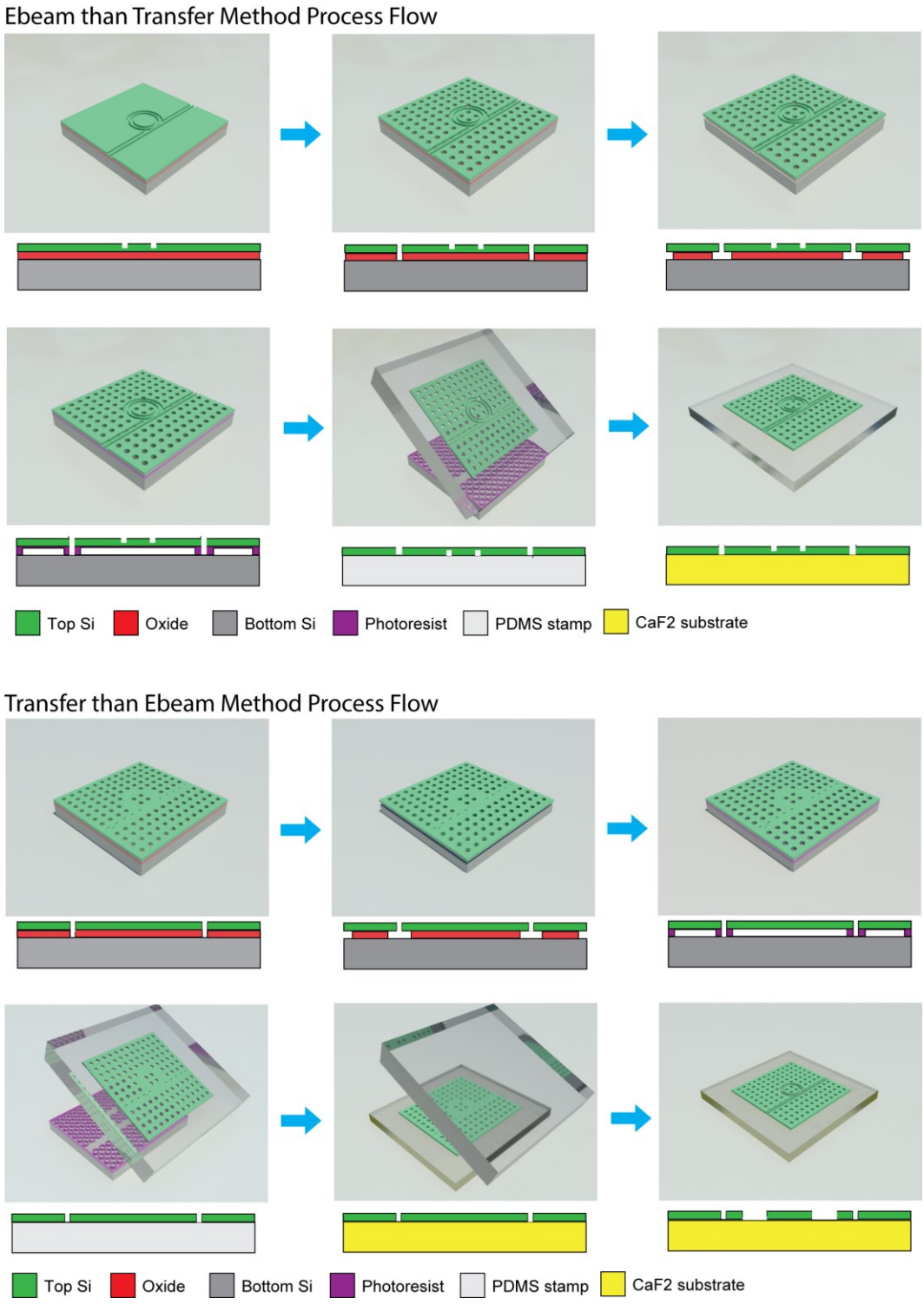

Figure 5.17 *3D illustrations of fabrication process flow of (a) Ebeam then transfer method and (b) Transfer then Ebeam method.*

5.4 Characterization of Mid-Infrared Silicon Photonic Devices

The mid-IR measurement setup employs a fiber butt-coupling configuration. A schematic diagram of the system setup is shown in Fig. 5.18. During the measurement, a CaF_2 lens (NA ~ 0.25) was used to couple TE polarized light from a 5.2 μm external cavity tunable quantum cascade laser (Daylight Solution, Inc.) into a customized InF_3 fiber (IRPhotonics Inc.). The output polarization from the waveguide was monitored using a wire-grid polarizer. Careful optimization of laser fiber alignment was implemented to minimize excitation of higher order fiber modes, since the optical fiber is multi-mode at the 5.2 μm wavelength (core/cladding diameters 40/150 μm). The optical fiber was butt coupled to the planar silicon-on-CaF_2 waveguides, and the optical output at the waveguide end facet was collected by another CaF_2 lens and imaged using an InSb Focal Plane Array (FPA). A liquid nitrogen cooled band pass filter centered at 5.2 μm was inserted into the optical path before the FPA to minimize thermal radiation noise from the ambient background.

An adiabatic inverse taper section of the waveguide as shown in Fig. 5.13a and Fig. 5.14a was inserted near the input facet to minimize coupling loss due to mode-size mismatch between the input fiber and the waveguide. Fig. 5.18c shows the far field image of the guided mode as captured by the FPA. The transmitted intensity was measured by integrating the number of counts on FPA pixels over the mode image, after subtraction of the thermal background contribution.

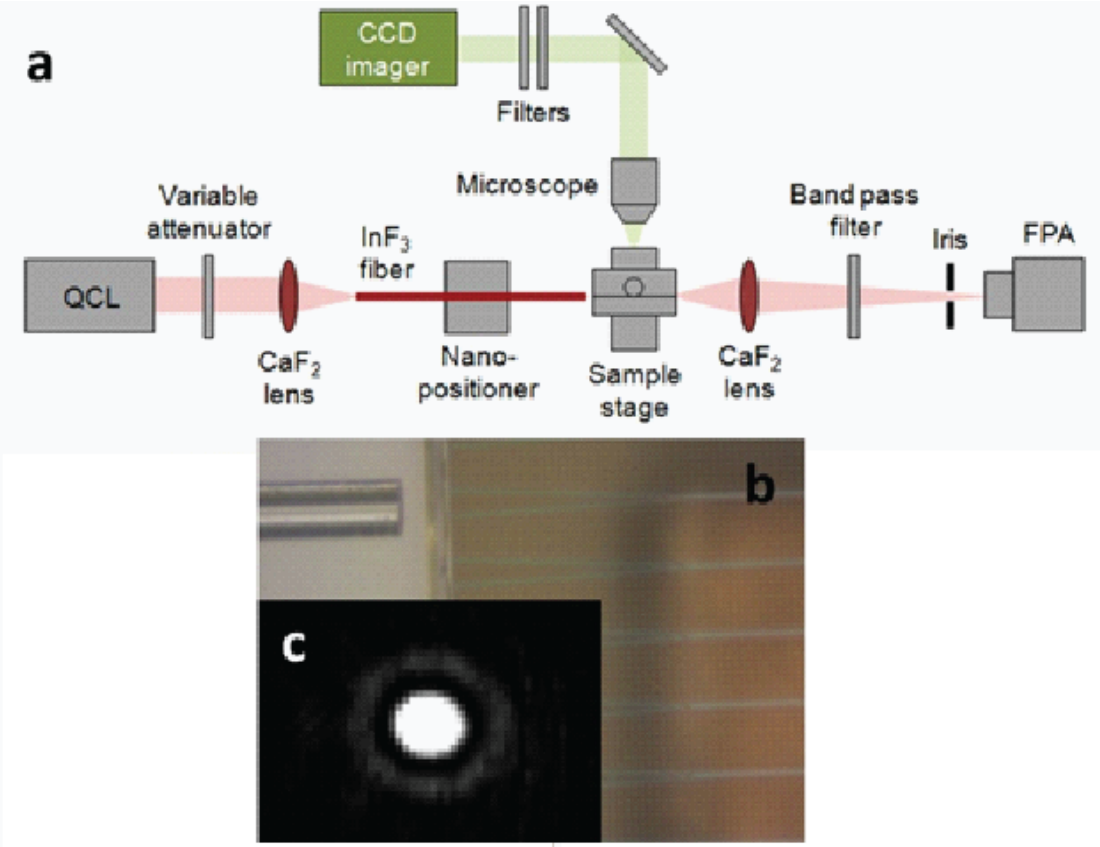

Figure 5. 18 *(a) Mid-infrared fiber butt-coupling measurement setup schematic; (b) top-view optical microscope image of a mid-infrared fiber butt-coupled to an silicon-on-CaF_2 waveguide with an inverse taper to reduce the coupling loss caused by mode-size mismatch; (c) far-field image of the TE guided mode from a single-mode silicon waveguide at 5.2μm;*

The measurement results of silicon photonic devices based on both rib structure and strip structure are shown in Fig. 5.19s. Along each waveguide, there are two ring resonators (as shown in Fig.5.6) whose radius is 50μm and 60μm, respectively. Therefore, the optical resonances could be sorted into two groups with different FSR. For rib structure based silicon photonic ring resonator as shown in Fig.5.19a, the FSR of

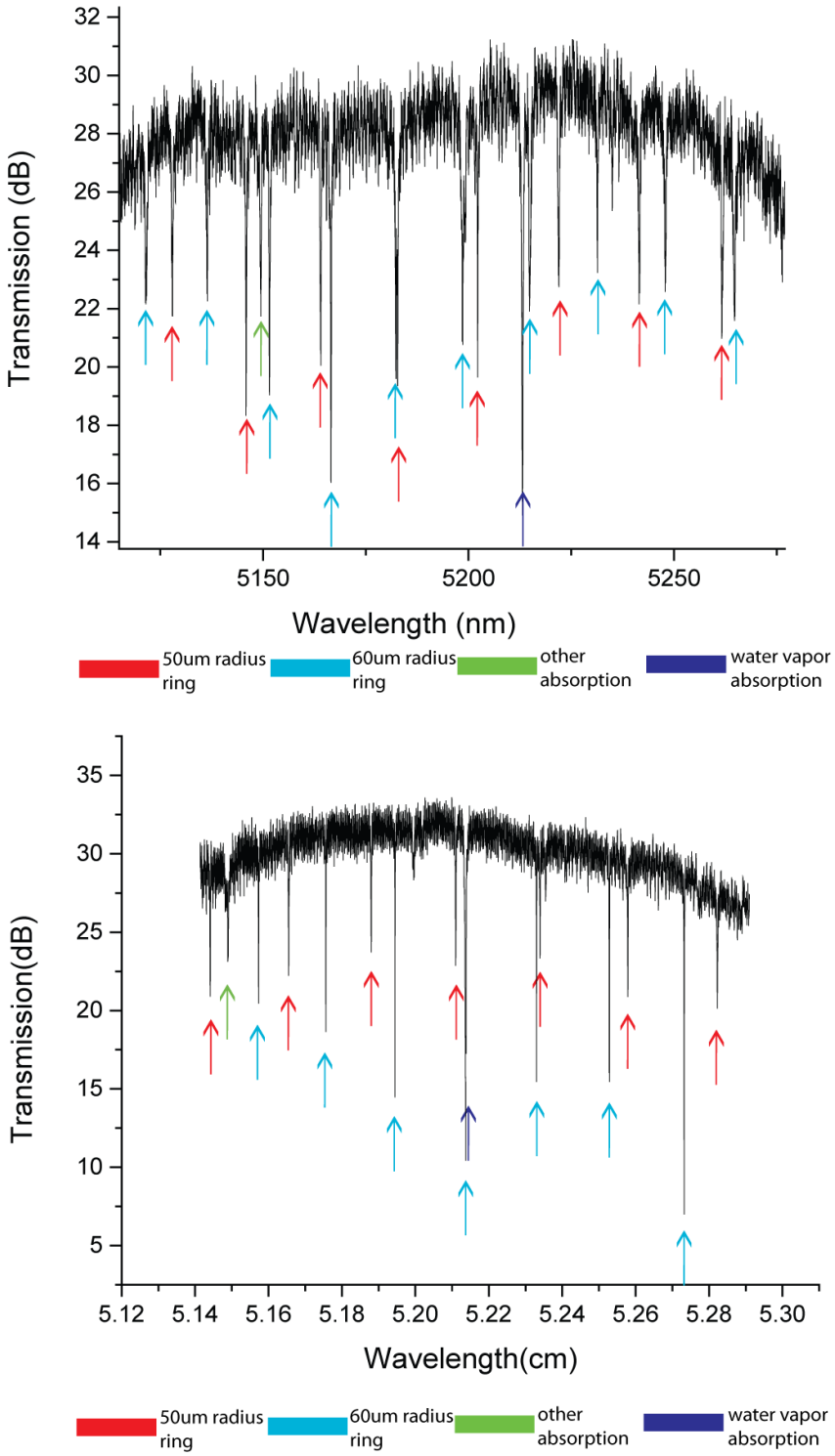

Figure 5.19 *Transmission spectrum of both (a) rib structure based and (b) strip structure based mid-infrared silicon ring resonator.*

these two sets of resonance is 17.2nm and 20.8nm, which agrees well with the radius ratio of these two different ring resonators. Due to the existence of water vapor and some unknown contamination, there are always two sharp dips around 5215nm and 5148nm wavelength, which has nothing to do with the optical resonance of the cavity. As we can see, the level of Fabry-Perot noise formed by the reflected light between two facets of the long waveguide is almost the same in both ridge waveguide and strip waveguide situation. The loaded quality factor for rib waveguide, on average, is around 25000, as shown in Fig. 5.20a and the extinction ratio of the resonance is between 8dB to 14dB. For the strip waveguide structure, the average loaded quality factor is around 45000, as shown in Fig. 5.20b and the extinction ratio of the resonance is between 10dB to 20dB. According to these values, the linear propagation loss for the 60μm radius ring resonator based on rib structure and strip structure is 4.37dB/cm and 2.43dB/cm, respectively. With these results, we could confirm the advantages brought by the strip waveguide structures. The benchmark value of the optical properties of the 60 μm radius ring resonators based on both of these two structures are listed in Table. 5.1.

	60um radius ring with rib waveguide structure	**60um radius ring with strip waveguide structure**
Average Quality Factor	25000	45000
Highest Quality Factor	32000	50000
FSR	about 20.2nm	about 22.8nm
Highest Extinction Ratio	about 14dB	about 25dB
Average Extinction Ratio	9dB	15dB
Intrinsic Quality Factor	45000~60000	80000~100000
Linear Propagation Loss	4.37dB/cm	2.43dB/cm

Table 5.1 *Optical performance of silicon-on-CaF_2 ring resonator with 60μm radius based on rib waveguide structure and strip waveguide structure.*

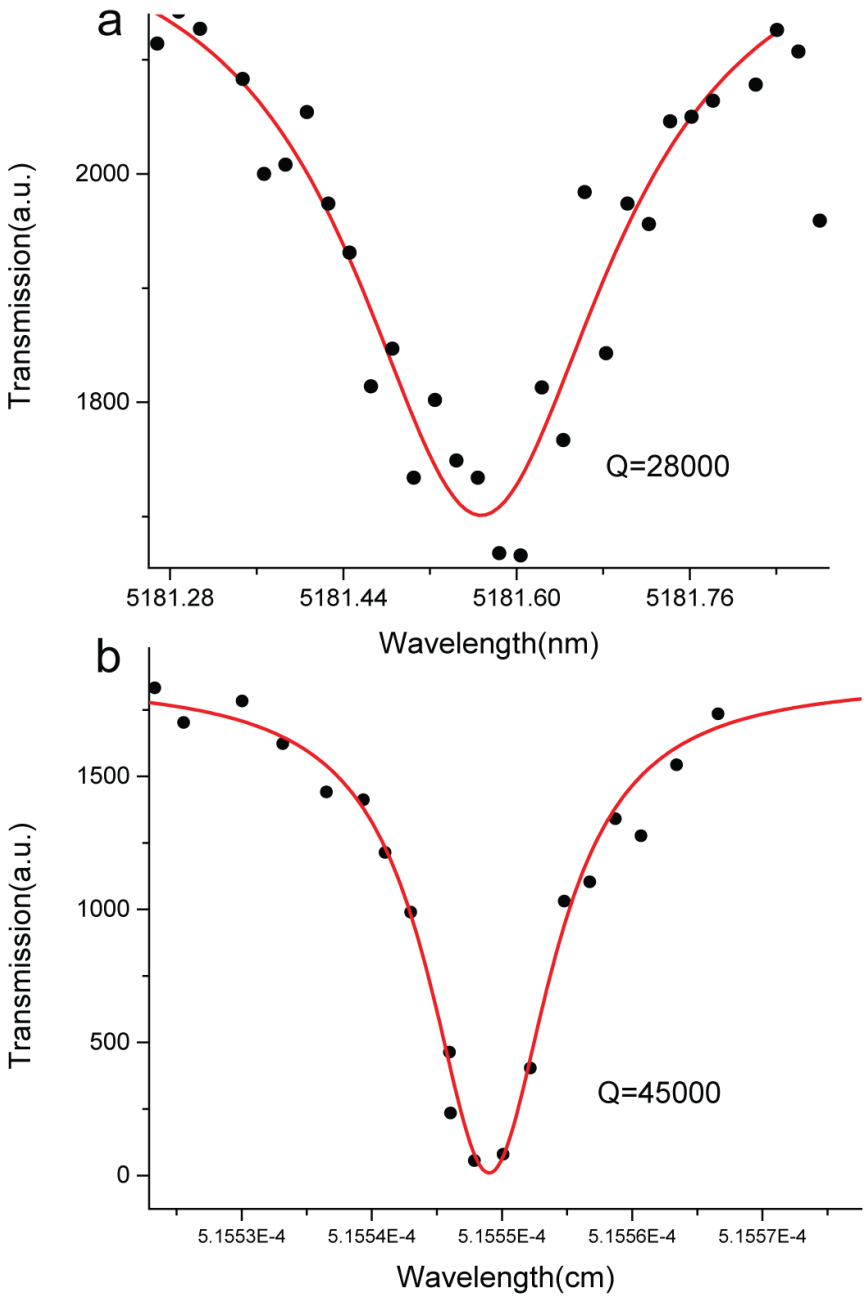

Figure 5.20 *One of the optical resonance of (a) rib structure based ring resonator with a loaded quality factor of 28000 and (b) strip structure based ring resonator with a loaded quality factor of 45000.*

5.5 Cavity Enhanced Mid-Infrared Spectroscopic Sensing

5.5.1 Principles of Cavity-Enhanced Absorption Spectroscopy

The basic operating principle of on-chip cavity-enhanced absorption spectroscopy is shown in Fig. 5.21. When the resonator is covered with certain type of analyte which is absorptive around the resonance wavelength, the molecules of analyte will interact with the evanescent field of the resonant mode, leading to optical cavity quality factor decrease and a change of the resonant peak extinction ratio. Also, with different mixture of different analyte, the alternation of effective mode index will lead to a shift of the optical resonance of the cavity. Therefore, both the change of dielectric constant and optical absorbing coefficient of the analyte could be quantified. In the absence of optically absorbing analyte, the resonator's resonant wavelength wavelength λ, quality factor (Q) and extinction ratio (ER, given in dB) are given by:

$$\lambda_0 = \frac{L}{N n_{\text{eff}}} \tag{5.9}$$

$$ER = 2\log\left(\frac{\sqrt{\sigma}-\sqrt{1-K}}{1-\sqrt{\sigma(1-K)}}\right) \tag{5.10}$$

$$Q = \frac{2\pi n_g L}{\lambda_0(\alpha L + K)} \tag{5.11}$$

$$\sigma = \exp(-\alpha L) \tag{5.12}$$

Here, λ_0 is the optical resonance wavelength, L denotes the cavity round-trip length, n_{eff} and n_{g} represents the effective and group indices of the resonant mode

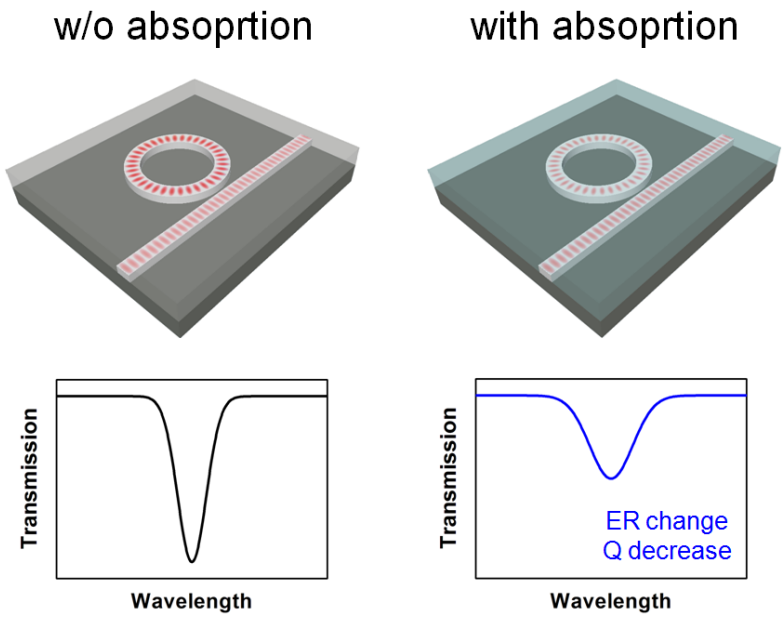

Figure 5.21 *Operation schematic of on-chip cavity-enhanced absorption spectroscopy: when optically absorptive analyte was covered onto optical cavity and interact with the evanescent field of the resonant mode, the excess optical loss leads to a quality factor decrease and extinction ratio change.*

respectively, N gives the azimuthal resonant mode order, K is the power coupling coefficient from the bus waveguide to the resonator, α is the total waveguide loss in the resonator, and σ corresponds to the round-trip power circulation coefficient. The unknown parameters include α, σ and K which can be determined by using equations (5.10)~(5.12) from the measured ER and Q values. Among other parameters, n_g can be calculated from the resonator's free spectral range (FSR) by using Eq.(2.16), and λ_0, ER, and Q can be fitted from the measured transmission spectrum. The total waveguide linear propagation loss α is given by the measured parameters as:

$$\alpha = \frac{2}{L}\ln\left(\frac{\sqrt{T_{\min}} - \sqrt{1-K}}{\sqrt{T_{\min}(1-\mathrm{K})} - 1}\right) \tag{5.13}$$

where $T_{\min} = 10^{-ER/10}$ is the transmission at the resonance frequency. The absorption loss induced by the analyte thus can be calculated from Eq. (5.13) by comparing the resonant peak *ER* before and after the introduction of analyte. Note that while Q factor is also modified by analyte absorption, the uncertainty is much larger when extracting the Q values from a Lorentz function fit of the resonance peaks. In contrast, using the measured ER value and Eq. (5.13) gives more reliable and consistent result of the total waveguide loss.

During the real spectroscopic sensing experiment, the analyte was first dissolved in certain type of solvent and then applied on top of the whole mid-infrared silicon photonic resonator, therefore, the total waveguide loss α is mainly attributed to three factors:

$$\alpha = \alpha_{\mathrm{wg}} + \Gamma\alpha_{\mathrm{s}}(1-c) + \Gamma\alpha_{\mathrm{a}}c = (\alpha_{\mathrm{wg}} + \Gamma\alpha_{\mathrm{s}}) + \Gamma\left(\alpha_{\mathrm{a}} - \alpha_{\mathrm{s}}\right)c \tag{5.14}$$

where α_{wg} is the intrinsic loss of the waveguide, α_{s} and α_{a} are the absorption coefficients of solvent, and the analyte, respectively, and c is the volume ratio of the analyte to solvent, and Γ denotes the optical confinement factor in the sensing region (i.e. the portion of mode field intensity outside of the waveguide and in the solution). From equation (5.14), it can be seen that the differential optical absorption coefficient $\Delta\alpha = \alpha_{\mathrm{a}} - \alpha_{\mathrm{s}}$ can be determined from the slope of the measured absorption vs. concentration curve ($\partial\alpha/\partial c$). The linear dependence of optical absorption on the analyte

concentration was experimentally validated through both FTIR spectroscopy and on-chip resonator measurements. The absorption coefficient of the analyte can subsequently be obtained by adding the known solvent absorption coefficient α_s to the differential optical absorption coefficient $\Delta\alpha = \alpha_a - \alpha_s$.

Besides the absorption coefficient, the refractive index change induced by solution in our dual-mode sensing demonstration can be independently evaluated from the measured resonant wavelength shift via

$$\Delta n = \frac{n_g}{\Gamma \lambda} \Delta\lambda \tag{5.15}$$

Since the change of the solution's refractive index when the analyte chemicals are added to the solvent is relatively small during our experiments (Δn<0.03*)*, the coupling coefficient *K* is assumed to be constant.

5.5.2 Mid-Infrared Spectroscopic Sensing of Single Analyte

In order to realize spectroscopic sensing, we change the radius size of one ring resonator so that its resonance will have a π phase difference with the other ring resonator around 5.2μm. Such design will make the optical resonances of these two ring resonators distribute evenly with each other along the working wavelength of the quantum cascade laser. The optical image and transmission spectrum of the modified device is shown in Fig. 5.22. As shown in Fig. 5.22a, the two sets of optical resonances are distributed uniformly along the scanning wavelength. However, there are still several discrete dips which are resulted from the existence of water vapor and other contaminations as

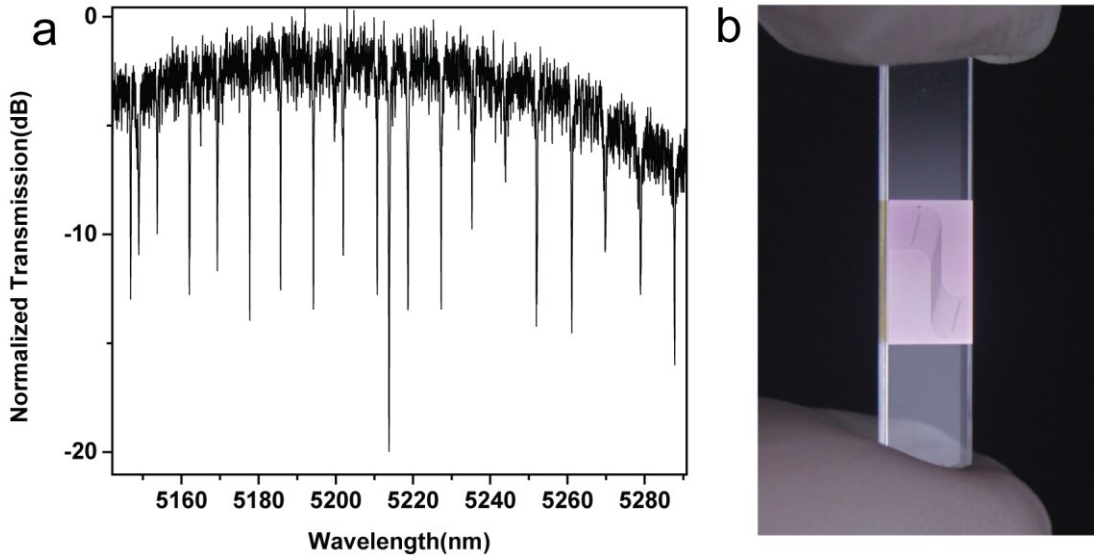

Figure 5.22 *(a)Transmission spectrum and (b) optical image of the newly designed mid-infrared silicon-on-CaF_2 ring resonators with evenly distributed optical resonances.*

mentioned before. The silicon-on-CaF_2 device could be utilized for spectroscopic sensing for both gas phase and liquid phase analyte at mid-infrared wavelength range. As a demonstration, a liquid phase analyte spectroscopic sensing platform has been realized. The chemicals utilized for the detection scheme are IPA, ethanol and toluene, the base solution is cyclohexane. The FTIR spectrums of each chemical are shown in Fig. 5.23, from which, the reason for choosing cyclohexane as the base solution could be easily told since no unique absorption peak exists along the QCL's working wavelength.

In order to screen out the discrete absorption dips caused by water vapor and other contaminations, reference waveguides without ring resonators have also been patterned on the new device, whose transmission spectrum could be seen in Fig. 5.24. With such reference transmission spectrum, all the unnecessary signals could be eliminated. In order

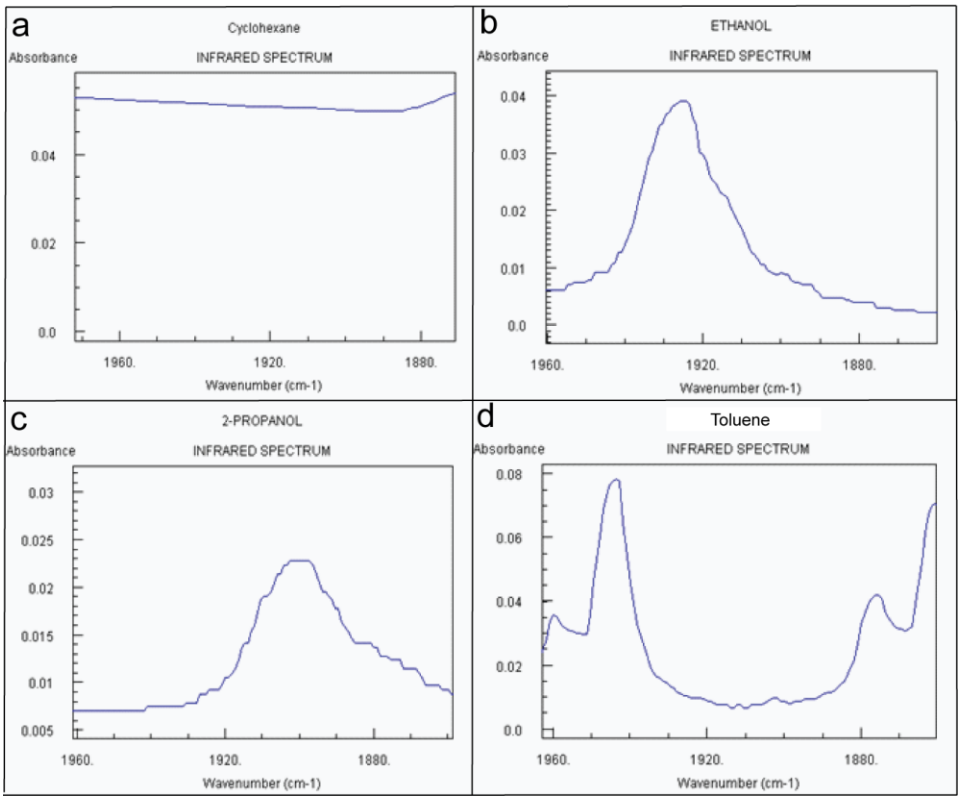

Figure 5.23 *FTIR absorption spectrum of (a) cyclohexane, (b) ethanol, (c) IPA, (d) toluene.*

to do so, the raw transmission spectra from the mid-infrared measurement (when the device is immersed into cyclohexane) is first normalized to cancel out the wavelength dependence of quantum cascade laser output power and laser-waveguide coupling efficiency. Fig. 5.24a and Fig. 5.24b are the measured transmission spectra from a reference waveguide (without resonators) and a micro-ring resonator in pure cyclohexane. Since the refractive index of cyclohexane is 1.42 at 5.2μm wavelength, the solvent itself will perform as a index matching layer which could dramatically increase the coupling efficiency between the mid-infrared fiber and the inversely tapered silicon waveguide up to 10 times. The normalization is executed by dividing the spectrum in Fig.5.24b with the

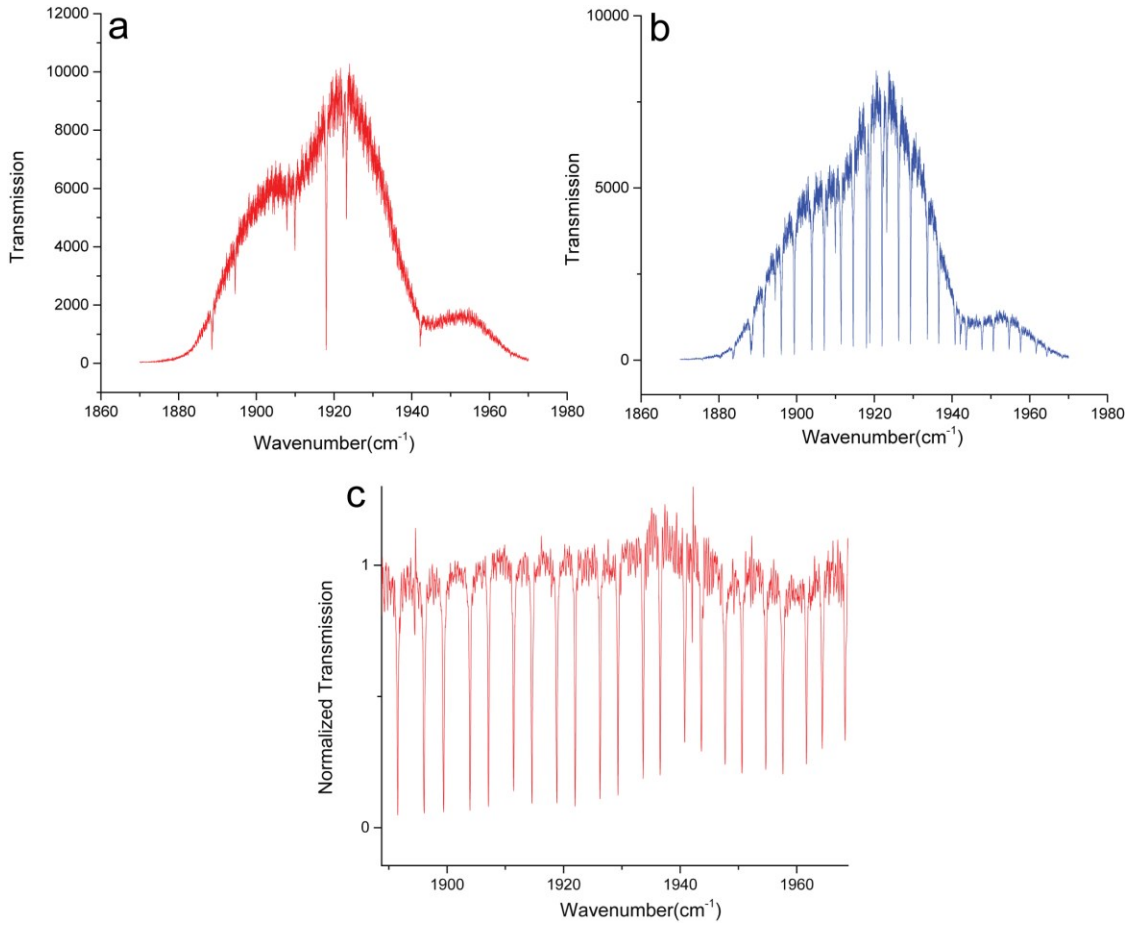

Figure 5.24 *Transmission spectra of (a) a stand-alone silicon waveguide and (b) a silicon waveguide coupled with ring resonator in pure cyclohexane; (c) normalized transmission of the micro-ring resonator in pure cyclohexane.*

one in Fig. 5.24a. An example of the normalized transmittance of the ring resonator is shown in Fig. 5.24c.

In the measurement, the micro-ring resonator is first immersed into a mixture solution of cyclohexane and IPA with different ratios from 0:1 to 0.4:1, the transmission spectrums are shown below in Fig. 5.25. Without normalization, it may be difficult to tell the difference of the transmittance between different concentrations of IPA. Therefore,

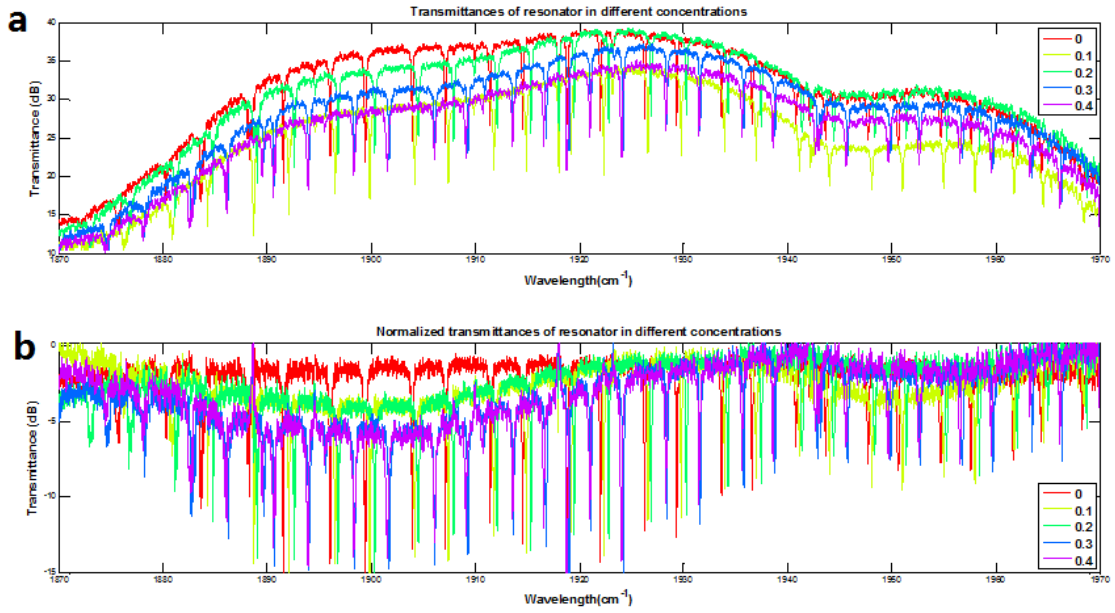

Figure 5.25 *(a) Raw and (b) normalized transmission spectrum of the MIR-SiNM rib waveguide immersed in mixtures of Cyclohexane and IPA with a ratio from 0:1 to 0.4:1.*

we normalize all the transmittance by using the method mentioned above and the results are shown in Fig. 5.25b. Obviously, the higher concentration of IPA in the mixture, the lower transmittance around 1900(cm^{-1}) wave number it will be, which is in good accordance with the FTIR absorption spectrum of IPA as shown in Fig. 5.23c. Besides the change of the transmittance, due to the change of refractive index of the mixture, the optical resonance also gradually blue shifted since IPA (n=1.38) has a smaller refractive index than cyclohexane. Same measurement has also been done for the other two analytes which are ethanol and toluene, the result of which could be seen from Fig. 5.26 and Fig. 5.27. Both of these two sets of measurements agree quite well with the trend of the FTIR absorption spectrum of the according chemicals. Since ethanol also has a refractive

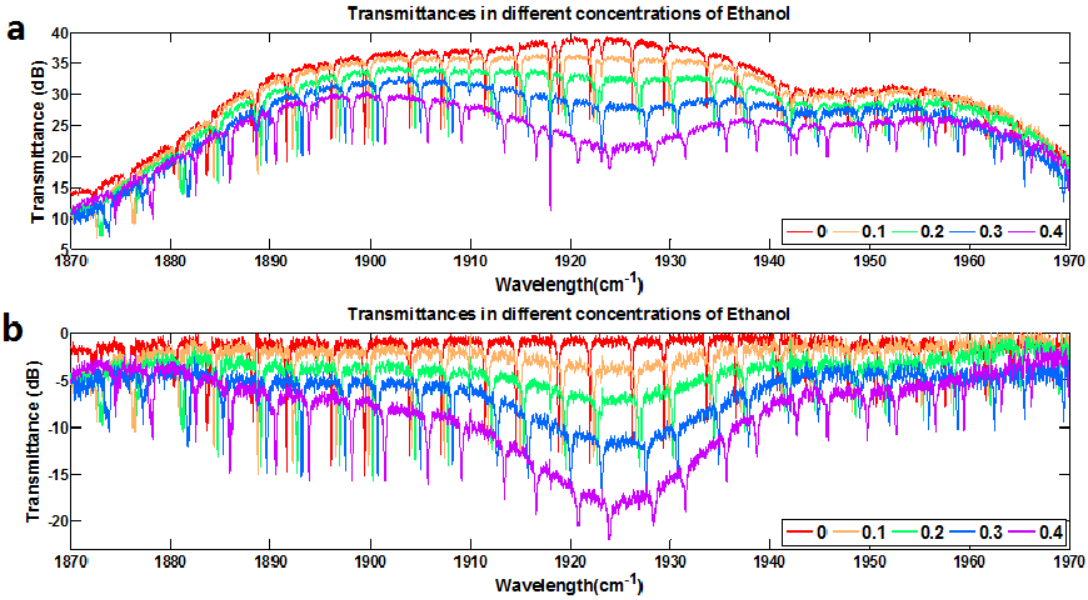

Figure 5.26 *(a) Raw and (b) normalized transmission spectrum of the MIR-SiNM rib waveguide immersed in mixtures of Cyclohexane and ethanol with a ratio from 0:1 to 0.4:1.*

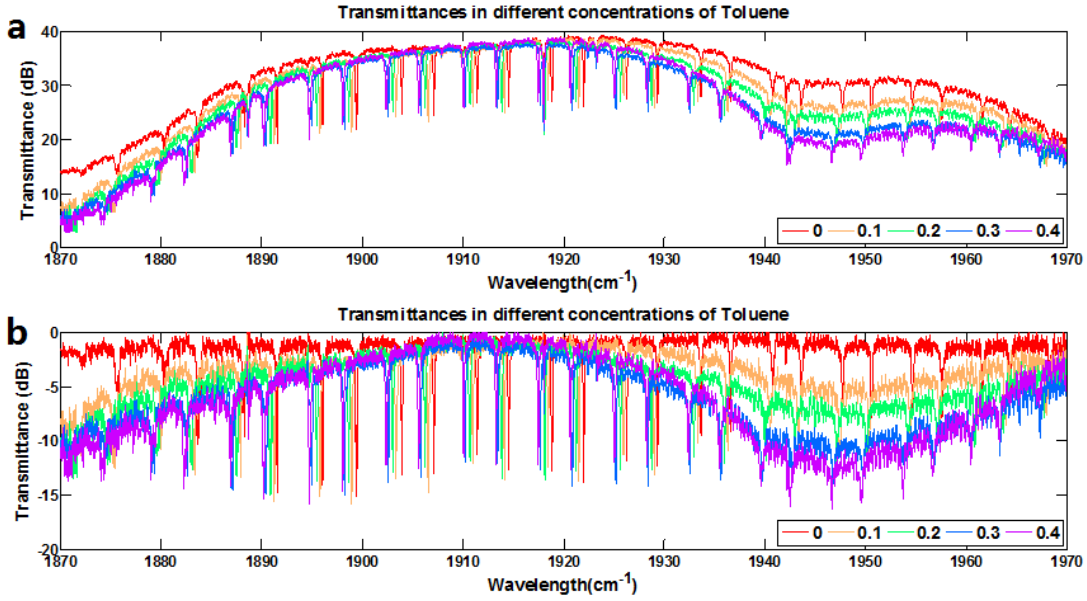

Figure 5.27 *(a) Raw and (b) normalized transmission spectrum of the MIR-SiNM rib waveguide immersed in mixtures of Cyclohexane and toluene with a ratio from 0:1 to 0.4:1.*

index (n=1.36) smaller than that of cyclohexane, with an increased mixture ratio of ethanol, the optical resonances will gradually shift to the shorter wavelength as well. However, the situation will be opposite for toluene because its refractive index (n=1.5) surpasses that of cyclohexane. The shift of optical resonance at specific wavelength (5191.4nm) with increasing concentration of either ethanol or toluene is shown in Fig. 5.28.

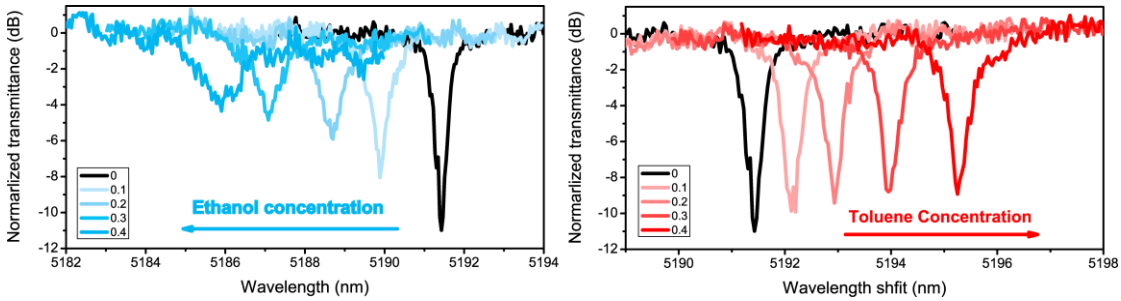

Figure 5.28 *Mid-Infrared optical transmission spectra of a silicon-on-CaF_2 micro-ring resonator in (a) ethanol/cyclohexane and (b) toluene/cyclohexane solutions of different concentrations. Decreasing quality factor and extinction ratio along with frequency shift of the resonance peak can be observed with increasing concentration of the analyte.*

With the alternation of the transmittance level and the shift of optical resonance, the change of both the dielectric constant and absorption could be derived. With these two parameters, such platform could be utilized to extinguish a wide range of mixtures, for example:

(1) Two chemicals with different absorption spectrum around mid infrared wavelength range and different refractive index.

(2) Two chemicals with similar absorption spectrum around mid-infrared wavelength but different refractive index.

(3) Two chemicals with different absorption spectrum around mid-infrared wavelength but similar refractive index.

(4) Mixtures of more than two chemicals, as long as their absorption spectrum and refractive index are known.

To obtain the excess optical loss in the micro-ring induced by the analyte chemicals, Lorentzian fitting was employed to fit the resonant peaks and to extract the resonant wavelength, quality factor and extinction ratio. The total propagation loss at the resonant wavelength is calculated by solving the equations (5.9)~(5.13). Excess optical absorptions induced by the analyte chemical was obtained by subtracting the waveguide loss in pure cyclohexane from the total propagation loss when the analytes were present, and normalized by the modal confinement factor (Γ) in the sensing region.

The on-chip resonator sensing mechanism is based on evanescent field interactions with the solutions. Fig. 5.29 shows the SEM cross-section of the silicon-on-CaF_2 rib waveguide used in the sensing experiments. The width of the waveguide is 1.8μm, the total height is 0.6μm, and the slab thickness is 0.12μm. Dimensions of the waveguides forming the ring resonators are identical to those of the bus waveguides. During the measurement, the entire chip surface was covered by the analyte solution, and the optical mode interacted with the target chemicals through evanescent field. Fig.5.29b shows the optical mode of the waveguide by using the FDTD simulation software, from which, the confinement factor was extracted, which is 0.17 [172]. The intensity of the

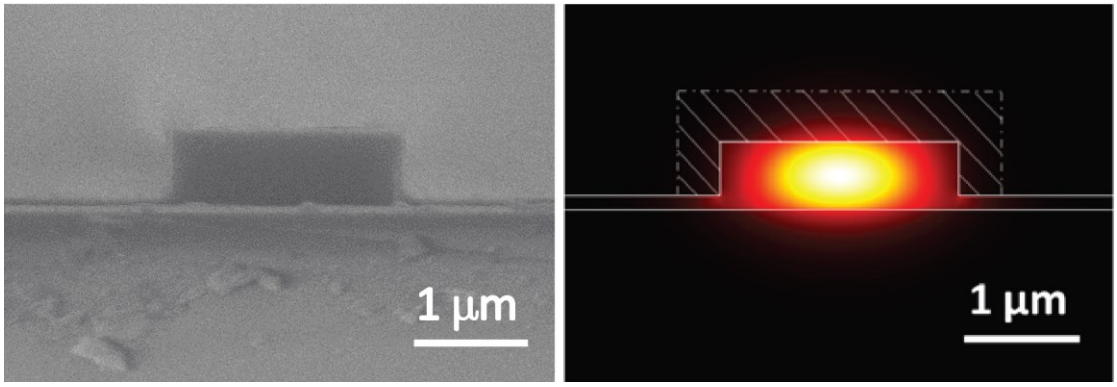

Figure 5.29 *(a) SEM cross-section of a Si waveguide on a CaF_2 substrate. (b) optical mode (intensity distribution) of the waveguide at 5.2 μm wavelength. The shaded area defines the sensing region A_{eva} where the majority of the evanescent field resides.*

evanescent field decreases exponentially away from the waveguide surface, and thus we define the effective sensing region A_{eva} as the area within one penetration depth of the evanescent field in the solution. The sensing region is represented by the shaded area around the waveguide core in Fig. 5.29b. The penetration depths are approximately 0.37 μm and 0.39 μm in the in-plane and out-of-plane directions, respectively. The total sensing volume V_{sen} of the ring resonator sensor is 0.6 pL, calculated using the equation:

$$V_{\text{sen}} = A_{\text{eva}} \times L \tag{5.16}$$

where L is the cavity length. Here we follow the definition by Wang et al. [173]. Based on the 3-σ criterion, the LOD in terms of mass loading is given by the product of the minimum detectable analyte volume with the analyte density:

$$\text{LOD}=\rho V_{\text{sen}} \times \frac{3\sigma}{\alpha} \tag{5.17}$$

where α is the peak absorption coefficient, and σ represents the measurement uncertainty. Table 5.2 below compares the key parameters of our resonator sensor with those of mid-IR waveguide evanescent sensors. The small sensing volume and the large modal confinement in the evanescent field underline the high detection sensitivity of our technology.

	Silver halide planar waveguide	**GaAs/$Al_{0.2}Ga_{0.8}As$ stripe waveguide (50 μm)**	**HgCdTe/CdZnTe planar waveguide**	**Si/CaF_2 ring resonator (our device)**
Modal confinement in the sensing region	N/A	>2.2%	~0.2%	17%
Penetration depth (d_p)	2 μm	0.6 μm	0.8 μm	0.4 μm
Beam waist (w)	N/A	50 μm	1 μm	1.8 μm
Coverage length (L)	10 mm	50 μm	3 mm	377 μm
Sensing volume (V_{sen})	1 μL	1.5 pL	1 nL	0.6 pL

Table 5.2 *Comparision with other mid-infrared sensing technology which include: silver halide planar waveguide*[196]*;* *$GaAs/Al_{0.2}Ga_{0.8}As$ stripe waveguide*[173] *and* HgCdTe/CdZnTe planar waveguide[197].

Fig. 5.28a shows the micro-ring transmission spectra when the device was immersed in ethanol/cylcohexane solutions of different concentrations, and Fig. 5.30b plots the excess optical absorption spectra of the ethanol derived using the methods mentioned earlier in this chapter. Transmission spectrum measurement is repeated 16 times for each concentration for statistical averaging. The differential optical absorption coefficient of the analyte (in this case, ethanol) at a particular wavelength was given by

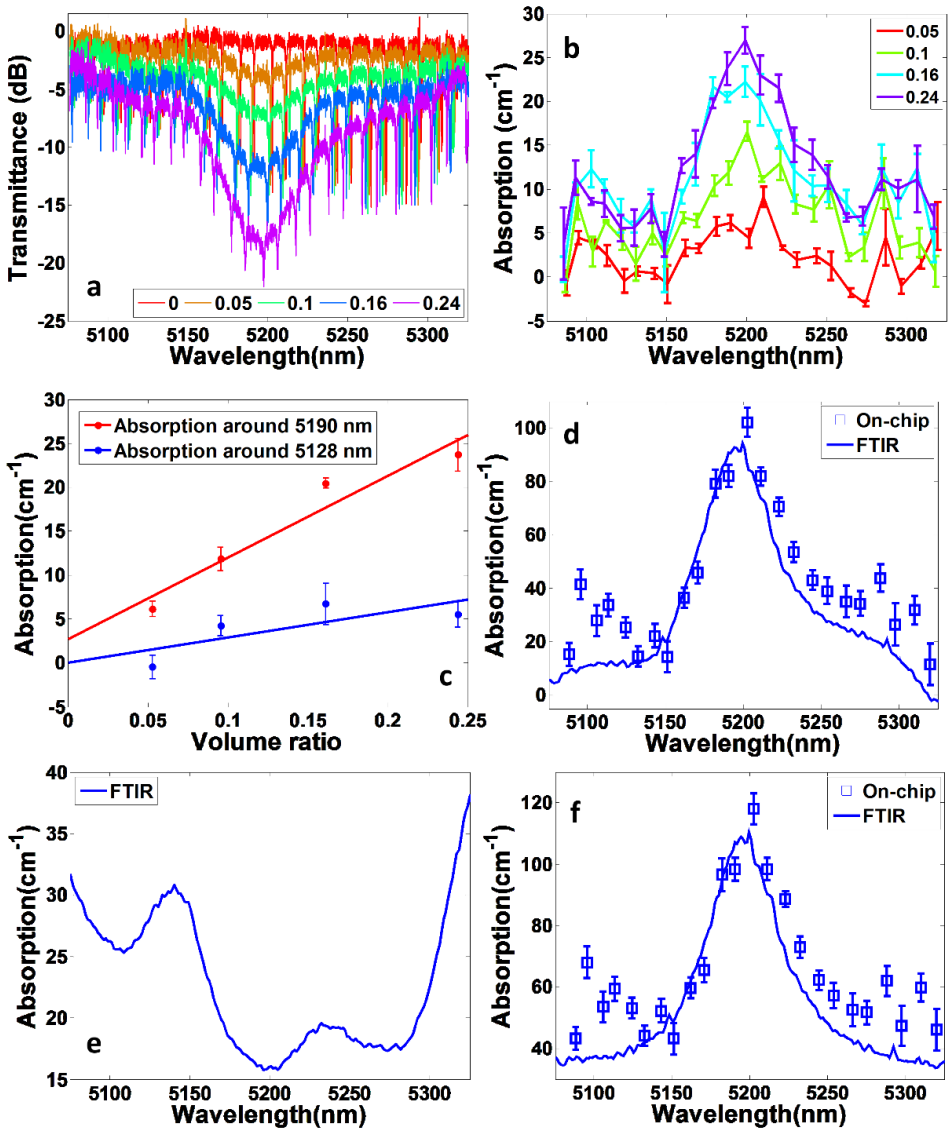

Figure 5.30 *(a) Normalized transmission spectra of ring resonator in ethanol/cyclohexane solutions of different concentrations; (b) excess absorption induced by ethanol; (c) linear fit of ethanol absorption as functions of ethanol volume ratio at two different wavelengths; (d) differential optical absorption coefficient of ethanol measured using our device (open square) and FTIR spectroscopy (solid line); (e) optical absorption coefficient of cyclohexane measured using FTIR spectroscopy; (f) optical absorption coefficient of ethanol measured using our device (open square) and FTIR spectroscopy (solid line).*

the slope of the chemical absorption *vs.* chemical volume ratio curve (Eq.(5.14)), as shown in Fig. 5.30c at two typical wavelengths. The optical absorption spectrum of ethanol was also independently quantified using a bench-top FTIR spectrophotometer. The absorption spectra of ethanol measured using our on-chip spectroscopy (open squares) and FTIR (solid line) are both plotted in Fig. 5.30d for comparison. As shown in the plot, the results from the two methods agree very well with each other. The relatively large deviation around 5100nm and 5300nm wavelength is attributed from the instability of the QCL at the boundaries of its scanning wavelength range. Lastly, absorption coefficient of the analyte (α_a) was obtained by summing the differential optical absorption coefficient of the solute (α_a-α_s) and the absorption coefficient of pure cyclohexane (α_s) measured with FTIR. Fig. 5.30e plots the absorption coefficient of pure cyclohexane measured using FTIR, and Fig. 5.30f gives the absorption coefficient of ethanol by using both on-chip spectroscopy (open-squares) method and FTIR (solid line) method, which agrees with each other quite well as well.

The same analysis method has also been applied for the measurement results of the other two chemicals: IPA and toluene. The comparison of the on-chip measurement results (open squares) and the FTIR measurement results for these two solutes are shown in Fig. 5.31s, from which, good agreement could be seen as well. The small mode volume of the micro-ring cavity further suggest a low detection limit of the technique down to 0.05ng for ethanol, 0.06ng for toluene, and 0.09ng for IPA by using equation (5.17). Also, due to the limitation of our mid-infrared laser, the measurement wavelength (around 5.2μm) in our measurement and experiments does not align with the major

absorption

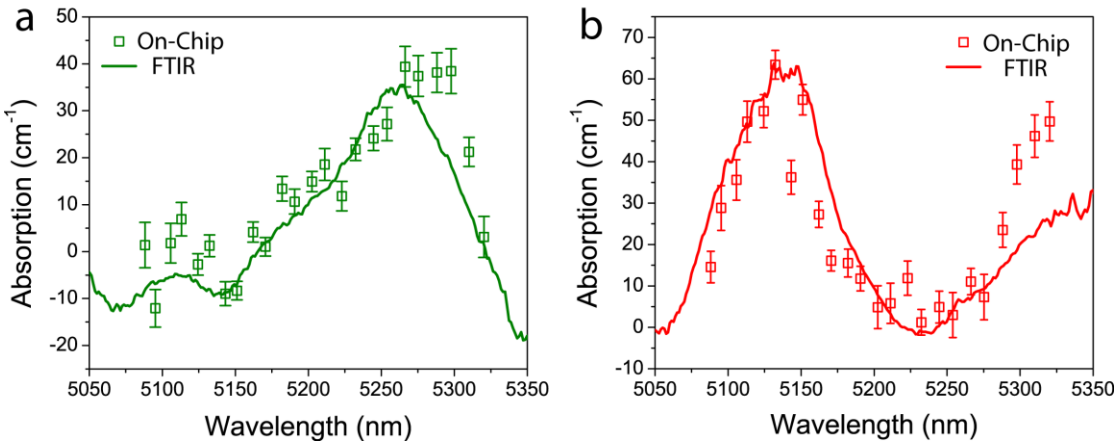

Figure 5.31 *(a) optical absorption coefficient of ethanol measured using on-chip cavity-enhanced method (open square) and FTIR spectroscopy (solid line). (b) Optical absorption coefficient of ethanol measured using our device (open square) and FTIR spectroscopy (solid line).*

peaks of the tested analytes. For example, assuming identical device optical performance and using a proper mid-infrared laser source, and LOD down to 1 pg, in principle, is expected simply by shifting the operating wavelength to 3.4μm, where the absorption of ethanol peaks is 50 times stronger than that at 5.2μm. The achieved high sensitivity of the cavity-enhanced detection method is attributed to the large mode confinement in the solution, the small device footprint and the high quality factor of the fabricated micro-ring resonator.

5.5.3 Mid-Infrared Spectroscopic Sensing of Multiple Analytes

The unique cavity enhanced mid-infrared spectroscopic measurement system could provide information of both the change of refractive index (real part of the complex

refractive index $\tilde{i}$) and the change of absorption (imaginary part of the complex refractive index) of the solutions in one measurement. Utilizing this capability, the method is capable to identify chemicals mixtures as long as their signature absorption and dispertion properties in the mid-infrared spectral region is known. The absorption coefficient (α) and the change of the refractive index (Δn) forms a parameter set that can be used to identify and quantify the concentration of a chemical. Here we described the method to quantitatively determine the chemical composition of a two-component mixture (ethanol and toluene in cyclohexane) using the measured values of the absorption coefficient and the refractive index change of the mixture solutions.

(a) Mean Value Calculation

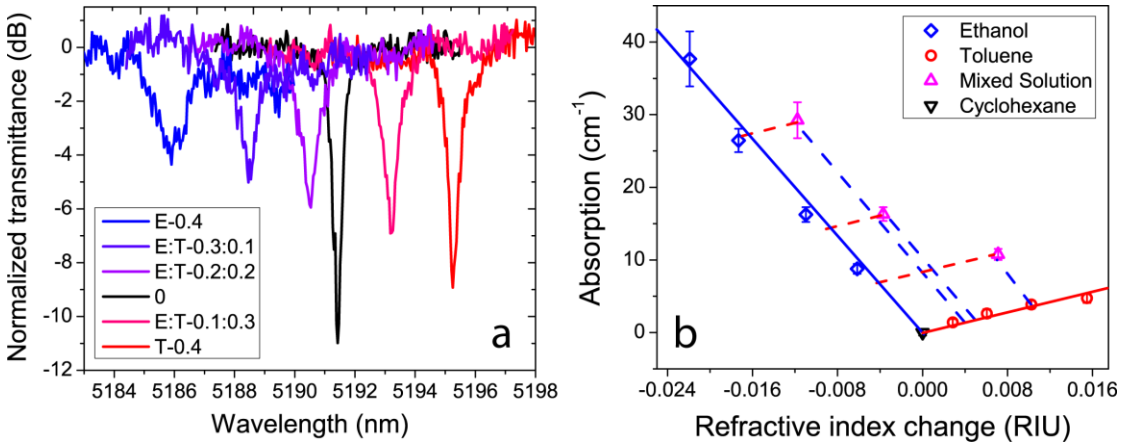

Figure 5.32 *(a) Transmission spectra measured from a microring immersed in mixture of ethanol and toluene in cyclohexane with varying concentration ratios as marked on the curves. (b) From the measured extinction ratio and resonance peak shift in (a), the absorption coefficient and refractive index change of the mixture (magenta, open triangles) are derived and plotted, along with results from calibration samples (ethanol, blue, open diamonds; toluene, red, open circles; blank solvent, black, open triangle).*

The measurement results are shown in Fig. 5.32. As we can see, with decreasing volume ratio of ethanol to toluene, the optical resonance changes from blue-shifted to red-shifted, which represents an increase of the refractive index of the mixture.

Firstly, two sets of (α, Δn) were collected by measuring solutions of only ethanol or toluene of different concentrations (c) in cyclohexane. The results in Fig. 5.32b of the main text show that the dependence of the parameter set (α, Δn) on concentration are linear and distinct for ethanol and toluene. It implies a simple linear transformation can project (α, Δn) to the concentration of the two chemicals in a mixture (c_e, c_t), where c_e and c_t are the concentration of ethanol and toluene respectively:

$$\begin{bmatrix} A & B \\ C & D \end{bmatrix} \begin{bmatrix} \Delta n \\ \Delta \alpha \end{bmatrix} = \begin{bmatrix} c_e \\ c_t \end{bmatrix} \tag{5.18}$$

In order to obtain the values of the elements (A, B, C, D) of the transformation matrix, measurement was done to calibrated the system using solutions with ethanol or toluene only, i.e. samples with (c_{e1}, c_{t1}=0) and (c_{e2}=0, c_{t2}), and the measured results are (α_{e1}, Δn_{e1}), (α_{t2}, Δn_{t2}). So the transformation of Eq. (5.18) leads to:

$$\begin{aligned} A \times \Delta n_{e1} + B \times \alpha_{e1} &= c_{e1} \\ C \times \Delta n_{e1} + D \times \alpha_{e1} &= c_{t1} = 0 \\ A \times \Delta n_{t2} + B \times \alpha_{t2} &= c_{e2} = 0 \\ C \times \Delta n_{t2} + D \times \alpha_{t2} &= c_{t2} \end{aligned} \tag{5.19}$$

Measurement was conducted on four pairs of samples of ethanol or toluene solutions with concentration c_{e1} and c_{t2} in each. Thus four sets of transformation matrix (A, B, C, D) were obtained by solving linear equations (5.19). Then, the mean value of the transformation matrix was calculated:

$$\begin{bmatrix} \overline{A} & \overline{B} \\ \overline{C} & \overline{D} \end{bmatrix} = \begin{bmatrix} \frac{1}{4}\sum_{k=1}^{4} A_k & \frac{1}{4}\sum_{k=1}^{4} B_k \\ \frac{1}{4}\sum_{k=1}^{4} C_k & \frac{1}{4}\sum_{k=1}^{4} D_k \end{bmatrix} \tag{5.20}$$

through which, the mean value of epsilon change caused by a specific mixture could be projected into the mean concentration of each chemical, which is ethanol and toluene here. And equation (5.18) could be rewritten into equation (5.21) as described below:

$$\begin{bmatrix} \overline{A} & \overline{B} \\ \overline{C} & \overline{D} \end{bmatrix} \begin{bmatrix} \overline{\Delta n} \\ \overline{\Delta \alpha} \end{bmatrix} = \begin{bmatrix} \overline{c_e} \\ \overline{c_t} \end{bmatrix} \tag{5.21}$$

By applying the measurement results from only toluene and ethanol at four different concentrations, which is shown in table 5.3, through equation (5.18) to (5.20), the mean value of each element of the transformation matrix could be obtained as shown in table 5.4 below:

pure ethanol ratio	pure toluene ratio	RIU(ethanol)	Absorption (ethanol)	RIU(toluene)	Absorption (toluene)
0.047801	0.074371	-0.00165	8.77012(dB)	0.00284	1.3841
0.087603	0.115456	-0.01099	16.24191(dB)	0.00604	2.62154
0.126003	0.181226	-0.01731	26.44745(dB)	0.01024	3.85452
0.214678	0.231181	-0.02191	37.6677(dB)	0.01548	4.73257

Table 5.3 *Measurement values of RIU and absorption at four different concentrations of solely ethanol or toluene*

$\overline{A}$	$\overline{B}$	$\overline{C}$	$\overline{D}$
-2.99022	0.00583	15.1967	0.01073

Table 5.4 *Mean values of the transformation matrix*

By plugging the values from Table. 5.4 into equation (5.21), the projected values of the concentration of each component in a mixture with known caused epsilon change could be obtained, as shown in Table. 5.5 below:

	RIU	Absor--ption	expected ethanol concentration	calculated ethanol concentration	expected toluene concentration	calculated toluene concentration
mixture 1	0.0061	9.83115 (dB)	0.04216	0.03908	0.15432	0.1482
mixture 2	-0.00434	14.89019 (dB)	0.09782	0.09979	0.09632	0.09382
mixture 3	-0.01421	23.18085 (dB)	0.17352	0.1776	0.03711	0.03279

Table 5.5 *Measurement RIU and absorption change of three different mixtures and the calculated concentration of each component.*

(b) Standard Deviation Calculation

To calculate the standard deviation of the projected concentration of chemicals, two standard rules should be strictly followed during all the calculation processes from Equation (5.18) to Equation (5.20):

(1) Addition and subtraction rule of values with standard deviation, which is if:

$$\begin{aligned} Total &= A + B - C - D \\ S_{Total} &= (S_A^2 + S_B^2 + S_C^2 + S_D^2)^{0.5} \end{aligned} \tag{5.22}$$

S_{Total} represent the standard deviation of the result and S_A to S_D represents that of the terms.

(2) Multiplication and division rule of values with standard deviation, which is if:

$$
\begin{aligned}
&Total = A \times B \div C \div D \\
&\frac{S_{Total}}{Total} = (\left(\frac{S_A}{A}\right)^2 + \left(\frac{S_B}{B}\right)^2 + \left(\frac{S_C}{C}\right)^2 + \left(\frac{S_D}{D}\right)^2)^{0.5}
\end{aligned}
\tag{5.23}
$$

Assuming the initial standard deviation of elements from Equation (5.18) is $S_{\Delta n_{e1}}, S_{\Delta n_{t2}}, S_{\Delta \alpha_{e1}}, S_{\Delta \alpha_{t2}}, S_{\Delta c_{e1}}, S_{\Delta c_{t2}}$, since:

$$
\begin{aligned}
A &= \frac{c_{e1} \times \Delta \alpha_{t2}}{\Delta n_{e1} \times \Delta \alpha_{t2} - \Delta n_{t2} \times \Delta \alpha_{e1}} \\
B &= \frac{c_{e1} \times \Delta n_{t2}}{\Delta n_{t2} \times \Delta \alpha_{e1} - \Delta n_{e1} \times \Delta \alpha_{t2}} \\
C &= \frac{c_{t2} \times \Delta \alpha_{e1}}{\Delta n_{t2} \times \Delta \alpha_{e1} - \Delta n_{e1} \times \Delta \alpha_{t2}} \\
D &= \frac{c_{t2} \times \Delta n_{e1}}{\Delta n_{e1} \times \Delta \alpha_{t2} - \Delta n_{t2} \times \Delta \alpha_{e1}}
\end{aligned}
\tag{5.24}
$$

the standard deviation of A to D could be calculated by using equation (5.22) and (5.24), which is:

$$
\begin{aligned}
S_A &= \left(\left(\frac{S_{\Delta \alpha_{t2}}}{\Delta \alpha_{t2}} \right)^2 + \left(\frac{S_{c_{e1}}}{c_{e1}} \right)^2 + \frac{S_{\Delta \alpha_{t2}}^2 \times \Delta {n_{e1}}^2 + S_{\Delta \alpha_{e1}}^2 \times \Delta {n_{t2}}^2}{(\Delta n_{e1} \times \Delta \alpha_{t2} - \Delta n_{t2} \times \Delta \alpha_{e1})^2} \right)^{0.5} \times A \\
S_B &= \left(\left(\frac{S_{\Delta n_{t2}}}{\Delta n_{t2}} \right)^2 + \left(\frac{S_{c_{e1}}}{c_{e1}} \right)^2 + \frac{S_{\Delta \alpha_{t2}}^2 \times \Delta {n_{e1}}^2 + S_{\Delta \alpha_{e1}}^2 \times \Delta {n_{t2}}^2}{(\Delta n_{e1} \times \Delta \alpha_{t2} - \Delta n_{t2} \times \Delta \alpha_{e1})^2} \right)^{0.5} \times B \\
S_C &= \left(\left(\frac{S_{\Delta \alpha_{e1}}}{\Delta \alpha_{e1}} \right)^2 + \left(\frac{S_{c_{t2}}}{c_{t2}} \right)^2 + \frac{S_{\Delta \alpha_{t2}}^2 \times \Delta {n_{e1}}^2 + S_{\Delta \alpha_{e1}}^2 \times \Delta {n_{t2}}^2}{(\Delta n_{e1} \times \Delta \alpha_{t2} - \Delta n_{t2} \times \Delta \alpha_{e1})^2} \right)^{0.5} \times C \\
S_D &= \left(\left(\frac{S_{\Delta n_{e1}}}{\Delta n_{e1}} \right)^2 + \left(\frac{S_{c_{t2}}}{c_{t2}} \right)^2 + \frac{S_{\Delta \alpha_{t2}}^2 \times \Delta {n_{e1}}^2 + S_{\Delta \alpha_{e1}}^2 \times \Delta {n_{t2}}^2}{(\Delta n_{e1} \times \Delta \alpha_{t2} - \Delta n_{t2} \times \Delta \alpha_{e1})^2} \right)^{0.5} \times D
\end{aligned}
\tag{5.25}
$$

Then combine equation(5.25) and equation(5.20), the standard deviation for the mean value of A to D will be:

$$S_{\overline{A}} = \frac{\sqrt{\sum_{k=1}^{4} S_{A_k}^2}}{\sum_{k=1}^{4} A_k} \overline{A} \qquad (5.26)$$

$$\vdots$$

Finally, the standard deviation of the projected concentration value of each analyte could be obtained through combing equation (5.26) and equation (5.21), which should be:

$$\begin{aligned} S_{c_e} &= \left(\left(S_{\overline{A}} \times \overline{\Delta n} \right)^2 + \left(S_{\overline{\Delta n}} \times \overline{A} \right)^2 + \left(S_{\overline{B}} \times \overline{\Delta \alpha} \right)^2 + \left(S_{\overline{\Delta \alpha}} \times \overline{B} \right)^2 \right)^{0.5} \\ S_{c_i} &= \left(\left(S_{\overline{C}} \times \overline{\Delta n} \right)^2 + \left(S_{\overline{\Delta n}} \times \overline{C} \right)^2 + \left(S_{\overline{D}} \times \overline{\Delta \alpha} \right)^2 + \left(S_{\overline{\Delta \alpha}} \times \overline{D} \right)^2 \right)^{0.5} \end{aligned} \qquad (5.27)$$

The calculated standard deviation of the mean value of the transformation matrix $(\overline{A}, \overline{B}, \overline{C}, \overline{D})$ is listed below in Table 5.6:

$\overline{S_A}$	$\overline{S_B}$	$\overline{S_c}$	$\overline{S_D}$
0.37453	5.08E-4	1.0884	6.748E-4

Table 5.6 *Standard deviation of mean value of the transformation matrix*

Then by plugging the values from Table 5.6 into equation (5.27), the standard deviation of the projected concentration of each chemical component in the mixture could be obtained, which is shown below in Table. 5.7:

	S.D. of ethanol concentration	S.D. of toluene concentration
Mixture 1	0.00706	0.01261
Mixture 2	0.00963	0.01638
Mixture 3	0.01389	0.0244

Table 5.7 *Standard deviation of the concentrations of ethanol and toluene determined in the mixture samples.*

(c) Result

The reults from mixture samples after the transformation is shown in Fig. 5.33. It can be seen that the concentrations of the two chemical components are quite close to the

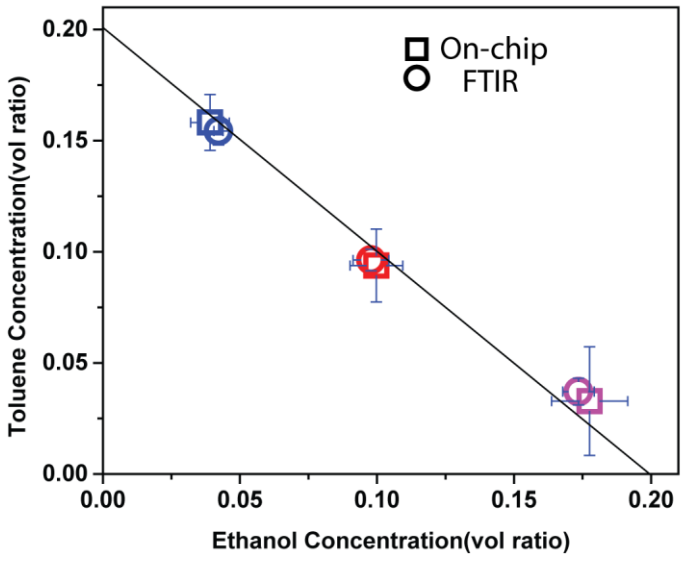

Figure 5.33 *After a linear transformation using a matrix determined through calibration, (α, Δn) can be converted to (c_e, c_t), the concentration of ethanol and toluene in the mixture (open squares), allowing the quantification of their values in a single measurement, in agreement with the nominal values (open circles) obtained by FTIR measurement.*

expected value with errors attributed to the evaporation during the measurement and uncertainties due to calibration inaccuracy. We thus conclude the on-chip cavity-enhanced mid-IR spectroscopy demonstrated here is promising to achieve chemical detection and quantitative analysis for a large variety of chemical species with many important applications.

5.6 Conclusion

In this chapter, by utilizing a modified transfer method, silicon based mid-infrared devices which include waveguides and ring resonators have been heterogeneously integrated on top of CaF2 substrates. Both strip structure and rib structure based photonic devices have been demonstrated. Without much optimization, the average loaded quality factor of the ring resonator based on each structure could already reach a benchmark value as 25000 and 50000, respectively. Besides, cavity-enhanced mid-infrared spectroscopic sensing of liquid phase chemicals has been demonstrated for the first time. As a demonstration, three different analyte which include IPA, toluene and methanol have been detected. Since our platform could detect the change of both dielectric constant and absorption, the concentration of each analyte in a mixture could also be quantitatively identified. A sets of experiments have been done with mixtures of ethanol and toluene with various volume ratio, the on-chip cavity enhanced spectroscopic sensing result agrees quite well with the FTIR measurement result, which proves the capability and reliability of our platform.

We also expect that the same approach can be readily applied to fabricate other novel mid-IR silicon photonic devices such as interferometers and photonic crystal cavities on CaF_2 substrates. The small mode volume of the photonic crystal cavity, coupled with the strong optical and thermal cavity nonlinearity, will enable ultrasensitive spectroscopic detection and analysis of chemicals in both gaseous and aqueous environments. We believe that this new method we have developed opens door to numerous possibilities of heterogeneous integration of silicon photonics with novel materials. In addition to mid-IR photonics, the method is also generically applicable to silicon photonic integration with other substrate materials with mechanical, electrical or optical properties non-native to silicon and confer unconventional functionalities on silicon photonic circuits. The examples of novel functions that can be potentially enabled by our technology include electro-optic modulation based on nonlinear crystals, flexible photonic integration on plastics, hybrid silicon-graphene photonics, and plasmonic enhancement using metals.

CHAPTER 6: NANOBEAM PHOTONIC CRYSTAL CAVITY BASED ULTRASENSITIVE CHEMICAL SENSOR

6.1 Overview of Chemical Sensor

6.1.1 Introduction of Chemical Sensor for Gaseous Analyte

With significant importance in the applications for industries and militaries, countless effort has been put into the research and optimization of gas phase chemical sensors. The basic principle of gas phase chemical sensor is to transduce the material property change caused by the absorption of certain analyte into a form of analyzable signal such as current or voltage. The sensitivity, selectivity and footprint of the chemical sensor largely depend on the mechanism of the signal transduction platform. Here, based on different sensing principles, we have sorted the gas phase chemical sensors into several categories listed below. Since later in this chapter, we are going to utilize a nanobeam photonic crystal cavity as the optical chemical sensor to detect the existence of gas phase Methyl Salicilate (MeS), in the overview we mainly focus on various chemical sensors designed for the purpose of detecting similar chemicals.

(a) Carbon Nanotube Based Gas Phase Chemical Sensor

By utilizing single-wall (carbon) nanotube (SWNT) electrode with hydrogen bonding polymer or molecular monolayer as the chemo-selective material [174], a type of chemicapacitor sensor has been successfully demonstrated. When the analyte was absorbed by the hydrogen bonding molecular monolayer, the capacitance change induced by the large electric field gradient of the SWNT will reflect the detectable concentration of the analyte.

When utilized to detect analyte similar to MeS, like DMMP (Dimethyl methylphosphonate), the LOD of the sensor functionalized with hydrogen bonding molecular monolayer is around 50ppb with a 90 percent signal recovery time of 4 seconds. The advantages of such type of devices include high sensitivity, fast response time and recovery time, reusability and relatively small footprint.

(b) Mechanical Oscillator Transducer Based Gas Phase Chemical Sensor

Utilizing surface functionalized mechanical oscillator as the transducer, a type of MEMS based gas phase chemical sensor has been developed. When any analyte was absorbed onto the surface of the oscillator, the oscillation frequency change will be used to determine the mass of analyte on the devices.

For detecting analyte similar to MeS, like DMMP, the LOD of the device by using 3-SAW(surface acoustic wave) array method is about 100ppb [175]. The advantages of such mechanical oscillator based gas phase chemical sensor include the capability to uniquely identify certain type of analyte without false alarm, achieve relatively high sensitivity and reusability. However, such device has long signal recovery time and large footprint.

(c) Chemicapacitor Based Gas Phase Chemical Sensor

Similar to the principle of SWNT based chemical sensor, a “chemicapacitor” sensor is based on a capacitor, which usually consists of a type of polymer. Such type of polymer will selectively absorb certain type of analyte, after which, its dielectric constant, hence the capacitance of the effective capacitor, will either increase or decrease.

Such change of capacitance will then be transduced into the change of current or voltage. Depending on the minimum detectable change of capacitance, the LOD will be decided.

For analyte similar to MeS, such like DMMP and DIMP (Diisopropyl methylphosphonate), by using parallel plate based chemicapacitor method, the LOD of the device is 2~3ppb [176]. The advantages of such type of gas phase chemical sensor include small energy consumption, reusability and high sensitivity. However, such type device also possesses a long recovery time and a relatively large footprint.

(d) Chemiresistor Based Gas Phase Chemical Sensor

Similar to chemicapacitor based gas phase chemical sensor, chemiresistor sensor also needs a functional layer which usually is a certain type of polymer. However, when absorbing the target analyte molecules, instead of presenting an alternation of its dielectric property, the resistance of the polymer will change.

No literature has ever reported the detection of MeS or similar analyte by using such type of chemical sensor. However, for detecting NO_2 and NH_3 gases, the LOD of a graphene based ultrasensitive chemiresistor sensor is 15ppb and 160ppb, respectively [177]. The advantages of such type of sensor are similar to that of chemicapacitor based gas phase chemical sensor, which include high sensitivity, reusability and small energy consumption. However, such type of device will be responsive to water vapor and become unusable after exposed to atmosphere for some time.

(e) Flexural Plate Wave (FPW) Based Gas Phase Chemical Sensor

Similar to mechanical oscillator based gas phase chemical sensor, the FPW based sensor will utilize the acoustic waves generated from a piezoelectric membrane material.

Compared to the SAW based devices, the active region on which the acoustic waves travel in the FPW device is a membrane whose thickness is much smaller than the acoustic wavelength. As a result, wave energy is present at both sides of the membrane and the entire membrane undergoes mechanical flexure. When certain type of analyte has been absorbed, the frequency shift of the FPW will be utilized to detect the concentration of the gas phase chemicals. With such flexural plate wave, in principle, a higher LOD should be achieved for such type of devices, compared with that of SAW based chemical sensor devices.

However, such type of device hasn't been utilized for the detection of MeS-like analyte. For water vapor, the reported LOD of the sensor is about 10ppb [178].

(f) Surface Plasma Resonance Based Gas Phase Chemical Sensor

By utilizing novel fabrication method, ultrasmall gap could be created between two metal antennas. With such structure, strong surface plasma resonance could be induced. With a functionalized surface of the antenna structure, the refractive index of the functional layer will change during the absorption process of the airborne analyte, which will be transduced to the shift of the surface plasma resonance frequency.

The state-of-the-art surface plasma resonance based gas phase chemical sensor could detect the change of refractive index as small as 2.45×10^{-4} RIU (refractive index unit) [179]. However, due to the low quality factor of the surface plasma resonance, such devices have a much lower LOD than that of other devices mentioned earlier in this chapter.

(g) Surface Enhanced Raman Scattering (SERS) Based Gas Phase Chemical Sensor

By utilizing the SERS effect, the airborne analyte which has been collected by the sensor could be identified qualitatively and quantitatively by using X-ray Raman Scattering (XRS) measurement.

Since the detection and the measurement are two separated procedures for SERS effect based gas phase chemical sensors, it requires that the binding of the airborne analyte with the substrate is an irreversible and permanent process, which will make such devices not reusable. The reported sensitivity for such devices is expressed in terms of detection limit time instead of limit of detection. For detecting benzenethiol, the detection limit time is about 6ppm/sec [180].

(h) Summary

The benchmark performance of these gas phase chemical sensors has been sorted and listed in Table 6.1 below. As we can see, the lowest LOD achieved for the detection of gaseous DMMP is about 2ppb, however, for MeS, this value is at least one order of magnitude larger [181].

With the fast development of high quality optical resonator, there is an emerging new type of high-performance chemical sensors which is called optical cavity based chemical sensor. We will briefly introduce such type of sensors in the next section and explain why we would like to choose such device as our sensing platform instead of conventional electrical- or mechanical- based devices.

Principle	LOD or LDT	Cons	Pros
Carbon Nanotube	50ppb (for DMMP)	High sensitivity, fast response time, reusability, relative small footprint	Not immune to electromagnetic disturbance, responsive to water vapor and multiple agents
Surface acoustic wave	100ppb (for DMMP)	Capability to uniquely identify certain type of analyte without false alarm by using 3-SAW array method, relatively high sensitivity, reusability	Not immune to electromagnetic disturbance, long recovery time, large footprint
Chemicapacitor	2ppb(for DMMP)	Small energy consumption, reusability, high sensitivity	Not immune to electromagnetic disturbance, long recovery time, relatively large footprint
Chemiresistor	15ppb(for NO_2)	Relatively high sensitivity, relatively small footprint, small energy consumption	Not immune to electromagnetic disturbance, long recovery time, responsive to water vapor, not reusable under certain circumstances.
Flexural Plate Wave	10ppb(for water vapor)	Similar to SAW based devices	Relatively large footprint, not immune to electromagnetic disturbance, not ultrahigh sensitivity.
Surface Plasma Resonance	2.45×10^{-4} RIU	Small footprint	Hard to make analyte interact with plasma resonator, low sensitivity, irreversible bonding of analyte to the substrate
SERS	6ppm/sec.(for benzenethiol)	Small footprint	Same as the surface plasma resonance based gas phase chemical sensors

Table 6.1 *Performance comparison of different type of gas phase chemical sensor.*

6.1.2 High-Q Cavity Based Optical Chemical Sensor

General optical sensors utilize a variety of signal transduction methods based on photonic attributes such as transmission, reflection, refractive index, polarization and absorption. Among all these mechanisms, the refractive index (RI) sensor, which include devices such as surface plasma resonance instruments (as mentioned in last section), diffraction gratings, optical fibers and resonant microcavities, has emerged as a promising tool for the detection of ultrasmall amount of analyte.

The basic principle of RI sensor is to detect the shift of resonance frequency induced by the change of effective refractive index which may attribute to the absorption of gaseous or fluidic analyte. The change of refractive index depends on the dielectric property of the analyte, which may not vary largely from device to device. Therefore, the sensitivity will be mainly decided by the FWHM of the optical resonance, or, in other words, the quality factor (Q) of the optical resonance. As the Q factor of a device increases, the photon lifetime increases, and the optical resonance linewidth will become narrower accordingly. Therefore, with the same effective refractive index change, the higher the quality factor, the higher transmission signal change could be obtained, which also means a higher LOD can be obtained. Therefore, that is the reason why ultrahigh Q optical cavity has been demonstrated already as chemical sensor with the capability to detect the existence of single molecule or single virus [182], [183]. Various different optical cavities have been utilized as the platform for ultra-sensitive optical chemical sensor, such as microsphere resonator [184], microtoroid resonator [185], microdisk resonator [186], microring resonator [187], microtube resonator [188] and photonic

crystal cavity resonator [189]. In order to compare the features of these optical resonators and their potentials as the platform for the purpose of ultrasensitive chemical sensing, we have listed the quality factor, CMOS compatibility and footprint of these structures in Table 6.2 below:

	Q factor	CMOS compatibility	footprint
Microsphere resonator	up to 2×10^6	not compatible	hundreds of micron in diameter
Microtoroid resonator	up to 1×10^8	not compatible	hundreds of micron in diameter
Microdisk resonator	up to 1×10^7(silica) 1×10^5(silicon)	not compatible(silica) compatible(silicon)	varies from tens of micron to hundreds of micron in diameter
Microring resonator	$\sim10^4$(silicon)	compatible(silicon)	varies from tens of micron to hundreds of micron in diameter
Photonic crystal cavity	$\sim10^4$(silicon)	compatible(silicon)	as small as 400nm by 10μm

Table 6.2 *Comparison of different optical cavities which have been utilized as optical chemical sensor*

In consideration of a combination of high quality factor, CMOS compatibility and small footprint, as we can see from Table 6.2 above, photonic crystal cavity will be the perfect choice. Among all the photonic crystal cavity structures, nanobeam photonic crystal cavity, which possesses the smallest footprint and relatively high quality factor will be specifically promising as the biosensing platform. And that is the reason why we would like to demonstrate a gas phase optical chemical sensor based on such photonic structure.

6.2 Fabrication Method and Measurement Setup

6.2.1 Fabrication Method

The pattern of the nanobeam photonic crystal cavity is defined by using Ebeam lithography first, and then transferred into the top silicon layer of the SOI wafer (220nm silicon/3000nm oxide) by using the RIE with a mixture of SF_6 and C_4F_8 gases. In order to realize selective and optimal chemi-absorption of specific types of analytes, the nanobeam surface needs to be chemically functionalized. As mentioned above, MeS, as a simulant of nerve agent gases, has important meaning to the homeland security applications and biomedical applications. Therefore, we specifically select a type of fluoroalcohol polysiloxanes polymer (Adiol, Seacoast Scientific Inc.) as the coating material for its strong and reversible bonding with MeS molecules. Meanwhile, such polymer possesses a high thermal stability and a strong adhesion with the silicon substrate. The polymer is used as purchased and dissolved in toluene to a concentration of 1mg/ml. The solution was then spin coated on the device substrate at 3000 rpm and the substrate was baked on a hotplate at 90 degree Celsius in ambient to evaporate the solvent. Such process resulted in a layer of polymer coating with a thickness in the range of 60-80 nm. The fabrication process flow is illustrated below in Fig.6.1. Since toluene is highly volatile and the polymer concentration is only 1mg/ml, therefore, the viscosity of the resulted solution is extremely low, to make sure an uniform coating of the device with the polymer, excess solution needs to be applied to the surface of the device during the spin coating process. Also, prior to the coating process, agitation is needed to achieve an uniform distribution of the polymer molecules inside the solution.

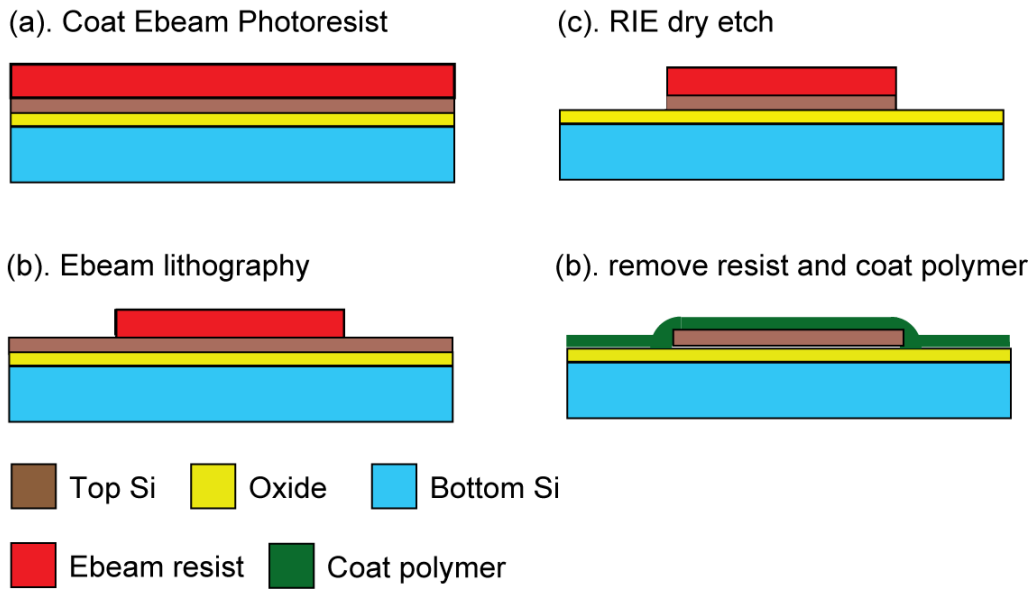

Figure 6.1 *Fabrication process flow for the nanobeam photonic crystal cavity.*

The optical and SEM image of the fabricated nanobeam photonic crystal is shown in Fig.6.2 a and b, respectively. As we can see, the nanobeam photonic crystal cavity is composed of two reflector sections and a L0 cavity. The reflector sections of the nanobeam cavity are designed with periodic structure of nine holes, etched all the way through the silicon layer, with periodicity 0.9α (α = 453.2nm); in addition, to precisely phase match the waveguide and Bloch modes, a linearly tapered section from the Bragg mirror section to the center of the cavity (from 0.5α to 0.395α) is designed with six holes, and also etched through the silicon layer; and finally, a bus waveguide is used to couple light by means of evanescent field into the nanobeam cavity.

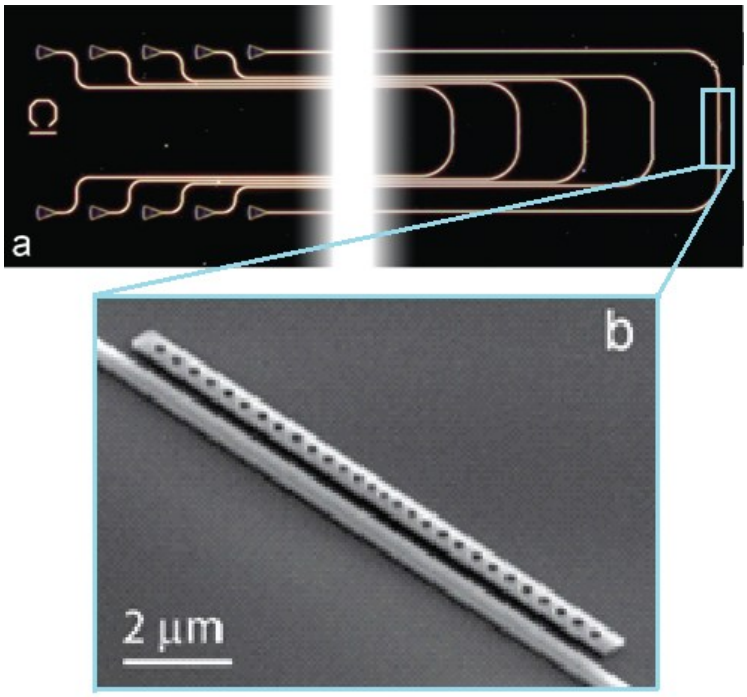

Figure 6.3 *(a) Optical image and (b) SEM image of the fabricated nanobeam photonic crystal cavity.*

6.2.2 Measurement Setup

The measurement setup needs to realize two purposes which are gas delivery with controllable analyte concentration and precise real-time optical performance measurement. The illustration of the measurement setup is shown in Fig. 6.3. The optical measurement part is exactly the same as what we use for the characterization of flexible telecomm silicon and silicon nitride based photonic devices which has been described in Chapter 4. For the gas delivery part, a gas standard generation system (Kin-Tek 491M) is utilized to generate gas flow with precise analyte concentration using dry nitrogen as the carrier gas. The mechanism of the standard gas delivery system is depicted in Fig. 6.3b,

the carrier gas was divided in two steams whose flow rate will be separately controlled by two MFCs (micro flow controllers). While one stream of carrier gas will pass through a heated chamber with a permeation tube with calibrated analyte emission rate, the other stream will combine with this one later and then be delivered to the sample. By controlling the ratio of these two streams of gas flow and a known emission rate of the permeation tube at certain temperature, the final concentration of the analyte that be delivered to the device could be precisely determined.

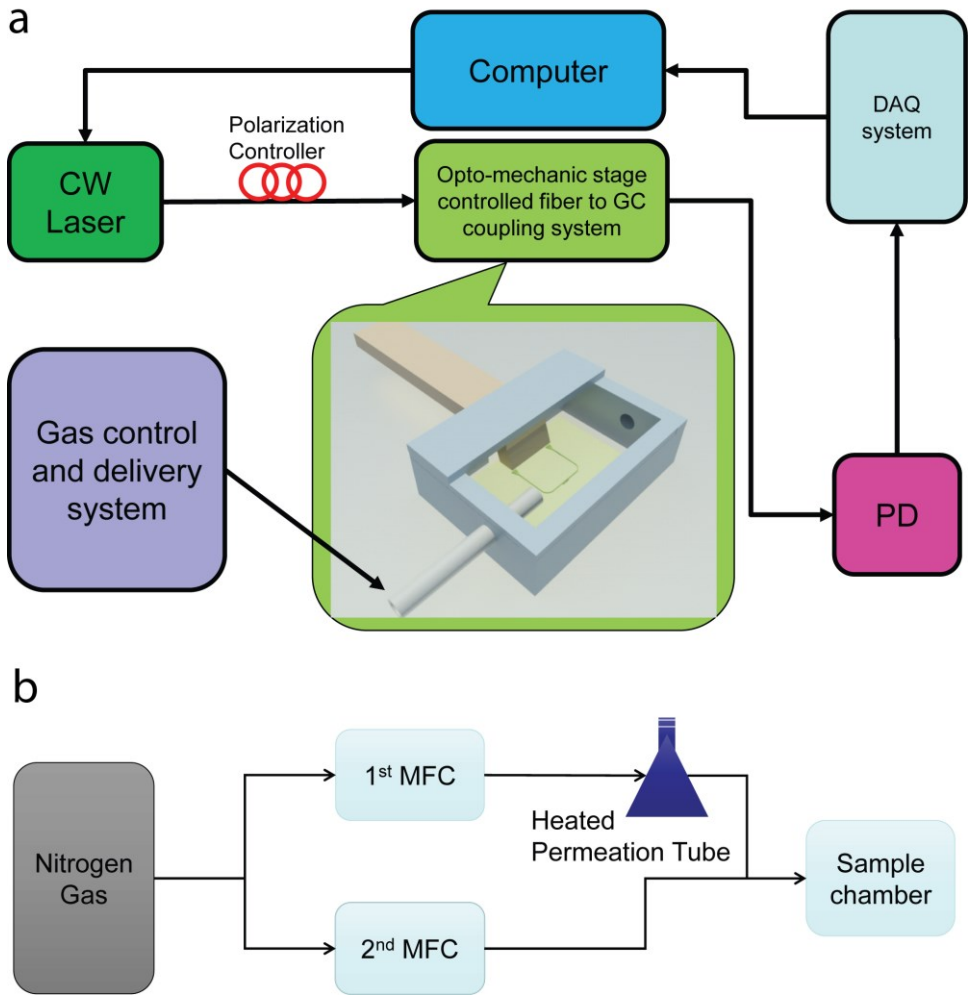

Figure 6.5 *(a) Measurement setup illustration. (b) Gas delivery system setup illustration.*

In order to well control the concentration of the analyte around the nanobeam photonic crystal cavity, a sealed chamber is constructed as shown in Fig. 6.3a. An inlet and outlet are designed at the two sides of the chamber separately, which to accomplish the gas delivery purpose and to maintain the concentration of the analyte inside the chamber.

6.3 MeS Sensing Experiments with Linear Optical Resonance

6.3.1 Measurement Protocols

In order to realize precise measurement of the existence of the gas phase chemicals, we firstly need to calculate the concentration of the analyte from the standard gas delivery system, which could be calculated by using equation (6.1) as shown below:

$$C = \frac{E * (22.4/M)}{F * 1000} \tag{6.1}$$

Where C denotes the concentration of the gas analyte in unit of ppm (parts per million), E is the emission rate of the permeation tube (at specific temperature) in unit of ng/min, M represents the molecular weight of the particular component compound in unit of g/mol, F is the dilution gas flow rate in unit of L/min at STP (standard temperature and pressure) condition. In our calculation of the analyte concentration, the value of E and M equals to 2034ng/min and 152g/mol, respectively.

The experiment is conducted with several steps:

(1) Turn on the nitrogen carrier gas flow without analyte for several minutes to make sure there is no chemical residue in the downstream of the gas delivery system.

(2) Wait for the permeation tube to be heated up to 100 degree Celsius, which is the calibrated temperature for the specific emission rate.

(3) Start to turn on the analyte gas flow and wait for the optical sensor to give relatively stable response signal, then turn off the analyte gas flow until the response signal recovers to its original value.

(4) Change the carrier gas flow rate but remain the analyte gas flow rate, which could lead to a change of the analyte concentration in the final output gas flow.

(5) Repeat step (3) and step (4).

During the optical measurement setup, we choose to use a probe laser measurement method. In order to get the highest response signal with the same amount of optical resonance shift, we need to slightly blue-detune the wavelength of the probe laser in reference to the wavelength of the optical resonance. The optical transmission spectrum of the nanobeam photonic crystal cavity prior to and after the application of the functional polymer layer is shown in Fig. 6.4a. A significant red shift of the transmission spectrum about 25nm could be clearly observed since the effective mode index has increased due to the introduction of the polymer. However, the quality factor of the device degrades from 50,000~80,000 to 5,000~8,000 after the application of the functional layer. Such significant drop in quality factors was attributed to optical absorption in the polymer layer. To improve the device performance, it is possible to

select polymers with low optical absorption at near-infrared range but high chemical selectivity with targeted analytes, although this is out of the discussion range of this dissertation. The optical resonance and the position of the probe laser is also shown in Fig. 6.4b, from which we can clearly see the probe laser is parked at the position with the highest slope value.

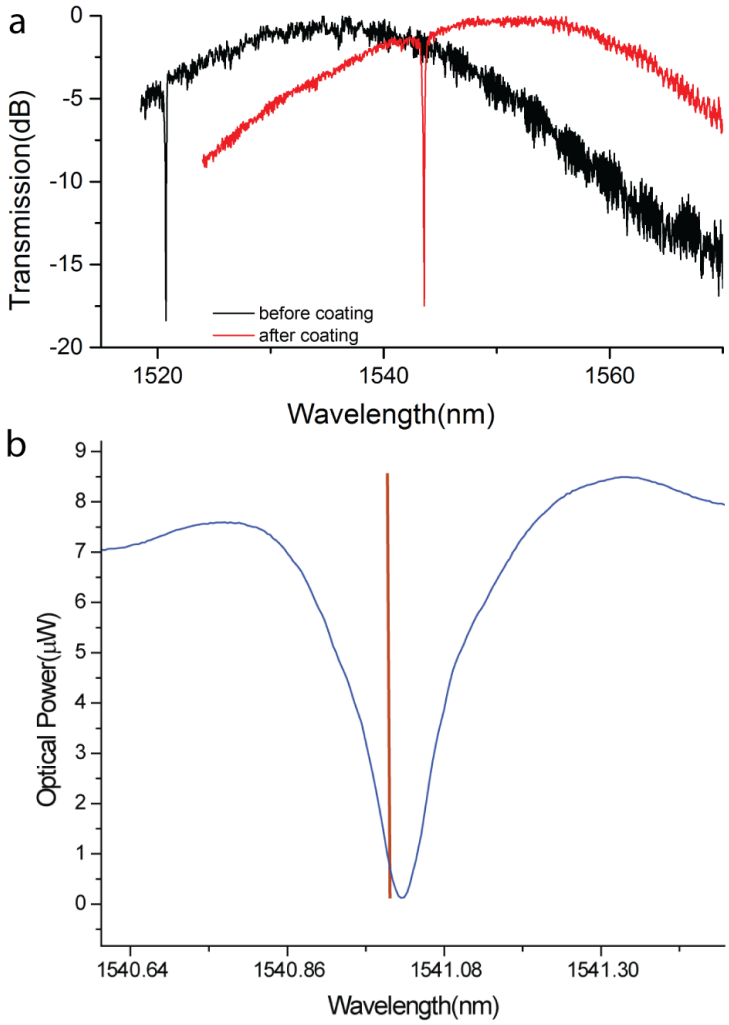

Figure 6.7 *(a) Transmission spectrum of the nanobeam cavity before (black line) and after (red line) the application of the Adiol polymer. (b) Probe laser is slightly blue-detuned to the optical resonance wavelength.*

Since silicon possesses a positive thermo-optic coefficient [190], when the heated gas flow is delivered onto the surface of the silicon device, the temperature change will also induce a red-shift of the optical resonance. In order to distinguish the refractive index change caused by the analyte absorption and the thermo-optic effect, a comparison experiment is needed, which simply contains two steps:

(1) Do a regular sensing measurement as described above from step (1) to step (3).

(2) Take out the permeation tube from the heated chamber and repeat step (1) to step (3).

The measurement result from the comparison experiment is shown below in Fig.6.5, the concentration of MeS that we utilize here is about 240 ppb (parts per billion). As we can see, the signal response difference with and without MeS analyte is more than 6 times, the response signal derived from the thermo-optic effect is around 3 times of the rms (root mean square) value of the system noise. However, we still like to screen out such effect since it will affect the later theoretical analysis. The strategy for realizing such purpose is actually pretty straightforward, we just increase the length of the tube between the outlet of the standard gas delivery system and the inlet of the sealed chamber, which may perform as a nature cooling system for the heated gas. Since the heated gas only occupy a very small portion among the total output gas flow, we only need to moderately increase the tube length by about 2 meters and the thermo-optic effect will no longer be observed.

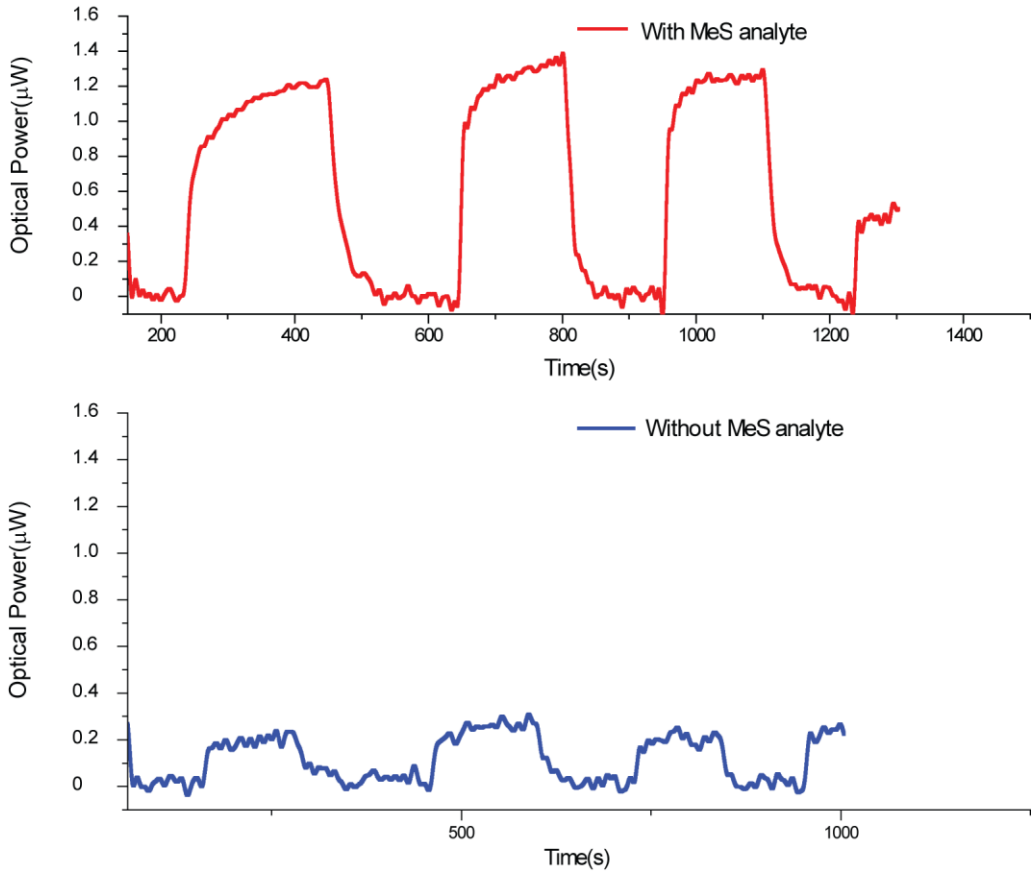

Figure 6.9 *Comparison sensing experiments with (red) and without (blue) MeS analyte while both deliver heated gas flow.*

6.3.2 Measurement Results and Theoretical Analysis

Because MeS has a dielectric constant larger than that of Adiol polymer, absorption fo MeS into the polymer caused an increase (red shift0 in the resonance wavelength of the surface functionalized nanobeam cavity. Therefore, upon exporsure to MeS analyte, the transmission of the blue-detuned probe laser will increase. Fig. 6.6 shows the optical transmittance change of the measured device when it is exposed to MeS

gas flow with varying concentration from 240 to 1200 ppb for 240 seconds to approach equilibrium state. During the experiment, the analyte gas flow rate is kept at a constant value of 50 sccm while the carrier gas flow rate was increased from 200 to 1200 sccm to gradually reduce the analyte concentration in the total flow during each test. It was confirmed in controlled experimental environment that changing the flow rate between such range with no analyte will only induce negligible response of the device.

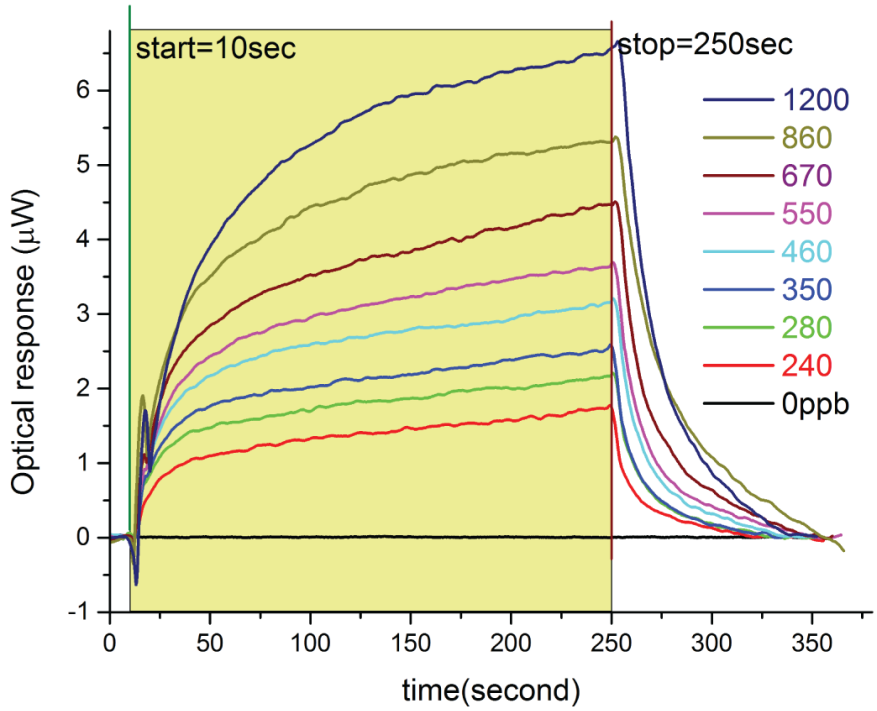

Figure 6.11 *The nanobeam cavity's optical response to 240 seconds exposure (shaded area in light green) of gas flow with varying volume concentrations of MeS, from low to high in eight steps respectively: 240, 280, 350, 460, 550, 670, 860, 1200 parts-per-billion. The black trace is the system noise measured without any gas flow.*

In order to calculate the LOD of such sensor device, we plot the highest optical power transmission at the plateau region versus the input MeS concentration in unit of ppb,

which is shown in Fig. 6.7. The standard error bar of each data point is obtained by 10 times of repeat measurements at each concentration step. As we can see, the response read through the optical device at the equilibrium state is in linear relationship with the concentration of the input MeS. The slight deviation at higher concentration of MeS may be attributed to the imprecision of the gas generator. By using three times of the standard deviation of the background noise divided by the slope of linear regression of responsivity, the LOD of the nanobeam cavity based device could be determined to be 1.5 ppb, which is one order of magnitude lower than the level achieved for MeS sensing by utilizing other chemical sensor[191].

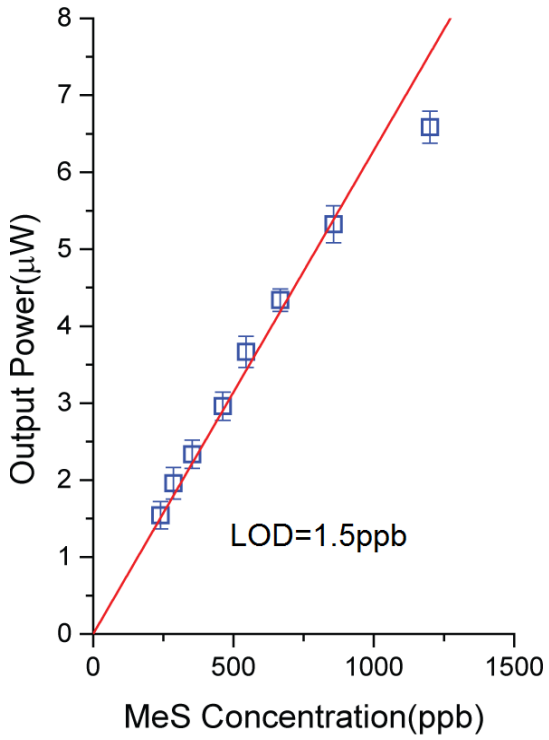

Figure 6.13 *The nanobeam's optical response versus MeS concentration (symbols) along with a linear fit (red line). The error bar is derived by repeat the measurement at the same concentration for 10 times and the calculated LOD is 1.5ppb.*

However, there is still much space for improvement to further increase the sensitivity of this platform, such as: highly compact package of a much smaller on-chip analyte delivery chamber, optimization of polymer thickness, optimization of the gas delivery system and etc.

The mechanism of the analyte movement inside the polymer is dominated by the diffusion process, which could be depicted by the Fick's diffusion law as shown below:

$$\frac{M_t}{M_\infty} = 1 - \sum_{n=0}^{\infty} \frac{8}{(2n+1)^2 \pi^2} \exp\left[\frac{-D(2n+1)^2 \pi^2 t}{t^2}\right] \tag{6.2}$$

where M_t and M_∞ denotes the mass of absorbed analyte by the polymer film at time t and equilibrium state, respectively. D is the diffusion coefficient of MeS in the Adiol polymer. According to the literatures[192], [193], when the diffusion process is far from reaching the equilibrium state, the diffusion equation (6.2) could be rewritten, for a polymer thickness of $L=2l$, as:

$$\frac{M_t}{M_\infty} = \frac{1}{l}\left(\frac{Dt}{\pi}\right)^{\frac{1}{2}} \tag{6.3}$$

Then, if the sensor's response is plotted as a function of the square root of diffusion time, there should be a linear rising part when t is small (which means the diffusion process is far from reaching the equilibrium state), by utilizing the slope of which we could derive the diffusion coefficient D under room temperature condition. The optical transmission versus the square root of time is shown in Fig. 6.8s, from which the existence of a linear portion of the plots could be clearly observed. Also, from equation (6.3) we can tell the slope of the plot is independent on the concentration of the analyte, which means the

linear portions at various concentration of the analyte should be parallel to each other and that's exactly what we can see from Fig. 6.8b.

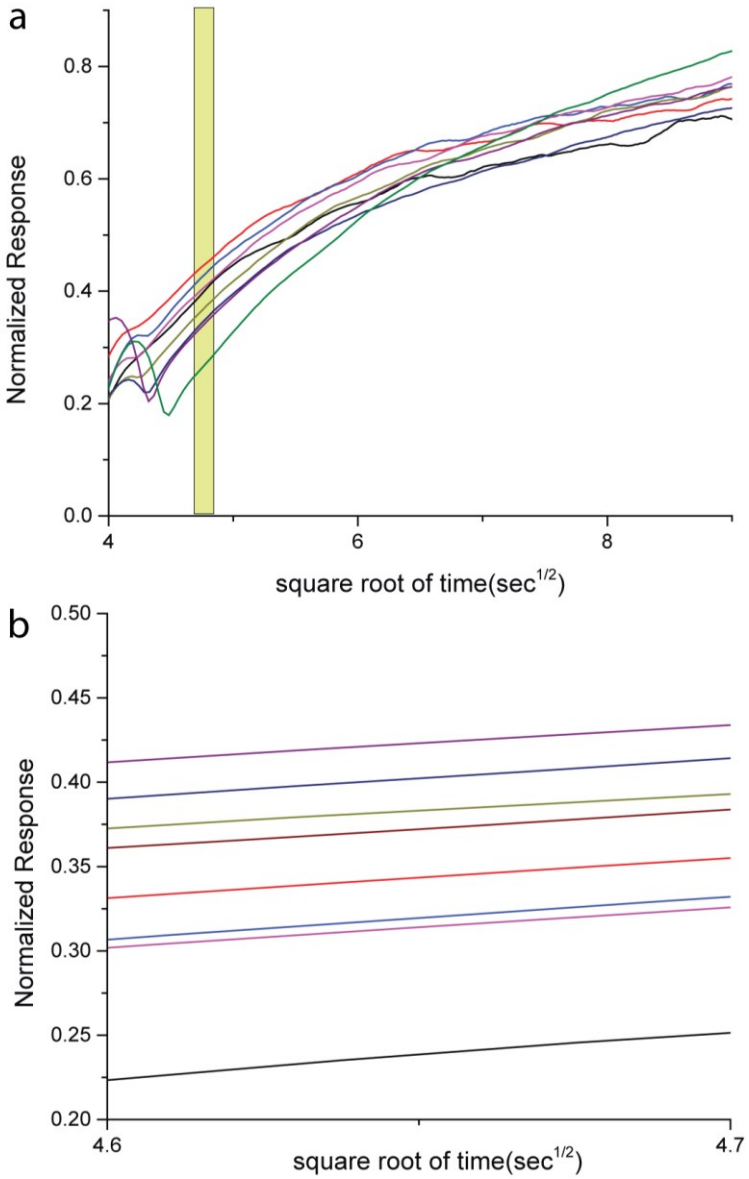

Figure 6.15 *(a) Normalized optical power transmission versus the square root of sensing time, the existence of a linear portion (shaded with light green) could be observed. (b) Enlarged view of the linear portion of the plots (shaded with light green in (a)).*

The thickness of the polymer film is measured to be 60nm to 80nm or even thinner, and we will use 60nm during the calculation. Then the diffusion coefficient could be calculated as $1.43*10^{-13}$ cm^2/s by using equation (6.3). Therefore for a polymer film with thickness of 60nm, it takes about 250 seconds of MeS exposure to make the diffusion process within the polymer layer to reach equilibrium state. However, the measurement results show that it takes longer than 250 seconds for the sensor's response to reach the plateau, such slower response is attributed to the large dead volume of the chamber and its large surface area where analyte can absorb onto, as well as the un-passivated walls of the tubing used in the experiment. All of these could be further improved by redesigning the sensor's packaging and gas handling system as already mentioned above. Nevertheless, the nanobeam photonic crystal cavity based chemical sensor already shows the highest sensitivity among all the devices for MeS detection.

The repeatability and stability test is also executed by gradually increasing the concentration of MeS from 46 ppb up to 662 ppb with four steps and then decreasing the concentration with the same four steps. The result is shown in Fig. 6.9, from which we can see that at the same concentration with same analyte exposure time, the response signal read through the optical chemical sensor is almost identical. The result proves the highly reversibility and repeatability of the diffusion process. Therefore, such device will be able to realize a highly reliable and reusable in-field real time detector for the detection purpose of MeS or similar nerve agent gas with a LOD as high as 1.5 ppb.

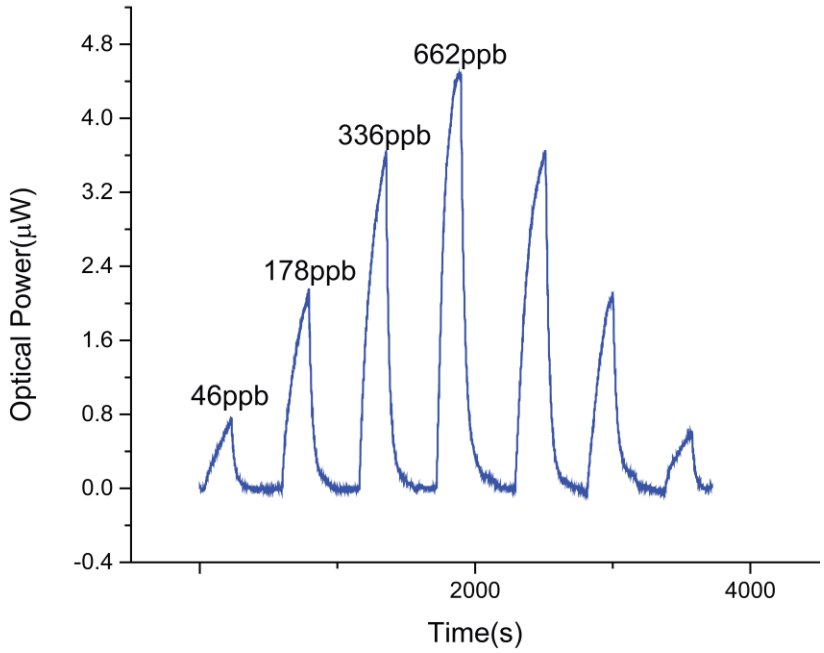

Figure 6.17 *Repeatability and reusability test of the nanbeam cavity based chemical sensor. The optical response is recorded while the device is exposed to MeS flow with changing concentration with several different steps.*

6.4 MeS Sensing Experiments with Nonlinear Optical Resonance

6.4.1 Thermo-optic Bi-stability Induced Nonlinear Optical Resonance

Silicon has a relatively high thermo-optic coefficient of 1.86×10^{4}/K, when a high quality factor optical cavity is fabricated on SOI chip, the multi-pass of large number of photons will cause internal heating of the cavity, which will further lead to the cavity's resonance wavelength to red-shift with increasing device temperature [194], [195]. Although after the application of polymer layer, the loaded quality factor of the nanobeam cavity is only around 7,000, however, when the probe laser power was increased, the nanobeam cavities were heated primarily due to absorptions in the polymer coating. The internal heating will still lead to the thermo-optic bi-stability effect, as has been observed in many other types of optical cavities with high quality factor [195]

In Fig.6.10a, the transmission of the nanobeam is measured when the probe laser power of 8 dBm is used. Due to thermally induced red-shift the resonance peak was broadened as the laser wavelength is swept forward and a sudden transition happens when the laser wavelength surpasses the drifting wavelength of the resonance. In Fig. 6.10b, the laser wavelength is swept finely in first forward and then backward direction near the wavelength where the sudden transition happens. Obviously, two stable sections and one bi-stable section could be observed as a hysteresis loop from the bi-directional sweeping transmission spectrum. Although often be considered as a nuance, such thermo-optic bi-stability could be utilized to achieve a threshold mode of chemical sensing which can set out an alarm of a critical level of culminate chemical exposure.

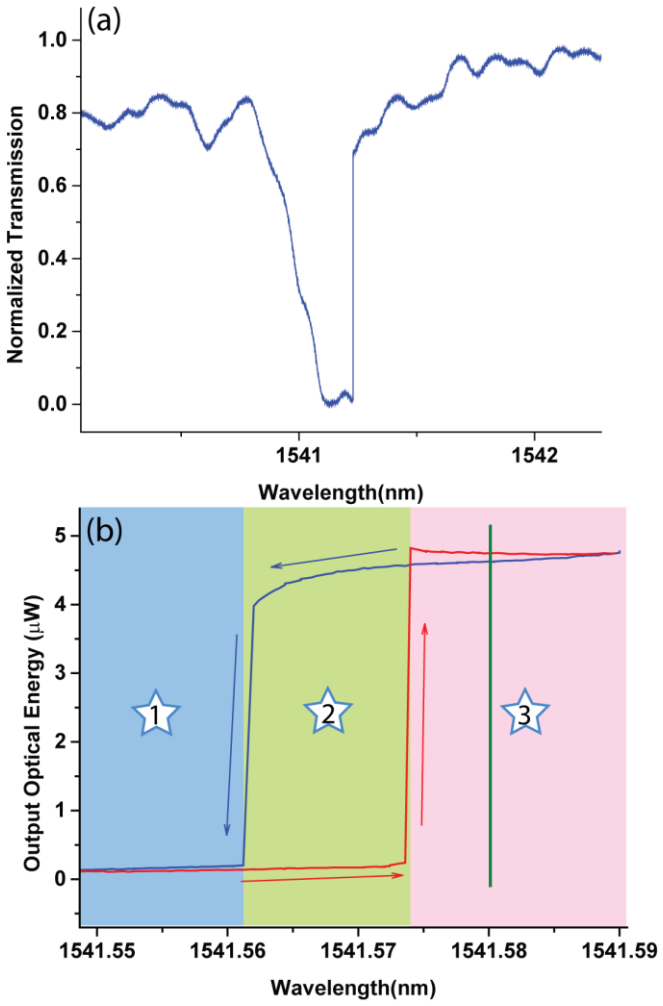

Figure 6.19 *(a) Transmission spectrum of the nanobeam photonic crystal cavity measured with 8dBm input laser power and by scanning the laser wavelength forward. The resonance peak is broadened with a sharp transition as the result of thermo-optic bi-stability. (b)Bi-directional fine scan of probe laser wavelength in the region near the sharp transition between*

6.4.2 Measurement Results and Theoretical Analysis

Similar to the measurement method we utilized for the linear optical resonance sensing experiments, we also adopt a probe laser detection scheme for the nonlinear

optical resonance sensing application. Then, the sensing experiment will be executed with following steps as shown in Fig. 6.11:

(1) At the beginning, we scan the probe laser wavelength in the backward direction (following the blue trace in Fig. 6.10b) and stop at one of the stable region (region 1) so that the system was at one of the bi-stable states with a high level of transmitted power of the device.

(2) Turn on the gas flow with specific analyte concentration within for certain period of time until a sudden transition of the response signal happens(the analyte residue remained in the gas delivery system has already been purged).

(3) Turn off the analyte gas flow immediately when the signal transition happens.

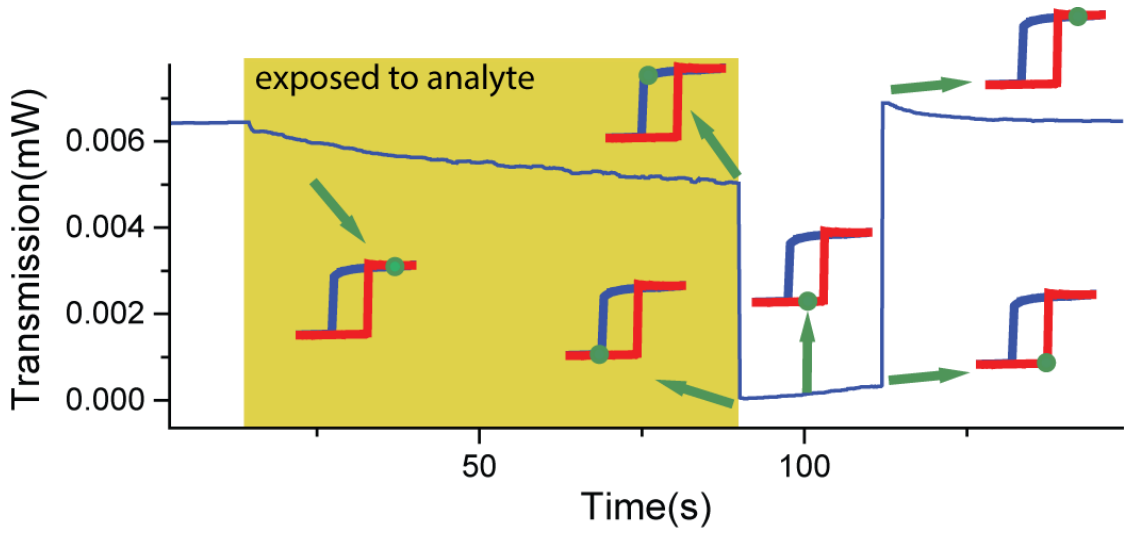

Figure 6.21 *The nanobeam sensor's response when it is operated in the bi-stable mode and exposed to MeS flow with 667ppb for certain period of time (shaded with brown yellow). The dark green circle in the symbols indicates the state of the device.*

As we can see from Fig. 6.11, when the nanobeam photonic crystal cavity is exposed to the analyte, due to the increase of effective mode index, the transmission spectrum will

start to red-shift, which equals to sweep the probe laser backward. Therefore, the optical response will follow the blue trace in Fig. 6.10b until it reaches the transition point between region 2 and region 3, where a sudden response signal drop will show up. After turning off the analyte gas flow, the transmission spectrum will start to blue shift back to its original position, which equals to sweep the probe laser forward following the red trace in Fig. 6.10b. When such shift meets the transition point between region 1 and region 2, another sudden increase of the optical response will appear. At fixed probe laser wavelength, the time it takes for the first transition to happen solely depends on the analyte mass uptaken rate by the polymer layer, which will be affected by the concentration of the analyte in the gas flow. Since the total mass uptaken by the polymer layer for the transition to happen will be a constant value (if the probe laser position is fixed). Therefore, by utilizing the thermo-optic bi-stability, we could implement a chemical dosage threshold sensor with this platform. In order to test the feasibility of this theory, we repeat such sensing experiment as described above under various concentration of the analyte with the same input optical power and fixed probe wavelength. The result is shown in Fig. 6.12a.

After exposure time *t*, according to equation (6.3), the mass uptaken by the polymer film could be expressed as:

$$M(t) = 2M(\infty)\left(\frac{Dt}{\pi 4l^2}\right)^{1/2} \tag{6.4}$$

Since the diffusion coefficient and film thickness is known and fixed, then the following relationship should be followed:

$$M(t) \propto M(\infty) t^{\frac{1}{2}} \tag{6.5}$$

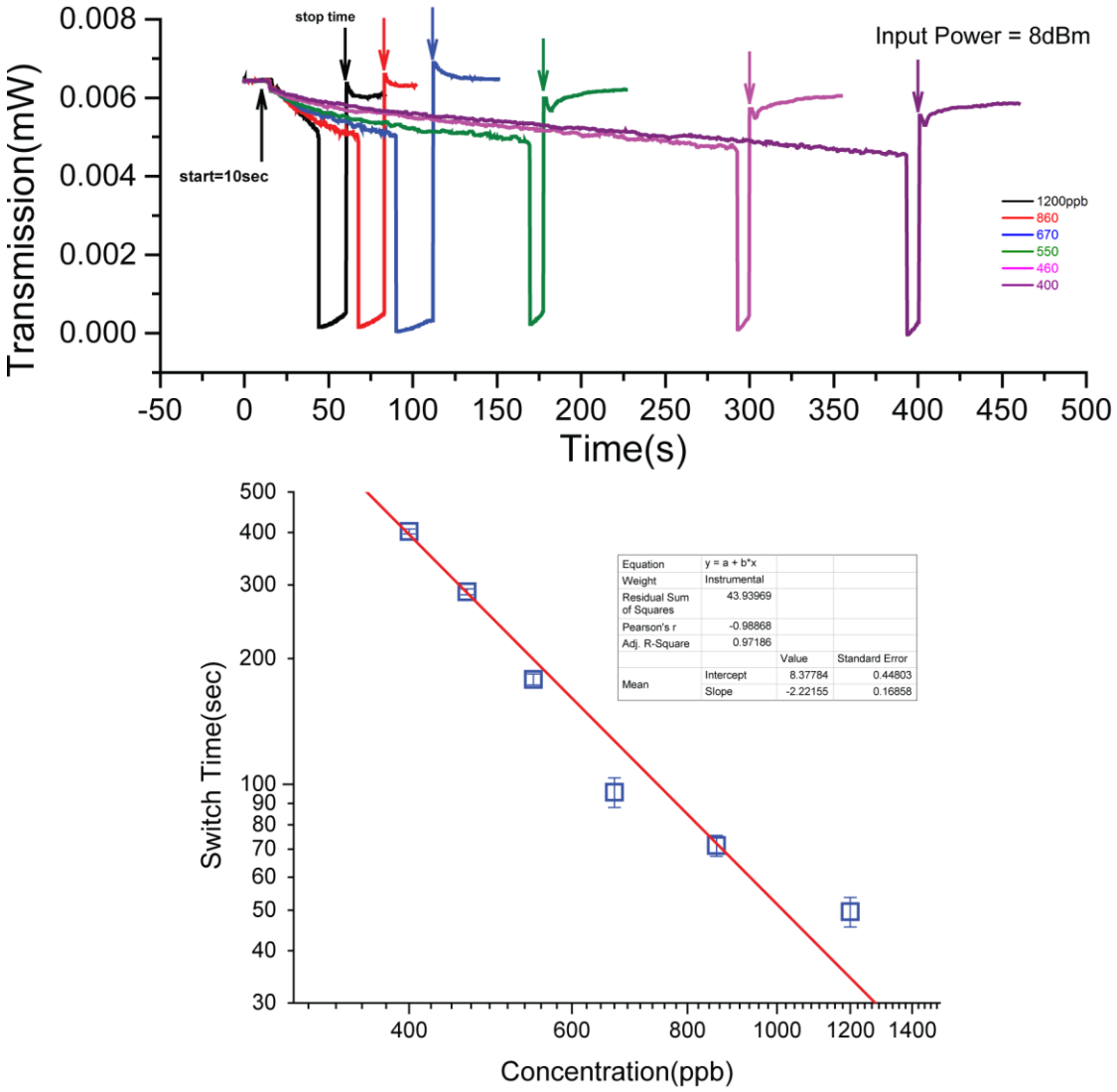

Figure 6.22 *(a) The nanobeam sensor's response when it is operated in the bi-stable mode and exposed to MeS flow with concentration from high to low respectively: 1200, 860, 670, 550, 460, and 400 ppb. The switching time increases as the concentration decreases. (b) Log-log plot of the switching time versus the MeS concentration (symbols). Red line is the theoretical fitting which shows good agreement.*

The equilibrium analyte mass $M(\infty)$ can be expressed as:

$$M(\infty) = c_{\mathrm{p}} V_{\mathrm{p}} = K c_{\mathrm{gas}} V_p \tag{6.6}$$

where c_{p} and c_{gas} are the analyte volume concentration in the polymer film and in the gas flow, respectively; K is the partition coefficient at equilibrium state; and V_{p} is the volume of the polymer film. Hence, the time it takes to absorb a threshold value of analyte mass M_{Th} in the polymer film can be expressed as:

$$t_{\mathrm{Th}} = \frac{\pi}{D}\left(\frac{M_{\mathrm{Th}}(\lambda_p)}{2KA_{\mathrm{p}}c_{\mathrm{gas}}}\right)^2 = \frac{\pi}{D}\left(\frac{m_{\mathrm{Th}}(\lambda_p)}{2Kc_{\mathrm{gas}}}\right)^2 \tag{6.7}$$

which equals to:

$$\log(t_{\mathrm{Th}}) = 2\log\sqrt{\frac{\pi}{D}}\left(\frac{M_{\mathrm{Th}}(\lambda_p)}{2KA_{\mathrm{p}}c_{\mathrm{gas}}}\right) \tag{6.8}$$

Therefore, the slope of $\log(t_{\mathrm{Th}})/\log(c_{gas})$ should equals to -2 which agrees excellently with the results as shown in Fig. 6.12(b).

Also, the value of the threshold mass could be tuned by change the wavelength of the probe laser. The further the position of the laser from the transition point, the larger the value of the threshold mass will be. If we presume the value of the threshold mass has a linear relationship with the wavelength offset value, then the square root of transition time should also have a linear relationship with the probe laser wavelength offset value, which is exactly what we can see in Fig. 6.13(b). In Fig 6.13(a), the analyte gas flow is turned off right after the switch happens, and the time between two transitions indicates the amount of mass taken up by the top surface polymer. The stand deviation from each data point is derived from 10 times of repeated measurements under the same conditions.

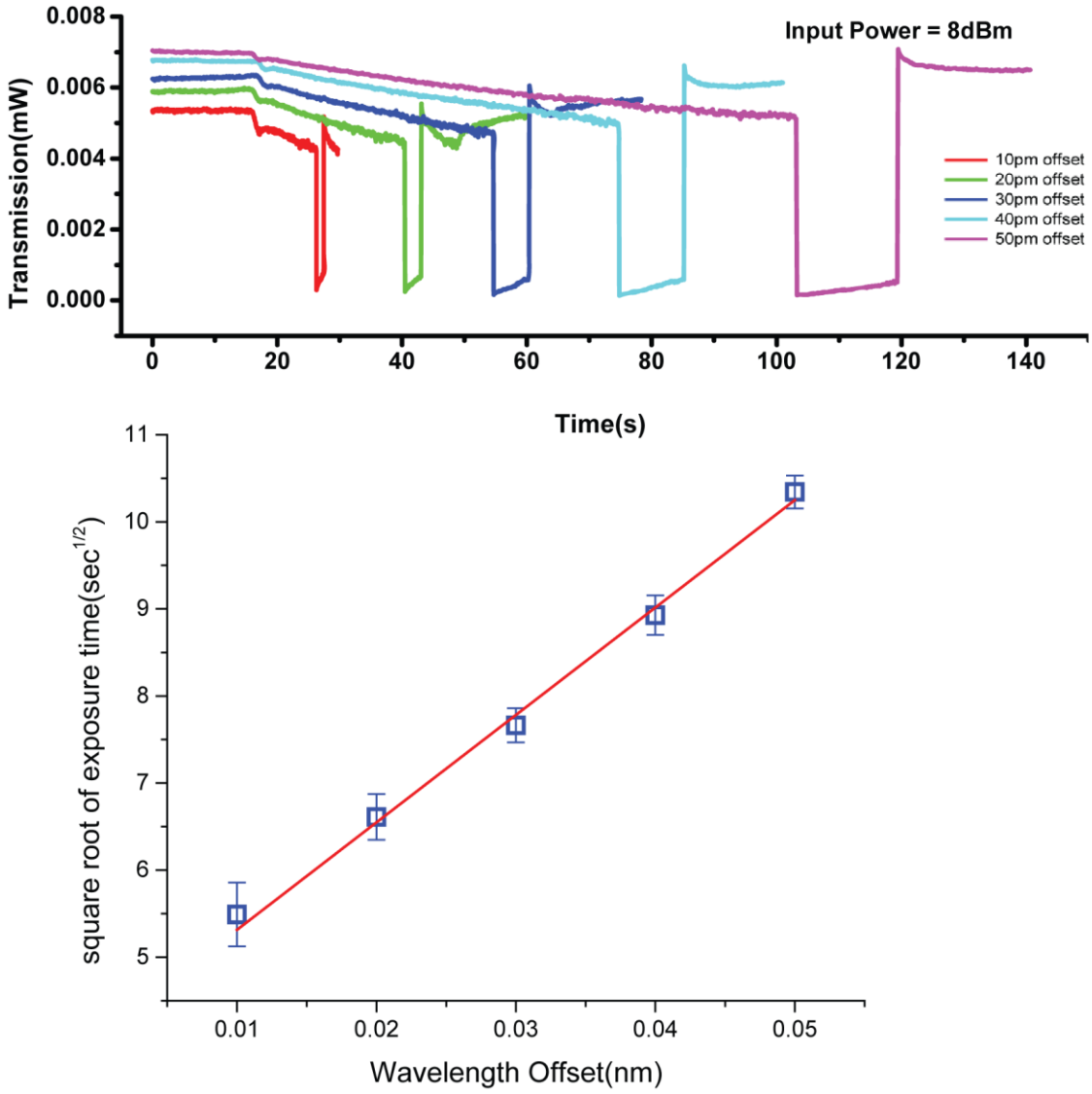

Figure 6.24 *(a) The nanobeam sensor's response when it is operated in the bi-stable mode and exposed to MeS flow with constant concentration at 1200 ppb but different offset distance of probe laser wavelength. The switching time increases as the offset value increases. b) Plot the square-root of switching time versus the input laser wavelength offset. Red line is a linear fitting curve, showing excellent linear relationship between the values of two axies.*

However, at even higher optical energy input, the probe laser could set its wavelength right inside the bi-stable region even before it is exposed to the analyte. The nonlinear resonance induced by the thermo-optic bi-stability at 8 dBm and 10 dBm probe laser input power is compared and shown in Fig. 6.14, the green line represents the position where we park the probe laser.

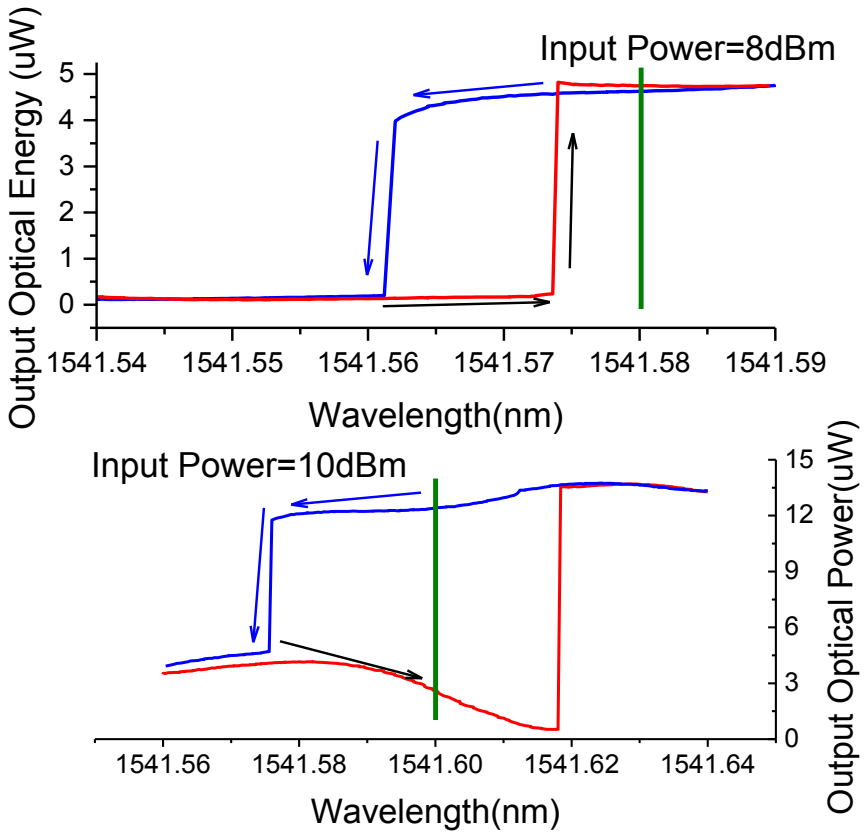

Figure 6.26 *Bi-directional scan of the bi-stable region with laser input power as 8dBm and 10dBm. The position of the probe laser wavelength is shown as a green line.*

While fixing the probe wavelength inside the bi-stable region when the input optical power equals 10 dBm as shown in Fig. 6.14, the same sensing experiment as shown in Fig. 6.12a has been done. The results of which are shown below in Fig. 6.15.

Obviously, if the device is working in this region, then the switching will only happen once and will only be able to be reset by some other triggering signals, such as thermal shock, laser power switching and etc. However, this one-time triggering mechanism may also have its unique application in detection of lethal chemical weapon in battlefield, where the signal switch back is not needed since emergency measures need to be immediately taken in case of the possible massive casualties. Such one-time only alarm trigger mechanism may also find some interesting applications in biomedical and industrial fields.

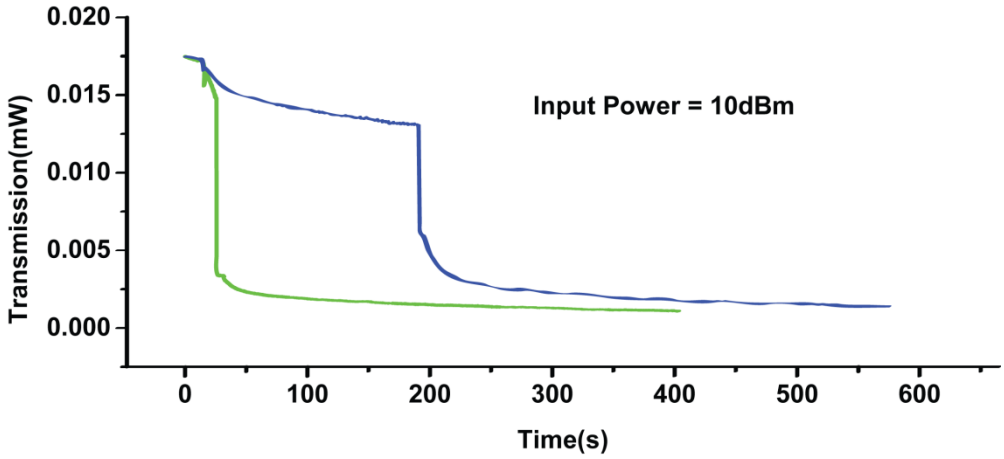

Figure 6.28 *The nanobeam sensor's response when it is operated in the bi-stable mode and exposed to MeS flow with two different concentration at 1200 ppb and 670ppb, the wavelength of the probe laser is set within the bi-stable region and the optical power of the probe laser is set to be 10 dBm.*

6.5 Conclusions

In this chapter, by utilizing a highly compact CMOS-compatible nanobeam photonic crystal cavity with a spun-on surface functionalization layer, we demonstrate an optical chemical sensor for the detection purpose of gas phase MeS with a LOD as low as 1.5 ppb, which is an order of magnitude better than other devices designed for the sensing of same type of analyte. Moreover, the thermo-optic bi-stability of the nanobeam cavity has been used to build a novel MeS dosage threshold detector, which will be able to present a large signal change when specific amount of analyte has been absorbed by the polymer layer.

According to the theoretical analysis of the measurement results, general design rules for such multi-function sensor have been provided. The proof-of-concept in this chapter demonstrates a versatile and highly integrated nanophotonic sensing platform which can be extended to detect other gas and liquid phase analyte, simply by replacing the Adiol polymer layer with other appropriate materials. Such sensing platform can find important applications in biomedical research, industrial and personal safety and production quality control.

CHAPTER 7: CONCLUSION

The main focus of this Ph.D. thesis has been on the development of heterogeneously integrated silicon nanophotonic devices for non-conventional applications such as stretchable optics, flexible optics, silicon based mid-infrared devices and optical chemical sensors. The reasons for the development of such heterogeneous integrated silicon photonic devices are that the potential of the silicon material is confined either by the inert characteristics of the buried oxide layer or the rigid and bulky form of the SOI platform. The purpose of this research is to uncover the potential of silicon photonics by either integrating them on substrates other than silicon dioxide or applying functionalization layer on top. Various stamp assisted bond-and-transfer fabrication methods have been developed to realize the heterogeneous integration process in order to realize the silicon-on-anything platform.

As a first demonstration, fully integrated silicon photonic devices include ring resonators, Mach-Zehnder interferometers and single mode waveguides working around 1550nm wavelength have been successfully transferred onto PDMS substrate. By utilizing such stretchable platform, the optical performance of the devices could be mechanically tuned. In other words, by measuring the optical performance change of the devices, the strain applied onto the PDMS substrate could be determined. Full theoretical analysis has been provided to explain the tuning mechanisms.

Then, in order to break the geometrical limitation imposed by the first transfer method, a modified photoresist pedestal assisted transfer method has been developed. As a demonstration, fully integrated silicon nitride and silicon photonic devices including

grating couplers, waveguide and side-coupled ring resonators have been successfully transferred onto thin and flexible plastic substrate. The optical performance of the device is not compromised during the transfer process and the final yield is close to one hundred percent.

With such modified transfer method, a silicon-on-CaF_2 platform which could fully utilize the potential of silicon in the mid-infrared range has been demonstrated. Fully integrated silicon photonic devices such as ring resonators, inverse tapered coupler and waveguides have been directly patterned on top of the CaF_2 substrate after the transfer process. With these devices, for the first time, we realize the cavity-enhanced mid-infrared spectroscopic sensing of multiple organic analytes. By comparing the experimental results with the FTIR measurement results, our platform demonstrates a great capability to realize precise spectroscopic sensing of various chemicals at the mid-infrared wavelength range up to 8 microns.

Finally, by applying a type of fluroalcohol polysiloxane polymer on top of a nanobeam photonic crystal cavity, we demonstrate an ultrasensitive optical chemical sensor for the detection of gas phase MeS. The LOD of such platform is as small as 1.5 ppb, which is one order of magnitude lower than other devices designed for the detection of the same type of agent. Moreover, by utilizing the thermo-optic bi-stability of the cavity, a novel chemical dosage threshold detector has been demonstrated with the very same platform, by utilizing which, an alarm signal could be triggered when specific amount of analyte has been absorbed by the functionalization layer.

In brief, a summary of the main contributions in these research efforts are listed as follows:

(1) First demonstration of fully integrated silicon photonic devices on stretchable PDMS substrates.

(2) Development of an optimized critical wet etch based transfer method specifically for the silicon photonic devices with extremely high aspect ratio.

(3) Successful demonstration of the mechanically tunable silicon photonic devices and utilization of them as strain sensors.

(4) Development of an optimized photoresist pedestal assisted transfer method for silicon photonic devices with arbitrary geometries.

(5) First demonstration of fully integrated silicon nitride based photonic devices on flexible substrates.

(6) First demonstration of fully integrated monocrystalline silicon based photonic devices including grating couplers on flexible substrates.

(7) Development of an adhesion layer free "transfer and then ebeam" method, which will be able to realize the silicon-on-anything platform.

(8) First demonstration of fully integrated silicon photonic devices on CaF_2 substrate which will be able to work at mid-infrared wavelength up to 8μm.

(9) With the silicon-on-CaF_2 platform, First demonstration of the cavity-enhanced mid-infrared spectroscopic sensing of various organic chemicals, with the silicon-on-CaF_2 platform.

(10) Demonstration of an optical chemical sensor based on nanobeam photonic crystal cavity with a LOD of 1.5 ppb for the detection of gas phase MeS.

(11) First demonstration of a chemical dosage threshold sensor by utilizing the thermo-optic bi-stability of the very same nanobeam photonic crystal cavity.

It is my hope that the contribution of the dissertation spurs the development of 3 dimensional integration of silicon photonics with both active and passive components by using the transfer-and-bond method. Moreover, such method could be widely adopted for the realization of innovative biomedical devices in the fields such as optogenetics, in-vivo diagnosis and etc.

Bibliography

[1] J. A Rogers, T. Someya, and Y. Huang, "Materials and mechanics for stretchable electronics.," *Science*, vol. 327, no. 5973, pp. 1603–7, Mar. 2010.

[2] T.-H. Han, Y. Lee, M.-R. Choi, S.-H. Woo, S.-H. Bae, B. H. Hong, J.-H. Ahn, and T.-W. Lee, "Extremely efficient flexible organic light-emitting diodes with modified graphene anode," *Nat. Photonics*, vol. 6, no. 2, pp. 105–110, Jan. 2012.

[3] A. Sugimoto, H. Ochi, S. Fujimura, A. Yoshida, T. Miyadera, and M. Tsuchida, "Flexible OLED Displays Using Plastic Substrates," *IEEE J. Sel. Top. Quantum Electron.*, vol. 10, no. 1, pp. 107–114, Jan. 2004.

[4] G. Gu, P. E. Burrows, S. Venkatesh, S. R. Forrest, and M. E. Thompson, "Vacuum-deposited, nonpolymeric flexible organic light-emitting devices," *Opt. Lett.*, vol. 22, no. 3, p. 172, Feb. 1997.

[5] Y.-H. Kim, D.-G. Moon, and J.-I. Han, "Organic TFT Array on a Paper Substrate," *IEEE Electron Device Lett.*, vol. 25, no. 10, pp. 702–704, Oct. 2004.

[6] K. Nomura, H. Ohta, A. Takagi, T. Kamiya, M. Hirano, and H. Hosono, "Room-temperature fabrication of transparent flexible thin-film transistors using amorphous oxide semiconductors.," *Nature*, vol. 432, no. 7016, pp. 488–92, Nov. 2004.

[7] S.-J. Kim and J.-S. Lee, "Flexible organic transistor memory devices.," *Nano Lett.*, vol. 10, no. 8, pp. 2884–90, Aug. 2010.

[8] G. H. Gelinck, H. E. A. Huitema, E. van Veenendaal, E. Cantatore, L. Schrijnemakers, J. B. P. H. van der Putten, T. C. T. Geuns, M. Beenhakkers, J. B. Giesbers, B.-H. Huisman, E. J. Meijer, E. M. Benito, F. J. Touwslager, A. W. Marsman, B. J. E. van Rens, and D. M. de Leeuw, "Flexible active-matrix displays and shift registers based on solution-processed organic transistors.," *Nat. Mater.*, vol. 3, no. 2, pp. 106–10, Feb. 2004.

[9] M. Kaltenbrunner, M. S. White, E. D. Głowacki, T. Sekitani, T. Someya, N. S. Sariciftci, and S. Bauer, "Ultrathin and lightweight organic solar cells with high flexibility.," *Nat. Commun.*, vol. 3, p. 770, Jan. 2012.

[10] S.-I. Na, S.-S. Kim, J. Jo, and D.-Y. Kim, "Efficient and Flexible ITO-Free Organic Solar Cells Using Highly Conductive Polymer Anodes," *Adv. Mater.*, vol. 20, no. 21, pp. 4061–4067, Nov. 2008.

[11] C. Lungenschmied, G. Dennler, H. Neugebauer, S. N. Sariciftci, M. Glatthaar, T. Meyer, and A. Meyer, "Flexible, long-lived, large-area, organic solar cells," *Sol. Energy Mater. Sol. Cells*, vol. 91, no. 5, pp. 379–384, Mar. 2007.

[12] J. Yoon, S. Jo, I. S. Chun, I. Jung, H.-S. Kim, M. Meitl, E. Menard, X. Li, J. J. Coleman, U. Paik, and J. a Rogers, "GaAs photovoltaics and optoelectronics using releasable multilayer epitaxial assemblies.," *Nature*, vol. 465, no. 7296, pp. 329–33, May 2010.

[13] T.-H. Kim, W. M. Choi, D.-H. Kim, M. a. Meitl, E. Menard, H. Jiang, J. a. Carlisle, and J. a. Rogers, "Printable, Flexible, and Stretchable Forms of Ultrananocrystalline Diamond with Applications in Thermal Management," *Adv. Mater.*, vol. 20, no. 11, pp. 2171–2176, Jun. 2008.

[14] a. J. Baca, M. a. Meitl, H. C. Ko, S. Mack, H.-S. Kim, J. Dong, P. M. Ferreira, and J. a. Rogers, "Printable Single-Crystal Silicon Micro/Nanoscale Ribbons, Platelets and Bars Generated from Bulk Wafers," *Adv. Funct. Mater.*, vol. 17, no. 16, pp. 3051–3062, Nov. 2007.

[15] J.-H. Ahn, H.-S. Kim, E. Menard, K. J. Lee, Z. Zhu, D.-H. Kim, R. G. Nuzzo, J. a. Rogers, I. Amlani, V. Kushner, S. G. Thomas, and T. Duenas, "Bendable integrated circuits on plastic substrates by use of printed ribbons of single-crystalline silicon," *Appl. Phys. Lett.*, vol. 90, no. 21, p. 213501, 2007.

[16] Y. Sun, H.-S. Kim, E. Menard, S. Kim, I. Adesida, and J. a Rogers, "Printed arrays of aligned GaAs wires for flexible transistors, diodes, and circuits on plastic substrates.," *Small*, vol. 2, no. 11, pp. 1330–4, Nov. 2006.

[17] K. J. Lee, M. a. Meitl, J.-H. Ahn, J. a. Rogers, R. G. Nuzzo, V. Kumar, and I. Adesida, "Bendable GaN high electron mobility transistors on plastic substrates," *J. Appl. Phys.*, vol. 100, no. 12, p. 124507, 2006.

[18] K. J. Lee, J. Lee, H. Hwang, Z. J. Reitmeier, R. F. Davis, J. a Rogers, and R. G. Nuzzo, "A printable form of single-crystalline gallium nitride for flexible optoelectronic systems.," *Small*, vol. 1, no. 12, pp. 1164–8, Dec. 2005.

[19] Y. Sun, W. M. Choi, H. Jiang, Y. Y. Huang, and J. a Rogers, "Controlled buckling of semiconductor nanoribbons for stretchable electronics.," *Nat. Nanotechnol.*, vol. 1, no. 3, pp. 201–7, Dec. 2006.

[20] Y. Sun and J. a. Rogers, "Fabricating Semiconductor Nano/Microwires and Transfer Printing Ordered Arrays of Them onto Plastic Substrates," *Nano Lett.*, vol. 4, no. 10, pp. 1953–1959, Oct. 2004.

[21] S.-H. Hur, D.-Y. Khang, C. Kocabas, and J. a. Rogers, "Nanotransfer printing by use of noncovalent surface forces: Applications to thin-film transistors that use single-walled carbon nanotube networks and semiconducting polymers," *Appl. Phys. Lett.*, vol. 85, no. 23, p. 5730, 2004.

[22] Y. Yang, Y. Hwang, H. a Cho, J.-H. Song, S.-J. Park, J. a Rogers, and H. C. Ko, "Arrays of silicon micro/nanostructures formed in suspended configurations for deterministic assembly using flat and roller-type stamps.," *Small*, vol. 7, no. 4, pp. 484–91, Feb. 2011.

[23] K. J. Lee, M. J. Motala, M. a. Meitl, W. R. Childs, E. Menard, a. K. Shim, J. a. Rogers, and R. G. Nuzzo, "Large-Area, Selective Transfer of Microstructured Silicon: A Printing- Based Approach to High-Performance Thin-Film Transistors Supported on Flexible Substrates," *Adv. Mater.*, vol. 17, no. 19, pp. 2332–2336, Oct. 2005.

[24] J.-H. Ahn, H.-S. Kim, K. J. Lee, S. Jeon, S. J. Kang, Y. Sun, R. G. Nuzzo, and J. a Rogers, "Heterogeneous three-dimensional electronics by use of printed semiconductor nanomaterials.," *Science*, vol. 314, no. 5806, pp. 1754–7, Dec. 2006.

[25] S.-I. Park, Y. Xiong, R.-H. Kim, P. Elvikis, M. Meitl, D.-H. Kim, J. Wu, J. Yoon, C.-J. Yu, Z. Liu, Y. Huang, K. Hwang, P. Ferreira, X. Li, K. Choquette, and J. a Rogers, "Printed assemblies of inorganic light-emitting diodes for deformable and semitransparent displays.," *Science*, vol. 325, no. 5943, pp. 977–81, Aug. 2009.

[26] S.-W. Hwang, H. Tao, D.-H. Kim, H. Cheng, J.-K. Song, E. Rill, M. a Brenckle, B. Panilaitis, S. M. Won, Y.-S. Kim, Y. M. Song, K. J. Yu, A. Ameen, R. Li, Y. Su, M. Yang, D. L. Kaplan, M. R. Zakin, M. J. Slepian, Y. Huang, F. G. Omenetto, and J. a Rogers, "A physically transient form of silicon electronics.," *Science*, vol. 337, no. 6102, pp. 1640–4, Sep. 2012.

[27] D.-H. Kim, N. Lu, R. Ma, Y.-S. Kim, R.-H. Kim, S. Wang, J. Wu, S. M. Won, H. Tao, A. Islam, K. J. Yu, T. Kim, R. Chowdhury, M. Ying, L. Xu, M. Li, H.-J. Chung, H. Keum, M. McCormick, P. Liu, Y.-W. Zhang, F. G. Omenetto, Y. Huang, T. Coleman, and J. A. Rogers, "Epidermal electronics.," *Science*, vol. 333, no. 6044, pp. 838–43, Aug. 2011.

[28] W.-H. Yeo, Y.-S. Kim, J. Lee, A. Ameen, L. Shi, M. Li, S. Wang, R. Ma, S. H. Jin, Z. Kang, Y. Huang, and J. a Rogers, "Multifunctional epidermal electronics printed directly onto the skin.," *Adv. Mater.*, vol. 25, no. 20, pp. 2773–8, 2013.

[29] Y. Sun and J. a. Rogers, "Inorganic Semiconductors for Flexible Electronics," *Adv. Mater.*, vol. 19, no. 15, pp. 1897–1916, Aug. 2007.

[30] D.-H. Kim, Y.-S. Kim, J. Wu, Z. Liu, J. Song, H.-S. Kim, Y. Y. Huang, K.-C. Hwang, and J. a. Rogers, "Ultrathin Silicon Circuits With Strain-Isolation Layers and Mesh Layouts for High-Performance Electronics on Fabric, Vinyl, Leather, and Paper," *Adv. Mater.*, vol. 21, no. 36, pp. 3703–3707, Sep. 2009.

[31] D.-H. Kim and J. a. Rogers, "Stretchable Electronics: Materials Strategies and Devices," *Adv. Mater.*, vol. 20, no. 24, pp. 4887–4892, Dec. 2008.

[32] T. Kim, J. G. McCall, Y. H. Jung, X. Huang, E. R. Siuda, Y. Li, J. Song, Y. M. Song, H. A. Pao, R.-H. Kim, C. Lu, S. D. Lee, I.-S. Song, G. Shin, R. Al-Hasani, S. Kim, M. P. Tan, Y. Huang, F. G. Omenetto, J. a Rogers, and M. R. Bruchas, "Injectable, cellular-scale optoelectronics with applications for wireless optogenetics.," *Science*, vol. 340, no. 6129, pp. 211–6, Apr. 2013.

[33] J. J. Boland, "Flexible electronics: Within touch of artificial skin.," *Nat. Mater.*, vol. 9, no. 10, pp. 790–2, Oct. 2010.

[34] J. Song, F.-Y. Kam, R.-Q. Png, W.-L. Seah, J.-M. Zhuo, G.-K. Lim, P. K. H. Ho, and L.-L. Chua, "A general method for transferring graphene onto soft surfaces.," *Nat. Nanotechnol.*, vol. 8, no. 5, pp. 356–62, May 2013.

[35] J. L. Tan, J. Tien, and C. S. Chen, "Microcontact Printing of Proteins on Mixed Self-Assembled Monolayers," *Langmuir*, vol. 18, no. 2, pp. 519–523, Jan. 2002.

[36] X. Feng, M. A. Meitl, A. M. Bowen, Y. Huang, R. G. Nuzzo, and J. A. Rogers, "Competing fracture in kinetically controlled transfer printing.," *Langmuir*, vol. 23, no. 25, pp. 12555–60, Dec. 2007.

[37] W. M. Choi, J. Song, D.-Y. Khang, H. Jiang, Y. Y. Huang, and J. a Rogers, "Biaxially stretchable 'wavy' silicon nanomembranes.," *Nano Lett.*, vol. 7, no. 6, pp. 1655–63, Jun. 2007.

[38] J. a Rogers, "Slice and dice, peel and stick: emerging methods for nanostructure fabrication.," *ACS Nano*, vol. 1, no. 3, pp. 151–3, Oct. 2007.

[39] S. Mack, M. A. Meitl, A. J. Baca, Z.-T. Zhu, and J. A. Rogers, "Mechanically flexible thin-film transistors that use ultrathin ribbons of silicon derived from bulk wafers," *Appl. Phys. Lett.*, vol. 88, no. 21, p. 213101, May 2006.

[40] T.-H. Kim, A. Carlson, J.-H. Ahn, S. M. Won, S. Wang, Y. Huang, and J. a. Rogers, "Kinetically controlled, adhesiveless transfer printing using microstructured stamps," *Appl. Phys. Lett.*, vol. 94, no. 11, p. 113502, 2009.

[41] Y. Y. Huang, W. Zhou, K. J. Hsia, E. Menard, J.-U. Park, J. a Rogers, and A. G. Alleyne, "Stamp collapse in soft lithography.," *Langmuir*, vol. 21, no. 17, pp. 8058–68, Aug. 2005.

[42] K. J. Hsia, Y. Huang, E. Menard, J.-U. Park, W. Zhou, J. Rogers, and J. M. Fulton, "Collapse of stamps for soft lithography due to interfacial adhesion," *Appl. Phys. Lett.*, vol. 86, no. 15, p. 154106, 2005.

[43] D. Li and L. J. Guo, "Micron-scale organic thin film transistors with conducting polymer electrodes patterned by polymer inking and stamping," *Appl. Phys. Lett.*, vol. 88, no. 6, p. 063513, Feb. 2006.

[44] A. P. Quist, E. Pavlovic, and S. Oscarsson, "Recent advances in microcontact printing.," *Anal. Bioanal. Chem.*, vol. 381, no. 3, pp. 591–600, Feb. 2005.

[45] S. Alom Ruiz and C. S. Chen, "Microcontact printing: A tool to pattern," *Soft Matter*, vol. 3, no. 2, p. 168, Jan. 2007.

[46] M. A. Meitl, Y. Zhou, A. Gaur, S. Jeon, M. L. Usrey, M. S. Strano, and J. A. Rogers, "Solution Casting and Transfer Printing Single-Walled Carbon Nanotube Films," *Nano Lett.*, vol. 4, no. 9, pp. 1643–1647, Sep. 2004.

[47] Y. Zhou, L. Hu, and G. Gru¨ner, "A method of printing carbon nanotube thin films," *Appl. Phys. Lett.*, vol. 88, no. 12, p. 123109, Mar. 2006.

[48] K. S. Kim, Y. Zhao, H. Jang, S. Y. Lee, J. M. Kim, K. S. Kim, J.-H. Ahn, P. Kim, J.-Y. Choi, and B. H. Hong, "Large-scale pattern growth of graphene films for stretchable transparent electrodes.," *Nature*, vol. 457, no. 7230, pp. 706–10, Feb. 2009.

[49] Y.-L. Loo, R. L. Willett, K. W. Baldwin, and J. A. Rogers, "Additive, nanoscale patterning of metal films with a stamp and a surface chemistry mediated transfer process: Applications in plastic electronics," *Appl. Phys. Lett.*, vol. 81, no. 3, p. 562, Jul. 2002.

[50] T. W. Odom, J. C. Love, D. B. Wolfe, K. E. Paul, and G. M. Whitesides, "Improved Pattern Transfer in Soft Lithography Using Composite Stamps," *Langmuir*, vol. 18, no. 13, pp. 5314–5320, Jun. 2002.

[51] C. F. Shih, "Cracks on bimaterial interfaces: elasticity and plasticity aspects," *Mater. Sci. Eng. A*, vol. 143, no. 1–2, pp. 77–90, Sep. 1991.

[52] J. W. Hutchinson and Z. Suo, *Advances in Applied Mechanics Volume 29*, vol. 29. Elsevier, 1991, pp. 63–191.

[53] P.-C. Lin, S. Vajpayee, A. Jagota, C.-Y. Hui, and S. Yang, “Mechanically tunable dry adhesive from wrinkled elastomers,” *Soft Matter*, vol. 4, no. 9, p. 1830, Aug. 2008.

[54] J. Nase, C. Creton, O. Ramos, L. Sonnenberg, T. Yamaguchi, and A. Lindner, “Measurement of the receding contact angle at the interface between a viscoelastic material and a rigid surface,” *Soft Matter*, vol. 6, no. 12, p. 2685, Jun. 2010.

[55] A. N. Gent, “Adhesion and Strength of Viscoelastic Solids. Is There a Relationship between Adhesion and Bulk Properties? †,” *Langmuir*, vol. 12, no. 19, pp. 4492–4496, Jan. 1996.

[56] A. N. Gent and S.-M. Lai, “Interfacial bonding, energy dissipation, and adhesion,” *J. Polym. Sci. Part B Polym. Phys.*, vol. 32, no. 8, pp. 1543–1555, Jun. 1994.

[57] M. A. Meitl, Z.-T. Zhu, V. Kumar, K. J. Lee, X. Feng, Y. Y. Huang, I. Adesida, R. G. Nuzzo, and J. A. Rogers, “Transfer printing by kinetic control of adhesion to an elastomeric stamp,” *Nat. Mater.*, vol. 5, no. 1, pp. 33–38, Dec. 2005.

[58] H. C. Ko, M. P. Stoykovich, J. Song, V. Malyarchuk, W. M. Choi, C.-J. Yu, J. B. Geddes, J. Xiao, S. Wang, Y. Huang, and J. a Rogers, “A hemispherical electronic eye camera based on compressible silicon optoelectronics.,” *Nature*, vol. 454, no. 7205, pp. 748–53, Aug. 2008.

[59] J. Rogers, “Multifunctional Epidermal Electronics Printed Directly Onto the Skin.”

[60] D. Chanda, K. Shigeta, S. Gupta, T. Cain, A. Carlson, A. Mihi, A. J. Baca, G. R. Bogart, P. Braun, and J. A. Rogers, “Large-area flexible 3D optical negative index metamaterial formed by nanotransfer printing.,” *Nat. Nanotechnol.*, vol. 6, no. 7, pp. 402–7, Jul. 2011.

[61] D.-H. Kim, R. Ghaffari, N. Lu, and J. A. Rogers, “Flexible and stretchable electronics for biointegrated devices.,” *Annu. Rev. Biomed. Eng.*, vol. 14, pp. 113–28, Jan. 2012.

[62] J. El-Ali, P. K. Sorger, and K. F. Jensen, “Cells on chips.,” *Nature*, vol. 442, no. 7101, pp. 403–11, Jul. 2006.

[63] A. J. DeMello, “Control and detection of chemical reactions in microfluidic systems.,” *Nature*, vol. 442, no. 7101, pp. 394–402, Jul. 2006.

[64] H. Craighead, “Future lab-on-a-chip technologies for interrogating individual molecules.,” *Nature*, vol. 442, no. 7101, pp. 387–93, Jul. 2006.

[65] S. K. Sia and G. M. Whitesides, “Microfluidic devices fabricated in poly(dimethylsiloxane) for biological studies.,” *Electrophoresis*, vol. 24, no. 21, pp. 3563–76, Nov. 2003.

[66] G. M. Whitesides, “The origins and the future of microfluidics.,” *Nature*, vol. 442, no. 7101, pp. 368–73, Jul. 2006.

[67] D. Janasek, J. Franzke, and A. Manz, “Scaling and the design of miniaturized chemical-analysis systems.,” *Nature*, vol. 442, no. 7101, pp. 374–80, Jul. 2006.

[68] A. del Campo and C. Greiner, “SU-8: a photoresist for high-aspect-ratio and 3D submicron lithography,” *J. Micromechanics Microengineering*, vol. 17, no. 6, pp. R81–R95, Jun. 2007.

[69] J. A. Rogers and C. Lee, “A diverse printed future,” pp. 7–8.

[70] S. Jeon, E. Menard, J.-U. Park, J. Maria, M. Meitl, J. Zaumseil, and J. a. Rogers, “Three-Dimensional Nanofabrication with Rubber Stamps and Conformable Photomasks,” *Adv. Mater.*, vol. 16, no. 15, pp. 1369–1373, Aug. 2004.

[71] G. B. Hocker and W. K. Burns, “Mode dispersion in diffused channel waveguides by the effective index method.,” *Appl. Opt.*, vol. 16, no. 1, pp. 113–8, Jan. 1977.

[72] R. A. Soref, J. Schmidtchen, and K. Petermann, “Large single-mode rib waveguides in GeSi-Si and Si-on-SiO/sub 2/,” *IEEE J. Quantum Electron.*, vol. 27, no. 8, pp. 1971–1974, 1991.

[73] G. T. Reed and V. M. N. Passaro, “Single-mode and polarization-independent silicon-on-insulator waveguides with small cross section,” *J. Light. Technol.*, vol. 23, no. 6, pp. 2103–2111, Jun. 2005.

[74] S. T. Lim, C. E. Png, E. a Ong, and Y. L. Ang, “Single mode, polarization-independent submicron silicon waveguides based on geometrical adjustments.,” *Opt. Express*, vol. 15, no. 18, pp. 11061–72, Sep. 2007.

[75] T. J. Kippenberg, R. Holzwarth, and S. A. Diddams, “Microresonator-based optical frequency combs.,” *Science*, vol. 332, no. 6029, pp. 555–9, Apr. 2011.

[76] M. Kuwata-Gonokami, “Laser emission from dye-doped polystyrene microsphere,” in *Proceedings of LEOS ’93*, 1993, pp. 300–301.

[77] R. Colombelli, K. Srinivasan, M. Troccoli, O. Painter, C. F. Gmachl, D. M. Tennant, A. M. Sergent, D. L. Sivco, A. Y. Cho, and F. Capasso, “Quantum

cascade surface-emitting photonic crystal laser.," *Science*, vol. 302, no. 5649, pp. 1374–7, Nov. 2003.

[78] A. M. Armani, R. P. Kulkarni, S. E. Fraser, R. C. Flagan, and K. J. Vahala, "Label-free, single-molecule detection with optical microcavities.," *Science*, vol. 317, no. 5839, pp. 783–7, Aug. 2007.

[79] L. He, S. K. Ozdemir, J. Zhu, W. Kim, and L. Yang, "Detecting single viruses and nanoparticles using whispering gallery microlasers.," *Nat. Nanotechnol.*, vol. 6, no. 7, pp. 428–32, Jul. 2011.

[80] L. Mescia, P. Bia, M. De Sario, A. Di Tommaso, and F. Prudenzano, "Design of mid-infrared amplifiers based on fiber taper coupling to erbium-doped microspherical resonator.," *Opt. Express*, vol. 20, no. 7, pp. 7616–29, Mar. 2012.

[81] W. Li, X. Sang, C. Yu, and X. Xin, "Characteristics of an all-optical parametric amplifier in a silicon microring resonator," *J. Opt.*, vol. 13, no. 7, p. 075501, Jul. 2011.

[82] K. J. Vahala, "Optical microcavities.," *Nature*, vol. 424, no. 6950, pp. 839–46, Aug. 2003.

[83] Z. Qiang, W. Zhou, and R. A. Soref, "Optical add-drop filters based on photonic crystal ring resonators," *Opt. Express*, vol. 15, no. 4, p. 1823, Feb. 2007.

[84] H. Li, Y. Chen, J. Noh, S. Tadesse, and M. Li, "Multichannel cavity optomechanics for all-optical amplification of radio frequency signals.," *Nat. Commun.*, vol. 3, p. 1091, Jan. 2012.

[85] Q. Xu and M. Lipson, "All-optical logic based on silicon micro-ring resonators," *Opt. Express*, vol. 15, no. 3, p. 924, 2007.

[86] N. Youngblood, Y. Anugrah, R. Ma, S. J. Koester, and M. Li, "Multifunctional graphene optical modulator and photodetector integrated on silicon waveguides.," *Nano Lett.*, vol. 14, no. 5, pp. 2741–6, May 2014.

[87] M. Nakazawa, K. Kikuchi, and T. Miyazaki, Eds., *High Spectral Density Optical Communication Technologies*. Berlin, Heidelberg: Springer Berlin Heidelberg, 2010.

[88] G. J. M. Krijnen, A. Villeneuve, G. I. Stegeman, P. V. Lambeck, and H. J. W. M. Hoekstra, "A versatile all-optical modulator based on nonlinear Mach-Zehnder interferometers." IEEE Computer Society Press, 25-Jul-1994.

[89] L. Liao, D. Samara-Rubio, M. Morse, A. Liu, D. Hodge, D. Rubin, U. D. Keil, and T. Franck, "High speed silicon Mach-Zehnder modulator," *Opt. Express*, vol. 13, no. 8, p. 3129, 2005.

[90] N. Fabricius, G. Gauglitz, and J. Ingenhoff, "A gas sensor based on an integrated optical Mach-Zehnder interferometer," *Sensors Actuators B Chem.*, vol. 7, no. 1–3, pp. 672–676, Mar. 1992.

[91] B. J. Luff, J. S. Wilkinson, J. Piehler, U. Hollenbach, J. Ingenhoff, and N. Fabricius, "Integrated optical Mach-Zehnder biosensor," *J. Light. Technol.*, vol. 16, no. 4, pp. 583–592, Apr. 1998.

[92] B. Sepúlveda, J. S. del Río, M. Moreno, F. J. Blanco, K. Mayora, C. Domínguez, and L. M. Lechuga, "Optical biosensor microsystems based on the integration of highly sensitive Mach–Zehnder interferometer devices," *J. Opt. A Pure Appl. Opt.*, vol. 8, no. 7, pp. S561–S566, Jul. 2006.

[93] Y. Baek, R. Schiek, G. I. Stegeman, G. Krijnen, I. Baumann, and W. Sohler, "All-optical integrated Mach–Zehnder switching due to cascaded nonlinearities," *Appl. Phys. Lett.*, vol. 68, no. 15, p. 2055, Apr. 1996.

[94] S. Kotiyal, H. Thapliyal, and N. Ranganathan, "Mach-Zehnder interferometer based design of all optical reversible binary adder," in *2012 Design, Automation & Test in Europe Conference & Exhibition (DATE)*, 2012, pp. 721–726.

[95] Hui-Wen Chen, A. Fang, J. Bovington, J. D. Peters, and J. E. Bowers, "Hybrid silicon tunable filter based on a Mach-Zehnder interferometer and ring resonantor." pp. 1–4, 2009.

[96] Z. Zhao, M. Tang, H. Liao, G. Ren, S. Fu, F. Yang, P. P. Shum, and D. Liu, "Programmable multi-wavelength filter with Mach-Zehnder interferometer embedded in ethanol filled photonic crystal fiber.," *Opt. Lett.*, vol. 39, no. 7, pp. 2194–7, Apr. 2014.

[97] M. Li, W. H. P. Pernice, and H. X. Tang, "Tunable bipolar optical interactions between guided lightwaves," *Nat. Photonics*, vol. 3, no. 8, pp. 464–468, Jul. 2009.

[98] B. Guha, A. Gondarenko, and M. Lipson, "Minimizing temperature sensitivity of silicon Mach-Zehnder interferometers.," *Opt. Express*, vol. 18, no. 3, pp. 1879–87, Feb. 2010.

[99] H. Li, Y. Anugrah, S. J. Koester, and M. Li, "Optical absorption in graphene integrated on silicon waveguides," *Appl. Phys. Lett.*, vol. 101, no. 11, p. 111110, Sep. 2012.

[100] H. Li, J. W. Noh, Y. Chen, and M. Li, “Enhanced optical forces in integrated hybrid plasmonic waveguides.,” *Opt. Express*, vol. 21, no. 10, pp. 11839–51, May 2013.

[101] J. Gosciniak and S. I. Bozhevolnyi, “Performance of thermo-optic components based on dielectric-loaded surface plasmon polariton waveguides,” *Sci. Rep.*, vol. 3, May 2013.

[102] M. Soltani, J. Lin, R. A. Forties, J. T. Inman, S. N. Saraf, R. M. Fulbright, M. Lipson, and M. D. Wang, “Nanophotonic trapping for precise manipulation of biomolecular arrays.,” *Nat. Nanotechnol.*, vol. 9, no. 6, pp. 448–52, Jun. 2014.

[103] G. T. Reed, G. Mashanovich, F. Y. Gardes, and D. J. Thomson, “Silicon optical modulators,” *Nat. Photonics*, vol. 4, no. 8, pp. 518–526, Jul. 2010.

[104] C. Sturm, D. Tanese, H. S. Nguyen, H. Flayac, E. Galopin, A. Lemaître, I. Sagnes, D. Solnyshkov, A. Amo, G. Malpuech, and J. Bloch, “All-optical phase modulation in a cavity-polariton Mach-Zehnder interferometer.,” *Nat. Commun.*, vol. 5, p. 3278, Jan. 2014.

[105] Y. Akahane, T. Asano, B.-S. Song, and S. Noda, “High-Q photonic nanocavity in a two-dimensional photonic crystal.,” *Nature*, vol. 425, no. 6961, pp. 944–7, Oct. 2003.

[106] S. Noda, M. Fujita, and T. Asano, “Spontaneous-emission control by photonic crystals and nanocavities,” *Nat. Photonics*, vol. 1, no. 8, pp. 449–458, Aug. 2007.

[107] B.-S. Song, S. Noda, T. Asano, and Y. Akahane, “Ultra-high-Q photonic double-heterostructure nanocavity,” *Nat. Mater.*, vol. 4, no. 3, pp. 207–210, Feb. 2005.

[108] J. Vučković and Y. Yamamoto, “Photonic crystal microcavities for cavity quantum electrodynamics with a single quantum dot,” *Appl. Phys. Lett.*, vol. 82, no. 15, p. 2374, Apr. 2003.

[109] H.-Y. Ryu, M. Notomi, and Y.-H. Lee, “High-quality-factor and small-mode-volume hexapole modes in photonic-crystal-slab nanocavities,” *Appl. Phys. Lett.*, vol. 83, no. 21, p. 4294, Nov. 2003.

[110] D. Englund, D. Fattal, E. Waks, G. Solomon, B. Zhang, T. Nakaoka, Y. Arakawa, Y. Yamamoto, and J. Vučković, “Controlling the Spontaneous Emission Rate of Single Quantum Dots in a Two-Dimensional Photonic Crystal,” *Phys. Rev. Lett.*, vol. 95, no. 1, p. 013904, Jul. 2005.

[111] H. Altug, D. Englund, and J. Vučković, "Ultrafast photonic crystal nanocavity laser," *Nat. Phys.*, vol. 2, no. 7, pp. 484–488, Jul. 2006.

[112] A. R. Md Zain, N. P. Johnson, M. Sorel, and R. M. De La Rue, "Ultra high quality factor one dimensional photonic crystal/photonic wire micro-cavities in silicon-on-insulator (SOI)," *Opt. Express*, vol. 16, no. 16, p. 12084, Jul. 2008.

[113] Q. Quan, I. B. Burgess, S. K. Y. Tang, D. L. Floyd, and M. Loncar, "High-Q, low index-contrast polymeric photonic crystal nanobeam cavities.," *Opt. Express*, vol. 19, no. 22, pp. 22191–7, Oct. 2011.

[114] J. Vuckovic, M. Loncar, H. Mabuchi, and A. Scherer, "Optimization of the Q factor in photonic crystal microcavities," *IEEE J. Quantum Electron.*, vol. 38, no. 7, pp. 850–856, Jul. 2002.

[115] Q. Quan and M. Loncar, "Deterministic design of wavelength scale, ultra-high Q photonic crystal nanobeam cavities.," *Opt. Express*, vol. 19, no. 19, pp. 18529–42, Sep. 2011.

[116] D. Taillaert, P. Bienstman, and R. Baets, "Compact efficient broadband grating coupler for silicon-on-insulator waveguides," *Opt. Lett.*, vol. 29, no. 23, p. 2749, 2004.

[117] G. Roelkens, D. Van Thourhout, and R. Baets, "High efficiency Silicon-on-Insulator grating coupler based on a poly-Silicon overlay," *Opt. Express*, vol. 14, no. 24, p. 11622, 2006.

[118] M. Li, W. H. P. Pernice, C. Xiong, T. Baehr-Jones, M. Hochberg, and H. X. Tang, "Harnessing optical forces in integrated photonic circuits.," *Nature*, vol. 456, no. 7221, pp. 480–4, Nov. 2008.

[119] Y. Chen, W. S. Fegadolli, W. M. Jones, A. Scherer, and M. Li, "Ultrasensitive gas-phase chemical sensing based on functionalized photonic crystal nanobeam cavities.," *ACS Nano*, vol. 8, no. 1, pp. 522–7, Jan. 2014.

[120] L. He and M. Li, "On-chip synthesis of circularly polarized emission of light with integrated photonic circuits.," *Opt. Lett.*, vol. 39, no. 9, pp. 2553–6, May 2014.

[121] D. Taillaert, F. Van Laere, M. Ayre, W. Bogaerts, D. Van Thourhout, P. Bienstman, and R. Baets, "Grating Couplers for Coupling between Optical Fibers and Nanophotonic Waveguides," *Jpn. J. Appl. Phys.*, vol. 45, no. 8A, pp. 6071–6077, Aug. 2006.

[122] F. Van Laere, T. Claes, J. Schrauwen, S. Scheerlinck, W. Bogaerts, D. Taillaert, L. O'Faolain, D. Van Thourhout, and R. Baets, "Compact Focusing Grating Couplers for Silicon-on-Insulator Integrated Circuits," *IEEE Photonics Technol. Lett.*, vol. 19, no. 23, pp. 1919–1921, Dec. 2007.

[123] L. Sun, G. Qin, H. Huang, H. Zhou, N. Behdad, W. Zhou, and Z. Ma, "Flexible high-frequency microwave inductors and capacitors integrated on a polyethylene terephthalate substrate," *Appl. Phys. Lett.*, vol. 96, no. 1, p. 013509, Jan. 2010.

[124] H.-C. Yuan and Z. Ma, "Microwave thin-film transistors using Si nanomembranes on flexible polymer substrate," *Appl. Phys. Lett.*, vol. 89, no. 21, p. 212105, Nov. 2006.

[125] K. Bradley, J.-C. P. Gabriel, and G. Grüner, "Flexible Nanotube Electronics," *Nano Lett.*, vol. 3, no. 10, pp. 1353–1355, Oct. 2003.

[126] G. Eda, G. Fanchini, and M. Chhowalla, "Large-area ultrathin films of reduced graphene oxide as a transparent and flexible electronic material.," *Nat. Nanotechnol.*, vol. 3, no. 5, pp. 270–4, May 2008.

[127] D. Sun, M. Y. Timmermans, Y. Tian, A. G. Nasibulin, E. I. Kauppinen, S. Kishimoto, T. Mizutani, and Y. Ohno, "Flexible high-performance carbon nanotube integrated circuits.," *Nat. Nanotechnol.*, vol. 6, no. 3, pp. 156–61, Mar. 2011.

[128] J. Yoon, L. Li, A. V Semichaevsky, J. H. Ryu, H. T. Johnson, R. G. Nuzzo, and J. A. Rogers, "Flexible concentrator photovoltaics based on microscale silicon solar cells embedded in luminescent waveguides.," *Nat. Commun.*, vol. 2, p. 343, Jan. 2011.

[129] H.-C. Yuan, J. Shin, G. Qin, L. Sun, P. Bhattacharya, M. G. Lagally, G. K. Celler, and Z. Ma, "Flexible photodetectors on plastic substrates by use of printing transferred single-crystal germanium membranes," *Appl. Phys. Lett.*, vol. 94, no. 1, p. 013102, Jan. 2009.

[130] S. Aksu, M. Huang, A. Artar, A. A. Yanik, S. Selvarasah, M. R. Dokmeci, and H. Altug, "Flexible plasmonics on unconventional and nonplanar substrates.," *Adv. Mater.*, vol. 23, no. 38, pp. 4422–30, Oct. 2011.

[131] I. M. Pryce, K. Aydin, Y. A. Kelaita, R. M. Briggs, and H. A. Atwater, "Highly strained compliant optical metamaterials with large frequency tunability.," *Nano Lett.*, vol. 10, no. 10, pp. 4222–7, Oct. 2010.

[132] A. Ghaffari, A. Hosseini, X. Xu, D. Kwong, H. Subbaraman, and R. T. Chen, "Transfer of micro and nano-photonic silicon nanomembrane waveguide devices on flexible substrates.," *Opt. Express*, vol. 18, no. 19, pp. 20086–95, Sep. 2010.

[133] X. Xu, H. Subbaraman, A. Hosseini, C.-Y. Lin, D. Kwong, and R. T. Chen, "Stamp printing of silicon-nanomembrane-based photonic devices onto flexible substrates with a suspended configuration.," *Opt. Lett.*, vol. 37, no. 6, pp. 1020–2, Mar. 2012.

[134] H. Yang, D. Zhao, S. Chuwongin, and J. Seo, "Transfer-printed stacked nanomembrane lasers on silicon," *Nat. ...*, no. July, 2012.

[135] L. Fan, L. T. Varghese, Y. Xuan, J. Wang, B. Niu, and M. Qi, "Direct fabrication of silicon photonic devices on a flexible platform and its application for strain sensing.," *Opt. Express*, vol. 20, no. 18, pp. 20564–75, Aug. 2012.

[136] L. Li, H. Lin, S. Qiao, Y. Zou, S. Danto, K. Richardson, J. D. Musgraves, N. Lu, and J. Hu, "Integrated flexible chalcogenide glass photonic devices," *Nat. Photonics*, vol. advance on, Jun. 2014.

[137] X. Xu, H. Subbaraman, D. Kwong, A. Hosseini, Y. Zhang, and R. T. Chen, "Large Area Silicon Nanomembrane Photonic Devices on Unconventional Substrates," *IEEE Photonics Technol. Lett.*, vol. 25, no. 16, pp. 1601–1604, Aug. 2013.

[138] D. A. Chang-Yen, R. K. Eich, and B. K. Gale, "A monolithic PDMS waveguide system fabricated using soft-lithography techniques," *J. Light. Technol.*, vol. 23, no. 6, pp. 2088–2093, Jun. 2005.

[139] M. Mohageg, A. Savchenkov, D. Strekalov, A. Matsko, V. Ilchenko, and L. Maleki, "Reconfigurable optical filter," *Electron. Lett.*, vol. 41, no. 6, p. 356, 2005.

[140] E. L. Wooten, R. L. Stone, E. W. Miles, and E. M. Bradley, "Rapidly tunable narrowband wavelength filter using LiNbO/sub 3/ unbalanced Mach-Zehnder interferometers," *J. Light. Technol.*, vol. 14, no. 11, pp. 2530–2536, 1996.

[141] N. Sherwood-Droz, H. Wang, L. Chen, B. G. Lee, A. Biberman, K. Bergman, and M. Lipson, "Optical 4x4 hitless slicon router for optical networks-on-chip (NoC)," *Opt. Express*, vol. 16, no. 20, p. 15915, Sep. 2008.

[142] E. J. Klein, D. H. Geuzebroek, H. Kelderman, N. Baker, and A. Driessen, "Reconfigurable optical add-drop multiplexer using microring resonators," *IEEE Photonics Technol. Lett.*, vol. 17, no. 11, pp. 2358–2360, Nov. 2005.

[143] D. Biegelsen, “Photoelastic Tensor of Silicon and the Volume Dependence of the Average Gap,” *Phys. Rev. Lett.*, vol. 32, no. 21, pp. 1196–1199, May 1974.

[144] Z. Y. Huang, W. Hong, and Z. Suo, “Nonlinear analyses of wrinkles in a film bonded to a compliant substrate,” *J. Mech. Phys. Solids*, vol. 53, no. 9, pp. 2101–2118, Sep. 2005.

[145] Y. Sun and J. A. Rogers, “Structural forms of single crystal semiconductor nanoribbons for high-performance stretchable electronics,” *J. Mater. Chem.*, vol. 17, no. 9, p. 832, Feb. 2007.

[146] H. Jiang, D.-Y. Khang, J. Song, Y. Sun, Y. Huang, and J. A. Rogers, “Finite deformation mechanics in buckled thin films on compliant supports.,” *Proc. Natl. Acad. Sci. U. S. A.*, vol. 104, no. 40, pp. 15607–12, Oct. 2007.

[147] N. Bowden, S. Brittain, A. G. Evans, J. W. Hutchinson, and G. M. Whitesides, “Spontaneous formation of ordered structures in thin films of metals supported on an elastomeric polymer,” vol. 393, no. 6681, pp. 146–149, May 1998.

[148] X. Chen and J. W. Hutchinson, “Herringbone Buckling Patterns of Compressed Thin Films on Compliant Substrates,” *J. Appl. Mech.*, vol. 71, no. 5, p. 597, Sep. 2004.

[149] G. B. Hocker, “Fiber-optic sensing of pressure and temperature.,” *Appl. Opt.*, vol. 18, no. 9, pp. 1445–8, May 1979.

[150] A. Yariv and P. Yeh, *Optical waves in crystals: propagation and control of laser radiation*. Wiley, 1984, p. 589.

[151] F. Schneider, T. Fellner, J. Wilde, and U. Wallrabe, “Mechanical properties of silicones for MEMS,” *J. Micromechanics Microengineering*, vol. 18, no. 6, p. 065008, Jun. 2008.

[152] K. Hoshino and I. Shimoyama, “Analysis of elastic micro optical components under large deformation,” *J. Micromechanics Microengineering*, vol. 13, no. 1, pp. 149–154, Jan. 2003.

[153] *Polymer Data Handbook*. Oxford University Press, Incorporated, 1999, p. 1018.

[154] Y. Amemiya, Y. Tanushi, T. Tokunaga, and S. Yokoyama, “Photoelastic Effect in Silicon Ring Resonators,” *Jpn. J. Appl. Phys.*, vol. 47, no. 4, pp. 2910–2914, Apr. 2008.

[155] D. Wu, Y. Yin, H. Xie, Y. Shang, C. Li, L. Wu, and X. Dai, "Controlling the surface buckling wrinkles by patterning the material system of hard-nano-film/soft-matter-substrate," *Sci. China Physics, Mech. Astron.*, vol. 57, no. 4, pp. 637–643, Feb. 2014.

[156] D. Martin Knotter and T. J. J. (Dee) Denteneer, "Etching Mechanism of Silicon Nitride in HF-Based Solutions," *J. Electrochem. Soc.*, vol. 148, no. 3, p. F43, Mar. 2001.

[157] R. Soref, "Mid-infrared photonics in silicon and germanium," *Nat. Photonics*, vol. 4, no. 8, pp. 495–497, Aug. 2010.

[158] R. A. Soref, S. J. Emelett, and W. R. Buchwald, "Silicon waveguided components for the long-wave infrared region," *J. Opt. A Pure Appl. Opt.*, vol. 8, no. 10, pp. 840–848, Oct. 2006.

[159] M. Bass, C. DeCusatis, J. Enoch, V. Lakshminarayanan, G. Li, C. MacDonald, V. Mahajan, and E. Van Stryland, *Handbook of Optics, Third Edition Volume IV: Optical Properties of Materials, Nonlinear Optics, Quantum Optics (set): Optical Properties of Materials, Nonlinear Optics, Quantum Optics (set)*. McGraw Hill Professional, 2009, p. 1152.

[160] Y.-C. Chang, V. Paeder, L. Hvozdara, J.-M. Hartmann, and H. P. Herzig, "Low-loss germanium strip waveguides on silicon for the mid-infrared.," *Opt. Lett.*, vol. 37, no. 14, pp. 2883–5, Jul. 2012.

[161] R. Shankar, I. Bulu, and M. Lončar, "Integrated high-quality factor silicon-on-sapphire ring resonators for the mid-infrared," *Appl. Phys. Lett.*, vol. 102, no. 5, p. 051108, Feb. 2013.

[162] T. Baehr-Jones, A. Spott, R. Ilic, A. Spott, B. Penkov, W. Asher, and M. Hochberg, "Silicon-on-sapphire integrated waveguides for the mid-infrared.," *Opt. Express*, vol. 18, no. 12, pp. 12127–35, Jun. 2010.

[163] F. Li, S. D. Jackson, C. Grillet, E. Magi, D. Hudson, S. J. Madden, Y. Moghe, C. O'Brien, A. Read, S. G. Duvall, P. Atanackovic, B. J. Eggleton, and D. J. Moss, "Low propagation loss silicon-on-sapphire waveguides for the mid-infrared.," *Opt. Express*, vol. 19, no. 16, pp. 15212–20, Aug. 2011.

[164] G. Z. Mashanovich, M. M. Milošević, M. Nedeljkovic, N. Owens, B. Xiong, E. J. Teo, and Y. Hu, "Low loss silicon waveguides for the mid-infrared.," *Opt. Express*, vol. 19, no. 8, pp. 7112–9, Apr. 2011.

[165] Y. Xia, C. Qiu, X. Zhang, W. Gao, J. Shu, and Q. Xu, "Suspended Si ring resonator for mid-IR application.," *Opt. Lett.*, vol. 38, no. 7, pp. 1122–4, Apr. 2013.

[166] Z. Cheng, X. Chen, C. Y. Wong, K. Xu, and H. K. Tsang, "Mid-infrared Suspended Membrane Waveguide and Ring Resonator on Silicon-on-Insulator," *IEEE Photonics J.*, vol. 4, no. 5, pp. 1510–1519, Oct. 2012.

[167] M. Bruel, "Silicon on insulator material technology," *Electron. Lett.*, vol. 31, no. 14, p. 1201, Jul. 1995.

[168] R. A. Johnson, P. R. de la Houssaye, C. E. Chang, M. E. Wood, G. A. Garcia, I. Lagnado, and P. M. Asbeck, "Advanced thin-film silicon-on-sapphire technology: microwave circuit applications," *IEEE Trans. Electron Devices*, vol. 45, no. 5, pp. 1047–1054, May 1998.

[169] C. Z. Gu, Y. Sun, J. K. Jia, and Z. S. Jin, "SOD wafer technology," *Microelectron. Eng.*, vol. 66, no. 1–4, pp. 510–516, Apr. 2003.

[170] A. Yariv, "Coupled-mode theory for guided-wave optics," *IEEE J. Quantum Electron.*, vol. 9, no. 9, pp. 919–933, Sep. 1973.

[171] J. N. Lee, C. Park, and G. M. Whitesides, "Solvent compatibility of poly(dimethylsiloxane)-based microfluidic devices.," *Anal. Chem.*, vol. 75, no. 23, pp. 6544–54, Dec. 2003.

[172] J. T. Robinson, K. Preston, O. Painter, and M. Lipson, "First-principle derivation of gain in high-index-contrast waveguides," *Opt. Express*, vol. 16, no. 21, p. 16659, Oct. 2008.

[173] X. Wang, S.-S. Kim, R. Rossbach, M. Jetter, P. Michler, and B. Mizaikoff, "Ultra-sensitive mid-infrared evanescent field sensors combining thin-film strip waveguides with quantum cascade lasers.," *Analyst*, vol. 137, no. 10, pp. 2322–7, May 2012.

[174] E. S. Snow, F. K. Perkins, E. J. Houser, S. C. Badescu, and T. L. Reinecke, "Chemical detection with a single-walled carbon nanotube capacitor.," *Science*, vol. 307, no. 5717, pp. 1942–5, Mar. 2005.

[175] R. A. McGill, V. K. Nguyen, R. Chung, R. E. Shaffer, D. DiLella, J. L. Stepnowski, T. E. Mlsna, D. L. Venezky, and D. Dominguez, "The 'NRL-SAWRHINO': a nose for toxic gases," *Sensors Actuators B Chem.*, vol. 65, no. 1–3, pp. 10–13, Jun. 2000.

[176] S. V. Patel, T. E. Mlsna, B. Fruhberger, E. Klaassen, S. Cemalovic, and D. R. Baselt, “Chemicapacitive microsensors for volatile organic compound detection,” *Sensors Actuators B Chem.*, vol. 96, no. 3, pp. 541–553, Dec. 2003.

[177] R. K. Paul, S. Badhulika, N. M. Saucedo, and A. Mulchandani, “Graphene nanomesh as highly sensitive chemiresistor gas sensor.,” *Anal. Chem.*, vol. 84, no. 19, pp. 8171–8, Oct. 2012.

[178] Q.-Y. Cai, J. Park, D. Heldsinger, M.-D. Hsieh, and E. T. Zellers, “Vapor recognition with an integrated array of polymer-coated flexural plate wave sensors,” *Sensors Actuators B Chem.*, vol. 62, no. 2, pp. 121–130, Feb. 2000.

[179] J. M. Bingham, J. N. Anker, L. E. Kreno, and R. P. Van Duyne, “Gas sensing with high-resolution localized surface plasmon resonance spectroscopy.,” *J. Am. Chem. Soc.*, vol. 132, no. 49, pp. 17358–9, Dec. 2010.

[180] K. B. Biggs, J. P. Camden, J. N. Anker, and R. P. Van Duyne, “Surface-enhanced Raman spectroscopy of benzenethiol adsorbed from the gas phase onto silver film over nanosphere surfaces: determination of the sticking probability and detection limit time.,” *J. Phys. Chem. A*, vol. 113, no. 16, pp. 4581–6, Apr. 2009.

[181] S. V Patel, S. T. Hobson, S. Cemalovic, and T. E. Mlsna, “Detection of methyl salicylate using polymer-filled chemicapacitors.,” *Talanta*, vol. 76, no. 4, pp. 872–7, Aug. 2008.

[182] L. He, S. K. Ozdemir, J. Zhu, W. Kim, and L. Yang, “Detecting single viruses and nanoparticles using whispering gallery microlasers.,” *Nat. Nanotechnol.*, vol. 6, no. 7, pp. 428–32, Jul. 2011.

[183] F. Vollmer, S. Arnold, and D. Keng, “Single virus detection from the reactive shift of a whispering-gallery mode.,” *Proc. Natl. Acad. Sci. U. S. A.*, vol. 105, no. 52, pp. 20701–4, Dec. 2008.

[184] S. Arnold, D. Keng, S. I. Shopova, S. Holler, W. Zurawsky, and F. Vollmer, “Whispering gallery mode carousel – a photonic mechanism for enhanced nanoparticle detection in biosensing,” *Opt. Express*, vol. 17, no. 8, p. 6230, Apr. 2009.

[185] A. M. Armani, R. P. Kulkarni, S. E. Fraser, R. C. Flagan, and K. J. Vahala, “Label-free, single-molecule detection with optical microcavities.,” *Science*, vol. 317, no. 5839, pp. 783–7, Aug. 2007.

[186] S. Lee, S. C. Eom, J. S. Chang, C. Huh, G. Y. Sung, and J. H. Shin, "Label-free optical biosensing using a horizontal air-slot SiNx microdisk resonator.," *Opt. Express*, vol. 18, no. 20, pp. 20638–44, Sep. 2010.

[187] K. De Vos, I. Bartolozzi, E. Schacht, P. Bienstman, and R. Baets, "Silicon-on-Insulator microring resonator for sensitive and label-free biosensing," *Opt. Express*, vol. 15, no. 12, p. 7610, 2007.

[188] V. A. Bolaños Quiñones, G. Huang, J. D. Plumhof, S. Kiravittaya, A. Rastelli, Y. Mei, and O. G. Schmidt, "Optical resonance tuning and polarization of thin-walled tubular microcavities," *Opt. Lett.*, vol. 34, no. 15, p. 2345, Jul. 2009.

[189] S. Mandal, J. M. Goddard, and D. Erickson, "A multiplexed optofluidic biomolecular sensor for low mass detection.," *Lab Chip*, vol. 9, no. 20, pp. 2924–32, Oct. 2009.

[190] J. Komma, C. Schwarz, G. Hofmann, D. Heinert, and R. Nawrodt, "Thermo-optic coefficient of silicon at 1550 nm and cryogenic temperatures," *Appl. Phys. Lett.*, vol. 101, no. 4, p. 041905, Jul. 2012.

[191] Y. Umasankar and R. P. Ramasamy, "Highly sensitive electrochemical detection of methyl salicylate using electroactive gold nanoparticles.," *Analyst*, vol. 138, no. 21, pp. 6623–31, Nov. 2013.

[192] M. Karimi, "Diffusion in Polymer Solids and Solutions," 2006.

[193] S. C. George and S. Thomas, "Transport phenomena through polymeric systems," *Prog. Polym. Sci.*, vol. 26, no. 6, pp. 985–1017, Aug. 2001.

[194] X. Yang, C. Husko, C. W. Wong, M. Yu, and D.-L. Kwong, "Observation of femtojoule optical bistability involving Fano resonances in high-Q/V[sub m] silicon photonic crystal nanocavities," *Appl. Phys. Lett.*, vol. 91, no. 5, p. 051113, Jul. 2007.

[195] V. R. Almeida and M. Lipson, "Optical bistability on a silicon chip," *Opt. Lett.*, vol. 29, no. 20, p. 2387, 2004.

[196] C. Charlton, A. Katzir, and B. Mizaikoff, "Infrared evanescent field sensing with quantum cascade lasers and planar silver halide waveguides.," *Anal. Chem.*, vol. 77, no. 14, pp. 4398–403, Jul. 2005.

[197] X. Wang, J. Antoszewski, G. Putrino, W. Lei, L. Faraone, and B. Mizaikoff, "Mercury-cadmium-telluride waveguides--a novel strategy for on-chip mid-infrared sensors.," *Anal. Chem.*, vol. 85, no. 22, pp. 10648–52, Nov. 2013.

[198] P. B. Deotare, M. W. McCutcheon, I. W. Frank, M. Khan, and M. Lončar, "High quality factor photonic crystal nanobeam cavities," *Appl. Phys. Lett.*, vol. 94, no. 12, p. 121106, Mar. 2009.

[199] S. Y. Lin, J. G. Fleming, D. L. Hetherington, B. K. Smith, R. Biswas, K. M. Ho, M. M. Sigalas, W. Zubrzycki, S. R. Kurtz, and J. Bur, "A three-dimensional photonic crystal operating at infrared wavelengths," vol. 394, no. 6690, pp. 251–253, Jul. 1998.